UNIVERSITÀ DEGLI STUDI DI GENOVA

ISTITUTO ITALIANO DI TECNOLOGIA

DIPARTIMENTO DI INGEGNERIA MECCANICA, ENERGETICA, GESTIONALE E DEI TRASPORTI

Corso di Dottorato in Ingegneria Meccanica
Curriculum: Tecnologie e Impianti
XXXIII ciclo

Ph.D. thesis

Investigation on the effect of low-pressure plasma treatment on the adhesion properties of different carbon-fiber-reinforced-polymer materials for structural adhesive bonding

Coordinator: Prof. Luca A. Tagliafico
Supervisor: Prof. Carla Gambaro

Ph.D. candidate: Dr. Marco Pizzorni

Date: 14/03/2021

2017-2020

Abstract

This three-part study, developed with the collaboration of the *Istituto Italiano di Tecnologia* (IIT), reports a systematic and quantitative evaluation of the effects induced by various low-pressure plasma (LPP) treatments on the adhesive properties of Carbon Fiber Reinforced Polymer (CFRP) substrates.

In particular, *Part A* of this work was focused on the surface activation of CFRP substrates, made via traditional vacuum-bag technique, which was performed using several combinations of LPP parameters. From the comparison with conventional pre-bonding preparations, it was possible to quantify the effectiveness of LPP in increasing the performance of adhesively-bonded CFRP joints. Further measurements of roughness and wettability were performed, and analyses via x-ray photoelectron spectroscopy (XPS) were also carried out, allowing identification of the morphological, physical and chemical phenomena involved in the treatments.

Then, a quantitative evaluation of the aging behavior of the adhesively-bonded joints was the topic of the subsequent *Part B*. Four significant sets of LPP-treatment conditions were selected, and then subjected to accelerated temperature-humidity aging. To assess the durability of the CFRP-adhesive system under severe aging conditions, tensile shear strength (TSS) testing and wedge cleavage test (WT) were performed in parallel.

The experimental findings showed that LPP treatment of the CFRP substrates results in increased short-term quality of the adhesive joint as well as in enhancement of its durability even under severe aging conditions.

The last part of the work (*Part C*) was inspired by the recent developments in additive technologies for the manufacturing of structural thermoplastic-composite parts. In this context, the mechanical and failure behavior were investigated of continuous carbon-fiber (CCF) composite materials built via Fused Filament Fabrication (FFF) technology when used as substrates for bonded joints. Notably, the experiments were focused on verifying how the additively-manufactured substrates respond to adhesive bonding when the interface interactions are increased by preparing the surface with LPP treatment.

This approach allowed detection of those criticalities that might limit the application of adhesive bonding to 3D-printed composite parts, with respect to that observed using traditional CFRP materials.

Summary

1. Introduction

1.1 Adhesive bonding of carbon-reinforced thermoset composites

The exponential diffusion of *Carbon Fiber Reinforced Polymer* (CFRP) materials in automotive and aerospace manufacturing [1–3] has led to a widespread and progressive search for techniques that allow creation of quality joints, at the same time minimizing deterioration of the substrate and damage to the fibers [4]. Therefore, adhesive bonding is now recognized as the best and least invasive method to obtain joints that ensure high mechanical strength and guarantee excellent quality over time and under different environmental conditions. Besides, adhesive bonding of plastic composites offers advantages over riveted structures, overmolding via mechanical interlocking or other mechanical joining techniques. This is because the adhesive layer yields a continuous bond between the two substrates, minimizes residual stresses, acts as a mechanical buffer between the adherends to absorb energy during impact, and also enhances fatigue-life of the components, preserving all mechanical properties and structural integrity of this material.
However, it is well known that obtaining the proper and desired characteristics is not easy or straightforward. Indeed, adhesive bonding requires an engineering of the entire process, which should involve geometric considerations about areas to be joined, the choice of the most appropriate adhesive according to the conditions under which the component will operate, and proper treatment of the surfaces to be joined. In fact, each adherend-adhesive system has specific properties that are highly dependent on the characteristics of the substrate. It follows that selection of high-performance substrate materials and adhesives having optimal properties might not be sufficient to fulfill the desired quality criteria required for the adhesive joint. For this reason, success of the adhesive bonding process is commonly related to pre-bonding operations (namely, degreasing and treatments) carried out on the faying surfaces to obtain essential characteristics such as good wettability, surface activation, increased chemical interactions between adherend and resin, and proper roughness extent for mechanical interlocking.
The most widely used treatments to prepare CFRP substrates for adhesive bonding are mainly based on the purely mechanical effect provided by roughness increasing and morphological modification obtained either during the composite manufacturing or before application of the adhesive on the substrate. One of the most common surface preparation techniques of CFRP is peel-ply, due to its great simplicity [5]. However, its use is not always justified, especially when high and long-lasting performance of the component is required [6]. Abrasive techniques are of course easier to perform, but, as Wingfield [7] argues, they require more care in avoiding defects or delamination which may badly affect the joint strength. Furthermore, even the risk of contamination brought about by these kinds of treatments has to be taken into account. This is obvious for abrasion and grit-blasting, but real for peel-ply as well. Indeed, as a state-of-the art review by Kanerva et al. [8] highlights,

despite allowing achievement of a more uniform surface, peel-ply often represents an inefficient preparation owing to the residues released after removal of the ply.
Mechanical abrasion is also a widely employed treatment, which - thanks to its effect on increasing surface roughness - enhances the resin capability of coming into contact with the substrate on which it is applied. Although widely adopted, even this method presents limitations: firstly, the variability of resulting surface conditions related to a different experience of the operator makes it difficult to reach suitable process repeatability. Secondly, the mechanical-only action, even if correctly performed, is not always sufficient to fulfil the quality criteria required for the joint [9]. In fact, the bonding process requires a holistic approach, since the premise for good adhesion of resin to substrate lies mainly in the chemical-physical affinity established between the parts involved [10–12]. In the specific case of CFRP substrates, this translates into the need for treatment to reach the following objectives:

- to increase the wettability of the substrate, *i.e.*, to enhance its surface free energy so that the adhesive is able to spread easily on substrate independently of its viscosity, without leaving voids, and filling any micro-cavities that may be present;
- to activate the surface, increasing functional groups already present or creating new ones, so that they can interact with the adhesive molecules by creating strong covalent bonds with them;
- not to damage the substrate surface, removing too much resin from its matrix until the fibers are uncovered or ruining the reinforcement fibers.

Hence, in recent years, valid alternatives have been sought and non-standard physical processes have garnered an increasingly widespread interest. Most of these are based on laser processes, which can be employed with different laser sources. As an example, Palmieri et al. [13] describe performance evaluations of peel-ply and laser ablation treatments, the latter performed by using a Nd:YAG laser-source. Interesting results are also shown by Oliveira et al. [14], who employed a Yb:KYW chirped pulse-regenerative amplification laser system, and analyzed its morphological effect by varying process parameters and direction of the carbon fibers. Use of laser, however, requires in-depth experience of the process and knowledge of the proper wavelength to adopt in order not to damage the substrate, as highlighted by Reitz et al. [15] with a comparison between UV- and IR-laser pretreatments for CFRP/aluminum adhesive joints.
As stated by Ebnesajjad and Landrock [6], among the physical treatments suitable for CFRP materials, plasma processes have also been increasingly attracting attention, thanks to advantages that include contaminant removal, surface activation, and ease in the process management and automatization. Specifically, use of plasma on carbon fibers as adhesion promoter to the polymer matrix is already well known [16–18]; in a similar way, the matrix can also be activated following exposure to plasma, both at atmospheric pressure or in vacuum conditions [19–22]. Plasma treatments of polymer substrates generally result in

morphological modification, oxidation and, thus, enhancement of surface wettability, as observed by Williams et al. [7] treating CFRP laminates with an atmospheric pressure He/O_2-plasma. As Baldan [8] explains, the more these effects are concurrent, the more the interactions between adhesive and adherends are stronger and more stable (in terms of both type and number of such interactions), and, consequently, the more the adhesive joint shows high resistance. In this regard, Iqbal et al. [23] recognized that plasma treatment is particularly suitable for treatment of high-performance polymer and composite materials, like polyetheretherketone (PEEK) and fiber-reinforced polyphenylene sulfide (PPS), respectively.

In this scenario, *Low-Pressure Plasma* (LPP) treatment also has the potential to play a key role. LPP seems to be preferred for complete preservation of the polymer matrix of CFRP substrates, which do not undergo any heating during treatment, avoiding even slight deterioration of the polymer. Thus, low-temperature plasma treatment is promising for pre-bonding activation thanks to its ability to modify the substrate surface without affecting the bulk properties. In addition, the process is highly reproducible since plasma affects the entire component to be treated even in case of complex surface geometry of the specimen.

In other terms, such a physical treatment may represent for CFRP what chemical etching treatment already represents for metal alloys based on Aluminum or Titanium [11,24], entailing increase of both strength and durability of the joints. However, LPP does not suffer the same disadvantages. In fact, although not always cheaper than other treatments, plasma preparation is of course more automatable. In this regard, consider a comparison with chemical treatments typically used on Ti-6Al-4V, such as SHA or NaTESi processes [11,25,26]. These envisage a series of critical steps, which contemplate use of hazardous materials and, thus, require highly-qualified personnel. Thinking about industrial implementation, this raises the need to provide adequate safety equipment and waste disposal systems, satisfying all strict requirements of the regulations (as an example, DIN 6701 in the railway industry). The chemical process must also be constantly monitored, programming periodic and close sampling of the chemical baths aimed at qualifying the maintenance of the solution integrity, as well as control of all electric parameters, where anodization is performed. Obviously, moreover entailing considerable operating costs, the automatization is certainly reduced compared to plasma treatment. The latter, indeed, does not require any special preparation of personnel: the operator introduces the material to be treated into the treatment chamber and starts the process according to a pre-defined procedure, setting only parameters such as treatment time and power. The costs referred to, in this case, are related to the initial investment of the machine (obviously connected to the dimensions of the chamber and the vacuum pumping system) and to the procurement of the process gas. However, like any other surface treatment (chemical, but also physical or mechanical), the need for extensive substrate preparation increases the overall cost of the process and is generally time-consuming, especially when the best treatment conditions are unknown.

Nevertheless, the evaluation of the treatment quality and related joint behavior cannot ignore the work conditions to which the assembled component will be subjected. Indeed, as stated by Sargent [27], “Designers are not usually concerned with the as-manufactured strength of

bonded joints, but with the lowest level to which the strength will fall during the life [of the component] due to adverse effects of the environment".
Thus, to establish success of LPP for CFRP substrates to be adhesively bonded, it is necessary to verify whether and how much its qualities are maintained even under severe ambient conditions. Budhe et al. [28] highlight that the most common environmental threats are indeed related to the effect of both temperature and moisture absorption; when they act simultaneously, hygro-thermal aging occurs, seriously affecting strength and durability of the composite joint. Indeed, most researchers (see Reis et al. [29] and Zafar et al. [30]) report an overall joint strength reduction during aging, the rate of which depends on exposure time and environment along with the adhesive system undergoing conditioning.

In view of such considerations, the evaluation of effects of various treatments on both short- and long-term properties of CFRP-to-CFRP adhesive-joining was the object of *Part A* and *Part B* of this work. The experimental results show that LPP treatment of the CFRP substrates results in an increased short-term quality of the adhesive joint as well as in enhancement of its durability even under severe aging conditions.

1.2 New developments in composite fabrication: additive manufacturing

In the wake of the wide diffusion of thermoset CFRP materials, in recent years, the technologies around reinforced thermoplastics have also seen rapid growth and evolution. Manufacturing sectors that are traditionally capable of substantial investments in promising materials and technologies (e.g. aerospace, motorsports, high-end automotive and robotics [31,32]) have witnessed the increasing application of such composite materials. It is now possible to fabricate components with exceptional strength, low-weight, high stiffness and versatility. These advantages have pushed thermoplastic composites to gradually overcome the barriers of those sectors in which they were first introduced, also thanks to parallel technological innovation in manufacturing processes. Among the latter, *additive manufacturing* (AM) has greatly simplified the production of composite components, making it more affordable in terms of equipment, costs and process management [33], garnering increased interest among both researchers and developers. This advance is also related to the possibility of combining the wide range of composite materials available today with a manufacturing process that allows great freedom in the design and customization of components.
Among all the AM technologies, *Fused Filament Fabrication* (FFF) is the most widely used prototyping method employing pure or filled polymer materials [34–38]. This technique allows the construction of parts through the extrusion of a thermoplastic filament, to generate the desired thickness as a sum of subsequent layers deposited on the printing bed.
As opposed to subtractive methodologies, this AM technology presents two fundamental features: direct manufacturing and layer-wise processing [32,36]. FFF is especially advantageous thanks to its process flexibility, robustness and reliability, low material wastage and relatively low cost of printers and consumables [33,37]. These factors have

brought about a progressive technological evolution, allowing new challenges to be faced and different fields of application. Despite this, FFF polymer-only parts generally present typical features that make them unsuitable for many structural applications. Indeed, their poor mechanical characteristics can limit the application of 3D-printed components with respect to injection-molded ones, due to an intrinsic non-homogeneity that leaves their main role as prototypes [39,40]. However, as mentioned before, the advances in material science and technology are having a significant impact on both the design and manufacturing approaches focused on AM, thanks to the possibility of enhancing the mechanical properties of the printed parts by introducing continuous fibers embedded in the polymer matrix. In particular, this advance has affected FFF, remarkably improving the mechanical performance of the so-built parts, with the aim of generating composite materials having performance and applications similar to those of traditional ones [31,41].

In this scenario, FFF of polymer composites is becoming a more and more promising solution for changing AM from a prototyping technology to an effective process to be employed in real-world applications. For this reason, several industries, namely aerospace, automotive, or robotics, are pushing AM as an alternative method for the production of their composite components [31].

Generally speaking, FFF technology dedicated to the fabrication of composite materials (also known as *Composite Filament Fabrication*) is based on the same principles as the more conventional one for the additive generation of polymer-only parts. Indeed, the components are created by depositing material, layer by layer, starting from three-dimensional (3D) geometries designed via Computer-Aided-Design (CAD) software, and imported into the 3D-printer affiliated software to set the infill pattern.

Although this method has been studied over the past decade, specifically focusing on polymer-matrix components filled with chopped fibers [42], additive processes for the manufacturing of continuous-fiber reinforced thermoplastics are still at an embryonic stage. Most of the literature focused on this topic is concentrated in the past three years (2017-2019), thus little is still known about the building criteria to adopt or the mechanical response of the 3D-printed composite parts.

Some of the preliminary works on this topic were carried out by Justo et al. [43], who performed tensile and compression tests, and by Blok et al. [44], who performed tensile and flexure tests on mixed polyamide and continuous carbon fiber composites made via FFF.

Chacón et al. [45] performed extensive testing on specimens in tensile and three-point bending conditions to assess the effect of build orientation, layer thickness and fiber volume content on the mechanical performance of components made via FFF.

The influence of other process parameters such as the build orientation (*i.e.*, 'flat' or 'on-edge', with respect to the printing bed) on the impact resistance of 3D-printed composites was investigated by Caminero et al. [46]. In a parallel study, the same authors also examined the interlaminar bonding performance of such materials, relating their behavior to process parameters such as layer thickness and fiber volume fraction [47]. Dickson et al. [48] compared different types of fibers (glass, carbon, and Kevlar), testing tensile and flexural specimens having a unidirectional arrangement of the fibers, by varying the number of the

layers built. Materials similar to the latter were also evaluated for creep and fatigue by Mohammadizadeh et al. [49]. The flexure behavior of 3D-printed specimens reinforced with continuous glass or carbon fibers, arranged unidirectionally, was then studied by Goh et al. [50]. Araya-Calvo et al. [35] specifically investigated the compressive and flexural response of continuous carbon-fiber (CCF) 3D-printed parts, focusing on the effect of factors such as the reinforcement type and distribution inside the specimen bulk. On their part, Mei et al. [51] evaluated the tensile properties of 3D-printed composite specimens made by arranging the fiber with a mixed-orientation. The tensile and flexural behavior of CCF test specimens was also assessed by Yu et al. [52], who focused on the influence that the number of fiber layers and concentric Onyx rings has on such properties.

Al Abadi et al. [53] performed experimental testing and developed an analytical model to help to predict the elastic properties of CCF components. Pyl et al. [54] carried out some exploratory work to characterize the change of mechanical resistance with varying fiber orientations, although only with a limited set of samples and only in traction.

The main results found in the literature are summarized in **Table 1.1**. Interestingly, a broad diversity of results can be observed, both in terms of numerical values of the tensile and flexural strengths, as well as in terms of testing methodologies and testing approaches.

This overview thus highlighted that several efforts have been (and are being) made to identify proper printing methods and related parameters for the fabrication of such materials. However, as also recently pointed out by Kabir et al. [41], there is still a lack of research on aspects that may be equally helpful to understand to what extent AM-CFRT materials can be used and what challenges remain. One of these is related to the small size of printers, which limits the dimension of the built components, making it usual that the final product might be realized by joining a number of additively-manufactured smaller parts. Alternatively, printed components, built to replace damaged components, might need to be joined to pre-existing parts. As a consequence, the design criteria at the basis of 3D-printing of composite components have to follow a ‘building-block’ approach, causing assembly operations to have to be integrated into the manufacturing process.

As previously stated, adhesive bonding is recognized as the best and least invasive joining method for pure or reinforced plastics today, ensuring excellent mechanical performance and guaranteeing high quality in different operative conditions. Such features appear perfectly suitable also to be combined with additively manufactured composite substrates, in order to obtain the maximum performance from adhesive joints. However, for its part, 3D printing must allow fabrication of composite components in such a way as to make any assembly operations possible, safe and reliable. Indeed, composite structures, and particularly those built additively, are inherently non-homogeneous. So, how does this aspect affect the joint behavior? To what extent is it possible to obtain quality joints with adhesively-bonded 3D-printed composites?

Hence, the third part of this experimental work was focused on verifying how the additively manufactured substrates respond to adhesive bonding when the interface interactions are increased by preparing the surface.

Table 1.1
Overview of studies on 3D-printing of CCF composites

Tensile strength (MPa)	Tensile modulus (GPa)	Flexural strength (MPa)	Flexural modulus (GPa)	Fiber orientation	Test standards	Fiber volume	Fill type	Contour rings	Fiber layers	Ref.
800	60	540	51	0°	ASTM D3039 / ASTM 790					Markforged
404				0°	ASTM D638-14	58%	Isotropic			Mohammadizadeh et al. [49]
236				0°	ASTM D638-14	58%	Concentric	5		
331				0°	ASTM D638-14	58%	Other	2		
600	13			0°	ASTM D3039	41%	Isotropic			Goh et al. [50]
		430	38.1	0°	ASTM D790	41%	Isotropic			
315	37			0°	ASTM D3039	40%	Concentric	12	10/20	Al Abadi et al. [53]
69	3.33			$[30°/45°/60°]_2$	ASTM D3039	11%	Concentric	2	6/32	Mei et al. [51]
64	3.2			$[15°/45°/75°]_2$	ASTM D3039	9%	Concentric	2	6/32	
79	3.51			$[0°/45°/90°]_2$	ASTM D3039	9%	Concentric	2	6/32	
719	58			0°	ASTM D638-14				18/26	Pyl et al. [54]
217	17.55			[0°/+90°]	ASTM D638-14					
133	10.89			[0°/90°/+45°/-45°]	ASTM D638-14					
48	4			[+45°/-45°]	ASTM D638-14				5/17	
123	3.9			0°		44%	Concentric	3	8/26	Yu et al. [52]
		270.6	17	0°	ASTM D6272-17	49%	Concentric	6	18/28	
701	68			0°	ASTM D3039	40%	Other			Justo et al. [43]
216	7.7	250.2	13	0°	ASTM D3039 / ASTM 790-10	11%	Concentric	6	8/26	Dickson et al. [48]
97	7.6	80.7	3.1	0°	ASTM D3039 / ASTM 790-10	2%	Isotropic		2/32	Chacón, et al. [45]
240	25.3	355.6	31.1	0°	ASTM D3039 / ASTM 790-10	15%	Isotropic		16/32	
437	51.7	423.5	39.2	0°	ASTM D3039 / ASTM 790-10	26%	Isotropic		28/32	
64	5.2	38.1	1.6	0°	ASTM D3039 / ASTM 790-10	2%	Isotropic		28/102	
177	17.6	122.3	6.9	0°	ASTM D3039 / ASTM 790-10	15%	Isotropic		74/102	
341	31.6	157.1	12.1	0°	ASTM D3039 / ASTM 790-10	20%	Isotropic		98/102	
968	62.5	485	31.2	0°	ASTM D638 / ASTM D7264	27%	Other			Blok et al. [44]
		83	5.16	0°	ASTM D790-15	17%				Araya-Calvo et al. [35]
		143.3	8.89	0°	ASTM D790-15	32%				
		231.1	14.17	0°	ASTM D790-15	49%				

2. Adhesive bonding

2.1 Overview

The term *adhesive bonding* refers to the technological process through which a permanent and continuous bond between two or more parts is obtained by means of the interposition of an *adhesive*. The latter is a non-metallic substance - of natural (glue) or synthetic (resin) origin - capable of achieving stable union as a result of a chemical reaction, called *cross-linking* or *polymerization*, between the resin and a proper *activator*. During this reaction, the adhesive molecules bind together to form the final polymer chains, determining the physical properties of the adhesive itself. Obviously, polymerization has to take place only after the adhesive has been deposited on the substrate and the two flaps have been joined. Therefore, the service life of an adhesive, along with quality and durability of the joint, are inextricably linked to two fundamental parameters:

- the *shelf life*, which indicates the storage period (in warehouse or refrigerator) of the product inside its unopened package before it loses its characteristics;
- the *pot life* or *work life*, namely the maximum time admitted for the application of the adhesive after mixing of its components.

Fig. 2.1 shows a schematization of an adhesive-bonded joint obtained via overlapping. In it, one can identify the two *adherends* (or *substrates*), each representing the surface portion that has to be coupled to the other by means of adhesive. The substrate has to be subjected to a preliminary, specific pre-bonding treatment that makes it suitable for bonding, eliminating contaminants and creating proper adhesion conditions. In addition, it might be necessary to preserve the effect of the treatment and avoid its deterioration before applying the adhesive. To do this, we resort to application of special paints, named *primers*, on the treated surface; these may only have a protective action against any recontamination, or also act as adhesion promoters, increasing the adhesion properties of the surfaces to be bonded.

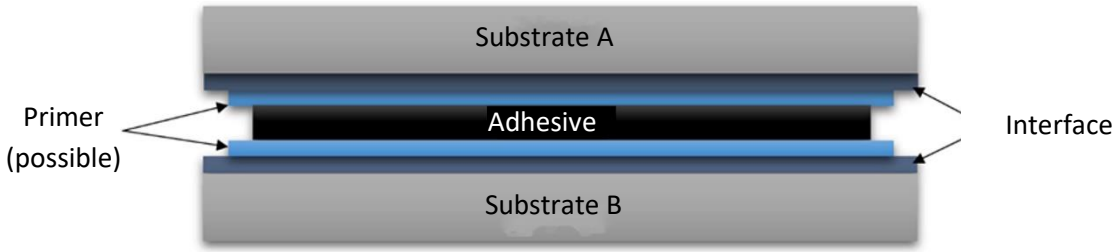

Fig. 2.1. Scheme of an adhesive-bonded joint.

The widespread interest in adhesive bonding as excellent alternative to more traditional joining methods is essentially related to various advantages, which are suitable and

appreciated in most of the more demanding applications requiring high quality standards and maintenance of suitable sealing characteristics even in extreme operating conditions.
Firstly, by eliminating the weight of rivets, bolts or (in case of welding of metals) of filler material, the use of adhesives allows one to obtain lightweight structures, especially when the application requires structural adhesives, for which small thicknesses of resin are commonly adopted.
An additional factor is that strength of a bonded joint made by overlapping two substrates is ensured by the *overlap area* and not by the component thickness; therefore, if a solution of this kind can be adopted, this allows use of thinner base materials, and this translates into a further weight reduction of the overall structure.
Adhesive bonding being a continuous-type joining, the so-made joints typically present a more uniform distribution of stresses on the joining portion (**Fig. 2.2**) compared to that obtained with riveted or bolted joints, in which the holes may affect the base-material integrity and determine local stress concentration. Moreover, the stress condition of a bonded joint is of lesser extent than that of an equivalent welded joint, since the latter undergoes the action of both external stresses and residual stresses originating during the weld bead solidification.

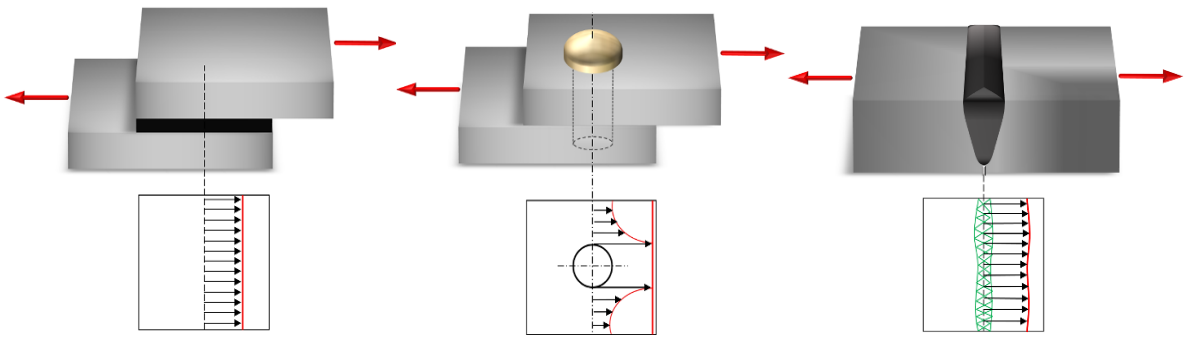

Fig. 2.2. Stress acting on different types of joints, from left to right: adhesive-bonded, riveted and welded joint.

It is also worth noting that, when thermosetting adhesives are used, there is certainly heating of the glued area, due to both the effect of heat generated during the polymerization reaction and any post-curing heating in an oven adopted to accelerate hardening of the resin. However, such temperatures are lower than those occurring in welding and brazing and, in any case, insufficient to cause distortions of the substrates or local alterations in the mechanical properties of the base material.
Furthermore, given their deformability, polymeric adhesives also play a key role in damping vibrations; compared to other kinds of joints, with the same thickness of the substrates, this also confers greater resistance to cyclic stresses, thus increasing fatigue life of the bonded joint. Moreover, the barrier effect of the resin layer also has to be highlighted towards crack propagation between one substrate and the other. This advantage, in principle, also manifests as protection against liquid infiltrations, which is assisted by the absence of holes, hence

allowing obtainment of joints that guarantee optimal hydraulic seal (obviously, the interacting fluid must be compatible with the adhesive and must not involve any resin degradation).
What is more, polymeric or ceramic adhesives allow electrical and thermal insulation between the adherends, thereby inhibiting galvanic corrosion. Nevertheless, in some applications it is necessary to make the adhesive conductive, and thus metal fillers are mixed into the resin (this is the case, for example, of adhesives dedicated to high temperature applications, which are typically filled with aluminum powders).
An essential advantage of adhesive bonding is found in the possibility of making effective assemblies even between materials of a dissimilar nature, such as steel and aluminum, glass and metals, metals and composites, metals and plastics, otherwise not weldable together. In fact, this assembly method generally preserves structural integrity and leads to stiffness of the product, even if made between components having different thicknesses, chemical state, thermal expansion coefficients or elasticity modules.
From a cost point of view, the realization of adhesive-bonded components is in line with other joining techniques. This method involves the use of specific equipment, particularly for the material storage (refrigeration systems are generally needed for conservation of resins), for surface preparations (tools for mechanical abrasion, systems for pickling and chemical baths, plants for plasma or laser treatment, etc.), for joint manufacturing as well as subsequent curing of adhesive (tools for mixing and application, ovens).
One of the difficulties encountered in design and construction of adhesive-bonded structures is related to exact knowledge and prevision of the effects of environmental agents on the adhesive system. When selecting an adhesive, it is necessary to consider both the operating thermal conditions and any temperature changes since, in many cases, the mechanical characteristics of the joint tend to decay at high temperatures, and thermal shocks can cause adhesive embrittlement. Humidity may also have negative effects on the joint behavior; indeed, the adhesive, especially if polymeric, can absorb water from the ambient, which migrates to the adhesive/adherend interface, weakening it. Besides, environments that are chemically aggressive or particularly exposed to X or UV radiation may determine adhesive degradation.
Before application of the adhesive, it is also necessary to pay particular attention to properly preparing the substrate surfaces in order to remove any contaminants that may compromise the adhesion interactions.
A limit is also found in the setting time of the adhesive, since productivity depends on the adhesive used and the time the latter needs to reach complete hardening; in some cases, therefore, this can affect large-scale production negatively. On the other hand, local repairs of the joint are difficult to carry out once hardening is obtained, and disassembly of the bonded component is often needed.
Finally, it is necessary to take into account the impact of the adhesive-bonding process on both the operator involved in the joint fabrication and the environment, because of toxicity of adhesives and high ignitability of the solvents used. This aspect has serious implications

on safety, and requires provision of appropriate systems for the end-of-life disposal of the assembled parts.

In view of the aspects briefly described above, it is evident that the positive outcome of an adhesive-bonded joint depends to a large extent on accuracy of the joint design; the latter, in turn, must always go hand in hand with the selection of adhesives and substrates best suited to the specific need.

2.2 Principles of adhesive bonding

Adhesive bonding is essentially based on two cooperating and synergic phenomena: the *cohesion* between internal molecules of the adhesive and the *adhesion* between adjacent molecules of substrate and adhesive (**Fig. 2.3**). The former is therefore an intrinsic property of the adhesive that, depending on the attractive forces established inside the bulk, may be taken as a measure of its mechanical strength. The greater the intensity of such forces (applied to obtain reciprocal displacements of the atoms present within the structure), the higher the cohesion of the material. On the contrary, affecting the actual adhesive-adhering contact area, the adhesion represents the ability of the resin to adhere to the support surfaces, creating stable bonds with them.

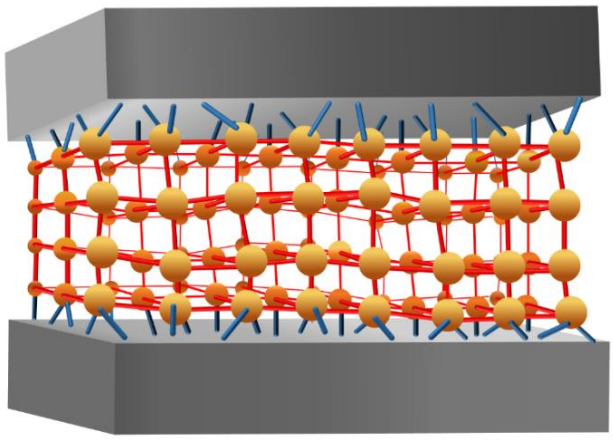

Fig. 2.3. Schematic representation of cohesive (red) and adhesive (blue) bonds.

The interaction forces, however, determine an imbalance in the thinner layers of the resin since the atoms present there, exercising their action in every direction, undergo an attractive action only inward. There follows a resulting attractive-force field that faces outward, which determines the surface tension of the adhesive and, hence, adhesion with the substrate in contact. In this regard, it is clear that the adhesive phenomena entirely involve the surface of the support. In other terms, they develop not only on the free surface of the material to be bonded, but also on any undesired elements deposited on it, the presence of which is inevitably detrimental for the joint strength. Indeed, whatever substrate interacting with the adhesive, this is a dynamic and often chemically indefinite region, which is affected by its

own basic composition, history and environment. Even the composition and morphology of the adhesive at the interface are not uniquely defined: for example, contaminants and products segregated from the substrates may catalyze or inhibit polymerization; in the same way, the solvents contained in the resin may react with the adherends, increasing segregations.
Hence, as mentioned before, the high number of unknown factors and variables prevent a precise knowledge of the interface state. It is thus essential to provide for an accurate preparation of the surfaces to be joined in order to control this region, create the proper surface conditions, and make the bonding process as reproducible as possible.
In light of these considerations, the possible stress conditions acting on the adhesive joints may cause different types of failure (**Fig. 2.4**):

- *Cohesive Failure* – CF (**a**): the cohesive bonds yield under the action of the load and, therefore, a cracking is observed more or less centered within the adhesive layer. Once complete failure has occurred, each substrate presents adhesive on its surface. This behavior is typically attributable to an incorrect choice of adhesive during the joint design;
- *Adhesive Fracture* – AF (**b**): the acting load causes breakage of the adhesive bonds with consequent separation at the interface: the entire layer of adhesive covers only one of the two substrates, whereas on the other the free surface is completely exposed. This type of failure is generally indicative of an unsuitable or ineffective pre-bonding treatment;
- *Substrate Failure* – SF (**c**): this involves one or both adherends, and is due to inadequate mechanical resistance of the base material to the stress applied; although, from the point of view of the quality of the adhesive bonding, this is the most desirable condition (the adhesive joint is intact), it is however attributable to an incorrect selection of the base material (or of the thickness of the pieces) by the designer.

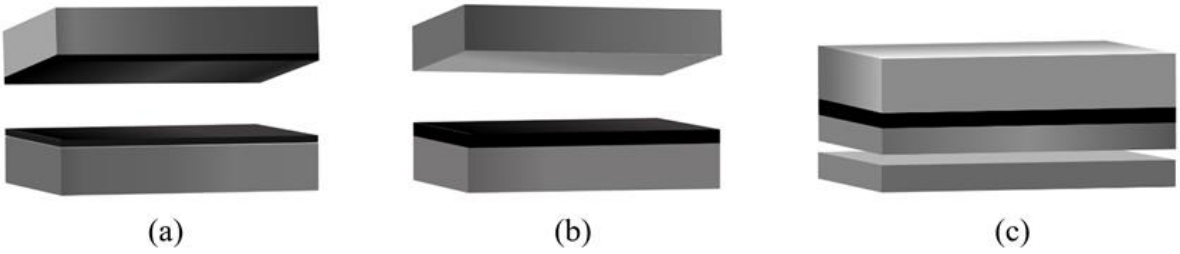

Fig. 2.4. Main failure modes of an adhesive joint: (a) de-cohesion, (b) de-adhesion and (c) substrate failure.

It should be pointed out that, in most of real-world cases, joint failure occurs almost always in compresence of several phenomena, so a fracture will never be completely de-adhesive nor totally de-cohesive in type. It follows that the following failure modes can also be defined:

- *Special Cohesive Fracture* – SCF: the failure surface occurs in the adhesive layer, but is positioned near the substrates, namely, where the adhesive is characterized by polymeric chains having high molecular weight. In this case, the ultimate resistance of the joint is not that of the adhesive. However, SCF (as well as AF) is common in case of high-modulus adhesives applied on rigid, thin substrates, even when optimal conditions for adhesion are guaranteed by the process; in this case, such a failure mode can be accepted on the basis of further evaluations of the joint performance decrease after aging;
- *Mixed Adhesive-Cohesive Failure* – ACF: this is the most common failure mode in real-world applications, in which breakage is partly de-adhesive and partly de-cohesive in type.

This confirms how an adhesive-bonded joint must be considered as a whole, composed of parts in intimate interaction with each other: only a holistic approach, in fact, can allow prediction of the behavior of the assembly during use.

2.3 Mechanisms and theories of adhesive bonding

Given the complexity of the adhesive processes due to combined effects of different factors and multiple variables, the study of the adhesion phenomena has been addressed over time by developing different theories, each focused on specific aspects. However, this work was carried out keeping the synergy between the phenomena involved– whether physical or chemical – always in evidence, in order to foster the holistic approach needed in this research field.

The most classic of the theories is the *mechanical* one, according to which success of adhesive bonding is directly related to phenomena of *mechanical interlocking* between resin and adherend. In particular, the probability of having adhesive bonds between adhesive and substrate increases proportionally with the contact area extent. The latter, with the same macroscopic geometric parameters, can be increased by acting on the substrate surface roughness (e.g., via mechanical abrasion or sandblasting). Therefore, the mechanical theory bases its validity essentially on two considerations:

- an increase in surface roughness corresponds to an increase in adhesion;
- the greater the dimensional compatibility of the adhesive molecules with the substrate interstices, the greater the adhesive strength (**Fig. 2.5**).

Fig. 2.5. Dimensional compatibility of the adhesive molecules with the irregularities of the substrate.

However, establishing a surface finishing as the only result of a treatment is indicative, but not sufficient to obtain the desired performance from the joint. Indeed, the increase in roughness has a limited influence on adhesion: if roughness exceeds a certain critical value, it may happen that the contact between the two materials is incomplete and, consequently, there will be a decrease in adhesion due to the voids generated between the materials. Speed and depth of the adhesive infiltration inside the surface irregularities are characteristics that depend on its viscosity: therefore, an increase in viscosity reduces the adhesive penetration, while generally allowing better control over the thickness of the resin applied.

A second theory is *electric*, according to which, when two different materials are brought into contact, a migration of charges occurs between them, with consequent generation of a double electric layer. In this way, the adhesive-adherend system behaves as a condenser, whose plates (*i.e.*, the two surfaces at the interface) can only be separated by doing work. This phenomenon is more evident in absence of humidity and is reflected in numerous experiments of peeling films from substrates (during the tests, electric discharges occur at the areas of separation of the two materials). On the other hand, there are some inconsistencies between expected and real behavior: first of all, the fact that, while one would expect low adhesion between identical materials and higher between different materials, in reality, exactly the opposite happens.

A further theory is the so-called *diffusion theory*, which is based on the phenomenon of mutual molecular solubility of polymeric materials (thus, only valid for polymers). In particular, this theory involves the inter-diffusion of macromolecules between the adhesive and the substrate across the interface.

In addition to those briefly described above, a further theory based on chemical interactions is widely appreciated. This is the *chemical theory*, according to which adhesion is achieved thanks to chemical bonds established between one or more chemical species present on the adhesive surface, and one or more species on the adherend, compatible with the former. Today, this represents the most robust and reliable theory for predicting, estimating and calculating the degree of adhesion of all classes of materials (polymers, metals, ceramics). In particular, its physical evidence is found in phenomena concerning interfacial free energy and the consequent concept of surface wettability.

Hence, in the next paragraph, the phenomena underlying the principles of wettability and contact angle will be defined. Then, some of the main models commonly used for this measurement will be described, so as to finally motivate the choice of the method adopted in the current analysis for the preliminary characterization of treated surfaces.

2.4 Interfacial contact and wetting equilibrium

The possibility of an adhesive to adhere to substrate is directly related to the proper wetting features of the surface of the latter. Indeed, to have adhesion, it is necessary that the adhesive is able to ‘wet’ the surface on which it is applied and, therefore, to spread on it as easily as possible.

It should be duly considered that, in general, poor surface wettability leads to poor adhesion, whereas the opposite is not true, since a highly-wettable surface does not uniquely identify a condition of good adhesion. Indeed, a surface can be wettable, but have bad adhesion with a specific adhesive; this is due to absence (or insufficiency) of chemical affinity between adherend and adhesive. This aspect makes wettability a necessary but not sufficient condition to establish the potential degree of compatibility in an adhesive-substrate system.

To understand the concept of surface wettability, the definition of *surface tension* (N/m) or *surface energy* (J/m^2) cannot be ignored. It represents the resultant of the attraction forces between the molecules in the material bulk and at the surface region, which tends to minimize the number of molecules present in the latter. Indeed, while the chemical units inside the material are in a stable equilibrium condition, those placed on the surface exert their action in all directions, but undergo an attractive action only inward. The presence of open bonds (*dangling bonds*) at the interface follows, which cause an outward attraction field, usually concerning the first 10 Å from the surface.
Thus, the theoretical approach to which we have to refer is the energy one, which finds its original expression in *Young's equation* (**Eq. 2.1**): this describes the behavior of a drop of liquid on a flat, ideally smooth surface, correlating the surface free energies of the solid γ_S (= γ_{SV} between solid and vapor state), of the liquid γ_L (= γ_{LV} between liquid and vapor state) and the interfacial energy γ_{SL} with the contact angle θ between drop and surface:

$$\gamma_L \cos\theta = \gamma_S - \gamma_{SL} \qquad (2.1)$$

In this regard, consider **Fig. 2.6**, in which a drop deposited on a solid surface is shown.

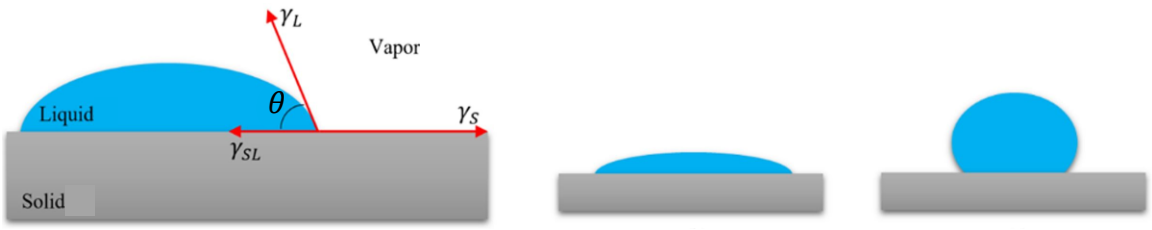

Fig. 2.6. (a) Contact angle and equilibrium among the surface energy components at the triphasic point. In (b) and (c), a schematic representation is also shown of surfaces having hydrophilic and hydrophobic behavior, respectively.

In accordance with Young's equation, in case (a), the drop is in a state of equilibrium due to balancing between the γ_S component (that tends to make the drop spread on the solid surface) and the γ_{SL} and γ_L components (that tend to oppose its expansion instead). The contact angle θ arises from the mechanical equilibrium between the aforementioned actions and, hence, is conventionally defined as the angle that the tangent to the liquid drop forms with the solid-

liquid interface tension at the point of coexistence of the three phases (solid, liquid and vapor), namely the *triphasic point*.
Ideally, θ angle can take values ranging from 0° (super-hydrophilic surface) to almost 180° (super-hydrophobic surface). Typically, a surface is considered wettable if θ < 90°, despite the increase in wettability following the decrease of this angle and, therefore, the tendency of $\cos\theta$ to one.
Through *Dupré's relation*, it is possible to express the work of adhesion as follows:

$$W_{adh} = \gamma_S + \gamma_L - \gamma_{SL} \qquad (2.2)$$

that, combined with **Eq. (2.1)**, provides the so-called *relation of Young-Dupré*:

$$W_{adh} = \gamma_L\,(1 + cos\,\beta) \qquad (2.3)$$

The latter highlights the dependence of the work of adhesion on the contact angle. A requirement for the optimization of W_{adh} is to adopt substrates having high surface free energy and minimize γ_{SL}. This occurs when $\gamma_L < \gamma_S$: under this condition, the liquid will have a natural tendency to spread over the solid support.
This is the reason why adhesive bonding of polytetrafluoroethylene (PTFE) material is difficult (indeed, its surface free energy is lower than that of any adhesive currently available). Therefore, this condition must guide the selection of any adhesive-substrate combination. As an example, consider coupling between polyethylene (γ_{PE} = 33 mJ/m^2) and epoxy resin (γ_{EP} = 45 mJ/m^2): since $\gamma_{PE} < \gamma_{EP}$, poor adhesion is obtained when liquid epoxy resin is applied on a solid PE substrate; *vice versa*, adhesion would be good.

In contrast to the surface tension of a liquid – the determination of which is possible through direct experimental methods –, the evaluation of the wettability properties and the determination of the surface energy of a solid substrate is possible only using indirect methods. These require, first of all, the empirical measurement of θ (as we shall see, here obtained via sessile drop technique).
Once the contact angle has been acquired using one or more test liquids of known characteristics, it is necessary to proceed with the determination of the surface energy of the substrate. However, Young's classical equation contains only two known quantities (θ and γ_L) and thus the problem is underdetermined. Hence, in order to establish the two unknown quantities γ_S and γ_{SL}, different mathematical models have been developed, allowing this equation to be solved analytically.
These models are based on the idea of partitioning the surface free energy into individual components. The interfacial tension γ_{SL} is indeed determined on the basis of different interactions that depend on the properties of both the liquid used and the solid investigated.
A first approach of this kind was experimented by Fowkers, who postulated that the total surface energy of a solid could be expressed as the sum of various contributions, each referred to a specific type of intermolecular force:

$$\gamma_S = \gamma_S^d + \gamma_S^p + \gamma_S^H + \gamma_S^i + \gamma_S^{ab} + \gamma_S^o \qquad (2.4)$$

where the terms represent, in order, the dispersive and polar components of the surface energy, the fractions connected to hydrogen bonds, to inductive phenomena, to acid-base interactions, while the last term refers to all the other possible interactions not considered previously. In this model, the dispersive component, γ_S^d, depends on London's interactions resulting from electronic dipole fluctuations. Such intermolecular forces are generated between the two interacting systems due to mutual attraction between atoms and adjacent molecules. The remaining Van der Waals' interactions due to the permanent dipoles (Keesom and Debye) are instead integrated in the inductive component γ_S^i .
Compared to Fowkers, Owens and Wendt considered that the total surface energy depended on dispersive and polar contributions only, according to the following **Eq. (2.5)**:

$$\gamma_S = \gamma_S^d + \gamma_S^p \qquad (2.5)$$

In this case, the polar component includes hydrogen, induced and acid-base interactions. On the contrary, the dispersive fraction assumes the same meaning as the previous model. The relationship used for this model is:

$$\gamma_{SL} = \gamma_S + \gamma_L - 2\left(\sqrt{\gamma_S^d \cdot \gamma_L^d} + \sqrt{\gamma_S^p \cdot \gamma_L^p}\right) \qquad (2.6)$$

where the solid-liquid interfacial tension is obtained from a geometric mean of the polar and dispersive components of the two phases; replacing Young's equation, **Eq. (2.6)** is equivalent to:

$$\sqrt{\gamma_S^d \cdot \gamma_L^d} + \sqrt{\gamma_S^p \cdot \gamma_L^p} = \frac{1}{2}\,\gamma_L\,(1 + cos\,\beta) \qquad (2.7)$$

Since both the unknown quantities γ_S^d and γ_S^p are present in the latter equation, a contact-angle measurement is needed using at least two different liquids (one polar and one dispersive) on the same surface. Consequently, a system of two equations in the form of **(2.7)** – each referred to one of the two liquids – has to be defined.
Starting from the same assumptions of Owens and Wendt about the additivity of the two fractions (polar and dispersive) of the surface energy, Wu proposed a similar model that uses a harmonic mean instead of the geometric one:

$$\gamma_{SL} = \gamma_S + \gamma_L - 4\left(\frac{\gamma_S^d \cdot \gamma_L^d}{\gamma_S^d + \gamma_L^d} + \frac{\gamma_S^p \cdot \gamma_L^p}{\gamma_S^p + \gamma_L^p}\right) \qquad (2.8)$$

which is only formally different from **Eq. (2.6)**. Replacing Young's equation in **Eq. (2.8)**, the following expression is provided:

$$4\left(\frac{\gamma_S^d \cdot \gamma_L^d}{\gamma_S^d + \gamma_L^d} + \frac{\gamma_S^p \cdot \gamma_L^p}{\gamma_S^p + \gamma_L^p}\right) = \gamma_L(1 + cos\,\theta) \qquad (2.9)$$

Also in this case, for the determination of the unknown quantities γ_S^d and γ_S^p, one resorts to the experimental measurement of the contact angles with two different liquids on the same surface. After this procedure, one proceeds with the analytical solving of a two-equation system, in which each equation refers to only one of the two test liquids.

2.5 Design and manufacturing of adhesive-bonded joints

As anticipated in Section 2.1, to obtain high performance from adhesive bonding, extreme care has to be paid to fundamental design aspects, such as definition of the operating conditions characterizing the joint life-cycle, choice of suitable substrates and adhesives on the basis of their compatibility, preparation of the adherends with adequate pre-bonding treatments, etc. In other terms, it is essential to consider the joint in such a way as to be perfectly integrated in the overall structure.
In the following, some essential aspects involved in the design and fabrication of bonded joints will be briefly explained and discussed.

2.5.1 Evaluation of joint performance and geometrical considerations

The ultimate strength of a bonded joint substantially depends on the mechanical characteristics of the materials that make it up, the contact extent (as well as number, dimensions, type and distribution of the voids), presence of residual stresses, morphology of the joint and loading mode.
Generally speaking, an adhesive-bonded joint can undergo five types of simple loading conditions (**Fig. 2.7**), namely - from most to least favorable: compression (a), shear (b), traction (c), cleavage (d) and peeling (e). It should be noted that the last two loading conditions are very similar; however, cleavage occurs with rigid substrates, while peeling is typical of systems in which one adherend is rigid and the other flexible.
In reality, these conditions are very often combined and lead to uneven stress distributions, typically due to misalignments, yielding or bending effects of the adherends.
After compression (which may rarely lead to joint failure), pure shear is the most desired loading mode, and therefore it should be pursued during the design stage. For this reason, adhesive joints are generally made with simple or, possibly, double overlapping, thus having resistance proportional to parameters such as overlap surface, rigidity of the substrates and thickness of the adhesive layer.

To ensure correct structural behavior of the joint, during the design phase it is good practice to observe two fundamental rules: the first suggests the uniform distribution of the stresses applied to the joint on the maximum allowable contact surface. The second rule aims at minimizing stresses that are normal to the surfaces on which the adhesive is applied, these being local (peeling and opening) or global (detachment due to normal stresses).

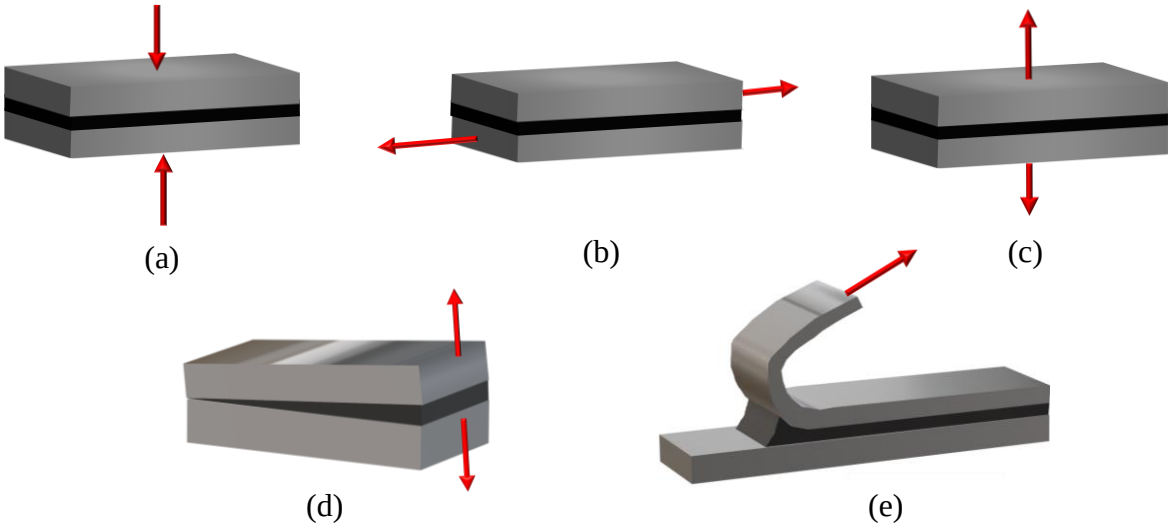

Fig. 2.7. Elementary stress conditions in adhesive bonding, from most to least favorable: (a) compression, (b) shear, (c) traction, (d) cleavage, and (e) peeling.

In this regard, **Fig. 2.8** provides an overview of some of the most suitable manufacturing solutions to meet these needs, compared to unfavorable design conditions of the joints.

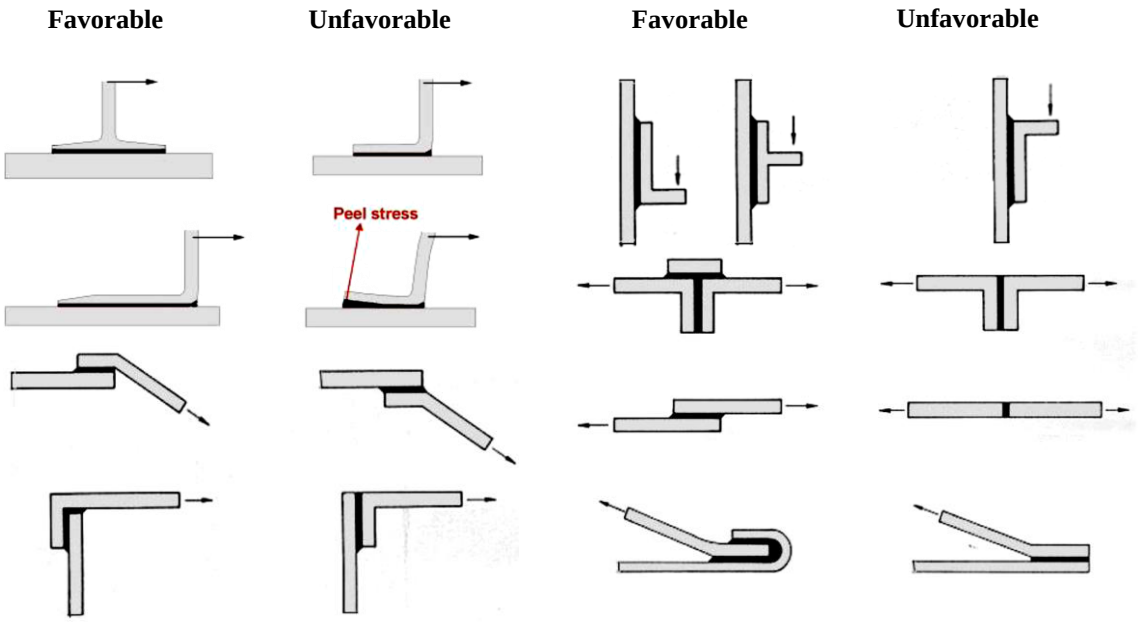

Fig. 2.8. Design criteria to maximize the bonding surface and minimize normal stresses.

In **Fig. 2.9**, the stress components arising in the thin adhesive layer of a single-overlap joint are illustrated. In the scheme, the joint is loaded by a pair of forces P, equal in value and opposite in sign, having their straight action lines contained in the mean plane of the parts to be joined. Albeit small, the substrate thickness causes bending moment to increase due to load misalignment. Notably, normal stresses σ_z (e.g., local peeling stresses) are due to the action of this bending moment, whereas shear stresses τ_{xz} and τ_{zy} represent the working stresses balancing the external forces P applied to the joint.

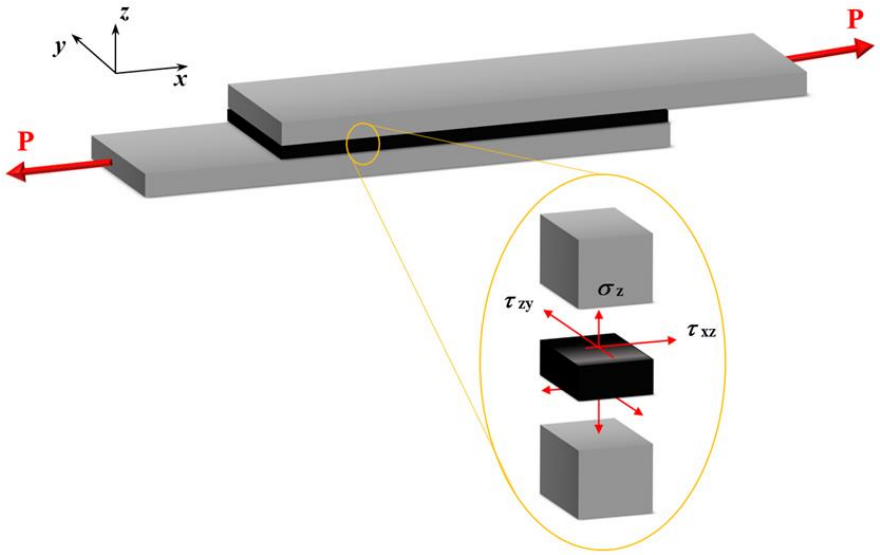

Fig. 2.9. Stress components in a single-lap joint configuration.

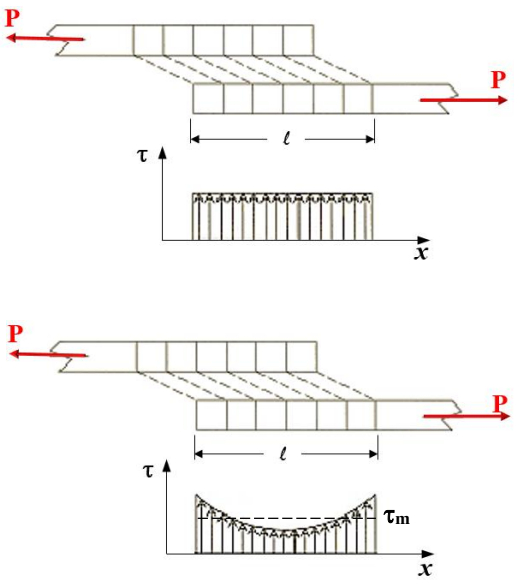

(a) If the adhesive is deformable in shear conditions and the adherends are perfectly stiff, the following equation is valid:

$$\tau = P/b\ell$$

(b) If the adhesive is deformable by shear and also the adherends are deformable, on the basis of the *shear-lag* model formulated by Volkersen, there is a non-uniform stress distribution, with concentrations at the edges of the joined area.

Fig. 2.10. Scheme of the shear stress distribution (a) in ideal conditions and (b) in accordance with the shear-lag model.

The distribution of the tangential stresses τ_{xz} on the total overlap length ℓ is not uniform. Indeed, this would be possible only if the substrate stiffness was infinitely greater than that

of the adhesive. Since the elastic properties of adhesive and substrate are at least comparable, one may expect a concentration of τ_{xz} stress at the two external edges of the adhesive layer, where the corresponding shear deformations achieve maximum values. Such considerations are summarized in **Fig. 2.10**

2.5.2 Criteria for adhesive selection

It follows that choice of the proper adhesive is therefore a trade-off among multiple factors (**Fig. 2.11**), the most important of which are summarized below:

- *substrate material*: an opportune adhesive-substrate combination emphasizes the adhesive performance of the joint;
- *design requirements*: sealants, threadlocker, structural adhesives, etc.;
- *equipment available*: refrigerators, dosers and mixers, ovens, extractor hoods, adhesive guns, etc.;
- *service conditions*: maximum and minimum service temperatures, presence of humidity, radiation sources, chemical factors acting on the adhesive system;
- *application*: simple bonding or additional sealing action, thermal or electrical insulation, corrosion protection, vibration damping, fatigue resistance;
- *use*: cost, need for pressure or heat for curing, use for prototypal or series production.

Given the huge number of applications that increasingly involve adhesive bonding today, the market is responding by enhancing availability of resins for specific uses. As previously mentioned, the horizon of applicability of adhesive bonding has thus been extended to the most demanding manufacturing fields in which, while preserving overall lightness of structures, it is necessary to meet requirements of high quality, safety and maintenance of excellent features even under high-load or temperature conditions. Structural adhesive bonding fits well in this panorama. Its primary goal is indeed to allow the joint to undergo stress levels close to its ultimate strength, making it possible to fully exploit the mechanical performance of the base material. Different families of resins belong to the class of structural adhesives; among them, epoxy, polyurethane, acrylic, cyanoacrylate and anaerobic are the most used. Their main advantages and limits are summarized in **Table 2.1**.

Fig. 2.11. Key factors involved in adhesive selection.

When choosing an adhesive, it is necessary to evaluate both its mechanical properties and its capability to adhere to the surfaces to be joined. Indeed, some adhesives may have better adhesion features on certain substrates than on others or, if applied on polymer supports, they might cause stress cracking phenomena.

It is also necessary to consider the performance required of the joint and the service conditions to be undergone by the structure. Some resins resist better than others to humidity, fatigue, thermal shocks, heat and UV radiations. As an example, in case the structure has to resist high temperatures, the choice will be directed to ceramic adhesives or thermosetting resins rather than to thermoplastic ones. In turn, if the structure is mainly subjected to impact or fatigue stresses, brittle resins, such as phenolic or epoxy, should not be used, unless elastomeric additives are used to increase their toughness. Then, if an assembly is characterized by small gaps to fill with the adhesive, cyanoacrylate adhesives will be chosen, thanks to their capability of penetration and uniform distribution. In case of metal structures characterized by significant overlapping of the flaps, the use of anaerobic adhesives – able to achieve complete polymerization in absence of oxygen – may be recommended.

In this work, a two-component, epoxy structural adhesive was used to manufacture all the composite joints, it having been recognized as the best solution to join substrates of this kind. Therefore, in the following paragraph, more details will be provided regarding such resins in terms of nature, process parameters and application.

Table 2.1
Advantages and limits of the most used types of structural adhesives.

Type	Advantages	Limits
Epoxy	High strength Good solvent resistance Good gap filling properties Good elevated temperature resistance Wide range of formulations Relatively low cost	Strongly exothermic reaction Need for refrigerated storage (especially if one-component) and high curing temperatures Short pot life Properties achievable only with exact mixing proportions (if two-component)
Polyurethane	Varying curing times Tough High mechanical resistance Excellent flexibility even at low T Moderate costs	Sensitivity to moisture, even after curing Poor resistance at high T Short pot life Need for special mixing and dispensing equipment
Acrylic	Good flexibility Good peel and shear strength No mixing required Curing at room temperature Moderate costs	Low resistance to high T Slower cure time than anaerobic or cyanoacrylates Toxicity Flammability Need for dispensing equipment
Cyanoacrylate	Rapid curing at room temperature One component High shear strength Long pot life Good adhesion on metal substrates	High cost Poor durability on some surfaces Limited solvent resistance Limited resistance at high T
Anaerobic	Rapid curing at room temperature Good solvent resistance Good resistance to high T No mixing Indefinite pot life Nontoxic High strength on most substrates Moderate costs	Not recommended for permeable surfaces Low gap filling properties and need for limited gaps

2.5.2.1 2-C epoxy adhesives

Two-component epoxy resins are an important class of polymeric materials characterized by the presence of two or more functional groups of the epoxy/oxirane type (**Fig. 2.12**). Generally speaking, the adhesive system consists of di-epoxy or poly-epoxy monomers (*e.g.*,

epichlorohydrin) based on bisphenol A, bisphenol F, novolacs etc., whereas the hardener is generally a poly-amine or a mercaptan.

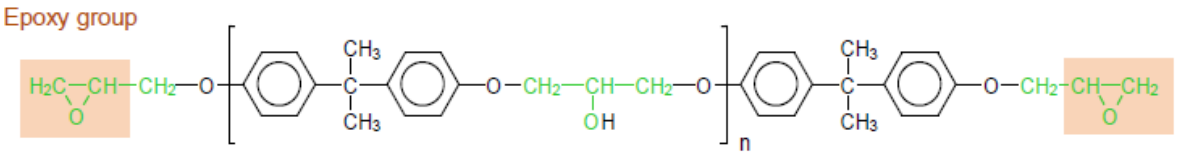

Fig. 2.12. Base chemical structure of an epoxy resin.

The material crosslinking is based on a *step-growth polymerization* (also known as *polyaddition*), namely, a polymerization mechanism in which bi-functional or multifunctional monomers react to form first dimers, then trimers, longer oligomers and eventually long chain polymers, gradually increasing the molecular weight of the resin (**Fig. 2.13**), causing it to achieve a *thermosetting* structure.

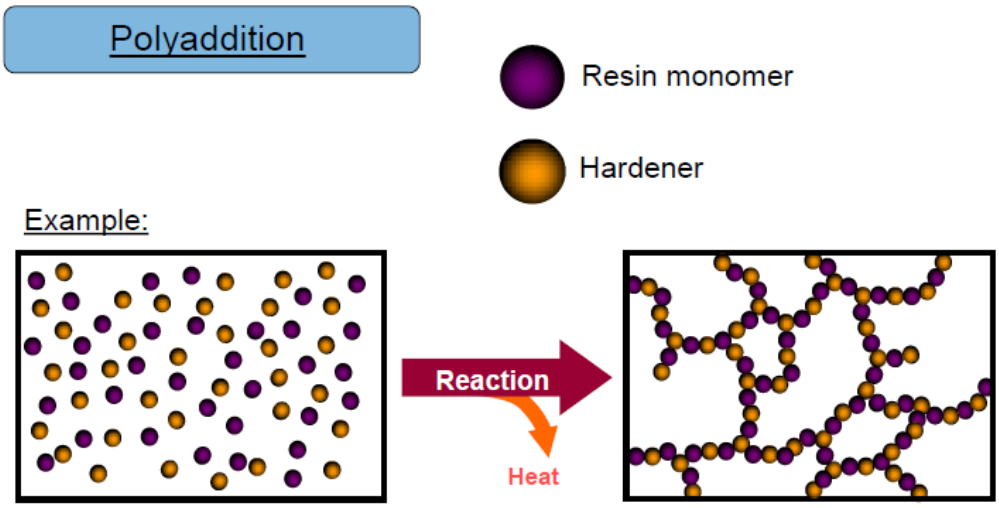

Fig. 2.13. Scheme of a polymerization exothermal reaction based on the polyaddition mechanism.

Among the different types of polymers constituting an epoxy adhesive system, it is worth mentioning the following families:

1) *Epoxy resins based on BISPHENOL A*: bisphenol A (BPA) is the product of the condensation reaction between a phenolic group and acetone. BPA epoxy resins have good resistance to many chemical species and generally have a rather viscous consistency, which can be reduced by mixing them with solvents, thinners, or reactive thinners (the latter are introduced to comply with the restrictions related to the emission of VOC, but they have negative effects on the resistance to chemical aggression). The reaction between bisphenol A and epichlorohydrin (ECH) takes place in three stages, leading to the formation of DGEBA resin (di-glycyl-ether of bisphenol A), a bi-functional resin consisting of two terminal epoxy groups;

2) *Epoxy resins based on BISPHENOL F*: bisphenol F (BPF) is an aromatic compound - having a structure similar to BPA, obtained from the reaction between phenol and formaldehyde – reacting with epichlorohydrin to form the epoxy resin. Compared to BPA resins, BPF resins have lower viscosity (solvents can be avoided), but higher costs;

3) *NOVOLACS epoxy resins*: like BPF, novolacs are also formed via the phenol-formaldehyde reaction. However, they have aromatic molecules with higher molecular weight, characterized by a higher number of reactive functional groups. Compared to BPA and BPF, one highlights the following differences:

   - higher degree of crosslinking;
   - lower viscosity (compared to BPA);
   - greater resistance to both chemical and thermal agents;
   - need for higher temperatures for crosslinking.

Concerning the hardener agents, as previously mentioned, the most common systems are based on amines or mercaptans; specifically:

1) The *amine-based hardeners* are distinguished in:

   a. Aliphatic polyamines → compounds characterized by high functionality; epoxy resins cross-linked with such hardeners have high reactivity at RT (and, therefore, limited pot life and polymerization times), good resistance to solvents, and high rigidity. Blushing phenomena may occur, consisting in formation of an oily surface patina due to the reaction of aliphatic amines with humidity and CO_2; this leads to whitening and difficult adhesion of the subsequent layers;
   b. Amido-amine → these are characterized by lower functionality and, consequently, lower degree of final crosslinking. Compared to aliphatic, they have greater flexibility, wettability (and therefore adhesion), and resistance to water, but less to solvents and acids. The pot life and crosslinking time are obviously longer;
   c. Aromatic amines → these are poorly reactive and, hence, require a reaction accelerator. Epoxies with aromatic amines, compared to those with aliphatic amines, have good flexibility, resistance to both T and chemical aggression, and longer pot life;
   d. Keto-amines → the hardener does not react with the epoxy group until it is released by the presence of water;
   e. Cycloaliphatic amines → this compound brings about properties such as UV stability, thermal stability, excellent resistance to chemical aggression, and high mechanical properties. Reaction times are shorter.

2) Being sulfur-based compounds (H-S), the mercaptan-based hardeners (also known as *thiols*) provide greater flexibility, toughness and resistance to humidity. Some mercaptan-based epoxy systems are characterized by a high reaction rate and can react even at low T (down to -20°C).

The 2-C adhesive systems obtained via polyaddition mechanism are rather sensitive to possible errors in the resin preparation and mixing of the components. Therefore, it is necessary to respect the indicated *mixing ratio*, possibly using dosers with static mixer to ensure the proper mixing of the two parts. This aspect becomes all the more important for manual procedures, in which mixing has to be performed until a homogeneous color is obtained, using containers of regular shape in order to avoid incorporating bubbles within the resin.
The viscosity of the non-crosslinked resin ranges between 150 and 1500000 mPa·s (at RT), so that it is essential to apply the adhesive at the temperature and within the times recommended by the TDS (**Fig. 2.14**).
The reaction is triggered as soon as the resin and hardener come into contact: the viscosity slowly increases up to a critical value beyond which it is no longer possible to apply the adhesive owing to its reduced wetting capability (and, thus, adhesion to the substrate). For this reason, when using a 2-C epoxy adhesive, strict control of the following two process parameters becomes indispensable:

- *Pot life*, which is defined as the time within which, at RT, the viscosity of the mixed adhesive doubles (or quadruples, in the case of low viscosity adhesives, <1000 cPs): within this time, it is necessary to complete the dosage of the two components, mix them properly, apply adhesive and, finally, assemble the substrates, fixing the joint. Such parameter depends on:
  - type of adhesive and its chemical nature;
  - temperature at which the adhesive is applied: T≃15°C is generally recommended so as not to have too low viscosity (which reduces the ease of application), but adequate reaction speed. Indeed, it should be noted that, for increases of 8-10°C in the environmental temperature, pot life and curing time are halved, whereas these parameters double for variations of 8-10°C below RT;
  - quantity of mixed adhesive, given the strongly exothermic reaction between resin and hardener.

- *Working life*, which is defined as the time within which the viscosity of the mixed adhesive is low enough to allow adhesive application on the substrate.

Notably, a typical 2-C epoxy resin can reach complete polymerization in about seven days at RT, although a *post-curing* in an oven is often also recommended to reduce residual stresses due to thermal expansion. Alternatively, it is possible to adopt a $T_{curing} > RT$ directly to increase the crosslinking speed (the viscosity variations are faster and the pot life shorter accordingly) along with the elastic modulus and the final strength of the adhesive; in fact, an increase in T_{curing} leads to an increase in the degree of conversion and polymerization.
In view of such considerations, it is clear that crosslinking phenomena are strictly dependent on both temperature and time. Specifically, the effects of the latter on the final structure of

the polymer can be studied using the so-called TTT (*Time-Temperature-Transformation*) diagrams (**Fig. 2.15**), constructed by observing the transformations undergone by the polymer during crosslinking at constant temperature (isothermal curing), for different values of T[1].

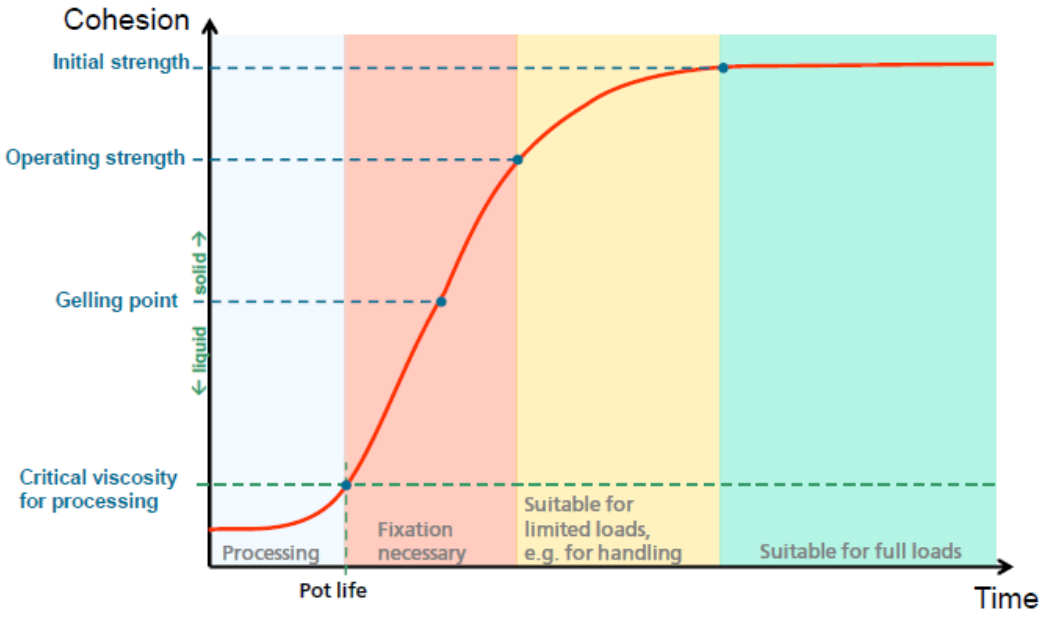

Fig. 2.14. The resin cohesion rate over time determines the application requirements for the adhesive.

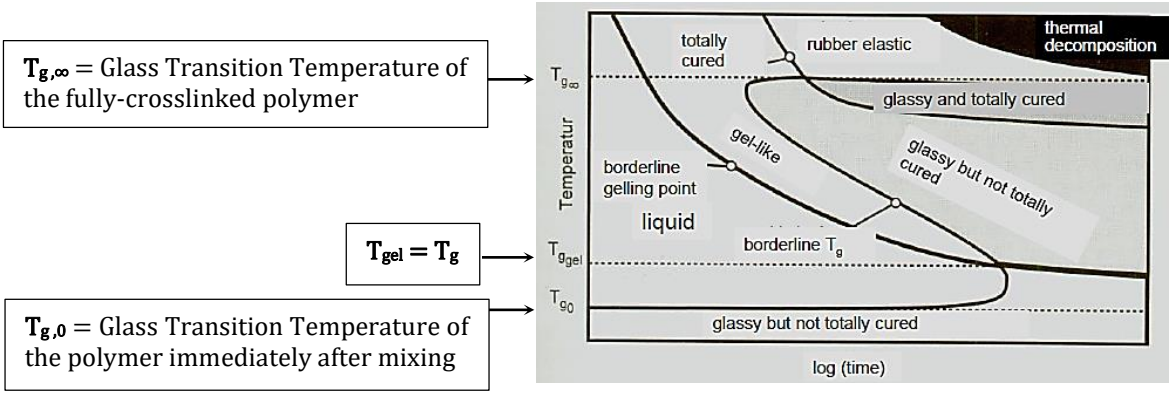

Fig. 2.15. Time-Temperature-Transformation diagram of a generic epoxy resin.

[1] As observable, during crosslinking of the thermosetting resin, the polymer undergoes two main transformations:

- *gellification*, in which chemical bonds are formed with an increase in viscosity. It consists of a transformation in the gel state having a soluble and an insoluble part (sol-gel) with viscoelastic properties;
- *vitrification*, namely, a transformation from the state of gel to that of a brittle solid that occurs when $T_g = T_{crosslinking}$.

2.5.3 Pre-bonding preparation criteria

Together with the design criteria and adhesive selection suitable for the application, the proper preparation of the faying surfaces is a fundamental requirement to ensure quality and reliability of an adhesive joint. Indeed, nature and surface conditions of the parts to be joined – as previously introduced – are key factors that strongly influence the adhesive effectiveness in creating sufficiently stable interfacial bonds with the substrate. For this to happen, the primary condition is that the surfaces of the latter must be clean and chemically compatible with the adhesive. In practice, this means performing a number of preliminary operations that might guarantee good wettability and adhesion, but also qualitative replicability of the joining results throughout the manufacturing process.
Generally speaking, pre-bonding preparations are aimed at achieving multiple objectives, including:

- to remove and prevent subsequent re-formation of any weak boundary layers at the interface. If it did not, joint failure would be located in correspondence of this boundary layer. In case of metal substrates, precipitates, impurities, oxides and humidity, but also residues of the fabrication process (such as lubricants, grease, coolants, particles resulting from tools) can be present on the surface. A similar issue is also found with polymer substrates, the surface of which is often rich in plasticizers and pigments, along with various types of contaminants absorbed from the atmosphere. This typically occurs with injection molded parts, for which application of adhesives is made difficult by the presence of detachment adjuvants used to remove the piece from the mold. Weak boundary layers can also form after bonding, such as stearates in polymeric films or aluminum hydroxides produced by the moisture absorbed by the adhesive;

- to maximize the degree of intimate molecular interaction between adhesive and substrate. This may require chemical modification to increase surface free energy. In addition, a suitable surface finishing can help to obtain satisfactory interfacial contact;

- to ensure that the level of intrinsic adhesion forces at the interface is sufficient to guarantee both initial resistance and durability of the joint over time. In case of low-energy surfaces (as with polymers), such a result can be achieved by means of pre-treatments that increase surface free energy, introducing chemical species capable of forming strong bonds with the adhesive;

- to generate a proper morphology of the substrate surface;

- to protect the substrate surface before adhesive bonding. This is often necessary for high energy metal surfaces. Indeed, after mechanical abrasion or chemical treatment, the surface is very reactive, not only towards adhesives, but also towards any atmospheric contaminations[2]. To meet this requirement and, at the same time, maintain flexibility of

[2] This is the reason why the technological procedures prescribe that degreased surfaces must be bonded immediately or protected within a few hours of treatment.

production, it is common practice to apply primers compatible with the adhesive as soon as the pre-treatment is completed.

Based on the previous considerations, it is clear that surface treatment represents a fundamental phase in the manufacturing cycle of a bonded component. This must be provided for each type of substrate and must be performed by competent, qualified personnel, as it requires careful control of the process parameters as well as of all boundary conditions (cleaning, treatment, handling); in other terms, competence and qualification of the staff involved must make it possible to demonstrate, in any event of litigation, that every procedure has been carried out according to the state of the art[3] and following appropriate criteria.

The considerations and objectives mentioned above are, in principle, valid for every type of substrate to be joined through adhesive bonding, and they have to be considered as a benchmark in most structural applications. Nevertheless, the choice of a specific surface treatment must be made according to aspects concerning the exact adhesive system, the base material employed as the substrate (nature, intrinsic criticalities and supply status of the material) and the design/application requirements (short- and long-term joint strength, operating environment, budget costs…).
For the sake of brevity, the content of the following paragraph is deliberately condensed to those pre-bonding procedures used to prepare plastic-matrix materials. For more details regarding surface treatments, the reader is invited to refer to the handbook of Wegman and Van Twisk [11].

2.5.3.1 Overview of surface preparation methods for plastic and composite materials

The adhesion properties of a plastic substrate are influenced by several factors such as surface energy, polarity and reactivity[4], structure and mobility of the polymer chains, and presence of additives. Similarly, in addition to these specific aspects of the polymeric substrate, a number of aspects related to the adhesive used also contributes to adhesion phenomena, namely, viscosity and rheological aspects, chemical nature and affinity with the substrate, mobility of the chains within the resin and surface tension.

[3] *E.g.*, EN 13887 (2003-11): "*Structural Adhesives. Guidelines for surface preparation of metal and plastic prior to adhesive bonding*".

[4] The *polarity* is related to the amount of polar or polarizable groups on the surface necessary to generate physical interactions (dipole-dipole, inductive and dispersive) with the adhesive. The *reactivity* is instead the ability of the substrate to establish chemical bonds following the reactions between the molecules of the adherend and those of the adhesive. Such chemical reactions are possible if at least one of the following conditions occurs:
- presence of functional groups (-COOH, -OH, -CHO) on the surfaces → present on a few plastics (EP, PF), but can be generated on many thanks to specific treatments;
- presence of reactive groups within the adhesive (generally epoxy or isocyanate groups);
- use of adhesion promoters implanted on the surface (generally epoxy groups or isocyanates) capable of reacting with both adhesive and substrate.

In principle, it is desirable to ensure that $\gamma_{C,substrate} \gg \gamma_{adhesive}$. Such a condition may be achieved increasing $\gamma_{C,substrate}$ by acting with specific treatments on the substrates.
Based on the chronological order in which these procedures are carried out, it is possible to identify three different phases of treatment: surface preparation (that is always needed), the treatment in the strict sense, and, eventually, a further post-treatment (the last two are optional, since their necessity has to be determined on the basis of design evaluations and application requirements).
In **Fig. 2.16** the operative flow related to surface pre-bonding preparations of plastic materials is schematized. Concerning the first phase, surface preparation commonly entails solvent degreasing of the faying areas. This operation must be performed with great care to avoid chemical damage, thus, selecting the proper type of cleaning agent depending on both the contaminants present and its compatibility with the surface. Plastic surfaces are generally prepared using *water-based solvents*; however, attention must be paid to the hygroscopicity of the material, to its sensitivity to aggression by acidic and/or base substances at high T, and to presence of surfactants (that might be a cause of stress cracking phenomena). *Organic solvents* can also be used, despite these enhancing the risk of chemical aggression of the polymer chains and degradation of the material properties, causing swelling (reversible after drying the substrate), morphological modifications, whitening, or stress cracking.

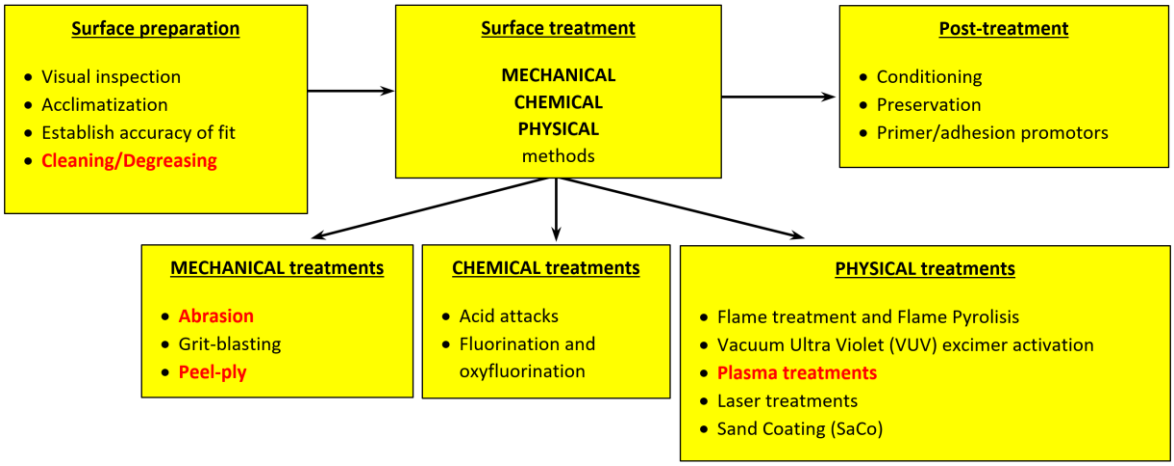

Fig. 2.16. Schematic operative flow for the pre-bonding preparation of polymer substrates. The cases investigated in this work are highlighted in red.

Based on the performance/application requirements that the adhesive joint has to attain, after wiping, a further pre-bonding treatment might be necessary. The latter can be of different nature depending on both the type of source employed and the modification brought about on the substrate surface [24]. Generally speaking, such treatments can be grouped into three main families: mechanical, chemical, and physical treatments. Since in this work mechanical treatments such as abrasion and peel-ply have been used as reference, for the sake of brevity, the main aspects related to such family alone will be presented. The next chapter, instead,

will be entirely dedicated to physical treatments based on plasma sources, whose effectiveness on CFRP materials is the main topic of this investigation.

Mechanical treatments of plastic surfaces are commonly based on *abrasion* processes, performed using abrasive papers (fine papers with grain ranging from 180 to 220, or 3M Scotch-Brite) or, in some cases, sandblasting, aimed at removing outer layers of material (skin-effect, low molecular-weight components, adsorbed contaminants). Affecting the surface roughness, this entails an increase in the extent of the actual contact area between adhesive and substrate. In many applications, mechanical abrasion is performed manually, since orbital machines could lead to localized heating of the polymer due to friction. Therefore, to obtain the most suitable abrasion conditions, the operator is required to properly control the pressure applied during procedure (in case of composites, an excessive pressure might expose or damage the reinforcement fibers), abrading homogeneously the entire surface with circular or (possibly) linear movements, in orthogonal directions to each other. It follows that, despite it being a economic, relatively simple method, the final performance of the joints is significantly affected by the operator's capability and, hence, often lacks repeatability.

Other types of mechanical treatments based on abrasive processes are those performed via grit- or sand-blasting, in which a jet of compressed air carrying abrasive particles is used both to remove residual contaminants from the surface preparation phase and alter the roughness of the substrate. The particles can be metallic or natural, non-metallic substances, spherical or polygonal in shape, with dimensions ranging between 0.2 and 2 mm. However, damage can occur on the polymer surface due to heating generated by the high kinetic energy of the particles in motion, and tribological phenomena (i.e., *tribo-plasma*). For this reason, when possible, a dry-ice blasting is often preferred. This treatment can be performed using solid dry-ice (CO_2-grit blasting) or liquid dry-ice (CO_2-snow-grit blasting). In the former, the substrate is struck by a jet of dry-ice pellets (at $T_{CO_2} \simeq$ -78.5°C), which cleans the surface by means of contaminant cooling and sublimation of the CO_2. In particular, at each impact, heat is removed from the surface; this leads to embrittlement of the contaminants, which are eliminated thanks to the violent expansion at the interface caused by the sublimation of solid CO_2. In turn, CO_2-snow-grit blasting uses liquid CO_2 that expands through a nozzle, resulting in a mixture of solid and gaseous CO_2. The removal of particle contaminants (down to 0.03 μm in size) and organic compounds is made possible by the simultaneous action of high-speed, gaseous flow carrying solid particles and the presence of CO_2 liquid-phase.

As mentioned, the mechanical treatments described so far are applicable to pure polymers as well as reinforced plastics and based on abrasive processes. Nevertheless, an increase in surface roughness can also be achieved by using special plastic films (in general, made of PE or PA) introduced as the outer layer during the manufacturing process of the laminate. This film – commonly used for composite materials – is named *peel-ply*: before adhesive application, the ply is peeled off from the substrate, freeing a surface having roughness extent and morphology compatible with adhesive bonding. Generally, no additional treatments are required. However, in the case of prolonged storage times, problems may occur of diffusion of the PE/PA or release agents on the substrate [8].

Hence, despite mechanical treatments being, in principle, cheaper and easier to perform, their effectiveness is not always sufficient to attain the quality requirements being pursued. For this reason, more valid alternatives have been sought and non-standard physical processes have garnered increasingly widespread interest. Among them, plasma treatment seems to have the potential to play a key role as effective promoter of adhesive phenomena, as discussed in the following and confirmed by the experimental results.

3. Plasma

3.1 General principles

Plasma is defined as a fully or even partially ionized gas composed of ions, electrons, photons, radicals and other neutral species present both in ground and excited state. In particular, ionization of neutral gases – the electronic density of which is balanced by the ionic one - involves generation of plasma. The latter, although globally neutral from an electronic point of view, contains free charge carriers that make the gas electrically conductive. Therefore, density of ions and electrons can be considered approximately the same and, hence, this is defined as the plasma density.

Providing energy (in the form of thermal, electrical or electromagnetic radiation) to a gas, phenomena of reorganization of the electronic structure occur and, consequently, excited species and ions are created. Indeed, in a plasma-state gas, two types of phenomena occur as a result of the collisions between electrons and neutral particles:

- *excitement* and *relaxation:* these are essentially due to elastic collisions between electrons and neutral species, which lead to an increase in kinetic energy of the particles;

- *ionization* and *recombination:* these are due to inelastic collisions. Specifically, if the electron energy is sufficiently high, each collision changes the energy structure of the neutral particles, ionizing them (**Fig. 3.1a**). However, such an ionized state has rather limited duration and the excited particles return to their neutral state, emitting a photon (**Fig. 3.1b**).

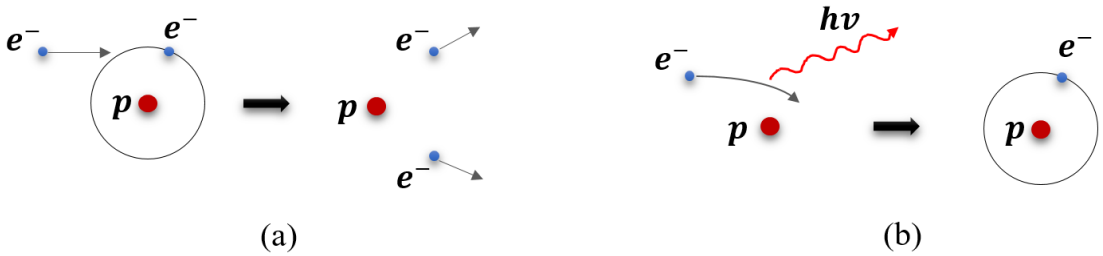

Fig. 3.1. Representation of (a) ionization and (b) recombination phenomena in a plasma gas.

It is clear that ionization and recombination processes proceed in parallel, so that the gas remains in neutral-plasma conditions. For this reason, an external source is required to provide energy by means of various kinds (such as X-, γ- or ultraviolet-radiation, electronic bombardment, electric or magnetic fields, strong heating) or to introduce easily-ionizable substances. It should be noted that, in industrial applications, use of electricity as the energy source is always preferable.

A gas can remain in plasma state as long as the supply of ionizing energy persists. When the latter ceases, the particles (ions and electrons) immediately recombine, returning the gas to neutral insulating state.
Based on the kinetic theory of ideal gases, the average velocity v of the disordered thermal motion of ions and electrons increases proportionally to the square root of the absolute temperature T of plasma, according to the following relationship:

$$v \propto 1.3 \cdot 10^4 \cdot \sqrt{\frac{T}{A}} \qquad (3.1)$$

where v is expressed in (cm/s), A is the atomic weight of the gas in (g), and T is expressed in (K). The latter has the physical meaning of average temperature among the temperatures of all various components of plasma, *i.e.*, ions and electrons, in case of fully-ionized plasma, or ions, electrons and neutral atoms, in case of partially-ionized plasma. It should be noted that, in case of heavy elements (*i.e.*, having high atomic number), the binding energy between electrons and nucleus is high and, thus, complete ionization can only occur for temperatures of a few million degrees. On the contrary, for gases such as oxygen, hydrogen or nitrogen, the overwhelming majority of atoms is ionized at temperatures of several tens of thousands of degrees.

In a fully-ionized-plasma gas, the electron temperature is considerably higher than that of ions ($T_\mathrm{e} \gg T_\mathrm{i}$). Furthermore, owing to their very low mass, electrons are the most mobile species in plasma, and hence responsible for transferring energy absorbed by the external source (*e.g.*, an electric discharge) to the other components of the system. According to the expression **(3.1)**, an increased absolute temperature of the gas corresponds to increasing particle velocity. This causes the collisions to be much more frequent and, consequently, determines a higher degree of ionization.
Given the aleatory nature of the ionization phenomenon and, on a physical level, the impossibility of achieving complete gas ionization, one needs to establish the conditions for which an ionized gas is considered plasma. The neutrality of plasma from a macroscopic standpoint has previously been mentioned; by defining the electron density n_e and the density of ions n_k with valence *k*, the neutrality condition can be effectively defined through the following expression:

$$n_\mathrm{e} = n_1 + 2n_2 + 3n_3 + \ ... + kn_k \qquad (3.2)$$

Assuming that only monovalent ions are present in the ionized gas, the previous relationship can be simplified in:

$$n_\mathrm{e} = n_\mathrm{i} \qquad (3.3)$$

where n_i is the ion density.
If **Eq. (3.3)** is not verified ($n_\mathrm{e} \neq n_\mathrm{i}$), the difference between n_e and n_i determines increasing electric fields, the intensity of which increases with the concentration of charged particles in the ionization volume. Such electric fields balance the particle flows, hence restoring neutrality. In other terms, plasma corresponds to that state of matter whereby the number of ions and electrons is so high that even the smallest variation of the ionic component, with respect to the electronic one, is impossible.
However, it may happen that local charge concentrations are generated in plasma, usually confined to rather small portions, characterized by means of a dimensional parameter (characteristic of each plasma) known as *Debye's length* (λ_D). Notably, **Eq. (3.3)** is verified only out of these regions and it is possible to study plasma as a macroscopically neutral system. In other words, the ionized gas must be contained in a volume whose characteristic size L satisfies the condition:

$$L \gg \lambda_D = \sqrt{\frac{K \cdot T_\mathrm{e} \cdot \varepsilon_0}{n^2 \cdot e}} \qquad (3.4)$$

where λ_D is Debye's length expressed in (m), K is Boltzmann's constant in (J/K), T_e is the electronic temperature in (eV), ε_0 is the dielectric constant in (F/m), n is the electronic density in (m^{-3}), and e is the charge of the electron in (C).
An ionized gas can be defined as plasma only if **Eq. (3.4)** is verified. Indeed, if $L \ll \lambda_D$, the electric fields due to $n_\mathrm{e} \neq n_\mathrm{i}$ would be too small and not able to restore charge neutrality.

3.2 Plasma generation

A source of energy persisting over time is needed to bring a gas to a plasma state and keep it in this condition. In the following, the most common methods for plasma generation will be analyzed, focusing on those of main interest from a technological and industrial point of view. These methods can be distinguished into two macro groups, both sharing the generation of an electric or electromagnetic field as the primary energy source for plasma ignition: *processes in direct regime* (DC) and *processes in alternating regime* (AC).

3.2.1 DC regime

To analyze the passage of a gas to plasma under direct voltage V and current I, it is necessary to introduce the concepts of discharge in a gas subjected to a constant electric field. The study is carried out through a discharge tube (completely analogous to a common neon tube) and thus having plane anode and cathode separated from each other by a distance *d*. **Fig. 3.2** shows the typical trend of the *V* - *I* characteristic curve.

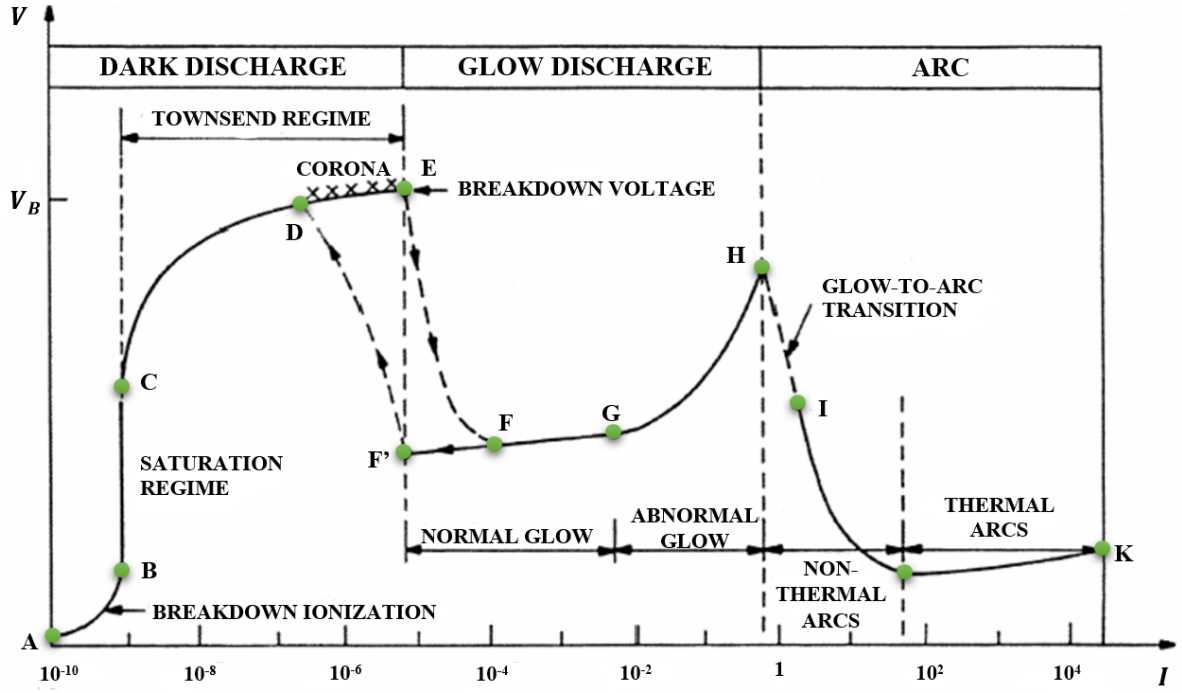

Fig. 3.2. *V* - *I* characteristic curve for a DC-powered discharge.

In the first region (*dark discharge* region), no visible radiation is emitted: beyond point C, voltage achieves levels such that the electric field accelerates electrons with sufficient energy to ionize atoms. There follows an avalanche multiplication of the charge carriers that makes the current increase exponentially.

After point E (*breakdown threshold*), there is the *glow discharge* region. This phase is characterized by the typical brightness of plasma. The fundamental feature of the dynamics of this region is that the electric field near the cathode surface - which accelerates the electrons emitted by the latter - is shielded and becomes zero at a certain distance from the cathode as a result of accumulation of positive charge due to electron escape. Under such conditions, the cathode voltage-drop across the cathode region stands at the minimum breakdown value. The main parameters characterizing *normal glow discharge* are shown in **Fig. 3.3**.

The brightest region is located in close proximity to the cathode. Indeed, in this area, electrons lose most of their energy during collisions with gas atoms, emitting light radiation. Beyond this area, the electrons must re-accelerate under the electric field action to acquire the energy necessary to ionize other gas atoms.

At point G of the *V* - *I* curve, both current and voltage increase: this is due to the fact that the entire cathode area is affected by the current flow and, thus, the value of current density is very high. This phase of unstable plasma is defined as *abnormal glow*. If *I* further increases, there is transition to the electric-arc regime. At this stage, the very high *I* values cause a drop of *V* between the electrodes. This drop can be divided into *anode drop*, *cathode drop* and *linear drop in the positive column*. The latter depends on the ionization degree of the gas (the more the latter is ionizable, the lower the value of ionization degree - **Fig. 3.4**).

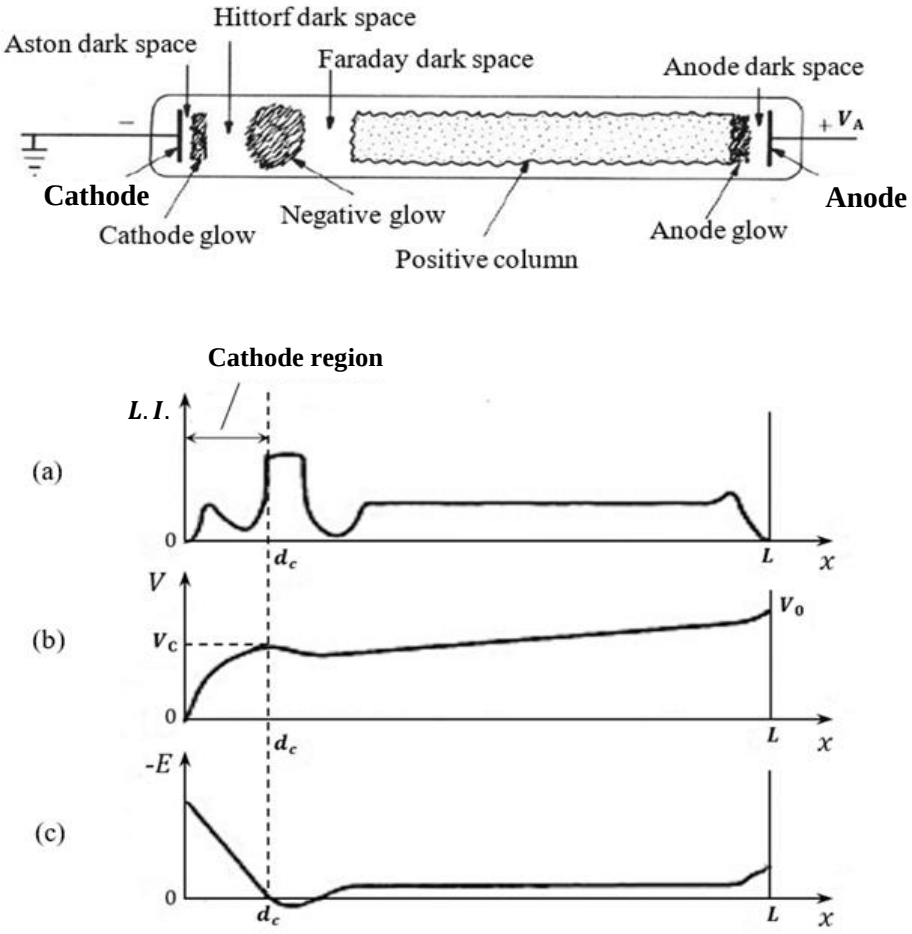

Fig. 3.3. Trends of (a) light intensity, (b) electric potential and (c) electric field in a cylindrical discharge tube.

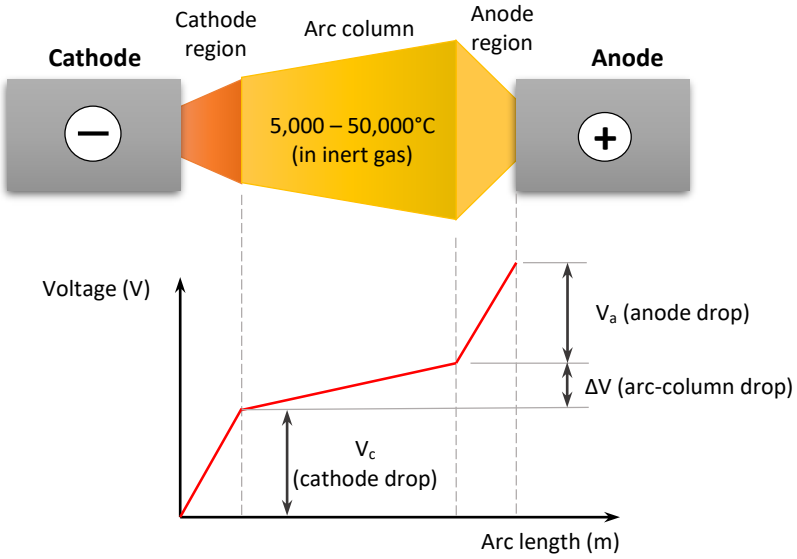

Fig. 3.4. Visible characteristics of an electric arc and typical trend of voltage drop along the axis.

The most used applications of DC plasmas concern both cutting and welding of metals; transferred/non-transferred arc plasmas, surface treatment, plasma with corona discharge and plasma with dielectric barrier discharge are also mentioned.

3.2.2 AC regime

The generation of plasma under voltage and alternating current is the preferable alternative for *glow-discharge* applications, compared to high-voltage DC sources. In an AC regime, the discharge is much more stable and local concentrations of charge do not form. For these reasons, it is the most used plasma generation technology in the technological and industrial field for operations such as etching, sputtering, Plasma Enhanced Chemical Vapor Deposition (PECVD), plasma grafting, cleaning and surface activation.
At the atomic level, the mechanisms that bring the gas to the plasma state are the same as in the case of DC regimes: electrons are accelerated by an electric field until they reach an energy level sufficient to ionize the gas atoms through inelastic collisions.
The substantial difference consists of the fact that the electric field is not constant but variable, since an alternating voltage is applied between the two electrodes, and each electrode plays the role of anode or cathode alternately. It follows that a further external control parameter has to be considered besides the fundamental parameters of voltage and current: this is the frequency ω of the alternating voltage, comparable with the characteristic frequencies of plasma created in the discharge. The frequency regime to be considered is that for which the following relationship is verified:

$$\omega_{pe} \gg \omega \gg \omega_{pi} \tag{3.5}$$

where ω_{pe} is the plasma frequency associated with electrons, ω_{pi} is the plasma frequency associated with ions and ω is the frequency of the alternating voltage.
The relationship (**3.5**) implies that there is a frequency ω (or a range of supply frequencies) for which the ions are too inertial and have low mobility to respond instantaneously to temporal variations of the electric field ($\omega \gg \omega_{pi}$). In turn, being the most mobile species within a plasma, electrons respond almost instantly to the temporal variations of the electric field ($\omega_{pe} \gg \omega$). **Fig. 3.5** shows the behavior of ions and electrons inside a plasma atmosphere, at various frequency ranges. Note that **Eq. (3.5)** is verified for power-supply frequencies higher than 1 MHz.

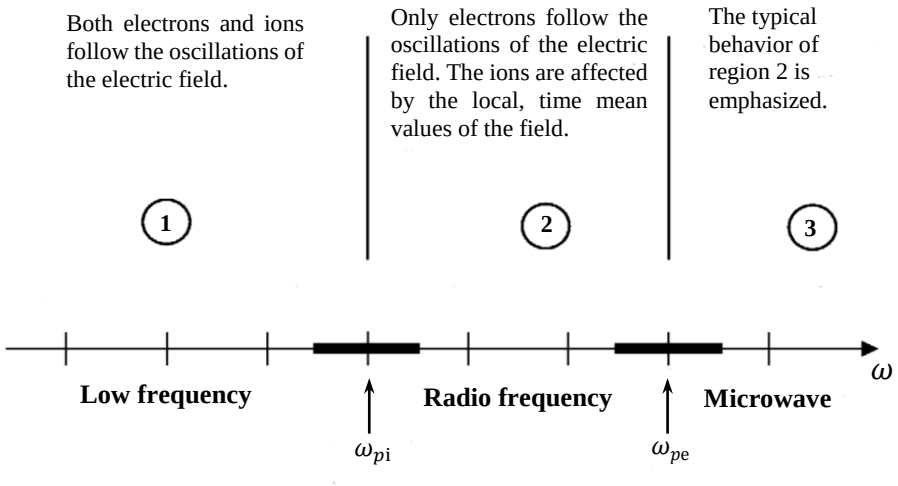

Fig. 3.5. Mobility of ions and electrons at various supply frequencies.

3.2.2.1 Radio-frequency plasmas

In the case of AC-regime plasma, the frequency range located between 1 MHz and 1 GHz is defined as the *radio-frequency* (RF) plasma region. In practice, most RF processes operate at constant frequency of 13.56 MHz. This value is not casual: in fact, since high-power radio frequency generates noise, interfering with radio signals and communications, the U.S. Federal Communications Commission (FCC) assigned specific frequency bands (including that mentioned earlier) for scientific research.

A first classification of RF plasmas can be made on the basis of the electrical characteristics of the discharge, which can be capacitive or inductive in type. *Capacitive discharges* are associated with non-magnetized systems in which the electrodes are in direct contact with plasma and the electric fields are caused by the time-varying voltage applied to the electrodes. In contrast, *inductive discharges* resulting from fields are caused by a variable magnetic flux, and the energy source is typically an antenna. However, this classification is rather weak; indeed, the plasma-discharge physics is complex since plasma is often characterized by coexistence of capacitive and inductive discharges.

A stricter classification can be made on the basis of the system configuration: *symmetrical* (*i.e.*, electrodes of the same area are used) or *asymmetrical* (electrodes having different areas). It should be noted that the greater the difference between the electrode areas, the greater the difference in potential between the electrodes. The reason for this has to be found in **Eq. (3.6)**, obtained from the inhomogeneous AC-plasma model by Child - Langmuir:

$$\frac{V_a}{V_b} = \left(\frac{A_b}{A_a}\right)^4 \tag{3.6}$$

where V_a is the voltage of the electrode "a", V_b is the voltage of the electrode "b", and A_a and A_b are the areas of the electrodes "a" and "b", respectively.

With a symmetrical configuration (**Fig. 3.6**), the potential oscillates around zero with a frequency equal to that of the power supply.

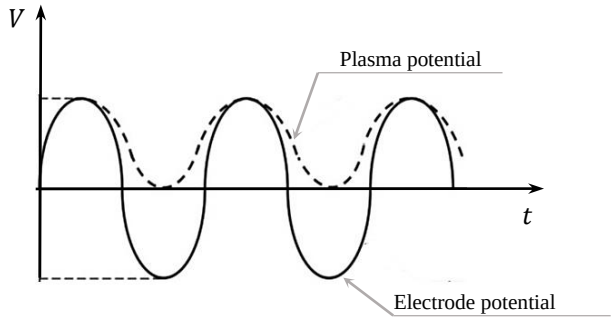

Fig. 3.6. Potential in symmetrical configuration.

In the asymmetric configuration (**Fig. 3.7**), there is a different trend due to the different mobility of ions and electrons. In fact, electrons being very mobile, they easily accumulate on the positively-charged electrode. However, when the same electrode is powered by the negative half-wave of voltage, very few ions reach it due to their low mobility. Since the ionic and electronic flows must be equal within a cycle, the system tends to move towards negative potential values, favoring the motion of ions in order to guarantee the balance between the charges that reach the electrodes. This negative-potential value is named *bias voltage.*

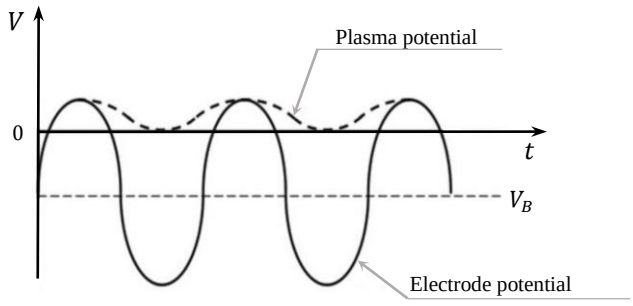

Fig. 3.7. Potential in an asymmetric configuration.

The asymmetrical configuration is functional for surface treatments with vacuum plasmas: adjusting the power input, it is indeed possible to act on the bias voltage and control the impact energy of ions and electrons. Furthermore, in these conditions the plasma temperatures remain close to room temperature, avoiding risks of degradation of the materials treated.

Basic components of a generation system with RF source are:

- the vacuum chamber and related pumping system;
- the RF generator, and the electronics for transmission and adaptation;
- the injection system for the gas to ionize.

- the system to initialize ionization.

3.2.2.2 Microwave plasmas

Microwave plasmas are generated by using an electromagnetic wave as external energy source. The main difficulty in this regime is to allow plasma to efficiently absorb the electromagnetic wave and obtain a high-frequency repetition of the discharge (**Fig. 3.5**). Conventionally, the frequency value of microwave sources stands at 2.45 GHz.
Basic components of a microwave source system are:
- the microwave source and microwave-guide system;
- the injection system for the gas to ionize;
- the system to initialize ionization.

3.3 Classification of plasmas based on temperature

Depending on the energy source and the conditions under which it is supplied, plasma parameters such as electronic density and temperature change. It is therefore possible to distinguish two macro categories:

- plasmas in *local thermal equilibrium* (LTE), also called *thermal plasmas*;
- plasma *not in local thermal equilibrium* (non-LTE), also called *cold plasma*.

In **Fig. 3.8**, the typical characteristics of each of these categories are defined, in terms of electronic energy, electronic density and electron mean free-path[5].

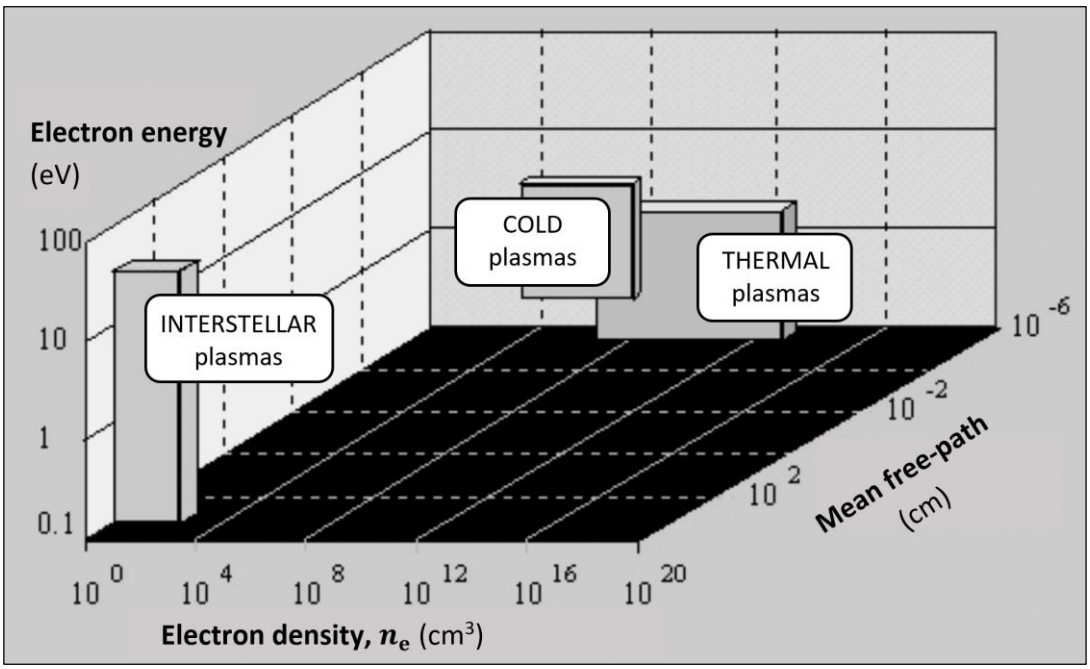

Fig. 3.8. Typical energies and average electronic densities for various types of plasmas.

[5] Average distance between two adjacent particles.

It should be noted that the temperature is not reported, but can be considered directly proportional to the electronic density: indeed, the electronic temperature is considerably higher than that of ions and, thus, higher electronic density corresponds to higher plasma temperature.

3.3.1 LTE plasmas (or thermal plasmas)

The mechanisms that govern the passage from gas to plasma state have already been discussed. When these phenomena take place in a gas subjected to atmospheric or higher pressure, the density of the gas (between 10^{21} and 10^{26} m^{-3}) is high enough to allow an effective redistribution of energy. This density, in fact, leads to a rather limited mean free-path and, consequently, to a high number of collisions between the particles. The high frequency of collisions allows an effective exchange of energy and, given the high interaction between ions and electrons, plasma can achieve thermal equilibrium. **Fig. 3.9** illustrates the trend of the ionic (T_i) and electronic (T_e) temperature in a plasma atmosphere, as a function of the pressure values [55].

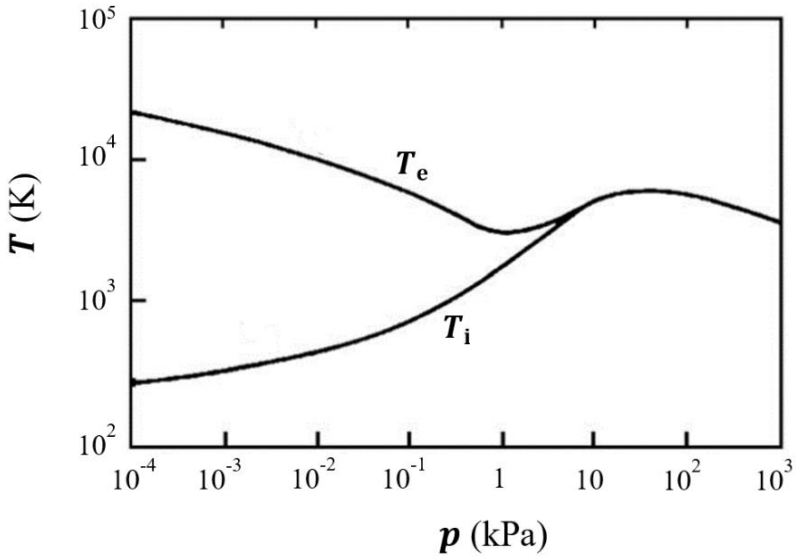

Fig. 3.9. Characteristic temperatures of plasma as a function of pressure.

It is clear that for plasmas at atmospheric pressure or higher, the ionic and electronic temperatures are completely comparable ($T_e \approx T_i$) and of the order of 10,000 K; therefore, such plasmas are defined as *LTE plasmas*.
Generally speaking, a plasma can be defined as LTE if the electron density n_e satisfies Griem's criterion, namely:

$$n_e = 9 \cdot 10^{23} \cdot \left(\frac{E_{21}}{E_{H^+}}\right)^3 \cdot \left(\frac{K\,T}{E_{H^+}}\right) \qquad (3.7)$$

where E_{21} is the energy difference between the ground state and the first excited level, E_{H^+} = 13.58 eV is the ionization energy of the hydrogen atom, T is the temperature of plasma, and K is Boltzmann's constant. Specifically, **Eq. (3.7)** highlights how the electronic density required by LTE plasmas is closely related to the energy of the first excited state.

3.3.2 Non-LTE plasmas (or cold plasmas)

As pressure decreases, the mean free-path between the particles increases, since their density decreases significantly, leading to lower frequency of collisions between them. In particular, when the particle density is less than 10^{19} m^{-3}, a *non-LTE plasma* is formed. Indeed, in systems at pressures lower than atmospheric, electrons are no longer able to effectively redistribute the energy acquired from the electric field. Such a condition is characteristic of the *cold-plasma* domain. In this phase, it is impossible to achieve thermal equilibrium between the various components of the system. Indeed, together with a population of electrons at temperatures of the order of 10^4-10^5 K, there is a population of ions and other reactive species, the temperature of which is close to room temperature (RT). Given the enormous difference between the masses of electrons and ions, the overall plasma temperature is governed almost unilaterally by the ionic temperature that, being close to RT, causes plasma to be defined as cold [22].
The ionization degree is very low (about one charged species per million neutral species). The interactions between high-energy electrons and the gas, despite not being so frequent to produce a homogeneous energy distribution, are however sufficient to create a concentration of reactive and unconventional species, which would not otherwise be possible at low temperature. As the pressure increases, the collisions necessarily increase: the electrons give energy to the ions and therefore we move towards thermal equilibrium in conditions of LTE plasma (**Fig. 3.9**). **Fig. 3.10** shows the concentrations and energies in a *glow discharge* of cold plasma.

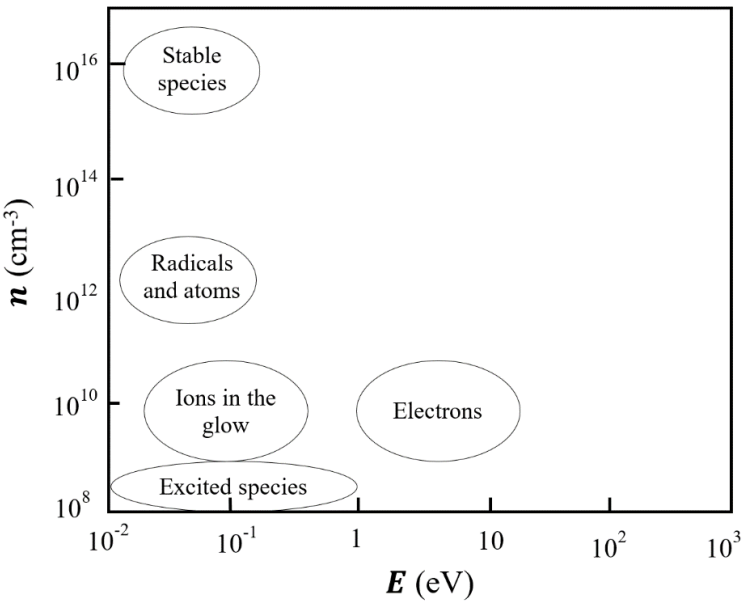

Fig. 3.10.
Typical concentrations and energies in a glow discharge of non-LTE plasma.

In recent years, cold-plasma technologies have garnered wide interest in several applications aimed at modification and treatment of surfaces [56]. The high reactivity of plasma is indeed exploited to alter the surface characteristics of materials: once plasma is generated (typically using RF or microwave sources), the substrate material is bombarded by high-speed electrons that, due to their high mobility, cause an accumulation of negative charges on the treated surface. This condition leads to increased difference in potential between the surface and the core regions of plasma. Positive ions are accelerated by the potential difference, in turn colliding with the substrate. Along with such physical bombardment, chemical reactions occur between the treated material and reactive species created in plasma, and continuous visible and UV radiations arise. The fact that the temperatures reached are close to RT makes it possible to treat easily-degradable materials such as polymers.

3.3.3 Atmospheric plasma jet

The LTE and non-LTE plasma classifications assume plasma temperature as the base distinction criterion. However, it was also said that LTE plasmas activate at pressures higher than atmospheric, whereas non-LTE plasmas trigger at pressure lower than atmospheric pressures. In principle, it would seem correct to classify plasmas according to the pressure of the environment in which the discharge occurs, thus distinguishing between low-pressure plasmas (non-LTE) and atmospheric-pressure or high-pressure plasmas (LTE).
In recent years, however, atmospheric-cold-plasma technologies have also been developed, thus making any pressure-based classifications of plasmas inadequate, or at least not rigorous. In such hybrid technologies, defined as *atmospheric plasma jet*, plasma is divided into two zones: a central zone, called *core* that is LTE, and a peripheral zone, named *plume*, which is non-LTE. *Pencil-like torches* have been introduced (**Fig. 3.11**). Exploiting the non-LTE zone, these are used to perform pre-bonding surface treatments at atmospheric pressure, without the need for pumping systems that create the vacuum needed to generate cold plasma [57].

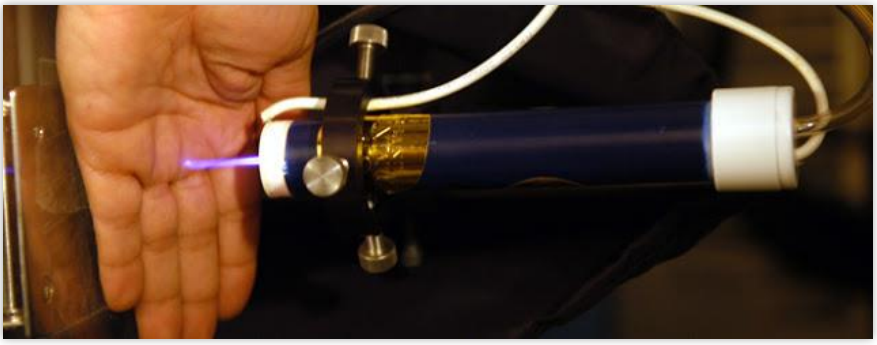

Fig. 3.11. Cold atmospheric plasma torches.

Using this technology, large devices for cold-plasma generation in atmospheric-pressure chambers (or directly in the atmosphere) have also been developed. Nevertheless, the

process parameters are less easily controllable than a cold plasma produced in a low-pressure environment.

3.4 Technological applications

Plasma is widely involved in many industrial processes and technological applications today. In the following, two macro sectors involving use of thermal and cold plasma respectively will be briefly analyzed.

3.4.1 Applications of thermal plasma

Due to the very high temperatures it is able to reach, thermal plasmas are essentially used in the metallurgical field, for operation such as cutting and welding of metals.

3.4.1.1 Plasma cutting

Plasma cutting (**Fig. 3.12**) has been developed quite recently and is used where traditional metal cutting technologies (*e.g.*, via oxyfuel cutting) give unsatisfactory results. Such technology has found wide application in the cutting of copper, nickel and aluminum alloys, of stainless steels, as well as unalloyed or low-alloyed steels. Due to the high temperatures required by the process, the plasma must be strongly ionized. In this context, DC sources are used, and the ionization of the gas interposed between the two electrodes takes place thanks to the formation of an electric arc that supplies the necessary energy. During plasma cutting, the metal sublimates without showing any trace of oxidation, which can instead be found with traditional oxyfuel cutting.

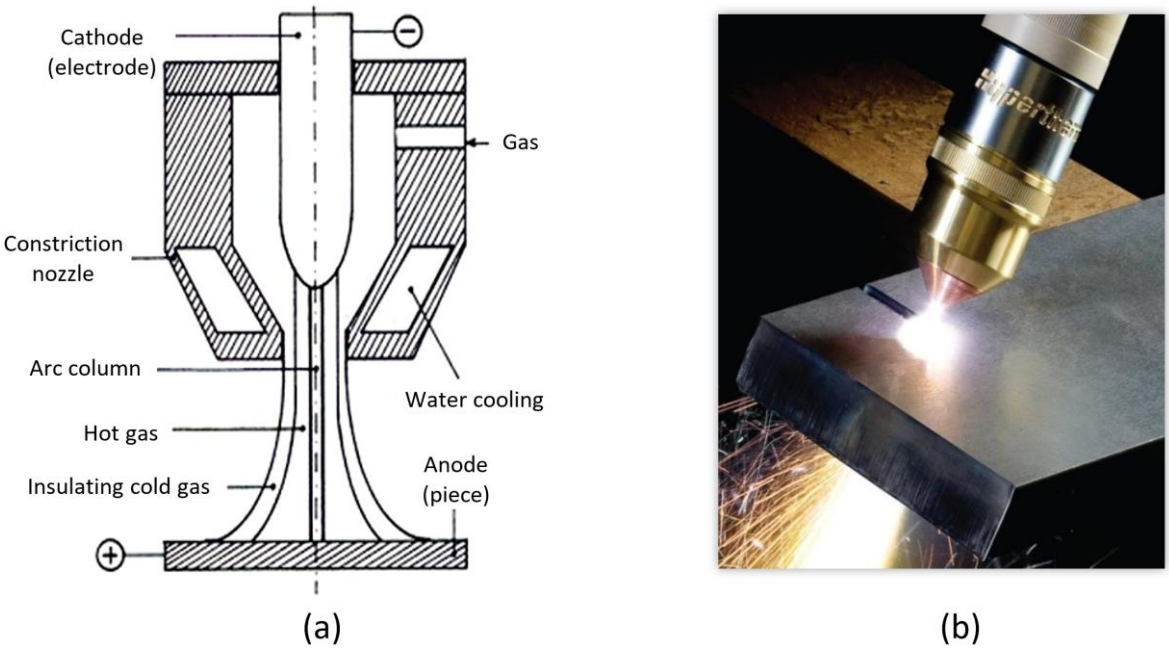

Fig. 3.12. (a) Plasma torch in transferred arc configuration and (b) example of a real plasma-cutting operation.

3.4.1.2 Plasma welding

Plasma welding (**Fig. 3.13**) is classified as an innovative welding technology, codified as PAW (*Plasma Arc Welding*) according to the ASME code for "Boiler and Pressure Vessels", or also referred to as process 15X (EN ISO 4063 standard). The equipment is completely identical to that used for plasma cutting. Depending on the current input set (which is determined on the basis of the thickness of the laminate to be welded), it is possible to distinguish three different welding processes: at low current (0.1-15 A), at medium current (15-100 A), and at high current (100-200 A). In the last two cases, the heat input is significant and it is possible to reach considerable depths in one pass with limited distortions, obtaining deep, narrow joints.

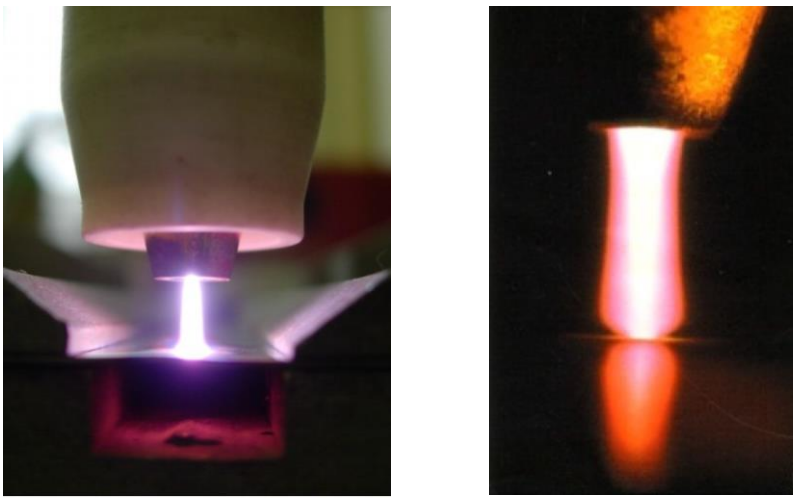

Fig. 3.13. (a) Microplasma torch and (b) arc plasma at high current (Argon, 150 A, 28 V) [58].

3.4.2 Applications of cold plasma

Despite the high number of applications of cold plasmas, they can all be traced back to surface modification operations: cleaning, activation, and coating. Generally speaking, a cold-plasma treatment entails generation of reactive chemical compounds on the surfaces not obtainable with traditional chemical processes. A considerable advantage is that only the outer surface layers of material are involved in the modification, thus leaving the properties of the bulk unaltered.
The main types of treatment are surface activation, plasma grafting, plasma etching and plasma film deposition (sputtering, PECVD).

3.4.2.1 Surface activation

Surface activation consists of the formation of free radicals on the substrate that make the surface more reactive. In fact, the surface exposed to plasma undergoes a continuous bombardment of electrons and ions, which allows removal of outer layers having low

molecular weight. As a consequence of the breaking of surface intermolecular bonds, the formation of free radicals occurs (**Fig. 3.14a**). This breakage is assisted by the presence of gases having affinity with the chemical composition of the substrate. As an example, in case of polyolefin substrates, it was found that radicals of oxygen help to break the bonds between the surface molecules and promote intermolecular bonding in the three dimensions.
As a result, new, highly-reactive polar groups form (**Fig. 3.14b**) and activation occurs. Such a condition is of particular importance in adhesive bonding, since directly correlated with the adhesion properties of the surface, primarily surface energy and wettability [59–63].

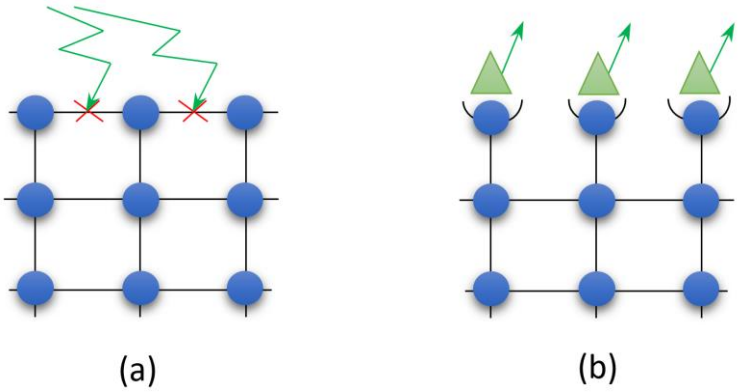

Fig. 3.14. (a) Breakage of surface molecular bonds and (b) subsequent formation of polar groups.

3.4.2.2 Plasma grafting

Plasma grafting is a process that allows modification of an activated surface, by introducing particular chemical groups (**Fig. 3.15**), by means of processing gases having chemical base similar to that desired on the active substrate [11,64,65]. As an example, in oxidizing plasmas - *i.e.*, those triggered in the presence of oxygen - the fragmentation of the molecules of plasma leads to introduction of chemical functionalities containing oxygen on the surface.

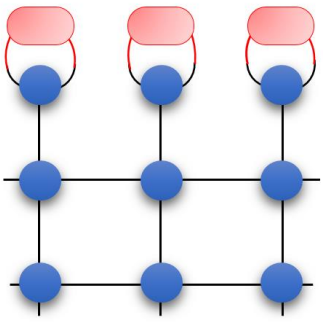

Fig. 3.15. Introduction of chemical groups on substrate activated via plasma treatment.

Typically, a polymeric material treated with an oxidizing plasma (**Fig. 3.16**) will present a surface characterized by the presence of a complex mixture of possible carbon-oxygen combinations. The C-O bond presents an asymmetrical charge distribution, oxygen having

an electronegativity significantly higher than carbon. Consequently, the chemical groups that contain C-O bonds behave like dipoles and can give rise to quite strong interactions with other dipolar molecules, such as those of water, adhesives or paints.

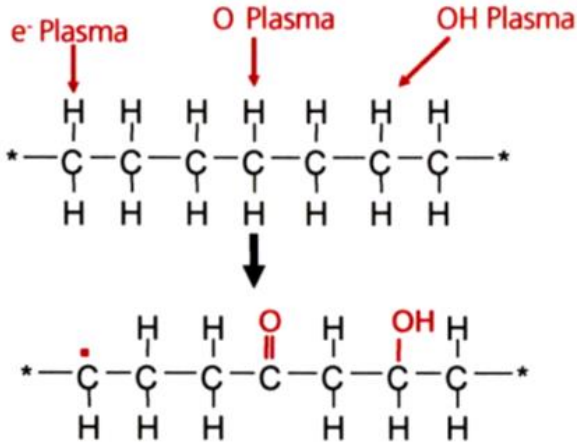

Fig. 3.16. Grafting process on the surface of polymeric substrates.

3.4.2.3 Plasma etching

Etching means the physical removal of surface material with consequent formation of volatile products, eventually extracted by pumping. Therefore, this process is commonly used for surface cleaning, but often also for the ablation of surface material to create grooves or micro-incisions. A typical application is that of printed circuit boards, where, to make the process selective, masks are used in order to treat only the uncovered parts of the substrate (**Fig. 3.17**).

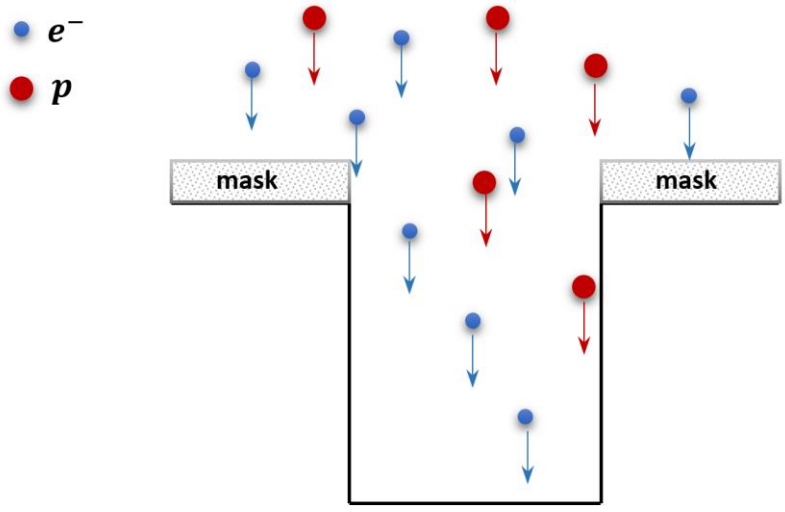

Fig. 3.17. Surface etching by means of plasma.

3.4.2.4 Plasma film deposition

The production of thin films plays a role of great interest at a technological and industrial level, owing to the increasingly frequent miniaturization of electronics. To date, several methods for the manufacturing of thin films exist. In this regard, **Fig. 3.18** illustrates a classification based on the original physical state of the material to be deposited. However, for the sake of brevity, only those methods involving non-LTE plasmas, *i.e.*, sputtering and PECVD, will be briefly described.

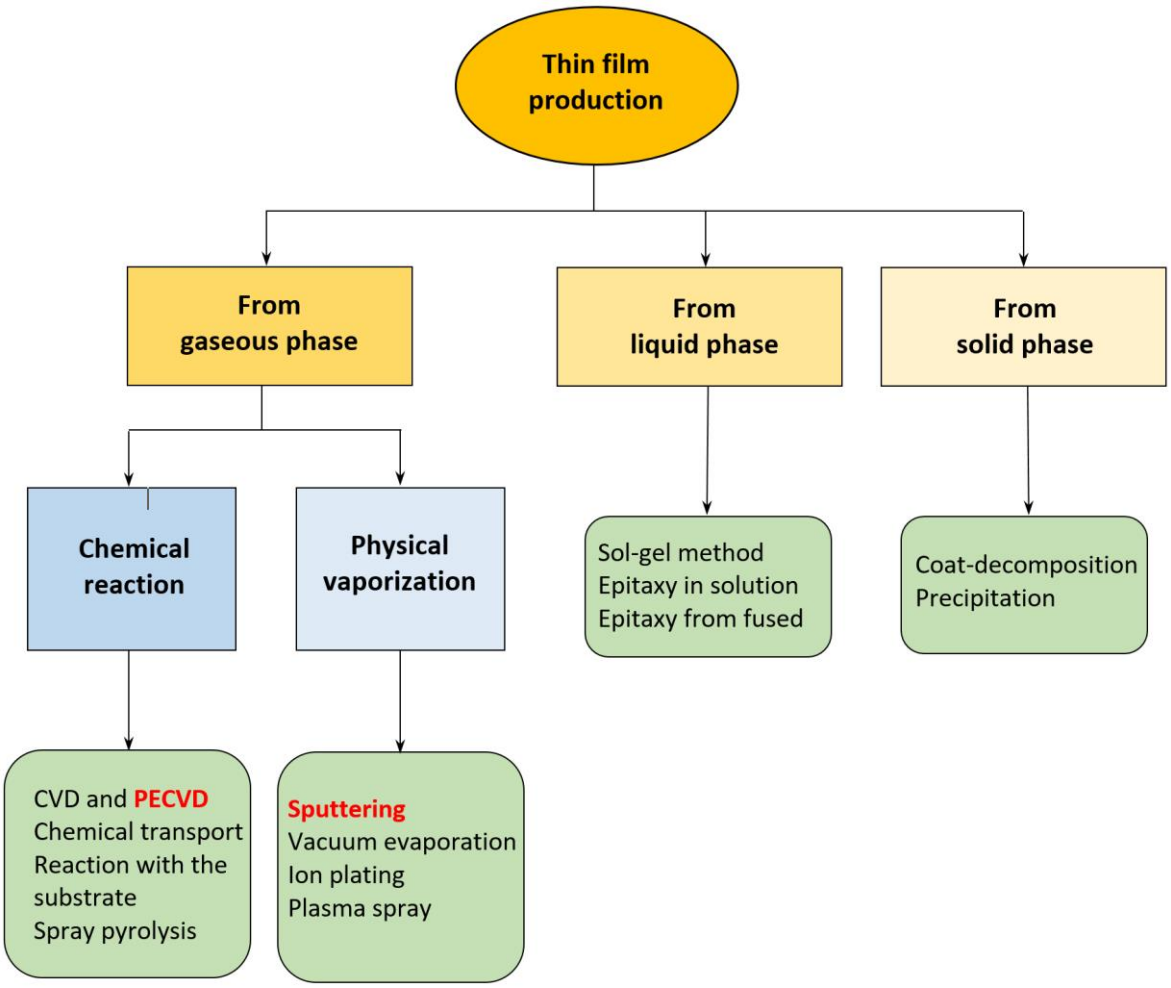

Fig. 3.18. Thin-film deposition techniques.

Sputtering

Sputtering is a process through which a solid material (named *target*) emits atoms, as a result of bombardment of high-energy, charged particles. The latter are ions of inert gas (typically argon) obtained in cold plasma conditions. During bombardment, the neutral-charge atoms are released from the target material. Consequently, not being affected by the electric field of the plasma, these are deposited on the substrate to be coated. Notably, the target is

connected to the negative electrode to ensure that ion bombardment takes place, while the substrate is connected to the positive electrode and is placed in front of the target to facilitate the deposition of the thin film (**Fig. 3.19**).
Such mechanism is possible only if the mass of the incident ion is greater than that of the target atom. It should also be noted that the emission does not occur as a consequence of a single collision, but of a series of collisions (otherwise the target atom would not have enough energy to reach the substrate).
Unlike most the thin film deposition techniques, the material constituting the target passes to the gas phase through a physical process, and not via chemical or thermochemical processes; for this reason, the process is known as *Physical Vapor Deposition* (PVD).

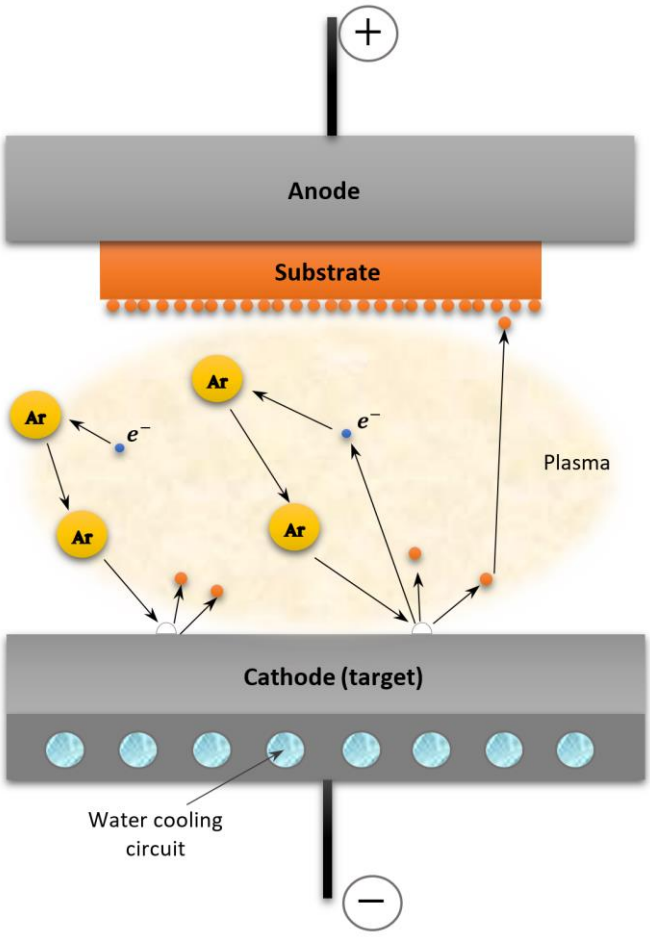

Fig. 3.19. Example diagram of the sputtering mechanism. For simplicity, the sputtering chamber, the pumping system and the generator are omitted.

Plasma Enhanced Chemical Vapor Deposition (PECVD)

Chemical Vapor Deposition (CVD) is a thin-film deposition method in which a gaseous molecular precursor is introduced, chemically reacts with an appropriate surface (substrate) and gives rise to formation of the film. Traditionally, the activation of a CVD process took place by thermal or photochemical means. More recently, for some applications, electric

discharges have been used as energy sources generating non-LTE plasmas (*Plasma Enhanced* CVD – **Fig. 3.20**). **Table 3.1** shows a comparison between the operating conditions in the CVD and PECVD processes. The PECVD offers various advantages: it operates at low temperatures, thus allowing coating of easily-degradable materials and ensuring high quality of the deposited film even with high process speeds. Furthermore, no characteristics of the substrate are altered.
Among all the applications of PECVD technologies, polymerization in plasma phase is, of course, worth noting: in this process, a fragmentation of the monomer (pure or mixed with other gases) occurs once the plasma is triggered. The molecules then react with other molecules forming a polymer that is deposited and grows on the substrate to be treated.

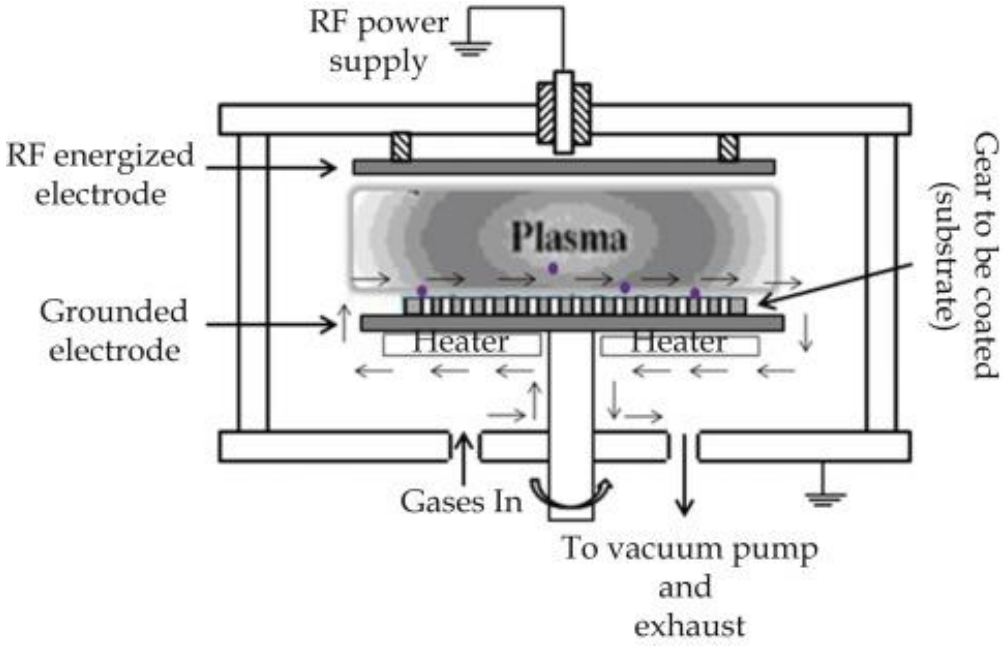

Fig. 3.20. Operative schematization of a PECVD reactor [66].

Table 3.1
Operating conditions for CVD and PECVD processes.

Parameter	CVD	PECVD
Pressure (Pa)	10^4 - 10^5	10 - 500
Substrate temperature (K)	700 - 2000	300 - 700
Deposition speed (nm/s)	1 - 5	0.3 - 2

4. Specifications of the experimental campaign

4.1 *Part A* and *B*: Effect of surface pre-bonding treatments on the adhesive properties of traditional composite materials

The investigation of the adhesion behavior of traditional CFRP substrates and the evaluation of the mechanical response of so-made adhesive joints were organized following two subsequent stages, the results of which were also published in [60] and [62], respectively.
In particular, the first stage (in the following indicated as '*Part A*') was focused on detection of both the chemical and physical effects that different treatments (specifically, low-pressure plasma) have on composite surfaces, in order to determine how and to which extent each preparation modifies the substrate and affects the ultimate resistance of the joint.
The subsequent step, from now on named '*Part B*', was dedicated to a real-world motorsport application of the adhesive system, which required a further optimization of the latter in terms of base material and process parameters, but also an in-depth evaluation of the joint behavior under severe environmental conditions, in order to estimate the system durability throughout its life-cycle.

4.1.1 Base materials

In the preliminary *Part A*, the CFRP laminates employed as substrates were manufactured with hand lay-up method, arranging 5 layers of 5H-T800-258gsm carbon plies, pre-impregnated with epoxy resin (the formulation of which is covered by industrial secret), with a 0°-orientation (**Fig. 4.1**). Consolidation and curing processes were performed using a vacuum bag in an autoclave for 2 h at 180°C and a pressure of 6 bar. The thickness of the specimens used was 1.55 mm.
As shown in the Results chapter, the mechanical characteristics of the joints resulted from *Part A*, led to adoption of an improved base material for the subsequent *Part B*, the latter requiring an optimized adhesive system also to undergo environmental aging. Hence, for this second stage, the CFRP material used as substrate for tensile shear strength (TSS) evaluation is shown in **Fig. 4.2**. This was manufactured arranging 7 layers of 2/2-twill carbon-plies with a 0°-orientation, pre-impregnated with epoxy resin via hand lay-up technique (also in this case, industrial secrecy was imposed on the matrix-resin formulation). A medium curing process was performed using a vacuum bag in an autoclave for 2 h at 135°C and a pressure of 6 bar. CFRP panels having thickness 1.55 mm and Young's modulus E equal to 70 ± 5 GPa were obtained. To perform wedge tests, 3mm-thick laminates were adopted. To limit water adsorption/absorption from the substrates, in all cases involving environmental aging, after cutting (performed via a water-jet technique), the laminate edges were sealed by applying a layer of the same epoxy resin employed as matrix.

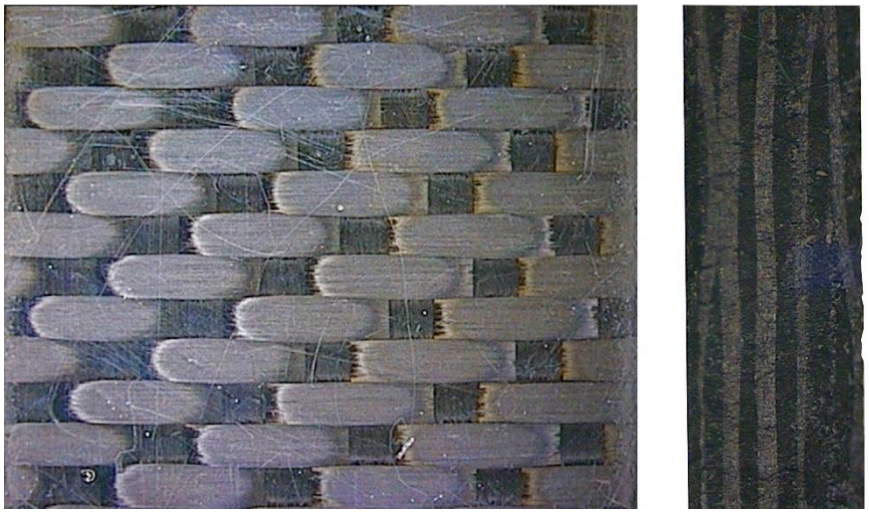

Fig. 4.1. Top view and cross-section of the CFRP used in *Part A*.

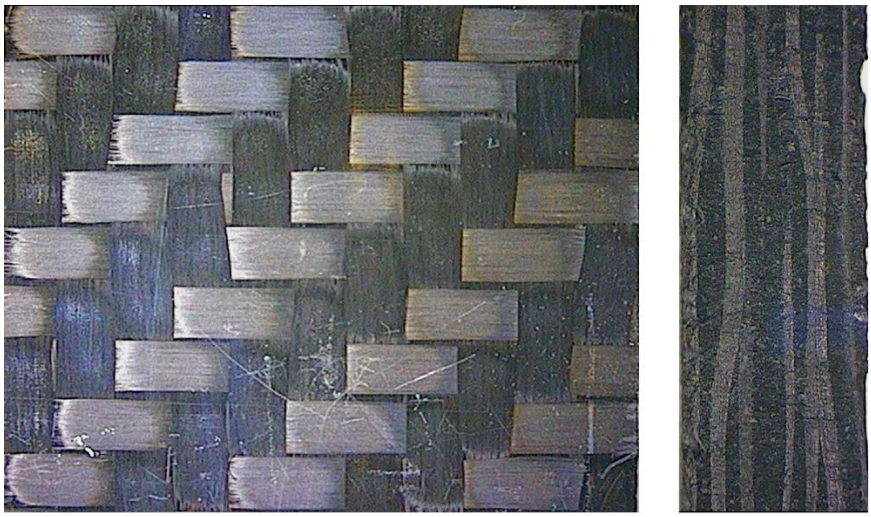

Fig. 4.2. Top view and cross-section of the CFRP used in *Part B*.

4.1.2 Surface pre-bonding preparations

4.1.2.1 Reference preparations

Before each treatment - except when peel-ply was used - all the substrates were preliminarily wiped with acetone to remove any trace of surface contaminant. **Table 4.1** shows all the preparations performed on CFRP substrates and used as references against which the results obtained after plasma treatments were evaluated.
Two sets of control samples are common to both the two aforementioned stages of the work, namely, those whose bond area was prepared with conventional methods such as solvent degreasing (representative of the as-received condition) and mechanical abrasion, respectively. Specifically, the former was carried out by using a cotton cloth soaked in

acetone, as shown in **Fig. 4.3**; the abrasion was manually undertaken using a 3M™ Scotch-Brite™ MX-SR abrasive (**Fig. 4.4**), by superimposing linear movements in directions varying by 45° between one pass and another.

Table 4.1
Summary of the traditional surface preparations carried out on the CFRP substrates.

Surface preparation	Description
Degreasing	Acetone wiping
Abrasion	Acetone wiping + Scotch-Brite™ MX–SR + Acetone wiping
Peel ply	Peel-ply removal from the top surface (only in *Part A*)

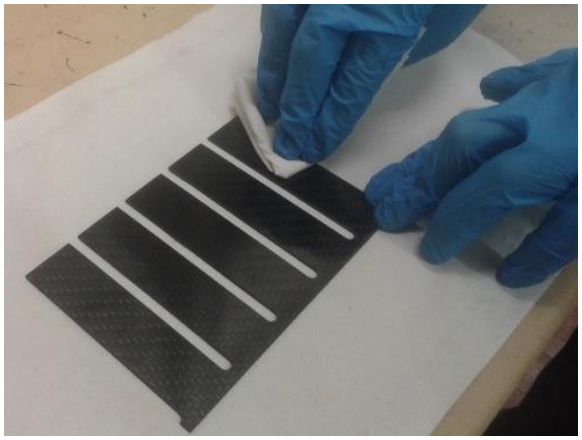

Fig. 4.3. Acetone wiping of the substrate surfaces.

Fig. 4.4. 3M™ Scotch-Brite™ MX-SR abrasive cloth used to perform manual abrasion of the substrates.

After abrasion, the surfaces were wiped again with acetone, in order to remove all debris of

the removed material or residual of the abrasive sponge from the outer layer.
For the samples with the peel-ply, no further cleaning procedure is normally required after its removal. This release ply consists of a layer of polyester fabric inserted between mold and consolidation step (**Fig. 4.5**). Thus, the joints made with this technique were bonded immediately after the removal of the protective ply. However, owing to the ineffectiveness of such surface preparation resulted from the characterization of *Part A*, peel-ply was not adopted in *Part B*.

Fig. 4.5. Removal of the polyester ply from the peel-ply composite substrate.

4.1.2.2 Low-Pressure Plasma treatment

To perform Low-Pressure Plasma (LPP) treatments, a Tucano multipurpose LPP reactor (Gambetti Vacuum Technology, Italy) was used (**Fig. 4.6**), the main characteristics of which are provided in **Table 4.2**.

Table 4.2
Technical specifications of the Gambetti Tucano LPP reactor.

Chamber dimensions	Ø 140 mm, L 310 mm
Power supply	13.56 MHz, 200 W
Sample-holder support	110 mm x 320 mm
Pfeiffer two-stage vacuum pump	2.5 m^3/h
Electrode-support distance	80 mm

This reactor, schematized in **Fig. 4.7**, is powered by a radio frequency (RF) generator that operates at a fixed frequency of 13.56 MHz, with maximum power of 200 W. Through two Mass Flow Controllers (MFC), a certain percentage of process gas (as a single gas and mixtures of two gases) is introduced into the vacuum chamber, where the samples to be treated are contained.

(a) (b)

Fig. 4.6. (a) Exterior and (b) interior of the Gambetti Tucano LPP reactor used.

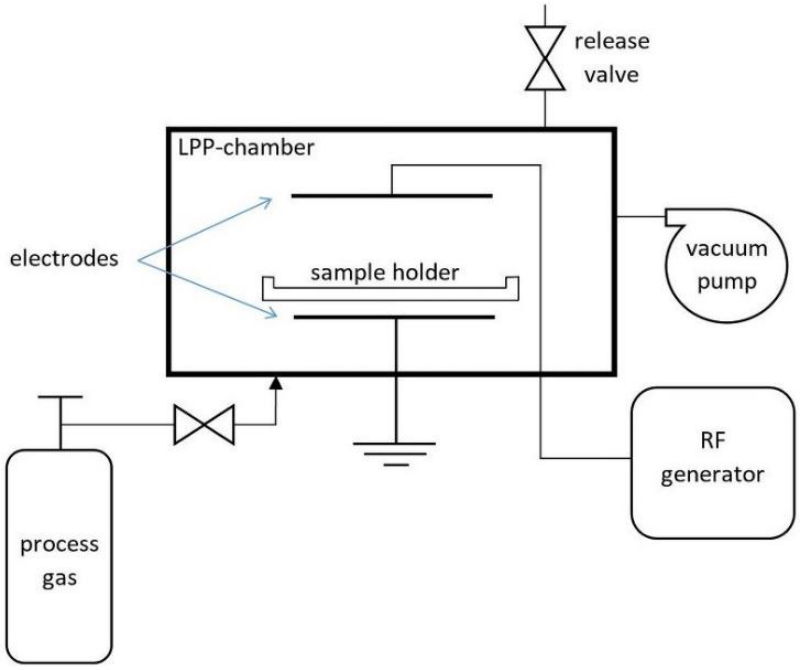

Fig. 4.7. Operating scheme of the LPP device employed for the surface treatments.

From a software point of view, this LPP reactor is managed by means of an integrated microcomputer, programmed by the user through an interface digital panel on which to set and display the process parameters, and monitor them during treatment (**Fig. 4.8**).
Upon completion of the programming stage, the treatment is started: the chamber is evacuated to a pressure level of 0.1 mbar, and then the RF power supply is switched on to ignite the plasma discharge between the two electrodes. At this stage, the display assumes the function of interface to monitor the progress of the treatment (**Fig. 4.9**). The label '*Plasma Ok*' indicates that plasma is regularly activated; such a condition can also be verified visually, through the front porthole. The color assumed by plasma depends on the process gas (**Fig. 4.10**).

Fig. 4.8. Control panel.

Fig. 4.9. Display in monitoring function.

(a) (b) (c)

Fig. 4.10. Typical colors of (a) air, (b) argon, and (c) oxygen plasmas.

In this study, the effect of different gases was investigated. In particular, air, oxygen, argon or nitrogen were studied in *Part A*, varying both exposure time and plasma power among the values listed in **Table 4.3**, for a total of 36 conditions to be considered. It should be noted that other time settings of 5 and 30 s were also considered, but these were then excluded due to the resulting instability of the treatment. Indeed, since plasma stabilization required more than 3 s, shorter treatments were not effective or not reproducible.

Table 4.3
LPP treatments carried out on the CFRP substrates in *Part A*.

Part A		
LPP	Acetone wiping + Plasma discharge with the following set-up parameters:	
	Power (W)	50, 100, 150
	Exposure time (s)	60, 180, 300
	Gas	Air, O_2, Ar, N_2

Based on the results obtained from the preliminary characterization, in *Part B*, only air or oxygen were used as process gases, again varying the other main process parameters (i.e., exposure time and treatment power), as reported in **Table 4.4**.

Table 4.4
LPP treatments carried out on the CFRP substrates in *Part B*.

Part B		
LPP	Acetone wiping + Plasma discharge with the following set-up parameters:	
	Power (W)	50, 100, 150
	Exposure time (s)	60, 180, 300
	Gas	Air, O_2

4.1.3 Adhesive

To avoid introduction of further variables in the system, a unique adhesive was selected for all the cases studied. Specifically, the substrates were joined using the 3M™ DP490 adhesive, the main technical characteristics of which are listed in **Table 4.5**. This is a two-component, thixotropic epoxy resin, designed for structural adhesive bonding requiring toughness and high mechanical strength, as well as excellent thermal and environmental resistance.
The adhesive was prepared by mixing two parts of epoxy resin and one part of amine-modified curing agent. Complete crosslinking was obtained through 14-h curing at RT, followed by post-curing in a reticulation oven for 1 h at 80°C, following the indications provided by the adhesive manufacturer.
The equipment shown in **Fig. 4.11** was used to apply the 3M™ DP490 adhesive on the substrates. This comprised the adhesive cartridge, the extrusion gun, a specific piston for adhesives having a 2:1 mix ratio, a labyrinth nozzle (*static mixer*) to ensure complete mixing of the two components, and a metallic spatula.

Table 4.5
Technical specifications of the 3M™ DP490 adhesive.

Characteristic	Base	Accelerator
	Epoxy	Amine-modified
Color	Black	White
Mix ratio	100	50
Work life	1.5 h @ 23°C	
Handling time	4÷6 h @ 23°C	
Curing conditions	7 days @ 23°C or	
	14 h @ 23°C + 1 h @ 80°C	

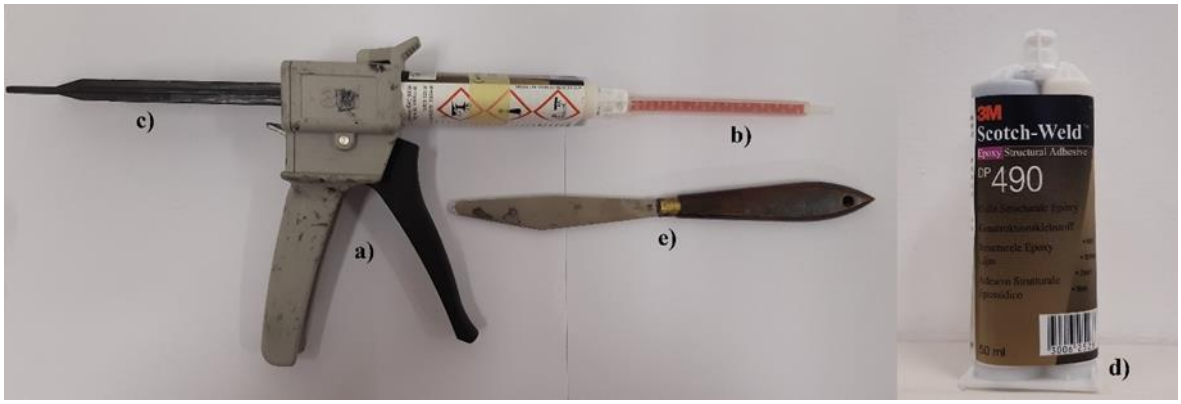

Fig. 4.11. Equipment for the adhesive application: (a) extrusion gun, (b) static mixer, (c) 2:1 piston, (d) 3M™ DP490 cartridge, and (e) metallic spatula.

4.1.4 Single-lap joint fabrication

In both *Part A* and *Part B*, TSS was evaluated in order to assess the effectiveness of the treatments on the mechanical performance of homogeneous CFRP-to-CFRP single-lap joints (SLJ). Laminates of dimensions 25 mm × 100 mm were obtained by cutting CFRP sheets with a water-jet technique, in accordance with the geometries established by the EN 1465 standard [67]. The latter made the simultaneous manufacturing of 5 identical specimens possible, as shown in **Figs. 4.12** and **4.13**. Consequently, for each set of treatment conditions, five repetitions (N=5) were performed, and the mean value will be reported in the Results section together with the related value of standard deviation.
Adhesive bonding was carried out within 15 min of each treatment, especially when LPP was performed, in order to exclude both any further surface modification and deterioration of the treatment effect due to contamination.
Referring to the realization steps shown in **Fig. 4.14**, the 3M™ DP490 adhesive was applied to the bond area of both substrates to be joined. A controlled thickness of adhesive was obtained using a sheet of non-stick paper with calibrated thickness (0.05 mm).

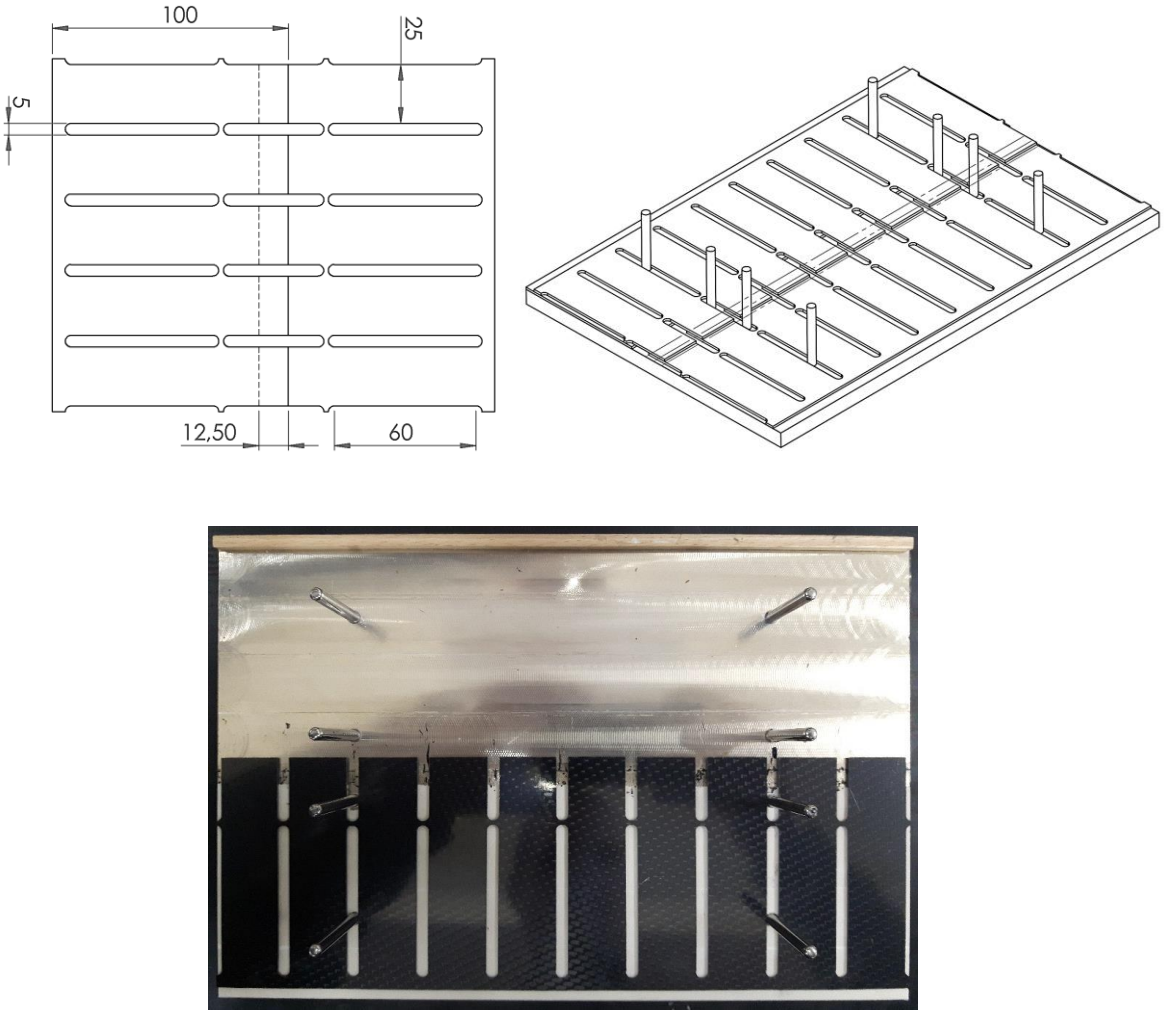

Fig. 4.12. Schematic of SLJ geometry according to EN 1465 (values in mm) and fixing table.

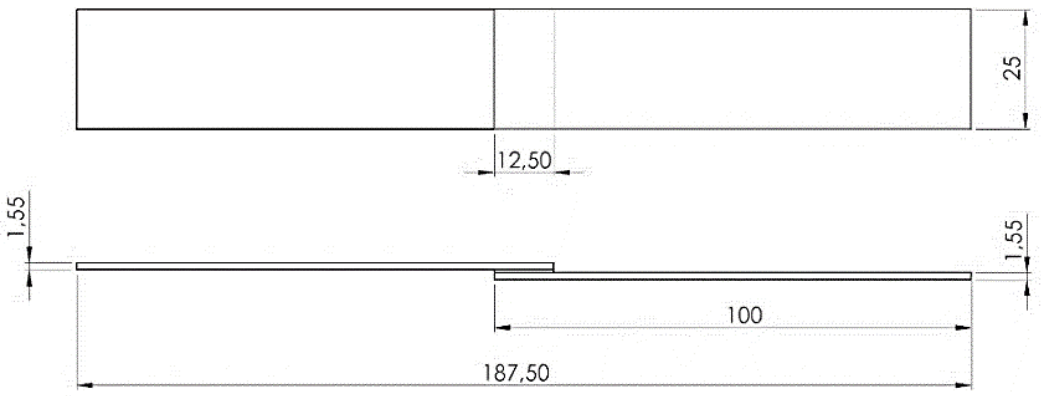

Fig. 4.13. Detail of a SLJ (values in mm).

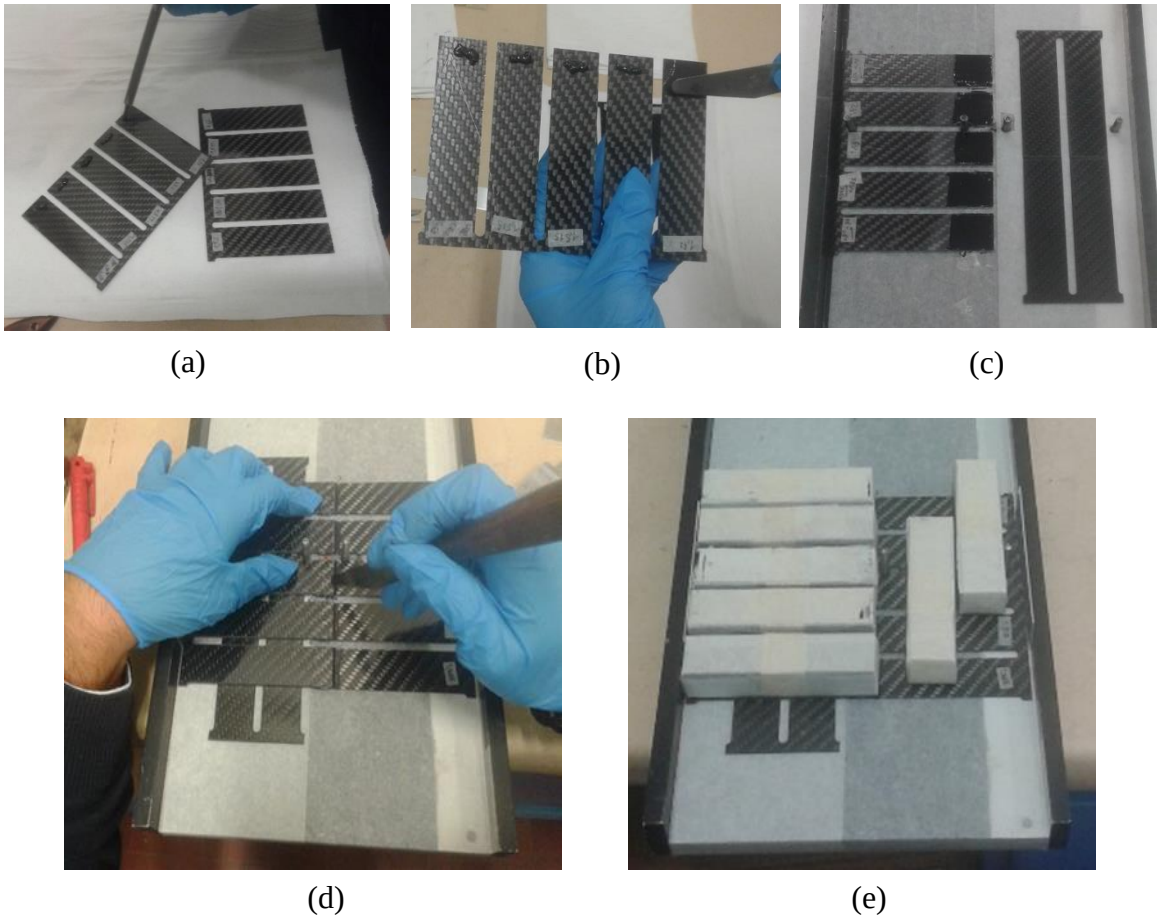

Fig. 4.14. Steps of the TSS-joint manufacturing: (a) adhesive extrusion and (b) application, (c) positioning of the laminates on the support, (d) removal of the excess adhesive after overlapping, and (e) load application.

The substrates were placed in contact with a 12.5 mm overlap along the major axis. Any excess adhesive present at the interface was expelled by pressing the joint and then removed, using the metallic spatula to create a regular arc-shape fillet along the two transversal edges of the joining area. Ad hoc fixing tables were used to ensure perfect alignment of the two substrates and maintain their position throughout the time needed for complete curing of the adhesive.

4.1.5 Mechanical characterization of joints

4.1.5.1 Testing machine

All the mechanical tests were carried out by using an Instron 8802 Universal Testing machine equipped with a 50 kN load cell (**Fig. 4.15**).
This machine is able to perform both static and dynamic tests, and consists of the following base elements:

- a structure housing the load actuation and detection system, which uses load cells with the possibility of working in both directions (traction and compression);
- a hydraulic unit that allows the movement of the actuator and tightening of the clamping heads;
- the electronic components, which perform all the functions of regulation, control and acquisition of the output signals from the transducers of load and deformation;
- the user interface, made via a PC connected to the control electronics. The affiliated *Console* software allows complete control and setting of the test machine. For the execution of static tests (traction/compression), the *Blue Hill* software is also provided, through which the user defines the procedure and sets the testing parameters.

Fig. 4.15. Instron 8802 universal testing machine and detail of the gripping system.

Using the remote control located on the machine front, it is possible to adjust the movement and fastening of the cross-head, also allowing opening and closing of the grip heads (detail

of which is provided in **Fig. 4.15**) as well as adjustment of the oil pressure. On the front, there is also a safety button, which allows the machine to be blocked and made safe in case of potentially dangerous events.

4.1.5.2 Tensile shear-strength testing

Tensile shear strength (TSS) testing was performed in accordance with ASTM D 1002, which provides for the specimen elongation at constant speed: the unidirectional tensile load is applied orthogonally to the cross-section of the specimen and slowly increases to a value so as to cause the sample failure.
In particular, the joints were tested to failure at a crosshead displacement rate of 1.3 mm/min using the testing machine previously described. A grip area of 25 mm × 25 mm was ensured. Here, shims having the same thickness as the specimen were placed, allowing alignment of the bond area along the centerline between the grip faces and minimize bending of the specimens at the joining area.
In **Fig. 4.16**, a scheme of the joint loading condition is illustrated, and a picture of a real specimen installed on the testing machine is also provided.

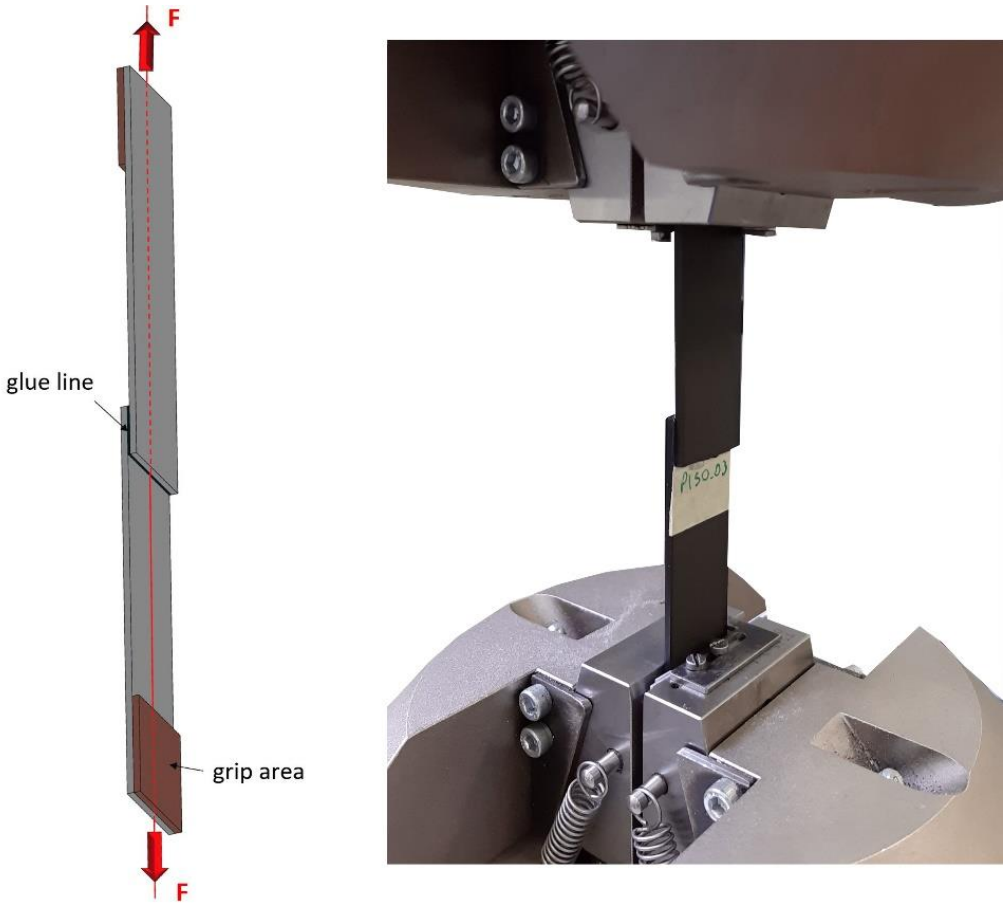

Fig. 4.16. Testing scheme for the TSS evaluation and real specimen installed on the machine before testing.

The shear strength, τ, was calculated by means of the following **Eq. (4.1)**:

$$\tau = \frac{F}{A_0} \qquad (4.1)$$

where F is the ultimate load at failure (N) and A_0 is the initial overlap area equal to 25 mm × 12.5 mm.

4.1.6 Morphological assessment

Owing to transparency of the epoxy matrix to laser sources, the morphological and roughness measurements required the use of an optical instrument. Hence, such analyses were carried out by means of a Zeta20 3D (Zeta Instruments, US) optical profilometer (**Fig. 4.17**) at the Materials Characterization laboratories of IIT. 3D images were acquired using a 20X magnification lens, with a single field of view of 664 μm × 498 μm. The roughness parameter S_q was extracted from the images, according to ISO 25178, which is suitable for anisotropic composite materials. Nine measurements (N=9) were taken for each sample, in order to achieve average values and related standard deviations.

Fig. 4.17. Zeta20 3D optical profilometer.

4.1.7 Surface chemical state analysis

To assess the chemical activation state of the differently treated surfaces, X-ray Photoelectron Spectroscopy (XPS) analyses were performed using a Kratos Axis Ultra^{DLD} spectrometer (**Fig. 4.18**), fitted with a monochromatic Al Kα source (1486.6 eV) operating at 15 kV and 20 mA. The analyses were carried out on areas of dimensions 300 μm × 700 μm each.

Wide scans were acquired by collecting the low-resolution signals (pass energy of 160 eV and steps of 1.0 eV). High-resolution narrow scans were performed at a pass energy of 20 eV and steps of 0.1 eV. Data acquisition was carried out in ultra-high vacuum (UHV) conditions, maintaining a base pressure below 6 x 10^{-9} mbar in the analysis chamber.

All spectra were charge calibrated to the main line of the C 1s spectrum (adventitious carbon), setting its binding energy value equal to 284.8 eV. Spectra were analyzed using CasaXPS software (version 2.3.18). Peak deconvolution and data fitting were carried out using Shirley-type background and Gauss-Lorentz profiles.

Fig. 4.18. Kratos Axis Ultra^{DLD} x-ray photoelectron spectrometer.

4.1.8 Contact angle measurement and surface free energy evaluation

The static-θ measurements were performed with *sessile drop technique*, using two different test liquids: deionized water and diiodomethane (CH_2I_2). Indeed, the former has a prominent polar behavior, whereas the latter is completely non-polar. Specific CFRP laminates were dedicated to this test, each treated with a different LPP condition. The measurements were performed with an Attension Theta Lite optical tensiometer (**Fig. 4.19**), depositing on each substrate five droplets per liquid and acquiring a total of 10 values of θ (right and left).

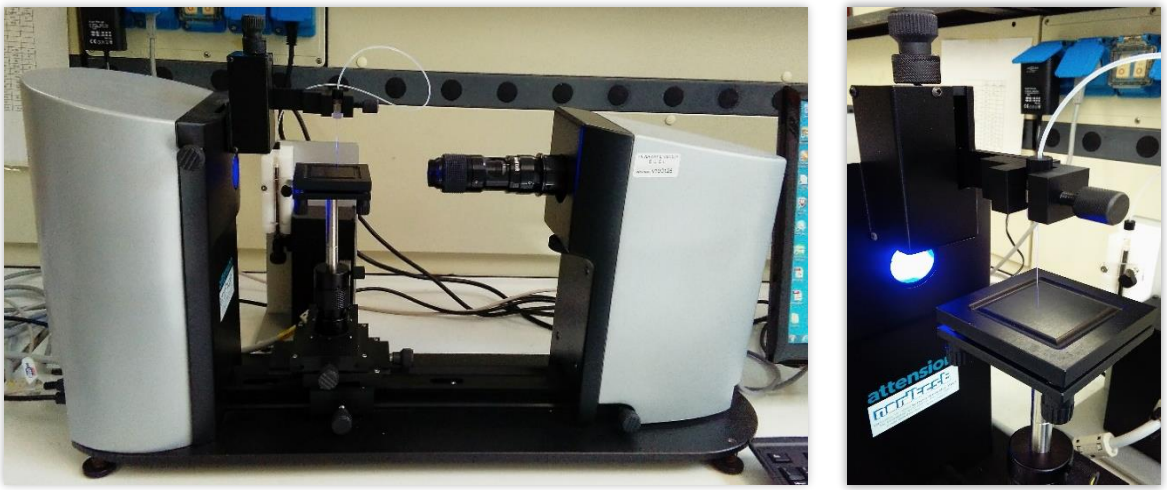

Fig. 4.19. Attension Theta Lite optical tensiometer used to perform the sessile drop technique.

A constant droplet volume of 3 μL and 2 μL was used for H_2O and CH_2I_2 respectively, to address the different density of the two liquids and thus prevent variations of the droplet shape due to gravity [68,69]. The images captured were then digitized using the dedicated software, One Attension.

To evaluate the surface free energy (SFE) of the substrates and appreciate its rise after plasma treatment, Wu's energy model was adopted [70,71]. This model is successfully applicable to relatively flat surfaces and is widely used to characterize materials having low-surface energy, as with polymer or composite substrates. As described in section 2.4, according to this model, by dividing the surface energy at the solid-vapor interface γ_S and at the liquid-vapor interface γ_L into their polar and dispersive parts (see corresponding *p* and *d* superscripts), it is possible to calculate the surface energies using a harmonic mean:

$$\gamma_{SL} = \gamma_S + \gamma_L - 4\left(\frac{\gamma_S^d \cdot \gamma_L^d}{\gamma_S^d + \gamma_L^d} + \frac{\gamma_S^p \cdot \gamma_L^p}{\gamma_S^p + \gamma_L^p}\right) \quad (2.8)$$

This, combined with Young's equation (2.1),

$$\gamma_L \cos\theta = \gamma_S - \gamma_{SL} \quad (2.1)$$

provides the following expression:

$$4\left(\frac{\gamma_S^d \cdot \gamma_L^d}{\gamma_S^d + \gamma_L^d} + \frac{\gamma_S^p \cdot \gamma_L^p}{\gamma_S^p + \gamma_L^p}\right) = \gamma_L(1 + \cos\theta) \quad (2.9)$$

where θ is the contact angle of liquid measured at the triphasic point.

The total surface tension of the two test liquids γ_L and their polar γ_L^p and dispersive γ_L^d components are known and reported in **Table 4.6**.

Table 4.6
Polar, dispersive and total surface tension of the test liquids used.

Liquid	$\boldsymbol{\gamma_L^p}$ (mN/m)	$\boldsymbol{\gamma_L^d}$ (mN/m)	$\boldsymbol{\gamma_L}$ (mN/m)
H_2O	51	21.8	72.8
CH_2I_2	0	50.8	50.8

The contact angles of both liquids on the solid surface were determined and, consequently, polar γ_S^p and dispersive γ_S^d fractions, whose sum gave the total surface energy γ_{SV} of the solid. To do this, the following system of equation was considered, where the subscripts W and DIM refers, respectively, to water and diiodomethane:

$$\begin{cases} 4\frac{\gamma_S^d \cdot \gamma_W^d}{\gamma_S^d + \gamma_W^d} + 4\frac{\gamma_S^p \cdot \gamma_W^p}{\gamma_S^p + \gamma_W^p} = \gamma_W\,(1 + cos\,\theta_W) \\ 4\frac{\gamma_S^d \cdot \gamma_{DIM}^d}{\gamma_S^d + \gamma_{DIM}^d} + 4\frac{\gamma_S^p \cdot \gamma_{DIM}^p}{\gamma_S^p + \gamma_{DIM}^p} = \gamma_{DIM}\,(1 + cos\,\theta_{DIM}) \end{cases} \quad (4.2)$$

To automate the solution of the system of equations (4.2) during the operational phase, the simple Excel code shown in **Fig. 4.20** was developed. Implemented with the chosen model, it allowed a faster achievement of the value of γ_{SL} related to each sample tested. The results were consistent with those found in the literature, to guarantee the reliability of Wu's model and the validity of the tool.

Input:
Properties of the test liquids.

Input:
Mean values of contact angle measured on the same surface with the two test liquids.

Output:
Dispersive, polar and global components of the surface free energy.

Solver with Wu's model implemented.

	A	B	C	D	E	F
1	γ_w	[mN/m]	72.8			
2	γd_w	[mN/m]	21.8			
3	γp_w	[mN/m]	51			
4						
5	γ_DIM	[mN/m]	50.8			
6	γd_DIM	[mN/m]	50.8			
7	γp_DIM	[mN/m]	0			
8						
9	Θ_w [°]	**34.8**	β_w [rad]	0.61	cosβ_w	0.82
10	Θ_DIM [°]	**29.7**	β_DIM [rad]	0.52	cosβ_DIM	0.87
11						
12	X=γd_s	[mN/m]	44.54			
13	Y=γp_s	[mN/m]	29.05			
14	γ_s	[mN/m]	**73.59**			
15						
16						
17			W	DIM		
18	γ_L(1-cosΘ_L)		132.58	94.93		
19	coef.XY		-158.62	-108.27		
20	coef.X		2314.36	0.00		
21	coef.Y		-1556.96	4822.27		
22	const.term		147402.07	0.00		

Fig. 4.20. Graphical interface of the Excel solver created for the SFE evaluation.

4.1.9 Accelerated aging procedure

The specific application at the basis of the study (particularly, of *Part B*) led us to employ a cyclic aging. The necessity was indeed to stress some of the extremely variable environmental conditions where adhesively–bonded CFRP body-shop components of motorsport vehicles might encounter during their life (i.e., between one race and the following), before being repaired or substituted: proximity to hot parts (e.g., exhaust or engine), asphalt-induced warming, presence of humidity, alternating with cooling during temporary stoppage of the vehicle in the pit. Given the severity of the application, it was necessary to further emphasize such conditions, in order to oversize the capability of the joints.

Hence, aging was carried out using a WEISS WK3 340-70 (Weiss Technik, Milan, Italy) climatic chamber (**Fig. 4.21**), repeating 56 times (for a total duration of 672 h) the D4 cycle suggested by EN ISO 9142 standard [72] and depicted in **Fig. 4.22**.

Fig. 4.21. WEISS WK3 340-70 climatic chamber.

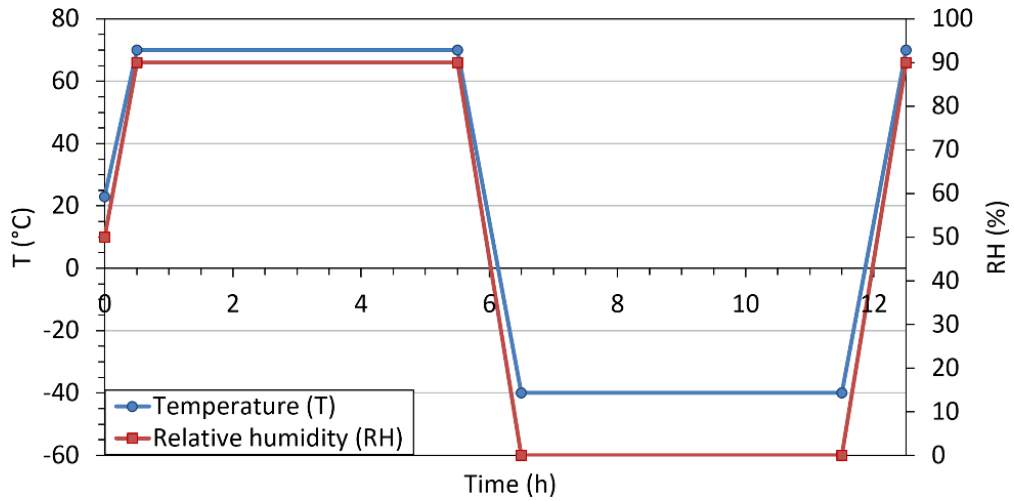

Fig. 4.22. D4 accelerated aging cycle as per EN ISO 9142 [72].

Among those proposed by the standard, D4 cycle best covers the range of temperatures foreseen for the long-term use of the CFRP-adhesive system and it is more demanding owing to thermal shock. Moreover, it is well known that coexistence of high temperature and humidity is one of the most severe aspects for adhesive joints [59].

Thus, the durability of the CFRP-epoxy adhesive system under accelerated aging conditions was evaluated for five different sets of adhesive-joints, namely the control abraded joints and those plasma-treated joints that presented the best and the worst mechanical performance with the two process gases investigated. In particular, the following two tests were performed:

- TSS testing on 5 sets of SLJ (manufactured as described in Section 4.1.4), respectively tested after 14, 28, 42 and 56 cycles of conditioning, which allowed us to quantify the loss rate of shear strength;
- wedge cleavage test (WT) performed as per ASTM D3762 [73], focusing on the influence of the combined action of mechanical (cleavage) and environmental stresses on the adhesive system, varying substrate pre-bonding treatment.

As regards the latter, the appropriate thickness of the adherends was determined by trial and error method; according to the related standard, the following **Eq. (4.3)** was indeed used to calculate the minimum admissible thickness in case of uniform symmetrical beams:

$$h = \sqrt{\frac{6Ta}{B\sigma_y}} \qquad (4.3)$$

where:

$h =$ adherend thickness normal to the plane bonding, (mm)
$a =$ crack length at maximum load, (mm)
$B =$ bond width, (mm)
$\sigma_y =$ tensile yield point of the substrate material, (MPa)
$T =$ 150% of the maximum load to start the crack in the adhesive bond, (N).

As Adams et al. argued [74], definition of the proper T value might be ambiguous, since it can be interpreted as the force required to cause the first crack (T_1, which is measureable during wedge insertion) as well as the peel force required to separate the adherends (T_2), which is related to the former by the following approximation:

$$T_1 = 0.8\,T_2 \qquad (4.4)$$

Since plastic deformation is to be avoided during wedge insertion as - if it occurred - the crack tip length could be reduced and the test compromised, the precautionary relationship **(4.4)** was implemented. Based on this, a thickness of 3 mm was ensured for both the adherends. Rectangular CFRP specimens of dimensions 150 mm × 25 mm × 3 mm were manufactured (**Fig. 4.23**).

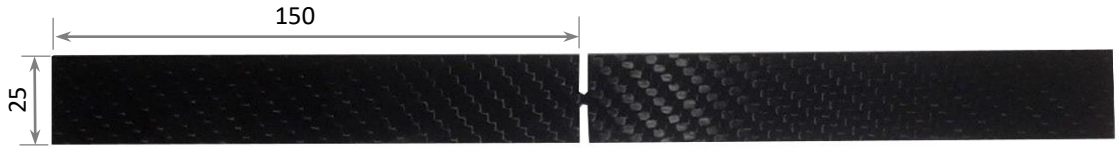

Fig. 4.23. Configuration of the WT substrates to couple via adhesive bonding (values in mm).

To perform the WT-joints, each faying surface was first wiped with acetone and then plasma-treated, on the basis of the results of the previous mechanical characterization carried out under standard environmental conditions. In **Fig. 4.24**, the manufacturing procedure for the WT is shown. The 3M™ DP490 adhesive was applied on the surface of both substrates, leaving an unbonded length of 35 mm at one end of the joint in which to insert the wedge.

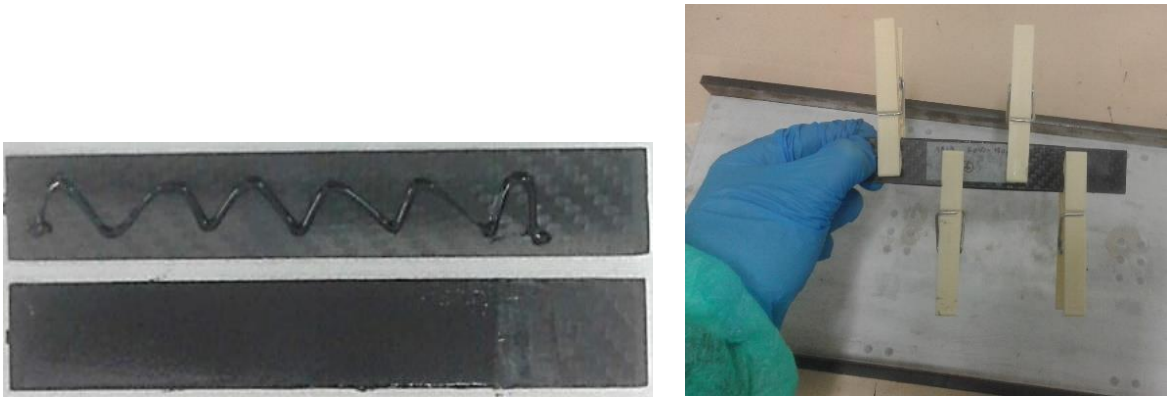

Fig. 4.24. Fabrication of the WT samples: (left) adhesive application and (right) joining.

A polytetrafluoroethylene comb-spacer was used to align the test samples during assembly procedure. Then, pressure was applied on the surface of each WT-joint in order to squeeze excess adhesive out and maintain the samples flat over time necessary for complete curing.
The next phase provided for introduction of an aluminum wedge between the two substrates (**Fig. 4.25**). As indicated by the reference standard, a constant wedge-driving speed of 30 mm/min was adopted, using a hydraulic press. The initial crack-length (i.e. the crack triggered at the wedge insertion) and its propagation inside the adhesive-layer and/or at the interface were measured by microscope. For each set of treatment conditions, ten WT joints were manufactured (N=10).
The system property determined by the wedge test was the adhesive fracture toughness associated to Mode I (G_{Ic}), expressed in (J/m^2), which represents the strain energy release rate during crack formation/propagation. It was calculated from crack length and specimen dimensions using the empirical **Eq. (4.5)** reported by Sargent [27] and based on linear-elastic beam theory:

$$G_{Ic} = \frac{Ey^2h^3}{16}\frac{[3(a+0.6h)^2+h^2]}{[(a+0.6h)^3+ah^2]^2} \qquad (4.5)$$

where:

E = Young's modulus of the substrate material, (Pa)
a = crack length, from the bearing edges of the wedge to the crack tip, (m)
h = thickness of the adherends, (m)
y = displacement of the adherends caused by wedge, (m).

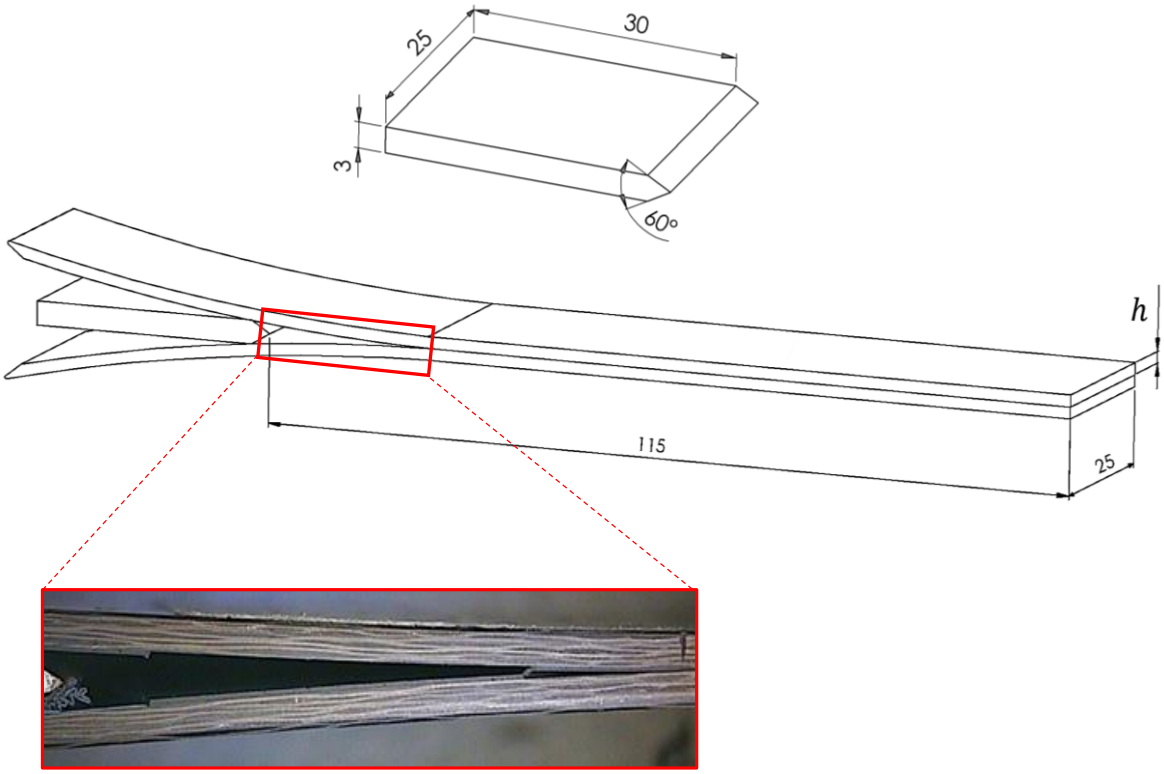

Fig. 4.25. Geometrical configuration of wedge and WT joint as per ASTM D3762 (values in mm) [73], and detail of the real joint opening at the wedge insertion.

4.2 *Part C*: Performance and applicability limits in adhesive bonding of 3D-printed composites

The third stage of this research work was focused on the evaluation of the mechanical response of adhesive joints made by manufacturing the substrates via Fused Filament Fabrication technology. Indeed, recent developments in additive technologies for the manufacturing of structural composite-material parts are progressively pushing many industries to consider positively the implementation of such processes in their own production. However, to be considered as a valid substitute for the more traditional polymer composites, additively manufactured (AM) composites have to satisfy similar performance requirements, needing in-depth optimization of the construction criteria, specifically of the process parameters that dictate the final quality of the 3D-printed part.
As also recently pointed out by Kabir et al. [41], there is still a lack of research on aspects that may be equally helpful to understand to what extent AM composite materials can be used and what challenges remain. One of these is related to the possibility that the final product might be realized by joining a number of smaller parts. Alternatively, printed components, built to replace damaged components, might need to be joined to pre-existing parts.
For its part, 3D printing must allow fabrication of composite components in such a way as to make any assembly operations possible, safe and reliable. Indeed, composite structures, and particularly those built additively, are by their nature non-homogeneous. So, how does this affect the joint behavior? To what extent is it possible to adhesively bond 3D-printed composites, obtaining quality joints?
Hence, the following experimental stage of the work was focused on verifying how the AM substrates respond to adhesive bonding when the interface interactions are increased by preparing the surface. In particular, the mechanical and failure behavior of an adhesive system made of a composite substrate having longitudinal arrangement of the continuous carbon fibers (CCF) and epoxy adhesive was investigated. The effectiveness of the LPP treatment on the adhesion properties was appraised again over that of conventional pre-bonding preparations (degreasing or abrasion).
Given the novelty of this adhesive system, more information about the construction criteria and the mechanical characteristics of the base material was believed necessary to allow any correlation to the mechanical behavior of the joints. Hence, surface analyses were carried out and TSS testing was performed to characterize the mechanical resistance of so-made adhesive joints. Their failure behavior was analyzed critically with respect to the non-homogeneity of the substrate structure.
In the following, the manufacturing of adhesive joints made by using a structural epoxy adhesive will be shown, and the relative step-by step fabrication criteria will be detailed.

4.2.1 3D-printer

In this investigation, two types of filaments supplied by Markforged® (Boston, USA) were employed to build the specimens:

- a Nylon-6 filament reinforced with chopped carbon fiber, traded as Onyx, having a nominal diameter of 1.75 mm;
- and continuous carbon fiber (CCF) embedded in a Nylon-6 matrix, which came in a diameter of 0.35 mm (in **Fig. 4.26**, a typical cross-section of the CCF filament is shown).

Prior to their use, the filaments were stored in a protective dry box, to avoid ambient humidity absorption. For the same reason, before each test, all the specimens were further dried for 1.5 h at 80°C.
All the composite specimens were printed at the Mechanical Workshop Facility of the *Istituto Italiano di Tecnologia* (IIT). A Markforged® Mark Two (Markforged® Inc., Boston, USA) FFF desktop 3D-printer was used (**Fig. 4.27**).

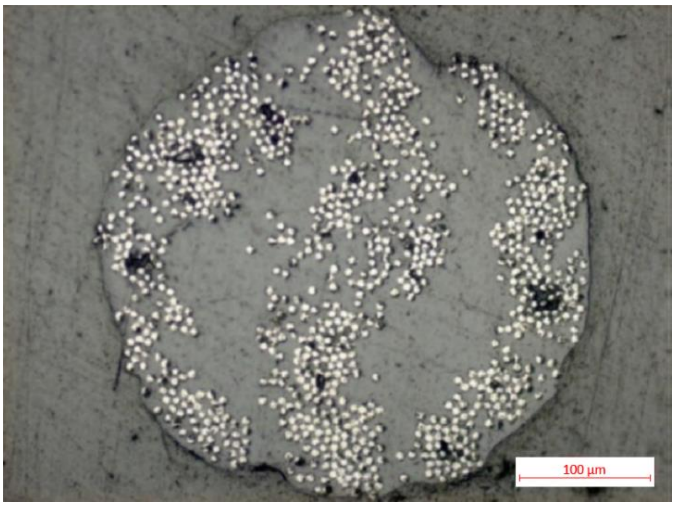

Fig. 4.26. Cross-section of the Nylon-6 filament reinforced with CCF.

The temperature of the printing heads for the Onyx and the continuous-fiber reinforced filament was set to 265°C and 270°C respectively, whereas the printing bed was non-heated. The accompanying slicing and pre-processing software, Eiger®, was used to set and adjust the most important printing parameters. Among these parameters, the fiber type, fill mode and fiber orientation, number of layers, number of Onyx rings to generate the outer shell can be cited. To make the results comparable between different builds, the thickness of each layer was set to 0.125 mm for both Onyx and CCF.
The specimen geometries were specifically created via computer aided design (CAD) software (SolidWorks 2016, Dassault Systems), exported as a stereolithography file (STL), and imported into Eiger®, through which the material-laydown path was defined.

As shown in the following, various test specimen geometries were considered to characterize both the tensile and flexural properties of the base material as well as the mechanical behavior of adhesive joints realized with a single-overlap configuration.

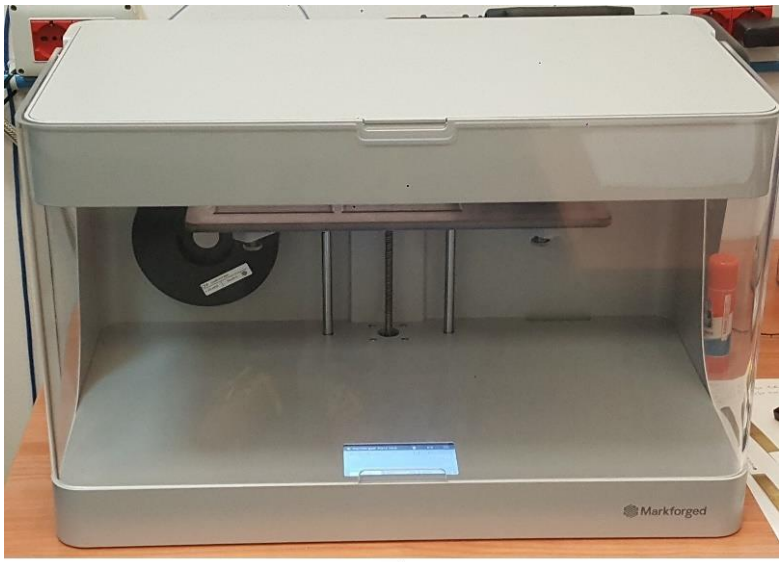

Fig. 4.27. The Markforged® Mark Two FDM desktop 3D-printer at the IIT laboratories.

As detailed in the scheme provided in **Fig. 4.28**, this device is equipped with two separate extrusion nozzles, one for Onyx and one for the CCF-reinforced wire.

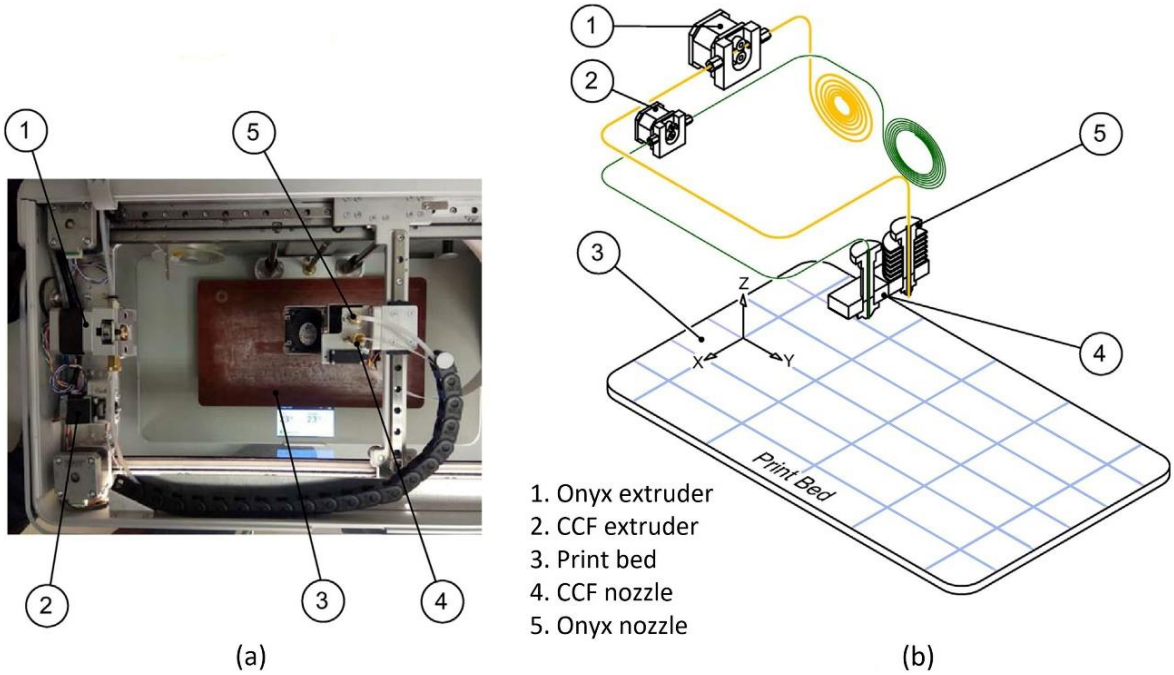

Fig. 4.28. Markforged® Mark Two FFF desktop 3D-printer. (a) General view and (b) scheme of the printing process.

4.2.2 Printing criteria

Each laminate was built on subsequent planes along the z-direction, each parallel to the printing bed ('flat' build mode, **Fig. 4.29**): the CCF layers were laid down horizontally and continuously, with a fill type defined as 'Isotropic'. It is worth noting that the term 'Isotropic' is a label given to the fiber pattern by Markforged®, and it does not define the mechanical properties of the final test specimen. In fact, an 'isotropic' fill type determines creation of a test specimen having a unidirectional laydown of the continuous fibers, thus resulting in anisotropic behavior of the specimen. Hence, the fiber was arranged, layer by layer, according to a 0°-orientation with respect to the longitudinal direction of the specimen.

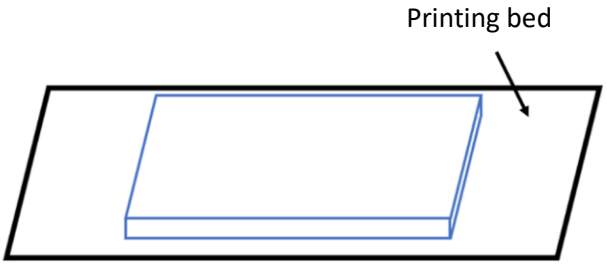

Fig. 4.29. 'Flat' printing mode: the part develops parallel to the printing bed.

It should be noted that Eiger® obliges the user to print every component by adding an outer protective shell made exclusively with the Onyx material (by means of layers arranged at angles +45° and -45° alternatively with respect to the axial direction), the extent of which is defined as a set-up parameter. In particular, each specimen was built with four Onyx layers on the bottom and four Onyx layers on the top. The floor layers avoided any fiber breakage while removing the specimen from the platform, whereas the roof layers were chosen for dimensional accuracy and symmetry.
Furthermore, each layer built was made as a combination of two infill arrangements of the material: the infill made of CCF laid following the aforesaid direction; and a concentric infill, consisting of two Onyx rings placed along the specimen perimeter (**Fig. 4.30**).

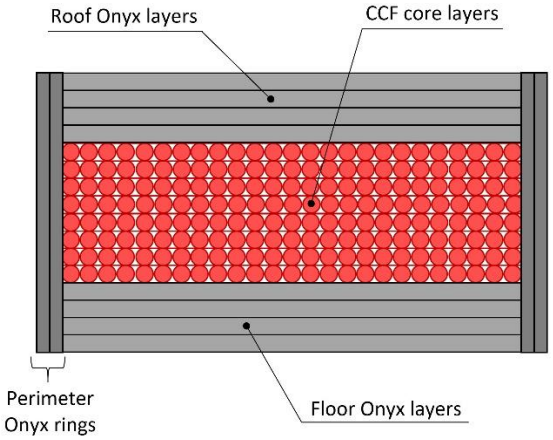

Fig. 4.30. Schematic representation of the 3D-printed composite cross-section.

4.2.3 Mechanical characterization of base material

4.2.3.1 Tensile specimens and testing procedure

Tensile testing was carried out on parallelepiped specimens of dimensions 157 mm × 16 mm × 3 mm (**Fig. 4.31**), in accordance with the indications provided by ASTM D3039 [75].

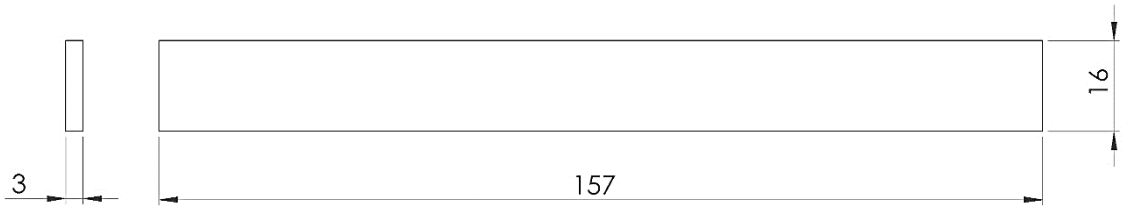

Fig. 4.31. Geometry of a tensile specimen according to ASTM D3039 (values in mm).

To obtain a proper CCF/Onyx ratio, the thickness was achieved by superimposing a total of 24 layers, each 0.125 mm thick, arranged as follows: 4 base layers of Onyx, 16 CCF layers having a 0°-orientation, and 4 top closing layers made of Onyx. These tensile specimens were then tested to failure at a crosshead displacement rate of 2 mm/min. Metallic shims of dimensions 25 mm × 50 mm were bonded at the grip areas to avoid any crushing or shifts of the sample during the tests (**Fig. 4.32**).
Having defined F as the force measured by the load cell and A as the sample cross sectional area, tensile stress was calculated as $\sigma = F/A$. The strain values, ε, were also calculated as the ratio between the displacement, ΔL, and the initial length, L_0, of the specimen.

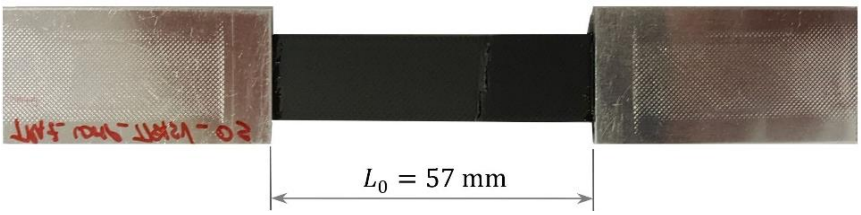

Fig. 4.32. Tensile specimen.

4.2.3.2 Flexural specimens and testing procedure

To determine the flexural properties of the material, specimens having dimensions 153.6 mm × 14 mm × 4 mm were built (**Fig. 4.33**), following the indications provided by ASTM D7264 [76]. In this case, the thickness was obtained as a superposition of 32 layers – again 0.125 mm in thickness each – comprising 4 base layers of Onyx, 24 layers made of CCF having a 0°-orientation, and 4 top layers of Onyx.

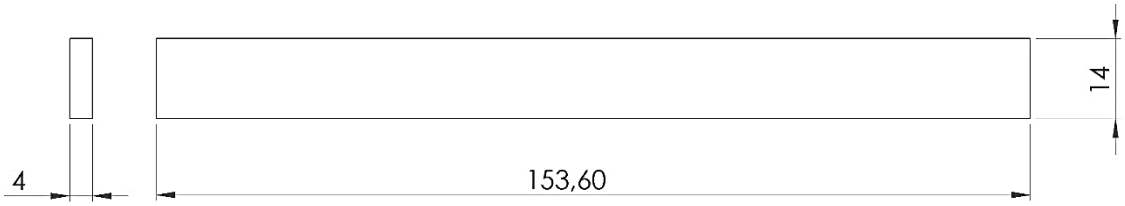

Fig. 4.33. Geometry of a flexural specimen according to ASTM D7264 (values in mm).

A three-point loading test method was carried out (**Fig. 4.34**).

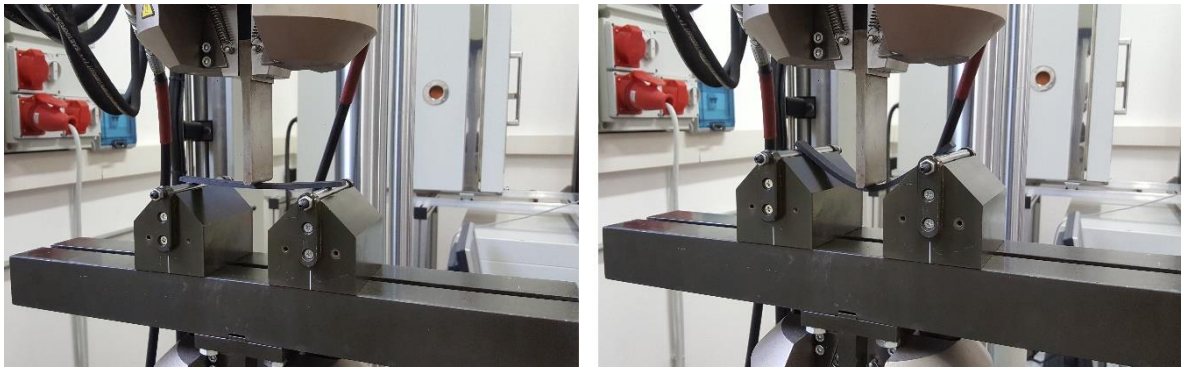

Fig. 4.34. Three-point flexural testing: starting position and advancement of the loading nose.

Thus, according to the aforesaid standard, the radius of both the loading nose and the two supports was 5.0 ± 1.0 mm, and the specimens were tested guaranteeing a span-to-thickness ratio (L/t) of 32:1 (i.e., a span between the supports equal to 128 mm). The crosshead (loading nose) movement speed was set to 1.0 mm/min.
During bending, the test specimen behaves as a beam simply supported at two points and loaded at the mid-span (**Fig. 4.35**), thus the bending moment increases from the support points to a maximum value at the mid-point: maximum stress occurs along a line at the center of the test specimen/beam, where the flexural stress, σ_f, is calculated with the following simplified equation:

$$\sigma_f = \frac{3PL}{2wt^2} \qquad (4.6)$$

where P is the load (N) corresponding to a deflection δ (mm), L is the length of the support span (mm), w and t are, respectively, width and thickness of the test specimen (mm), for a bending moment M equal to $PL/4$.
However, when L/t exceeds 16:1 (as in this investigation), **Eq. (4.6)** has to include additional terms in order to take into account the significant end forces developed and relatively large deflections at the support noses. It follows that σ_f has to be calculated using the following equation:

$$\sigma_f = \frac{3PL}{2wt^2}\left[1 + 6\left(\frac{\delta}{L}\right)^2 - 4\left(\frac{t}{L}\right)\left(\frac{\delta}{L}\right)\right] \quad (4.7)$$

where δ is the deflection of the centreline of the specimen at the mid-span (mm). The corresponding strain value at the outer surface is calculated as follows:

$$\varepsilon_f = \frac{6\delta t}{L^2} \quad (4.8)$$

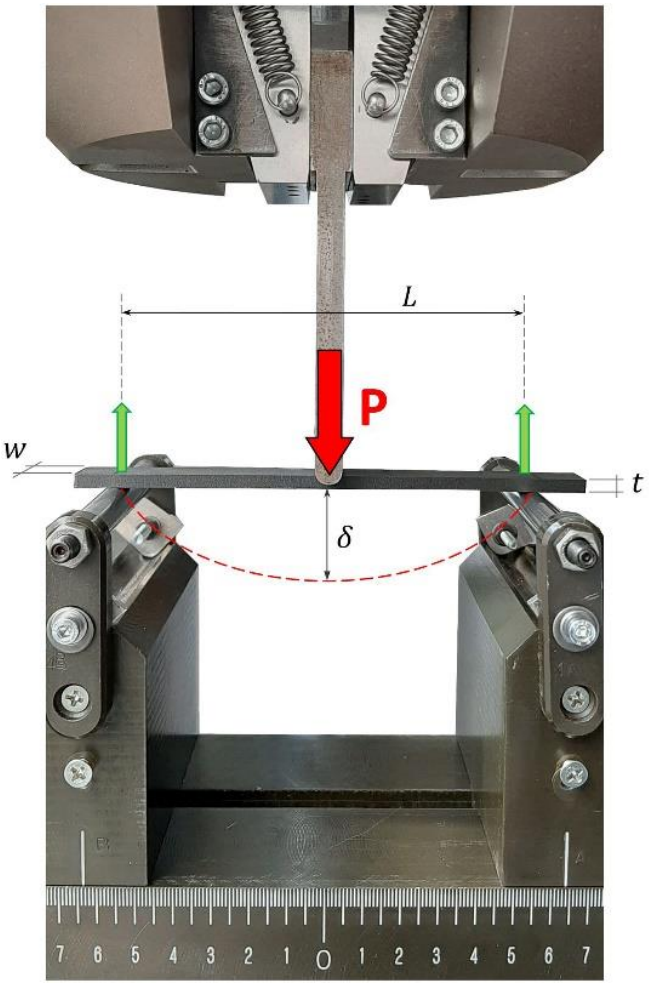

Fig. 4.35. Three-point flexural testing scheme.

4.2.4 Substrate fabrication

A single overlap configuration of the joints was adopted to assess the adhesion properties of the surfaces and evaluate the shear performance of such adhesive system. To do this, at first, laminates having the dimensions displayed in **Fig. 4.36** were fabricated by stacking subsequent layers having CCFs with unidirectional 0°-orientation with respect to the axial dimension of the specimens (i.e., along the direction of the load applied during mechanical

testing), to maximize the performance of the substrate and, hence, of the joint (**Fig. 4.37**). In particular, each substrate was made of 16 layers (to obtain an overall sample thickness of 2 mm), comprising four floor layers made of Onyx, eight core CCF layers, and four roof layers chosen for dimensional accuracy and symmetry. The final thickness of each layer was set to 0.125 mm for both Onyx and CCF. As in previous cases, Onyx was also laid along the specimen perimeter to generate, layer by layer, two concentric rings. It follows that each substrate consisted of a CCF infill enclosed within a protective shell of Onyx-only.

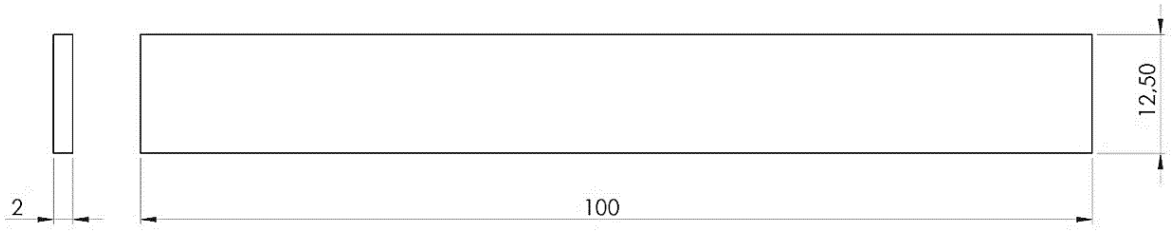

Fig. 4.36. Geometry of the substrate used to fabricate the adhesive joints (values in mm).

4.2.5 Surface pre-bonding preparations

To make any comparison possible, the surfaces of the 3D-printed composite substrates were prepared by using the same treatments as those of conventional CFRP joints. Thus, two sets of samples, i.e., solvent degreased and mechanically abraded respectively, were employed as references for the mechanical comparison with a number of joints the surface of which was plasma treated.

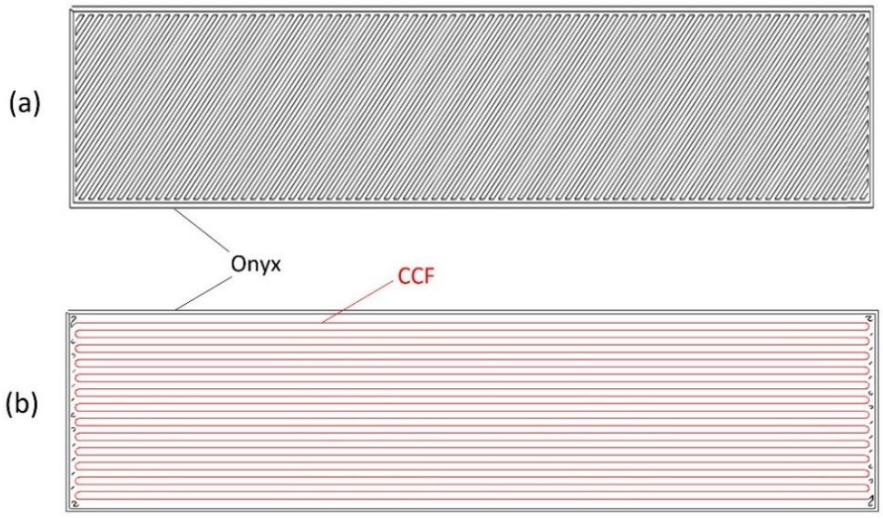

Fig. 4.37. (a) Laydown pattern of the outer Onyx-only layers and (b) unidirectional fiber pattern (0°) of a generic core-layer.

In **Table 4.7**, all the treatments performed on the 3D-printed composite substrates are listed. As observable, in this investigation, atmospheric air only was used as the process gas,

varying plasma power among the values listed in the aforesaid table; the exposure time was fixed at 180 s, since this had already been found to be effective in LPP treatments on polyamide materials [59].

Table 4.7
Summary of the surface treatments carried out on the AM CFRT substrates.

Part C		
Surface treatment	Description	
Degreasing	Acetone wiping	
Abrasion	Acetone wiping + 3M™ Scotch-Brite™ MX-SR + Acetone wiping	
LPP	Acetone wiping + Plasma treatment with the following set-up parameters:	
	Power (W)	50, 100, 150
	Exposure time (s)	180
	Gas	Air

4.2.6 Adhesive-joint manufacturing and mechanical testing

Shear testing was performed to assess the mechanical response of the adhesively-bonded CFRT-to-CFRT joints. The composite substrates were built additively, one by one, following the printing criteria described in Section 4.4.1, in accordance with the geometries suggested by ASTM D1002 for the manufacturing of SLJ (**Fig. 4.38**).

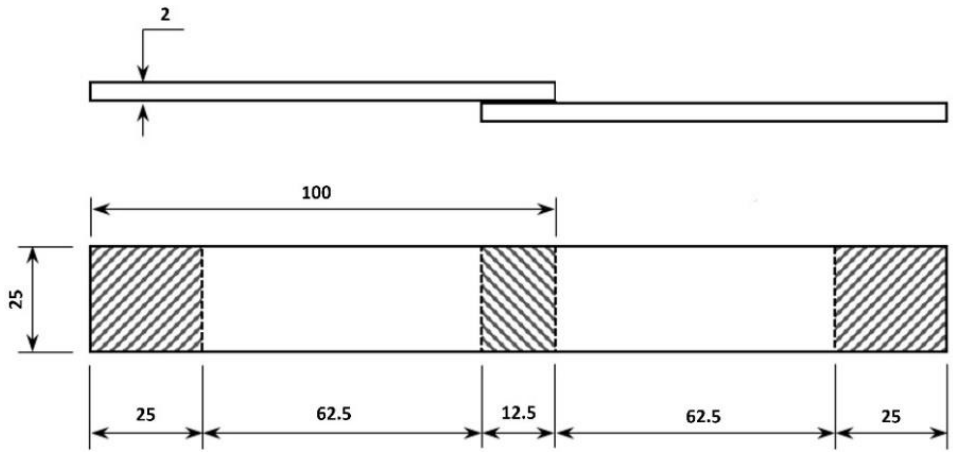

Fig. 4.38. SLJ geometry, according to ASTM D1002 (values in mm).

Five specimens per set of treatment conditions were made and then tested (N=5), allowing obtainment of the mean values to be provided in the Results chapter together with the related values of standard deviation.

The method used to apply the adhesive and fabricate the joints (illustrated in **Fig. 4.39**) as well as the mechanical testing conditions were perfectly the same as those described in the previous Section 4.1.4, to which to refer for more details.

(a)

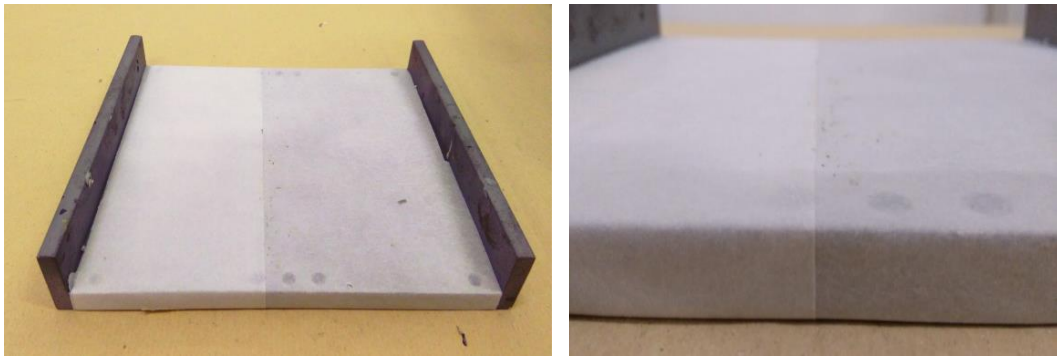

(b)

(c)

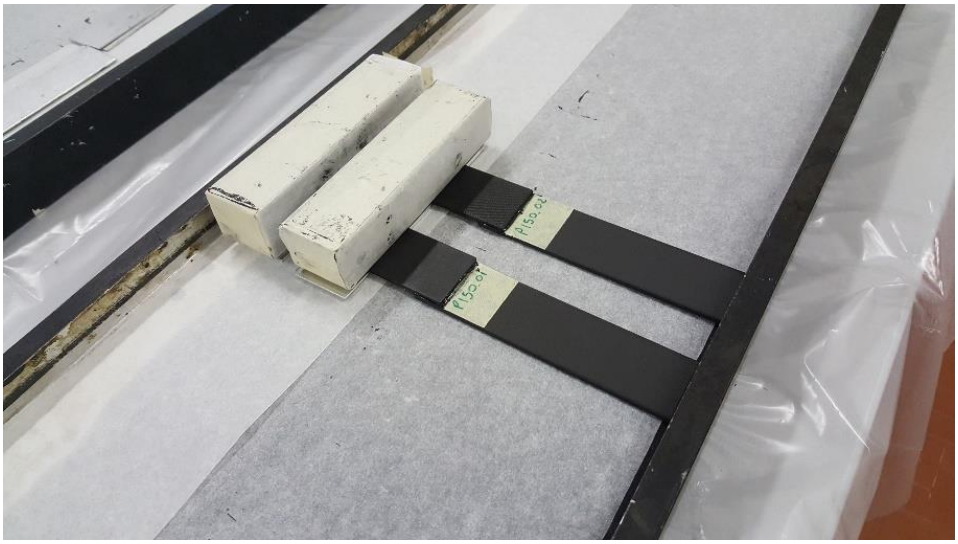

Fig. 4.39. (a) Support table and thickness control, (b) set up of the overlap area, and (c) joint fabrication.

4.2.7 Morphological and chemical assessments

Morphological analyses were carried out using a Talyscan 150 (Taylor Hobson, US) non-contact laser profilometer (**Fig. 4.40**). Surface portions were acquired, setting a scan speed of 4500 µm/s and steps spaced 5 µm apart. Data processing was carried out through the associated TalyMap 3D software, with which the roughness parameters were extracted. The same instrument and settings were also used to acquire the fracture profiles for the failure mechanism evaluation.
Regarding the chemical state evaluation, all the analyses were performed using the Kratos Axis Ultra^{DLD} spectrometer, at the same set-up conditions described in Section 4.1.7.

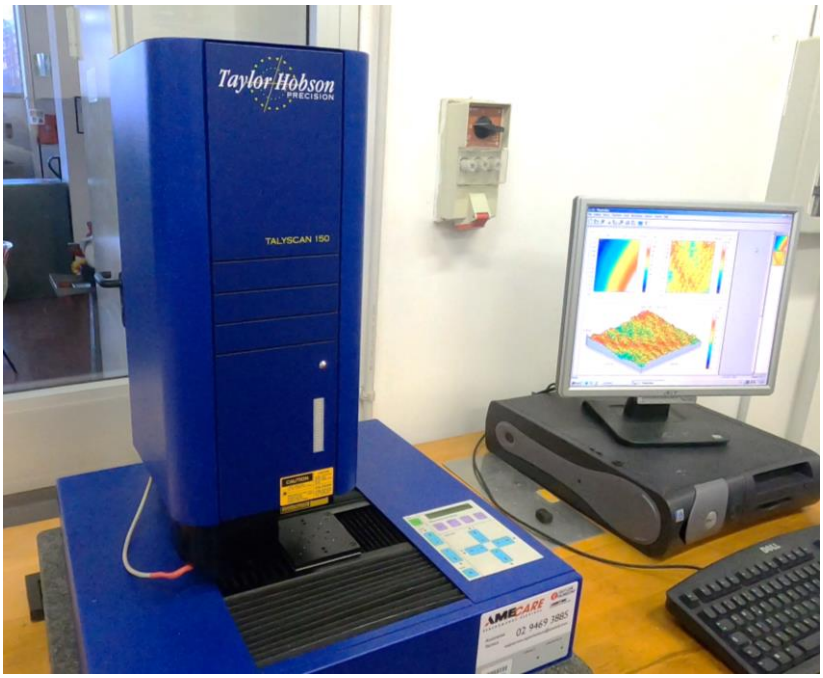

Fig. 4.40. Talyscan 150 laser profilometer.

5. Results and discussion

5.1 *Part A*: Effect of LPP treatment on CFRP

5.1.1 Mechanical performance of adhesive joints

As said previously, this stage of the work aimed at investigating the effects of cold-plasma treatment on 5-layer CFRP substrates by varying the most relevant parameters of the process. Mechanical tests highlighted an increase in shear strength of the adhesive bonded joints thanks to the use of plasma treatment if compared to traditional preparations, such as abrasion or peel-ply. However, the improvements in performance observed with the plasma-treated joints are closely related to the power-time-gas combinations adopted during the process. Hence, the need to investigate a large number of treatment conditions by combining parameters, since - for instance - an increase of the exposure time, and perhaps even adopting a high power, does not necessarily entail the possibility of obtaining the best result.
To determine a base reference for the comparison, the degreased-only SLJ were tested first, resulting in average TSS-value equal to 15.4 ± 0.3 MPa. The two traditional pre-bonding methods were then mechanically characterized, and TSS of the abraded joints stood at 18.8 ± 0.3 MPa, whereas for the peel-ply it was only 11.9 ± 0.5 MPa.
Hence, in **Table 5.1**, the results are reported of shear strength measurements for the different plasma treatment conditions, with the indication of the range of maximum relative differences of the means against the abrasion and peel-ply treatments, respectively.

Table 5.1
Significant results of shear strength measurements for the different plasma treatment conditions. The relative differences are those of the means against the abrasion and peel-ply controls.

Gas		P (W)	t (s)	TSS, τ (MPa)	$\tau_{max} - \tau_{min}$ (MPa)	Range of difference vs abrasion (%)	Range of difference vs peel-ply (%)
Air	τ_{max} @	150	60	27.3 ± 0.7	11.7	+ 44.7 ÷ – 17.6	+ 128.4 ÷ + 30.1
	τ_{min} @	50	180	15.5 ± 0.9			
Oxygen	τ_{max} @	150	300	26.7 ± 0.2	4.4	+ 41.7 ÷ + 18.6	+ 123.7 ÷ + 87.1
	τ_{min} @	100	300	22.3 ± 1.1			
Argon	τ_{max} @	50	180	26.0 ± 0.5	5.7	+ 38.1 ÷ + 7.69	+ 118.0 ÷ + 70.0
	τ_{min} @	50	300	20.3 ± 1.1			
Nitrogen	τ_{max} @	150	300	25.5 ± 0.5	5.7	+ 35.5 ÷ + 5.0	+ 113.8 ÷ + 65.7
	τ_{min} @	50	60	19.8 ± 1.6			

The errors associated with the means are the standard deviations of the measurements. The last three columns in **Table 5.1** highlight the spread of values in the measurements obtained. In particular, the two rightmost columns allow one to compare this spread with the abrasion and peel-ply controls, respectively, against which improvements are represented by '+' signs, while a '–' sign represents a decrease in performance. However, owing to low efficiency of the peel-ply preparation, from then on it was decided to compare all the results obtained with LPP treatments to the case of abrasion only. The improvement in joint performance is more evident in those cases where Air and O_2 (+44.7% and +41.7% respectively) are used as process gases, followed by Ar (+38.1%) and N_2 (+35.5%). This increase is referred to the most successful power-time combination found for each gas. In fact, thanks to an overview of all the treatment combinations performed, it is clear that the mechanical behavior of adhesively bonded joints is mostly influenced by the process gas used, which is the information stressed in **Fig. 5.1**.

The bar charts presented in **Fig. 5.1** show the same mean and error data as in **Table 5.1**, grouped in such a way as to stress the trends emerging for the different gases used. Generally speaking, it appears that at low power (50W) Oxygen always results best or second best, while the second best fluctuates between Argon and Nitrogen among the different combinations of power and time, with Air always resulting the worst. Conversely, at intermediate (100W) and high power (150W), Air seems to be the most effective gas at all times, with Oxygen usually resulting second. In particular, at the highest power (150W), Nitrogen performs better than Argon, unlike the intermediate power case (100W).

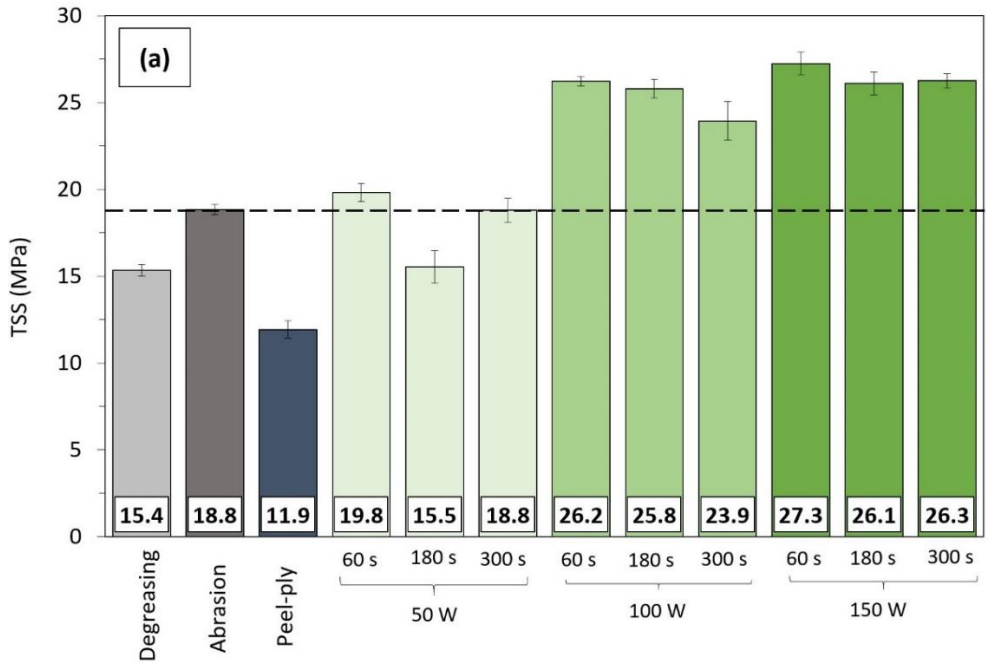

Fig. 5.1. Bar-chart plot reporting the TSS-test results obtained with different plasma treatment conditions of power and exposure time, grouped according to the plasma process-gas: (a) Air, (b) Oxygen, (c) Argon, and (d) Nitrogen. Black dotted line represents the reference mean value of shear strength of the abraded control joints. (Continues)

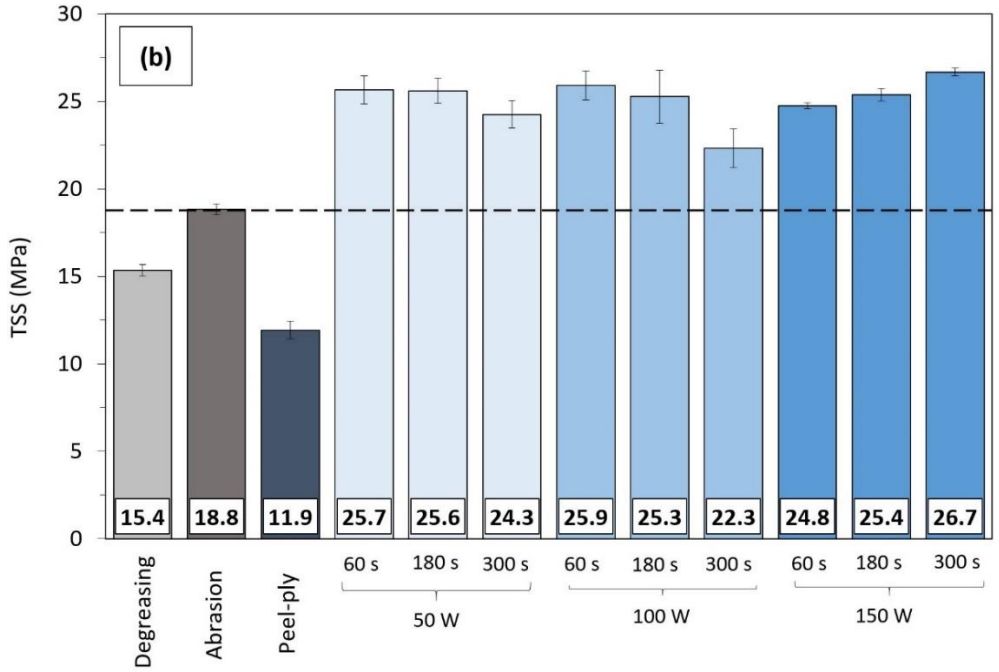

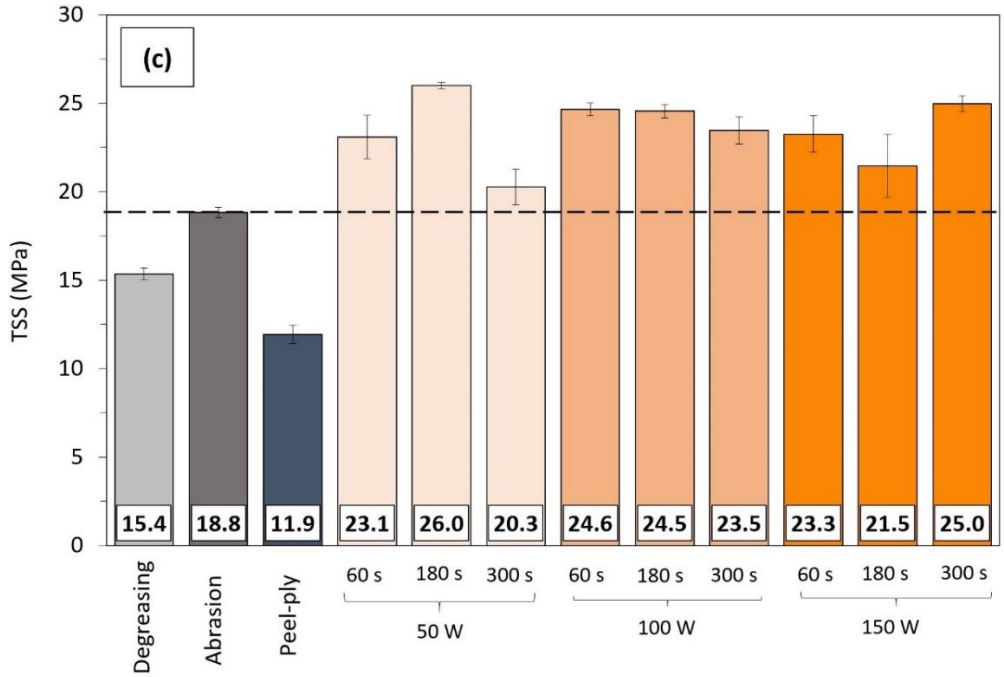

Fig. 5.1. (Continues)

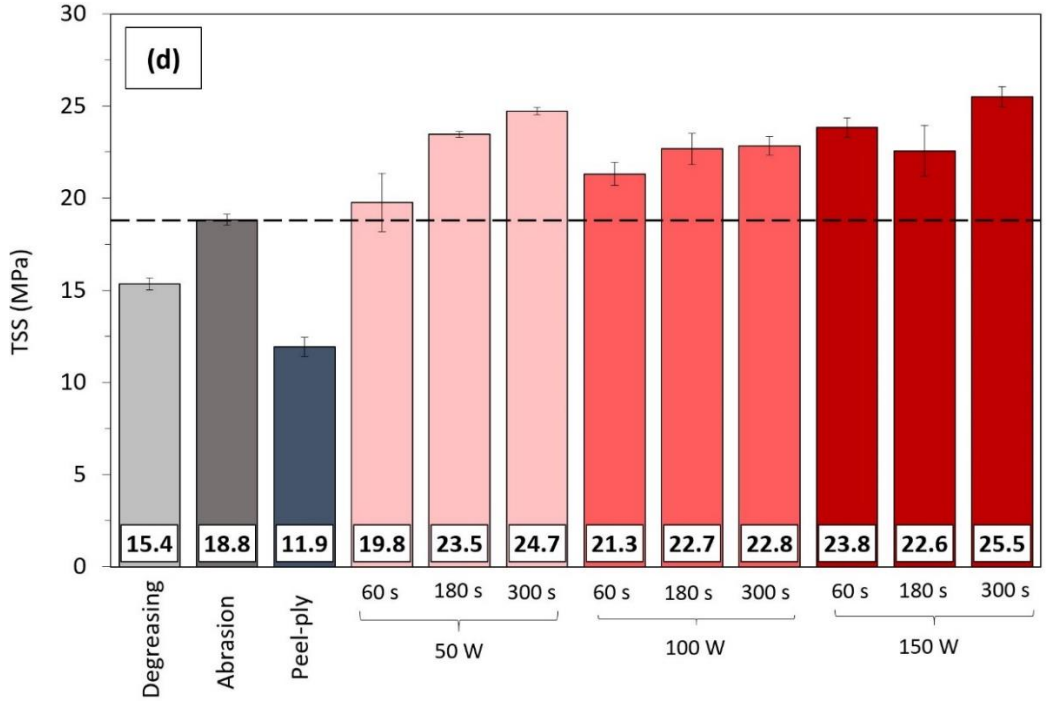

Statistical analysis via Pearson's correlation factors (f_P) was then carried out, in order to evaluate, for each gas, whether and how much the variations of power-input and process-duration affect shear strength. The results obtained are reported in **Table 5.2**: the linearity relationship is to be intended as 'weak' for $f_P < 0.3$, 'moderate' if between 0.3 and 0.7, 'strong' for f_P ranging from 0.7 to 1.

Table 5.2
Influence of the process-parameters on the tensile shear strength, statistically evaluated with Pearson's correlation factor analysis.

Gas	Plasma-parameter influence on TSS (Pearson's correlation factor, f_P)	
	Power	Time
Air	Strong (0.88)	Weak (-0.15)
Oxygen	Weak (0.15)	Moderate (-0.36)
Argon	Weak (0.03)	Weak (-0.18)
Nitrogen	Moderate (0.33)	Moderate (0.68)

Hence, with an air-plasma treatment (**Fig. 5.1a**), CFRP joints present high strength when the process involves high power (≥ 100 W), even if the exposure time is limited (60 s). By contrast, the use of a lower powered air-plasma is not sufficient to determine an increase in mechanical performance: almost no relevant variations in the joint strength were obtained at all compared to the reference (abraded), even when prolonged treatment times are used. Thus, it follows that, for an air-plasma treatment, the power value chosen for the process seems to play a more meaningful role (power input and strength statistically resulted in a

strong linear relationship, with $f_P = 0.88$), while the duration of exposure, however, can be limited to obtain excellent results.

When Argon was used as process gas (**Fig. 5.1c**), the best mechanical response was obtained from joints treated using a combination of low power (50W) and mid-high time (180 s). However, it was sufficient simply to increase treatment time to 300 s to determine a considerable loss of mechanical resistance. Despite this, adopting a power input of 100 W, the shear strength of the joints presented a trend that was almost constant through time, with low values of standard deviation especially when time did not exceed 180 s. However, even adopting Pearson's statistical analysis, to uniquely identify an overall trend of the mechanical response with process parameter is not easy, since the correlation between shear strength and the two process parameters investigated resulted very weak in both cases.

Then, with a Nitrogen-plasma treatment, mechanical strength increased with the rise of both power and exposure time values (**Fig. 5.1d**). In particular, a minimum shear strength corresponded to the softer treatment condition (50W/60s), while the maximum was obtained with the most invasive combination (150W/300s). Both power and time parameters statistically result in a direct relationship with shear strength, although time input seems to have stronger influence on performance variations. It should also be noted that an increase of the treatment duration generally entailed a relevant reduction in result dispersion, which became small in all the cases in which an exposure of 300 s was set.

Finally, TSS tests of Oxygen-plasma treated samples witnessed a minor variation of mechanical performance when varying both power and time inputs (**Fig. 5.1b**). In particular, these results highlighted a limited difference between the best and the worst value of shear strength (only 4.4 MPa ca.) obtained with this gas. This reflects the fact that, in general, use of Oxygen may entail a more manageable and less fallacious process, since effectiveness of the treatment might not be affected by any setting error of the operator. However, always referring to **Fig. 5.1**, it is evident that – even if the most effective treatment corresponded to the highest values of both parameters – excellent results can also be reached adopting a brief low-powered process. And this is especially advantageous when high productivity is required.

In view of the above results, it can be concluded that the shear strength of the joints confirms the importance of the vacuum plasma as a pre-bonding treatment for CFRP substrates. The effectiveness of plasma treatment is highlighted also observing the overlap fracture surfaces of the joints, as shown in **Fig. 5.2**, which is illustrative of the failure mode obtained after the two aforesaid traditional treatments and the best plasma ones. In **Fig. 5.2** one can see a clear evolution from states of complete de-adhesion for the surfaces where the peel ply has been removed to an almost completely de-cohesive mode for plasma treated substrates. In this regard, as discussed in the following sections, the reason for this behavior is to be sought both in a morphological modification and in the surface activation state brought about by plasma. This activation involves both an increase of the wettability properties of substrate and a change of the surface chemical state with generation of polar groups at interphase that let adherend create stable bonds with the adhesive. Thus, because from mechanical data it was not possible to draw a clear conclusion, more experiments were carried out, which are

described and discussed in the following.

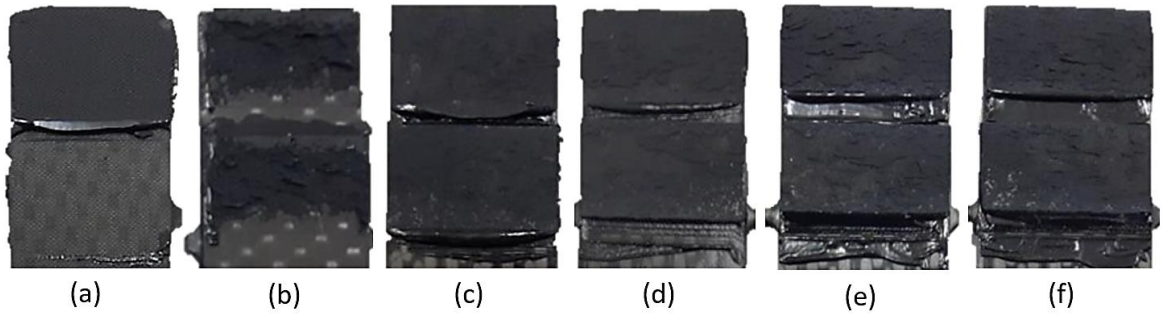

Fig. 5.2. Fracture areas of joints adhesively bonded after the following treatments: (a) peel-ply removal, (b) abrasion, (c) Air-plasma, (d) Oxygen-plasma, (e) Argon-plasma, (f) Nitrogen-plasma. The cases of plasma treatments shown are for the most performing power-time settings.

5.1.2 Morphological analysis

Starting from the experimental findings of the mechanical characterization, surface morphological analyses were performed on the degreased-only (representing the as-received surface, only wiped with acetone and not further treated), abraded and peel-ply substrates as well as on those plasma-treated samples among those reported in **Table 5.1** for which only the best and worst plasma conditions were selected. In this way, it was also possible to correlate the choice of plasma power and time to creation of different topological structures on the CFRP surfaces differently treated. In this regard, **Fig. 5.3** reports 2D top-view optical images acquired simultaneously, for a given gas, on the CFRP surfaces plasma-treated according to the worst (left) and the best (right) power-time settings; below each image, the corresponding treatment conditions and the related S_q-values measured are reported.

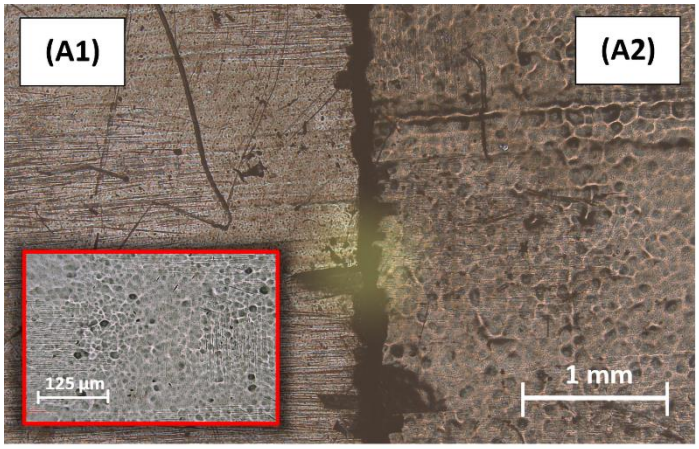

	P (W)	t (s)	S_q (µm)
(A1)	50	180	0.52 ± 0.48
(A2)	150	60	0.90 ± 0.06

Fig. 5.3. Top-view 2D optical images of the CFRP substrates acquired with a 2.5X magnification lens. The substrates were treated with: (A1, A2) Air-plasma, (B1, B2) Oxygen-plasma, (C1, C2) Argon-plasma, and (D1, D2) Nitrogen-plasma. The half images on the left and on the right show the surface of the worst (e.g. A1) and the best (e.g. A2) plasma treatment conditions, respectively. In the tables on the bottom of the images, the respective S_q roughness parameter values are also reported. (Continues)

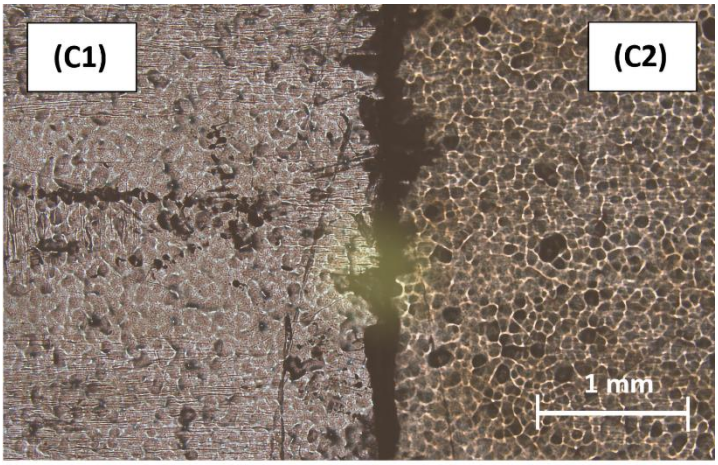

	P (W)	t (s)	S_q (µm)
(C1)	50	300	0.66 ± 0.06
(C2)	50	180	0.77 ± 0.04

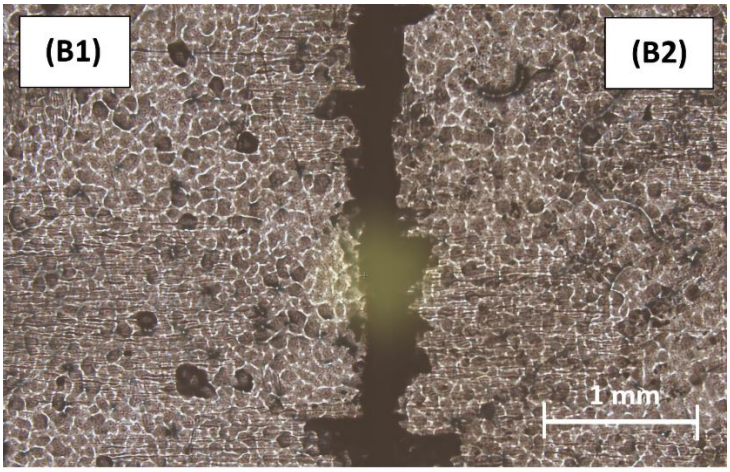

	P (W)	t (s)	S_q (µm)
(B1)	100	300	0.75 ± 0.05
(B2)	150	300	0.87 ± 0.14

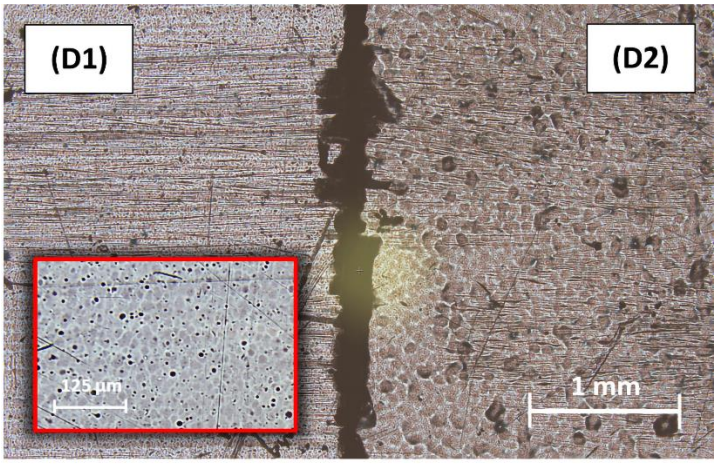

	P (W)	t (s)	S_q (µm)
(D1)	50	60	0.44 ± 0.04
(D2)	150	300	0.65 ± 0.35

It is clear that the extent of surface modification is strictly related to the power-time combination used, and this behavior confirms the previous considerations about the different significance of power and time combinations on the different processing gas.
In general, regardless of the gas used, the best plasma-treated CFRP presented a surface conformation which was rich in crater-shaped valleys. To understand this type of surface modification, it should be considered that the plasma consists of electrons, ions, photons and molecules having high kinetic energy, which is furtherly enhanced in the vacuum ambient of the processing chamber [77]. These high energy particles actually bombard the surface of the substrate, thus leaving the sign of their impact on it, which is the base of the plasma-etching phenomenon observed by Tang et al. also on activated carbon fibers [18].
It should be noted that the highest power (150 W) works best on increasing the S_q roughness of the substrate when air, oxygen and nitrogen are used to generate the plasma atmosphere. In particular, an exposure of only 60 s to a 150-W air-plasma was enough to reach an average S_q of 0.90 μm, which is close to that found on the abraded surface (0.92 ± 0.10 μm). Instead, although using air for a longer time, low plasma power did not allow us to obtain a significant modification of the surface: for the treatment with air at 50W-180s combination, S_q was only 0.52 μm - i.e., less than that measured on the sample before treatment (0.76 μm). However, also in this case tiny craters were created due to the etching effect, as visible in the inset to **Fig. 5.3a** on the left (A1) surface, acquired with a 10X magnification. A similar behavior was also observed on nitrogen-plasma treated surfaces (see inset to **Fig. 5.3d**, left half i.e. D1), where both the most powerful treatment and the least invasive one originated surfaces having roughness values which were smaller (0.65 and 0.44 μm respectively) than that obtained on the only-degreased surface.
As regards the results obtained using the other process gases, oxygen plasma as well as argon plasma generated morphologically similar surfaces both on the most and least-performing substrates. In particular, surfaces treated with O_2-plasma presented an average S_q-value of 0.87 μm at maximum power and time, and 0.75 μm reducing power to 100 W. In contrast, morphological modification of Ar-plasma treated substrates is observable only adopting a low-powered plasma (50 W); it was also interesting to note that maximum roughness (0.77 μm) is not much higher than that before treatment and – as well as mechanical strength – it was obtained with an intermediate treatment duration of 180 s, whereas the minimum one (0.65 μm) was obtained increasing the exposure time to 300 s.
In view of these results, one can conclude that surface modification due to plasma plays a prominent role in the mechanical interlocking between adhesive and CFRP substrate, thanks to both an increase - in many cases - of the surface roughness and above all to a modification of the texture of the surface. This is clear when comparing the degreased-only control surface (**Fig. 5.4a**) to the plasma-treated surfaces.
Even when the term of comparison is the worst plasma-treated surface - such as in cases A1 or D1 - where on the larger scale (2.5X magnification) the same horizontal lines due to the original fabrication process of the piece appear, still on the microscale (10X magnification) the plasma-treated surface shows tiny craters, whereas the control only goes on showing the same horizontal lines. These horizontal lines are related to the impression of vacuum bag

during the CFRP manufacturing.

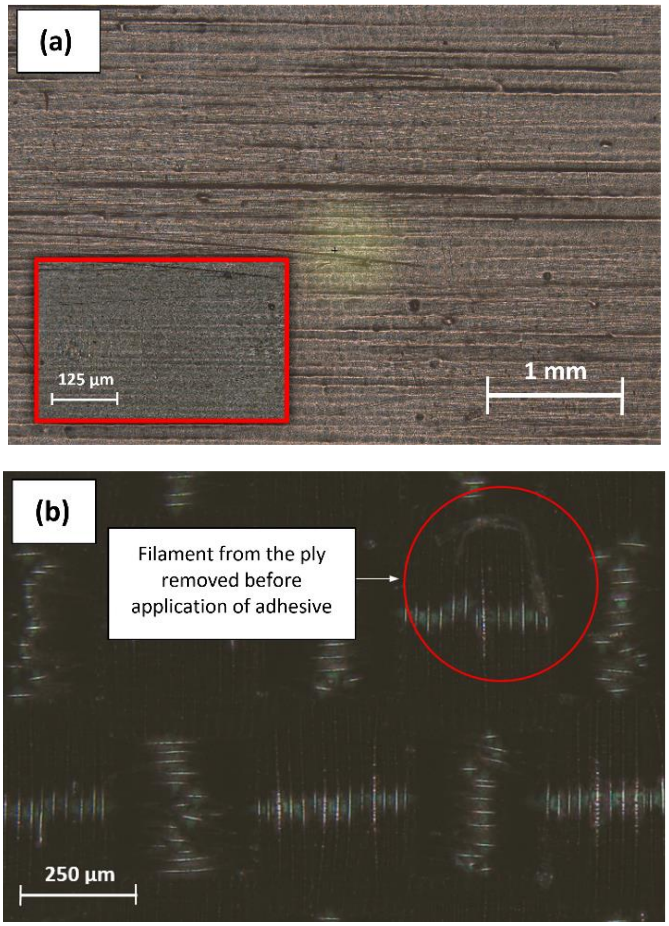

Fig. 5.4. (a) Degreased-only control surface and (b) detail of the surface effect of the peel-ply removal from the CFRP substrate: topography is repetitive and shows a great increase in roughness, but traces of contaminant are easily detectable and lead to a reduction of the adhesive capability of the substrate.

Roughness results are in accordance with trend of the shear strength. However, this analysis also proved that improvement in mechanical performance of the joints is a consequence of concurrent causes and effects, such as surface activation and thus chemical interaction between adhesive and substrate, and absence of contamination on the surface to be adhesively bonded. Indeed, such a consideration, together with the morphological assessments carried out, allowed us to find a possible explanation for the mechanical behavior presented by the joints bonded after peel-ply removal. In this regard, **Fig. 5.4b** shows an image of such a surface immediately after having removed the fabric ply, i.e. in that condition before the adhesive is applied. Traces of polyester filaments are clearly visible since they presumably remained trapped in the epoxy matrix during consolidation of the composite. Obviously, these filaments of releasing material are detrimental to adhesion and may undermine the effect of mechanical interlocking (in this case, S_q value was 11.05 ± 1.91 µm), as indeed highlighted during mechanical tests.

5.1.3 Evaluation of surface chemistry through XPS

XPS analyses of CFRP were carried out before and after plasma treatment in order to investigate what chemical modifications occur on surfaces and how these contribute to the observed wettability properties. Wide scan acquisitions allowed us to identify the chemical composition of the CFRP substrates investigated, within a 10-nm depth, comparing the degreased-only control surface and the plasma treated samples whose surfaces were modified using the best parameters' settings found, for each gas, during the mechanical characterization. As shown in **Fig. 5.5** and also reported in **Table 5.3**, independently of the process gas used, plasma treatment determines an increase in oxygen content together with a decrease of the C 1s peak, i.e. an oxidative effect that is reflected in an increase of the oxygen/carbon ratio (with +242.9% using oxygen, +207.1% with air, and +178.8% and +100% with nitrogen and argon respectively), compared to the untreated CFRP surface.

Table 5.3
Atomic percentages of oxygen and carbon, and related O/C ratio, obtained through XPS analysis in (a) survey mode and area percentage of each chemical species quantified from deconvolution of (b) C 1s and (c) O 1s peaks.

Surface treatment	Atomic percentage (%)			Area percentage (%)						
	O 1s (a)	C 1s (a)	O/C ratio	C-C C-H (b)	C-N (b)	C-O (b)	O-C-O C=O (b)	O-C=O (b)	C-OH C-O-C (c)	O-C=O (c)
Degreasing LPP	12.1	87.9	14	70.6	14.5	9.9	2.6	2.4	52.3	47.7
Air	30.1	69.9	43	50.3	16.9	21.3	6.1	5.0	70.4	29.7
Oxygen	32.4	67.7	48	43.4	19.4	24.5	8.4	4.4	67.3	32.7
Argon	21.6	78.4	28	57.6	14.1	16.1	5.8	6.5	61.1	38.9
Nitrogen	28.0	72.0	39	47.8	19.2	21.1	7.0	5.1	69.6	30.4

Thus, starting from this low-resolution analysis, two specific energy regions were selected, providing a targeted survey aimed at photographing the specific effect of treatment in terms of oxidation and activation of the CFRP substrates. These regions are located around C 1s (280 ÷ 294 eV) and O 1s (528 ÷ 540 eV) peaks. The shape of both the carbon and the oxygen peaks varied appreciably from one substrate to another, depending, for each gas, on the surface modification involved by using the specific optimized set of parameters.
Deconvolution of C 1s peak made it possible to identify a number of carbon components (**Fig. 5.6a**) related to: a single bond between carbon and carbon or carbon and hydrogen (C-C, C-H) positioned at 284.8 eV, carbon singly bound to nitrogen (C-N) at 285.9 eV and with oxygen (C-O) at 286.6 eV. Furthermore, a peak corresponding to carbon forming two single bonds or one double bond with oxygen (O-C-O, C=O) was recognized at 287.8 eV, while the carboxyl group (O-C=O) was found at 289.5 eV [78,79]. Thus, as shown by deconvolving C 1s, before vacuum plasma treatment C-C/C-H bonds are predominant,

whereas treated substrates present a simultaneous decrease of concentration of these species and rise of peaks corresponding to bonds between carbon and oxygen.

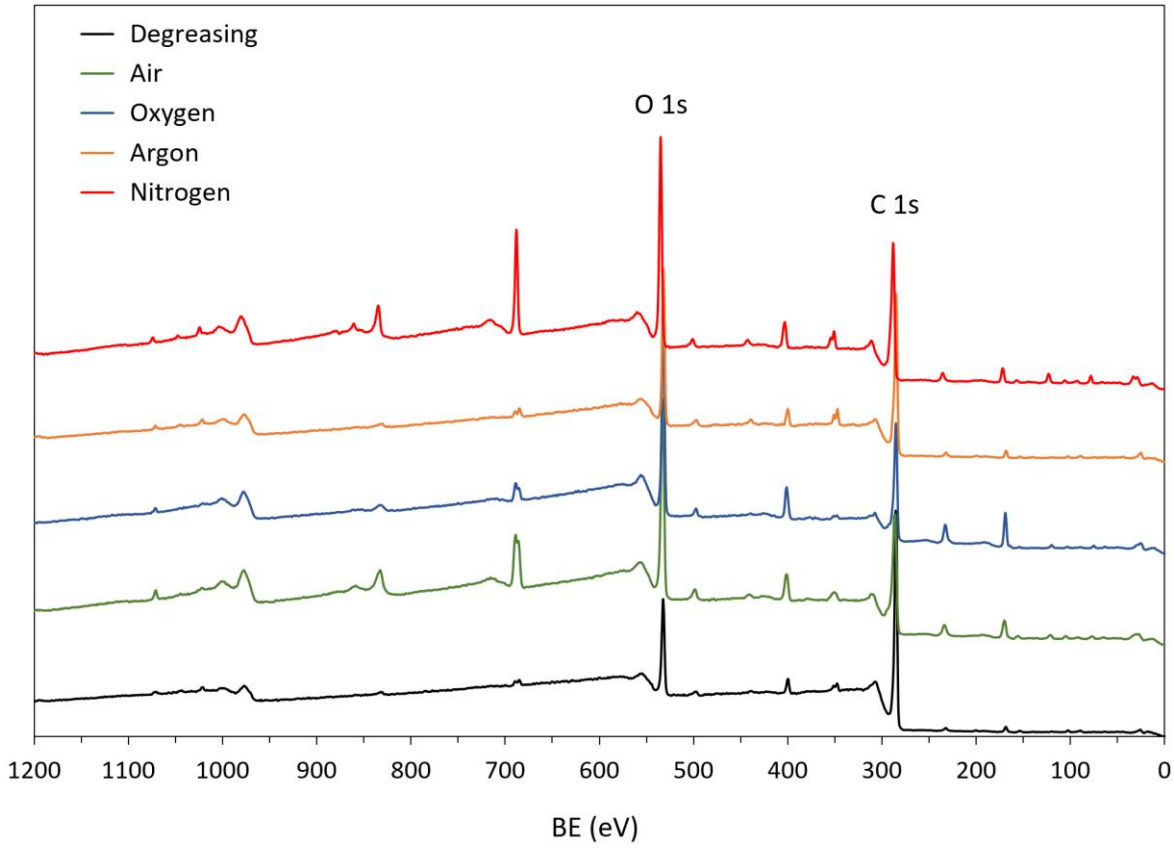

Fig. 5.5. Wide-scan XPS spectra acquired before ('Degreasing') and after LPP treatments. Each plasma-treated CFRP spectrum is referred to the power-exposure time combination which gave, with the specific process gas, the best mechanical result (see **Table 5.1**).

This suggests that – regardless of the type of process gas used – plasma treatment changes the surface chemical state of the CFRP substrates, forming new functional groups as a result of the break of the original single bonds C-C or C-H. Indeed, comparing pre- and post-treatment conditions, the decreasing trend of these bonds is believed to be the direct effect of increasing of the various oxidative reactions that occurred during plasma treatment, which involve generation of single or double bonds between oxygen and carbon atoms. Obviously, this behavior is emphasized when optimized O_2-plasma treatment was performed, which represents the clearest case in which a substantial reduction of C-C/C-H bonds (-43.4% compared to the reference) is followed by an equally clear increase of oxidized species. Indeed, free radicals can be created on the surfaces treated, which can then couple with active species from the plasma environment; these reactions are believed to be essential for the changes in the surface functionalities [18,80].

A high-resolution survey on O 1s spectrum and subsequent deconvolution of this peak also highlighted the presence of two different chemical species (**Fig. 5.6b**), which can be

considered as confirmation of the high activation and oxidation of the CFRP plasma-treated substrate: a first one, at about 531.8 eV, interpreted as oxygen making two single bonds with carbon (C-O-C) or carbon forming one single bond with a hydroxyl (-OH); and a second one (at 532.8 eV) corresponding to an O-C=O group. Always referring to **Table 5.3**, it should be noted that the latter seems to decrease after all plasma treatments, whereas the percentage of the former increases. However, the reason for this behavior is believed to be related to the fact that the number of C-OH bonds rises more steeply than the O-C=O ones, rather than to an effective decrease of this second species. Thus, similarly to that found analyzing C 1s,

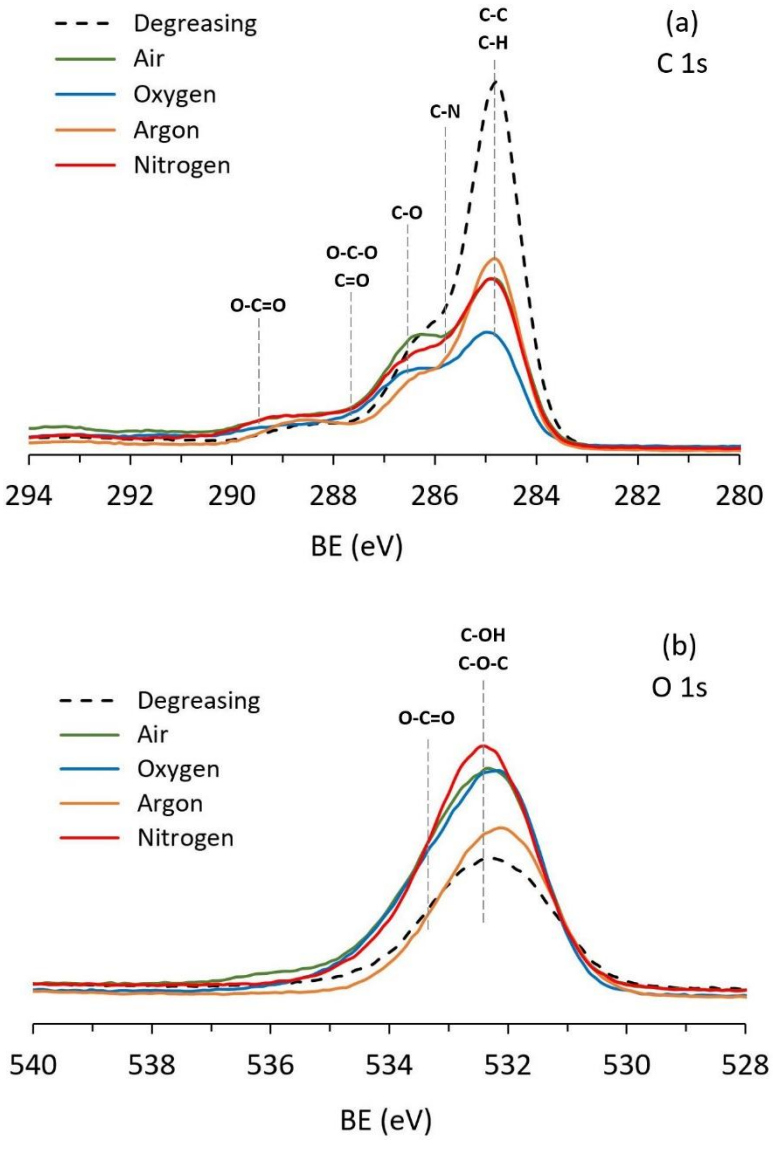

Fig. 5.6. Comparison of the high-resolution XPS spectra acquired before and after LPP treatment of the CFRP substrates: (a) C 1s and (b) O 1s peaks, shown as superposition of the pre- and post-treatment curves. Each plasma-treated CFRP spectrum is referred to the power-exposure time combination which gave, with the specific process gas, the best mechanical result (see **Table 5.1**).

such newly formed functional groups, as well as the introduction of additional groups, ensure an enhancement of the surface polarity and, consequently, could develop its hydrophilic behavior, as discussed in the following section. These increased polar groups supplied more reactive sites for interfacial bonding between the epoxy matrix of CFRP laminate and epoxy adhesive and thus could lead to an improvement of performance of the so-treated, adhesively-bonded joint.

5.1.4 Wettability and surface energy measurements

The results of measurements of CA with the two different probe liquids selected, H_2O and CH_2I_2, are presented in **Table 5.4**, where the average value of θ and related standard deviation are reported.

Based on the previous characterization, the number of plasma environments to be tested was reduced, selecting only those power conditions which allowed the adhesively bonded joints to reach the highest mechanical strength. Thus, wetting analyses were performed only on substrates treated at plasma powers of 50 W and 150 W, neglecting the case at intermediate power of 100 W. The exposure-time parameter was maintained variable between 60, 180 and 300 seconds. Indeed, experimental results indicated that increasing plasma treatment time is not always helpful in enhancing the wetting properties of epoxy-based composite. As comparators, abrasion and peel-ply techniques were adopted to define a reference value for both CAs and surface energy; moreover, measurements were also performed on degreased-only substrates, representing the zero-condition common to all the plasma-treated surfaces.

As shown in **Table 5.4**, all plasma treatments generally involved a reduction of CAs compared to the three references, already after the first minute of treatment, independently of both process gas and power; this reduction was more evident with deionized water droplets rather than to CH_2I_2 ones. This behavior could be related to the oxidizing effect of the plasma itself, which introduces or stimulates – as previously shown – the increase of polar species on the CFRP surface, developing its hydrophilicity. Indeed, as known, plasma treatment leads to an increase in surface energy of the solid treated. In this regard, the bar chart in **Fig. 5.7** reports surface energy results obtained by implementing the CAs measured to Wu's energy model, defining the related polar and dispersive fractions of this quantity for each set. Considering the case where air was used as process gas, contact angle trend followed exactly the aforesaid considerations, progressively declining with the rise of both the time spent by the substrate under plasma exposition and the power set for treatment. However, it was interesting to note that maximum mechanical strength did not correspond to maximum wettability of substrate. The experimental tests highlighted this aspect also when oxygen or argon were used; in the former case, θ values of both liquids decreased with time adopting a 50-W power, but tended to progressively rise again at 150 W.

It should be remembered that the highest value of mechanical shear strength was obtained with the parameter setting of 150W/300s, which corresponded even to the highest water-θ value reached with O_2-plasma treatment. Similarly, in the latter case (argon), maximum mechanical performance was obtained for the lower θ values at 50W, which were not the

absolute smallest ones however.

Table 5.4
Results of the contact angle analysis performed on CFRP using deionized water and diiodomethane. The values related to the best plasma settings are marked in bold.

Surface treatment				θ_{H_2O} (deg)	$\theta_{CH_2I_2}$ (deg)
Degreasing				82.5 ± 0.6	46.1 ± 0.4
Abrasion				79.2 ± 0.9	26.7 ± 1.5
Peel-ply				50.1 ± 0.8	25.1 ± 0.6
LPP	Gas	P (W)	t (s)		
	Air	50	60	39.0 ± 3.4	45.0 ± 1.4
			180	32.5 ± 0.5	41.7 ± 0.3
			300	29.1 ± 0.6	29.9 ± 0.8
		150	60	**29.1 ± 0.1**	**30.0 ± 0.2**
			180	28.6 ± 1.0	30.7 ± 1.2
			300	25.6 ± 0.3	31.3 ± 0.6
	Oxygen	50	60	33.9 ± 0.7	43.0 ± 0.7
			180	29.9 ± 0.5	42.0 ± 0.8
			300	27.2 ± 0.5	29.4 ± 0.6
		150	60	29.1 ± 0.1	28.3 ± 0.5
			180	32.2 ± 0.1	27.9 ± 0.1
			300	**34.8 ± 0.1**	**29.7 ± 2.1**
	Argon	50	60	51.0 ± 3.6	38.3 ± 0.5
			180	**28.8 ± 1.4**	**37.7 ± 0.3**
			300	31.7 ± 0.4	33.9 ± 0.1
		150	60	28.4 ± 0.3	38.0 ± 1.3
			180	22.4 ± 0.5	33.7 ± 3.2
			300	22.4 ± 0.8	26.2 ± 1.3
	Nitrogen	50	60	39.6 ± 1.2	45.3 ± 0.3
			180	36.8 ± 0.4	50.8 ± 1.4
			300	29.8 ± 0.1	33.8 ± 0.2
		150	60	29.2 ± 0.6	40.8 ± 1.0
			180	27.4 ± 0.2	32.6 ± 0.4
			300	**25.7 ± 1.1**	**21.7 ± 1.2**

Thus, by observing the experimental findings, a strict correspondence between shear strength and minimum-θ /maximum-γ_S was highlighted only on nitrogen plasma-treated samples. Such a behavior is however not unexpected and it is to be intended as confirmation of the idea that surface wettability is a necessary, but not sufficient condition for bonding, to which it is thus not possible to uniquely relate the success of an adhesively bonded joint [81,82].
Making comparisons among the results obtained, of course, is not easy; indeed, the study is focused on both the same type of treatment (plasma) with several experimental parameters and different treatments with different kinds of surface modifications: chemical and

morphological for plasma, but mostly morphological using peel-ply and abrasion. To understand and control adhesive phenomena, however, a holistic approach is needed.
As shown in Section 5.1.2, progressive enhancement of surface roughness and creation of a proper morphology lead to an improvement in mechanical performance of the adhesive joints, since an increase of the roughness ratio generally means enlargement of the actual contact area and, thus, of the effective interface between adhesive and substrate. But, as experimentally observed in this work and also pointed out by many authors [63,83], to have strong adhesion, the adhesive must wet the surface and have rheological properties sufficient to penetrate within the surface irregularities. Consequently, topological evaluation cannot ignore considerations about wettability of the surface, since the non-wetting may prevent adhesive bonds from forming at all. In this regard, the wetting analysis results highlighted some main characteristics of the CFRP substrates according to the specific treatment performed.
Abrasion and peel ply have similar dispersive SFE components (45.7 mJ/m^2 and 46.2 mJ/m^2 respectively) but peel-ply polar contribution is almost treble (21.4 mJ/m^2) that obtained with abrasion (7.9 mJ/m^2). Indeed, abrasion with Scotch-Brite™ MX–SR results in a surface with a non-well-balanced ratio between polar and dispersive SFE fractions, which clearly leans toward the latter, whereas the polar component is low and almost the same as the only-degreased surface. On the contrary, vacuum plasma treatment creates polar groups on the surface, leading to a higher polar SFE fraction. Thus, considering that also surface topography is particularly affected by this treatment (although to a lesser extent if compared to abrasion and, even more so, peel ply), it could be concluded that the increase in TSS performance after plasma treatment is due to concomitant effects of mechanical interlocking and chemical modification of the CFRP epoxy-matrix; in other words, as statistical analysis also revealed, shear strength obtained on plasma-treated SLJs is strictly influenced by both surface roughness (the related Pearson's coefficient is almost one) and increase of the O/C ratio ($f_P = 0.53$). Hence, the experimental findings suggested that the predominating adhesion mechanisms in the shear strength of epoxy-bonded CFRP substrates are those which represent a premise for steady chemical interactions between surface and adhesive, i.e. chemical bonding.

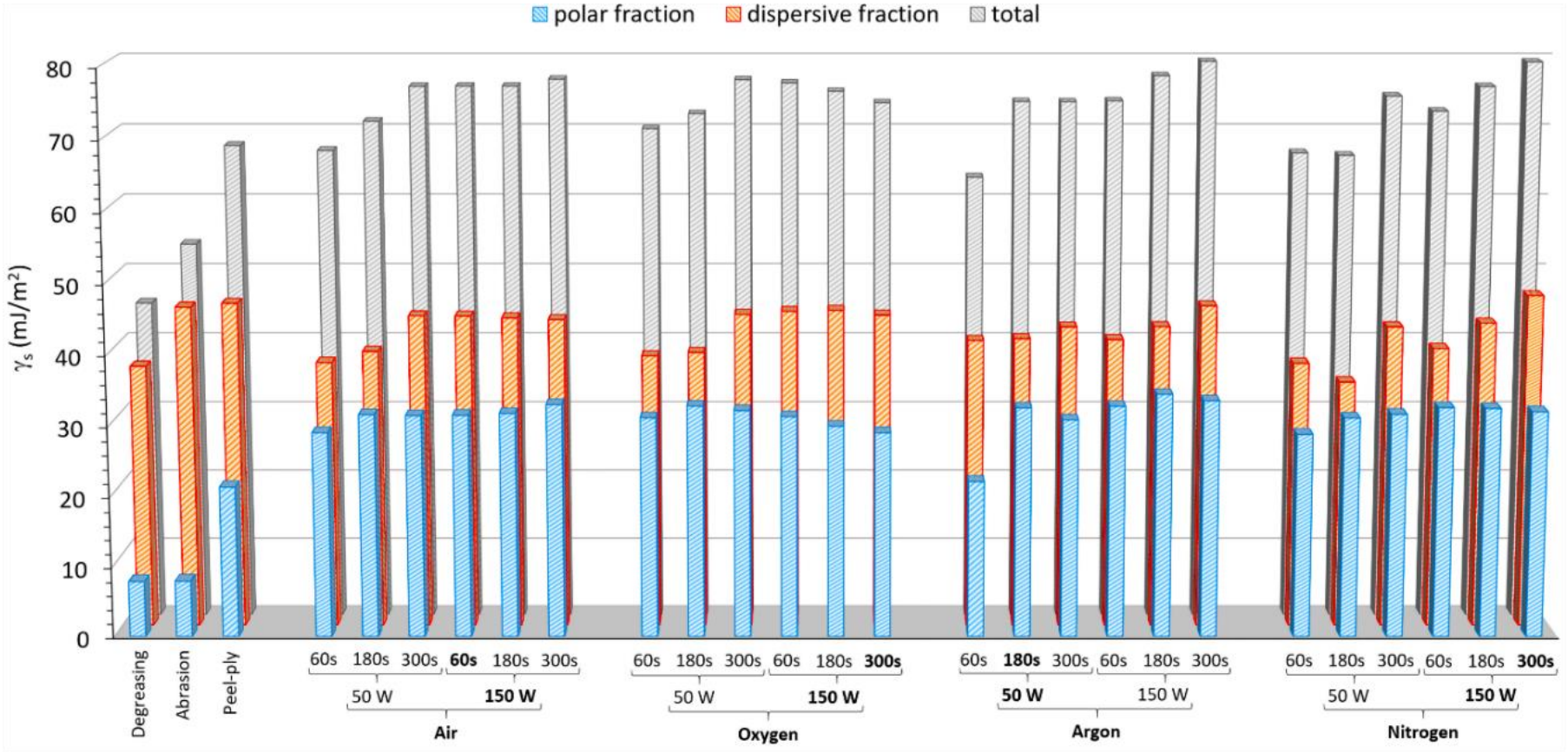

Fig. 5.7. Representation of the polar, dispersive and total fractions of the SFE calculated with Wu's energy method implemented with the CAs acquired on the untreated, abraded, peel ply and plasma-treated CFRP surfaces. Values related to the best plasma settings are marked in bold.

5.2 *Part B*: Accelerated aging of the adhesive system

As mentioned in the previous chapter, the second stage of this work involved a modification of the adhesive system in terms of substrate used; specifically, the carbon reinforcement was changed to seven layers of 2/2-twill carbon-plies with a 0°-orientation, pre-impregnated with epoxy resin using a hand lay-up technique. Also in this case, the formulation of the epoxy resin is covered by industrial secret and, thus, is unknown. Nevertheless, it was assumed that both the chemical and physical effects of the surface preparations observed on the resin used in *Part A* were almost the same with the material of *Part B*, their nature being similar.
Hence, the observations of section 5.1 are reasonably still valid for the following investigation, which was instead focused on the adhesive-bonding performance when this is stressed by severe ambient conditions.
Based on the results of *Part A*, in this case, it was believed sufficient to adopt Air or Oxygen only as process gases, also avoiding the use of a peel-ply as a reference preparation because of its ineffectiveness. In such conditions, the TSS testing was repeated in standard environment (23°C, 50%RH) to determine the starting performance of such an adhesive system, to which the subsequent results after the joint aging were referred. An additional Wedge Cleavage test was then implemented to determine the assembly behavior when a crack propagates along the glue line.

5.2.1 SLJ strength under standard laboratory conditions

As said earlier, owing to the variation in the base material, a preliminary trial campaign was carried out by testing differently plasma-treated joints to determine, for both air and oxygen, which sets of joints to select for aging. In this regard, **Fig. 5.8** displays the results of shear strength obtained testing the SLJ under standard laboratory conditions (23°C, 50%RH); the number present at the base of each column represents the average value of shear strength (expressed in MPa), whereas the standard deviations of the associated measurements are displayed as bar-errors.
As previously mentioned, TSS was first measured for two sets of control joints, respectively prepared via simple acetone wiping and mechanical abrasion; the former stood at 22.7±3.8 MPa, whereas the latter stood at 25.7±0.4 MPa. Thus, as in *Part A*, it was decided to compare all the results obtained with LPP treatments to the case of abrasion only, since the intrinsic low efficiency of the only-degreasing preparation does not allow considering it as a valid reference.
It is clear that, also with this substrate, low pressure plasma confirms to be an effective and successful pre-bonding treatment of CFRP. Indeed, for all the cases analyzed, an overall increase in the mechanical performance of the joints was observed, compared to the abraded reference samples. However, with respect to the previous mechanical investigation, many differences were observed in the joint response to the various treatment conditions, meaning that it would not have been possible to adopt the same, optimized process parameters for both cases.

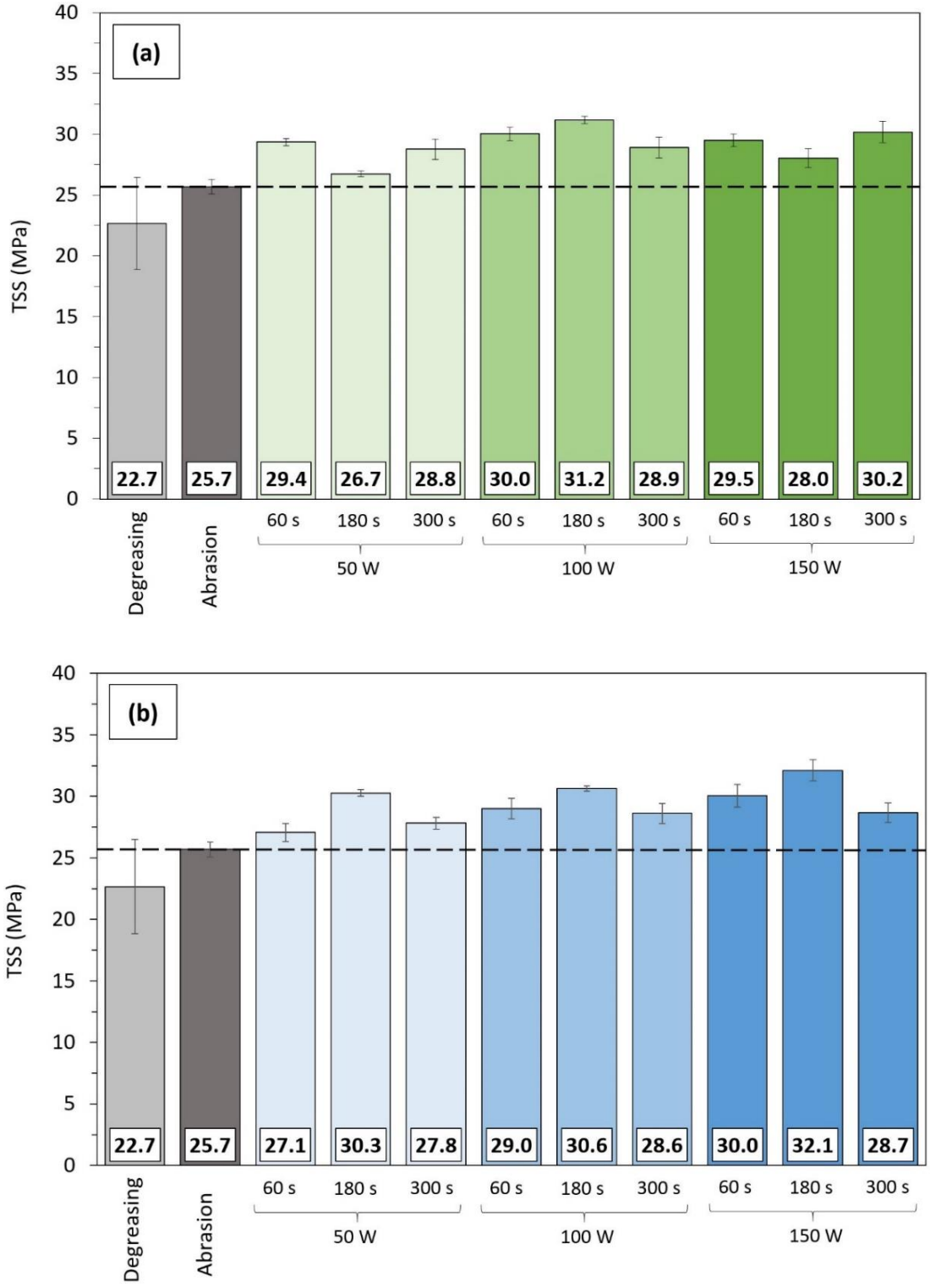

Fig. 5.8. Bar chart reporting the TSS testing (at 23°C, 50% RH) results obtained with different plasma treatment conditions of power and exposure time, using (a) air and (b) pure-O_2 as process gases. Black dotted line represents the reference mean value of shear strength presented by the abraded control samples.

With air-plasma treatment (**Fig. 5.8a**), SLJ presented an increase in shear strength variable from a minimum of +4.0% (with the 50W/180s set) to a maximum of +21.4% (100W/180s). In particular, when low-powered air-plasma was employed, the worst results were obtained for intermediate exposure-time (180 s), whereas at the extremes (60 s and 300 s) shear-strength values were higher and comparable (+14.3% and +12.0% respectively). On the contrary, 180 s was the best duration when a 100W-powered LPP treatment was performed, providing an enhancement of +21.4% in mechanical performance of the joints; for extreme time values, the shear strength resulted lower than the previous one (+16.9% at 60 s and +12.5% at 300 s). Setting power to 150 W, a behavior similar to the 50W-case was observed: a first increase of +14.8% was obtained at 60 s, followed by a decrease at 180 s (+9.1% over the abraded samples), while a +17.5% was reached by exposing the substrates to plasma for 300 s. Hence, to define uniquely a trend of the mechanical response with process parameters is not easy. Even in this case, a statistical analysis by Pearson's correlation factors (f_P) was therefore carried out to evaluate whether and how much the variations of both power input and process duration affect shear strength. As reported in **Table 5.5**, the statistical analysis stressed that, for an air-LPP treatment, power input has a moderate direct influence on shear strength, whereas the relationship between exposure time and performance of the joints is much weaker and not linear. This suggests that, in this case, once the process gas is fixed, power is the most meaningful of the two process parameters, since increasing power input may statistically result in a linear increase of the mechanical performance. Evidence of this is to be found observing that maximum strength relating to each power level was obtained at different treatment time.

With regard to O_2-LPP (**Fig. 5.8b**), the so-treated samples witnessed a more pronounced improvement when an intermediate treatment duration (180 s) was set at every power-input: +17.9% with a 50W-plasma treatment, +19.2% at 100 W and +25.0% at 150 W; even in this case, Pearson's factor analysis clearly confirms that major strength variations are due to changes in the power set-up, whereas the time-parameter appears to have no significant influence in linearizing them. Indeed, a more defined TSS-pattern can be recognized since extreme values of time-parameter always corresponded to less prominent increases of the joint performance, compared to the control reference.

It should be noted that such a result highlights a fundamental aspect: from a comparison of the mechanical findings and related statistical analysis between *Part A* and *B*, the prominence of both power and time parameters was different, especially in the case in which oxygen was used, resulting in a reversed influence of the two variables on shear strength. Hence, it is clear that any evaluation of the influence of a process parameter on the joint resistance is valid for the specific adhesive system, but it does not have absolute value. Indeed, if the system changes (even in a small part), its response changes as well, making experimental testing the only way to know and predict the mechanical behavior of the adhesive system.

In addition to measurement of mechanical performance, observation of the overlap fracture surface is required to define the success of a pre-bonding treatment. This is all the more interesting when long-term adhesion properties have to be evaluated. In fact, as experience

suggests, an increase in mechanical performance owing to a specific surface preparation – especially if observed with tests carried out under standard and controlled laboratory conditions – is a necessary but not sufficient condition to guarantee a long-lasting and efficient life-cycle for the joint. Indeed, as observed in *Part A*, macroscopic mechanical behavior of a joint is closely related to the capability of the resin to generate strong and stable adhesive bonds with the substrate on which it is applied. This is obviously linked to the intrinsic characteristics of the adhesive used (base-resin and activator) as well as to surface conditions such as good wettability and high surface free energy, proper morphology according to the adhesive rheological properties, and chemical activation at the interface.
The role of plasma in creating these good-adhesion conditions has already been studied, and is also confirmed by the fracture mode observed after TSS testing.

Table 5.5
Influence of the process-parameters on TSS, statistically evaluated using Pearson's correlation factor analysis.

Gas	Plasma-parameter influence on TSS (Pearson's correlation factor, f_P)	
	Power	Time
Air	Moderate (0.32)	Weak (-0.12)
Oxygen	Moderate (0.53)	Weak (-0.09)

As expected, 100% adhesive failure (AF) occurred when no treatment was performed (**Fig. 5.9a**), meaning that adhesive-adherend interface was the weakest part of the only-degreased CFRP samples. Considering the latter as a base condition, a first deviation from this undesired behavior was observed after abrasion (**Fig. 5.9b**), i.e., adopting a technique only aimed at increasing the effect of mechanical-interlocking between the substrate and the resin applied: in this case, a mixed failure mode (80%AF-20%CF on average) was obtained.

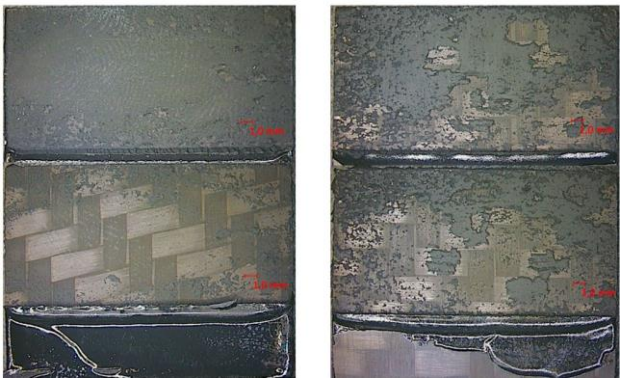

(a) (b)

Fig. 5.9. Fracture surfaces of (a) degreased-only and (b) abraded samples.

The cohesive-fracture was in fact identified as near-Substrate Cohesive Failure (SCF), because localized in the adhesive layer but affecting the interphase zone. When LPP treatment was performed, the overall fracture behavior of the samples was characterized by cohesive failure within the adhesive. In particular, an SCF-CF mixed mode was observed treating the substrates with those parameter combinations that brought about lower TSS values. However, in a small number of specimens related to these cases, an AF-SCF occurred, as shown in **Fig. 5.10**. But the latter behavior was different from that observed on the untreated specimens. Indeed, traces of the epoxy-matrix from the substrate material were found on the adhesive-side, leaving the fibers uncovered on the adherend-side. Such traces followed the regularity of the woven carbon-fiber and were localized at the interweaving zones, where resin is generally thicker, statistically richer in porosities or voids, and where stress concentrations take place. This kind of failure is of course related to the intrinsic non-homogeneity of the composite substrates; but this also suggested that, even if the overall TSS was lower than that achievable with more effective plasma processes, the interaction forces between adhesive and substrate were stronger than the cohesive ones in the bulk of the matrix. As detailed in Section 5.3, this aspect is all the more evident when 3D-printed composites are used as substrates in adhesive bonding, owing to high non-homogeneity of the manufacturing process.

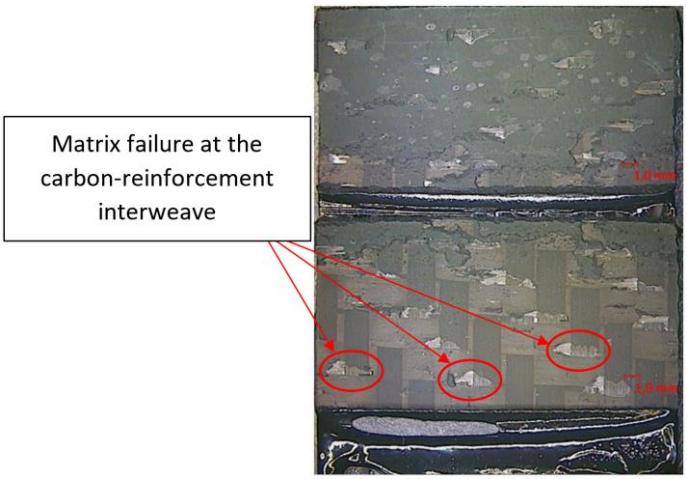

Fig. 5.10. Substrate failure of a low-performance LPP-treated sample.

Fracture-area analysis highlighted a progressive reduction of the extent of the SCF-zone with an improvement in mechanical performance (**Fig. 5.11**). This means shear strength of the joints increased where adhesion forces overcame cohesive forces, as stressed for the joints treated with the best parameter conditions. Hence, in view of both the mechanical findings and the aforesaid observations, the sets of plasma-treated joints listed in **Table 5.6** were subjected to conditioning. Only the set of abraded joints was used as a reference.

Table 5.6
Significant results of TSS measurements for the different plasma treatment conditions to be evaluated under accelerated aging. The relative difference is that of the mean values against the abrasion control.

Gas		P (W)	t (s)	TSS, τ (MPa)	$\tau_{max} - \tau_{min}$ (MPa)	Range of difference vs abrasion (%)
Air	τ_{max} @	50	180	26.7 ± 0.3	4.5	+ 4.0 ÷ 21.4
	τ_{min} @	100	180	31.2 ± 0.3		
Oxygen	τ_{max} @	50	60	27.1 ± 0.7	5.0	+ 5.4 ÷ 25.0
	τ_{min} @	150	180	32.1 ± 0.9		

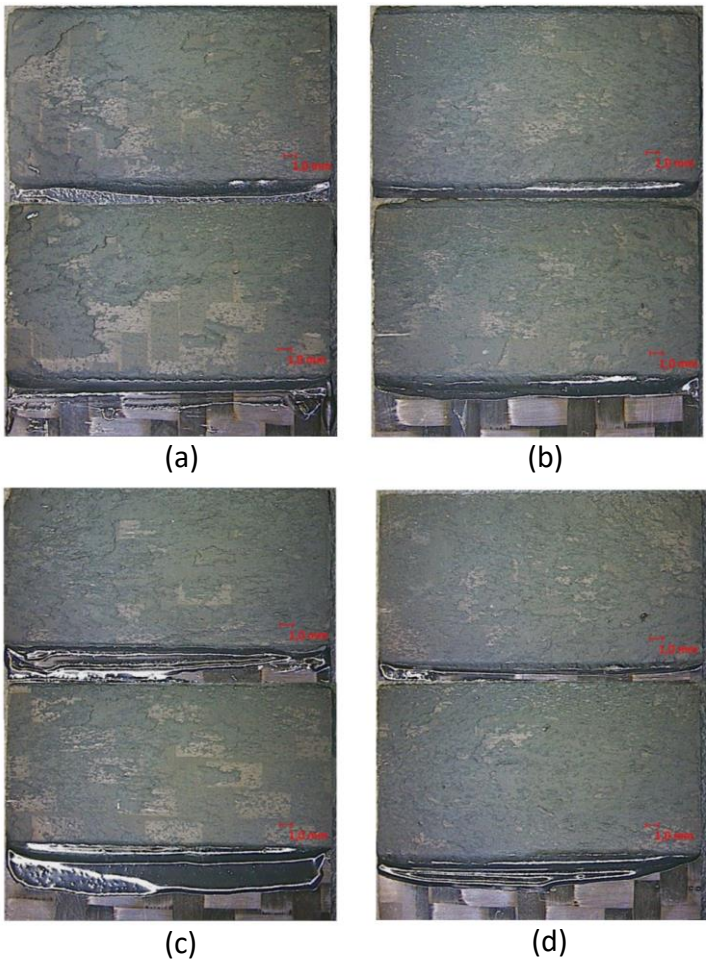

Fig. 5.11. Fracture surfaces of samples LPP-treated with the following gas/power/time set-ups: (a) air/50W/180s, (b) air/100W/180s, (c) O_2/50W/60s and (d) O_2/150W/180s. Based on the mechanical characterization, (a) and (c) correspond to the worst plasma conditions for the two gases, whereas (b) and (d) to the best ones.

5.2.2 SLJ strength under accelerated aging conditions

The five sets of SLJ previously selected were placed in a climatic chamber to undergo the D4 aging cycle. For each set, twenty samples were first made in order to perform five repetitions (N=5) of TSS testing every 168 h and evaluate the mechanical performance trend over a total aging duration of 672 h (i.e. 4 weeks).
However, after the first 168 h it was observed that the two best LPP-treatments presented a comparable downward path of the TSS, with a loss in performance which stood at -10.8% and -8.2% for air and O_2 respectively compared to that obtained with the same treatments under standard environmental conditions. On the contrary, for the two worst-cases, the trend was ascending, with an increase in TSS of +5.7% using air and +8.8% using oxygen. Such behavior was to be expected, as attributable to the effect of further post-curing due to the part of D4 cycle at 70°C, which is, indeed, very close to the post-curing temperature condition of the adhesive (80°C). Hence, this suggested that, in the first half-cycle of aging (5 h), the shear strength of the joints had enhanced, reaching values that were higher than those originally obtained in standard environmental conditions. A similar behavior was not clearly observable with the best air and O_2 LPP-treatments, but it was expected to exist in the latter cases as well, hidden in the curve traced between 0 and 168 h. Thus, to confirm these considerations, further SLJ were manufactured preparing the substrates with the five aforesaid treatments, and then tested after 5 h at 70°C in a climatic chamber. In this regard, refer to **Fig. 5.12**, which shows the TSS curves corresponding to the four different plasma treatments compared to the control (dotted red line).

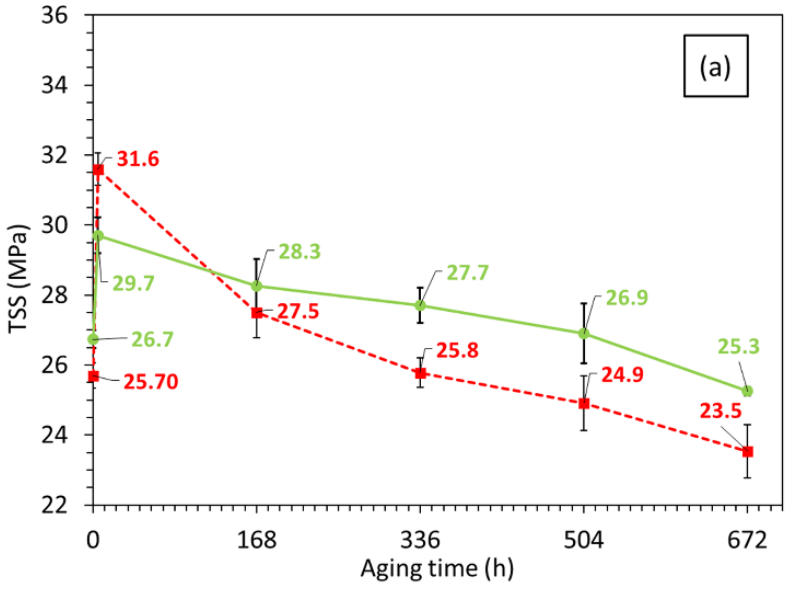

Fig. 5.12. Aging lines for samples LPP-treated with the following gas/power/time set-ups: (a) air/50W/180s, (b) air/100W/180s, (c) O_2/50W/60s and (d) O_2/150W/180s. Red dotted line is related to the abraded sample employed as a reference. (Continue)

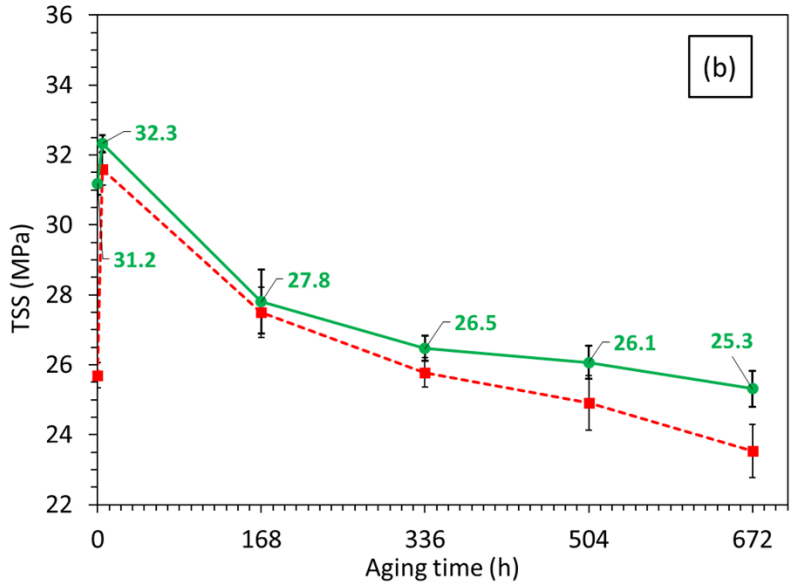
(b)
TSS (MPa)
Aging time (h)
32.3
31.2
27.8
26.5
26.1
25.3

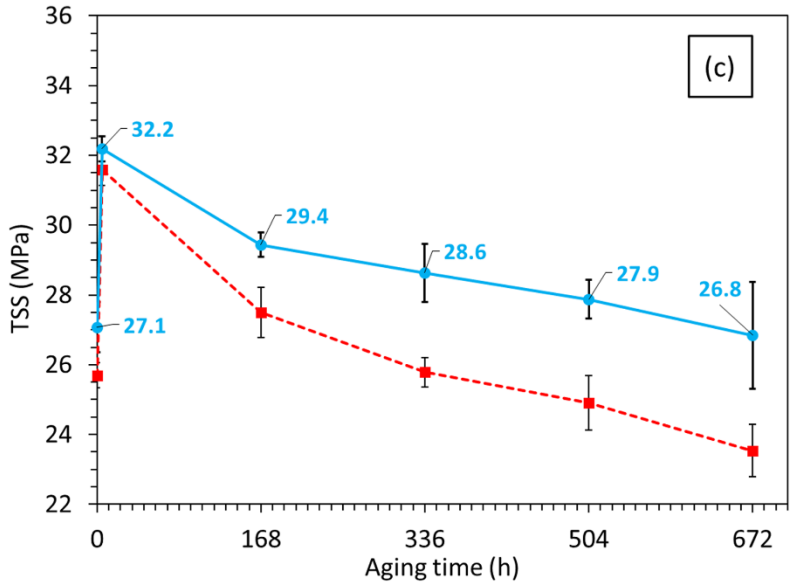
(c)
TSS (MPa)
Aging time (h)
32.2
27.1
29.4
28.6
27.9
26.8

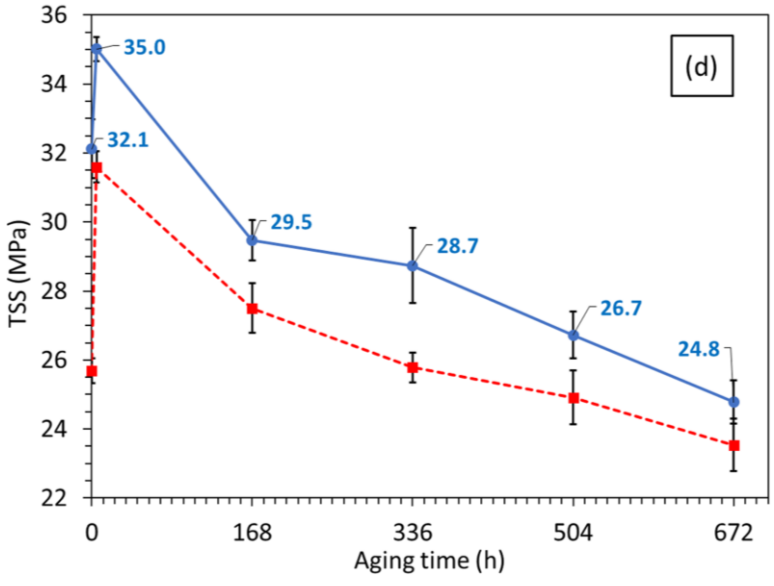
(d)
TSS (MPa)
Aging time (h)
35.0
32.1
29.5
28.7
26.7
24.8

As shown, such prolonged permanence at high temperature resulted in a substantial improvement in mechanical characteristics of the adhesive, thanks to the higher grade of polymerization reached. This was obtained with the control abraded samples (+5.9 MPa than that before post-curing) as well as the joints differently LPP-treated: on average, +3.0 and +1.2 MPa setting LPP on air/50W/180s and air/100W/180s respectively; similarly, employing O_2/50W/60s and O_2/150W/180s, enhancements of +5.1 MPa with the former and +2.9 MPa with the latter were obtained.
As regards failure mode of the LPP-treated joints, neither AF nor SCF were observed, since they indeed failed cohesively independently of the process parameters employed. Similar improvement was obtained on the reference abraded samples as well, where the original adhesive debonding switched to SCF on most of the fracture surfaces.
In view of the findings above, D4 aging should be intended as actual after the post-curing effect due to the initial half-cycle; hence, from now on, shear-strength values of the post-cured SLJ will be considered as the references against which performance worsening is evaluated.
Surface treatment ruled the initial mechanical behavior of the joints, but also determined different performance decay-rate over conditioning period. Indeed:

- after post-curing, the reference abraded-SLJ reached an average shear-strength only slightly lower than that obtained after two of the four LPP-treatments investigated (i.e. air/100W/180s and O_2/50W/60s), and higher than that measured on the joints pre-treated with air/50W/180s. However, abrasion proved not to have particular effectiveness in maintaining mechanical performance under severe aging conditions: after just 336 h, TSS was similar to that obtained before post-curing and continued to deteriorate, reaching poor values at the end of aging (-25.5% in mechanical strength);

- SLJ treated with the low-powered plasma – namely air/50W/180s (**Fig. 5.12a**) and O_2/50W/60s (**Fig. 5.12c**) – presented two different behaviors during the first phase (0-168 h), but similar losses in performance during the second and the third week of accelerated aging. However, in the last 168 h, air-plasma treated samples showed a steeper slope for the TSS, which reached a final mean value that was 15.0% lower than the original one (29.7±0.5 MPa). Contrariwise, performance decrease-rate of the O_2-LPP treated joints was almost constant week by week: in this case, the decrease was of 16.6%, but final joint strength was higher (26.8±1.5 MPa) than all the other cases examined;

- despite having excellent mechanical behavior at the beginning of the aging period, the two plasma treatments initially selected as the best, namely air/100W/180s (**Fig. 5.12b**) and O_2/150W/180s (**Fig. 5.12d**), presented a pronounced loss of performance during the first week of conditioning (-14.0% and -15.8% respectively). As regards the former parameter combination, the slope steepness of the line representative of the TSS-trend progressively reduced during aging, and the overall decrease in mechanical performance measured after 672 h stood at -21.7%. On the contrary, employing the O_2/150W/180s set,

the reduction in shear strength was less gradual and was down by -29.2% at the end of the aging period.

Hence, as highlighted by the experimental results, the choice of a specific parameter-combination to be adopted for the plasma process should take into account the final use conditions of the adhesively-bonded joint/component. Indeed, treatments that bring about excellent short-term properties, might not preserve the same durable effectiveness under environmental conditions which differ from standard, and vice versa. Considering the two cases with air, by employing the higher-powered treatment, excellent mechanical resistance is reached in the short-term, even without any further post-curing of the adhesive, whereas the same is not possible with the low-powered one. However, durable properties during the aging period were obtained even with the latter treatment (in fact, the slope of the line for the air/100W/180s treatment is very similar to that of the reference until 336 h), resulting that, at the end of the aging, the LSS-values reached with the two air-treatments appeared identical (25.3 MPa on average after 336 h). Similar conclusions can be drawn considering the two oxygen-plasma treatments investigated in parallel: high-powered plasma provides for excellent initial resistance (especially when post-curing is performed), but its qualities are less stable over time. On the contrary, low-powered plasma seems to emphasize durability of the joint in an environmentally hostile atmosphere, although a post-curing of the adhesive proved to be effective to obtain quality joints even for short-term applications.

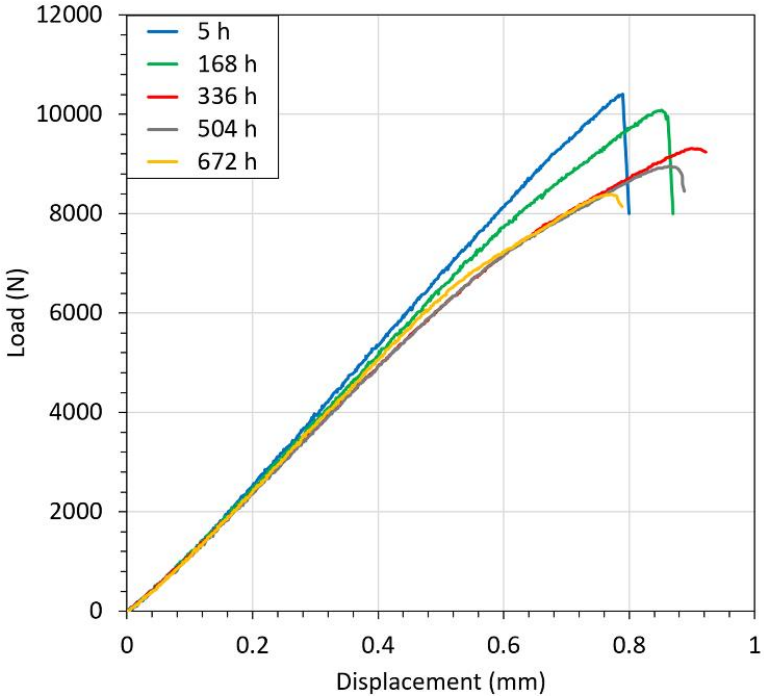

Fig. 5.13. Load-displacement curves of plasma-treated joints subjected to aging.

Based on the aforesaid observations, one can conclude that low-pressure plasma treatment generally resulted in a remarkable improvement of the short-term quality of the joints, but it

also provided optimal characteristics to maintain performance under severe aging conditions. This is true in principle if LPP is compared to the traditional treatment of abrasion of the faying surfaces. Indeed, since the failure mode continued to be mostly of the cohesive type, the loss in performance observed is believed not to be attributable to a decrease in the interface interactions. Rather, it is presumably related to the adhesive degradation occurring throughout aging, and, hence, to plasticization due to humidity adsorption (more prominent in the first stages of aging), as suggested by the gradient decrease before failure distinctive of the load-displacement curves of joints subjected to aging (refer to **Fig. 5.13**, where the curves of the air/100W/180s treated specimens are reported as an example).

5.2.3 WT: crack opening, propagation and fracture energy evaluation

The wedge cleavage test can be divided in two subsequent stages, which provide different information about the adhesive system investigated. A first stage, corresponding to the insertion of the wedge into the specimen at RT, allows definition of the effectiveness of the treatment adopted before bonding: indeed, initial crack length, a_0, (and related fracture energy in Mode I, $G_{Ic,0}$) serves as a datum confirming that both substrate preparation and adhesive cure have been satisfactory. A second stage provides for monitoring of the crack propagation during accelerated aging under severe environmental conditions. Here, crack growth is mainly based on properties of the entire adhesive system, i.e. toughness, thermal resistance/steadiness, hygroscopicity, of both the adhesive and the substrate. For a stable system such as that studied, crack propagation rate is higher during the first hours of aging, whereas it reduces with time, and values of a scarcely grew, progressively tending to an asymptote. For this reason, crack length was recorded 24, 48 and 72 h after having placed the specimens in the climatic chamber and then alternating intervals between 72 and 96 h, for a total duration of 672 h. In **Fig. 5.14**, the measurements of crack length, a, and related fracture energy, G_{Ic}, values are plotted to show their trends over the aging period. All the conditioned specimens did not present any premature/complete rupture, so that, for each set of treatments, the values at every point are reported as an average over the original ten replications.

As shown, during wedge-insertion phase, the main differences in behavior between the various LPP-preparations and the abrasion have been highlighted. In particular, the abraded specimens (red lines) presented greater values of a_0 which provided for an average of 47.8 mm, corresponding to $G_{Ic,0}$ about 569 J/m^2. Conversely, with all the LPP-treated samples, a minor extension of the initial cracks was measured and, hence, higher values of energy release rate (almost twice the control) were obtained: on average, 1181 J/m^2 with air/100W/180s and 1267 J/m^2 with air/50W/180s, whereas 1208 J/m^2 and 1188 J/m^2 respectively with O_2/50W/60s and O_2/150W/180s treatments.

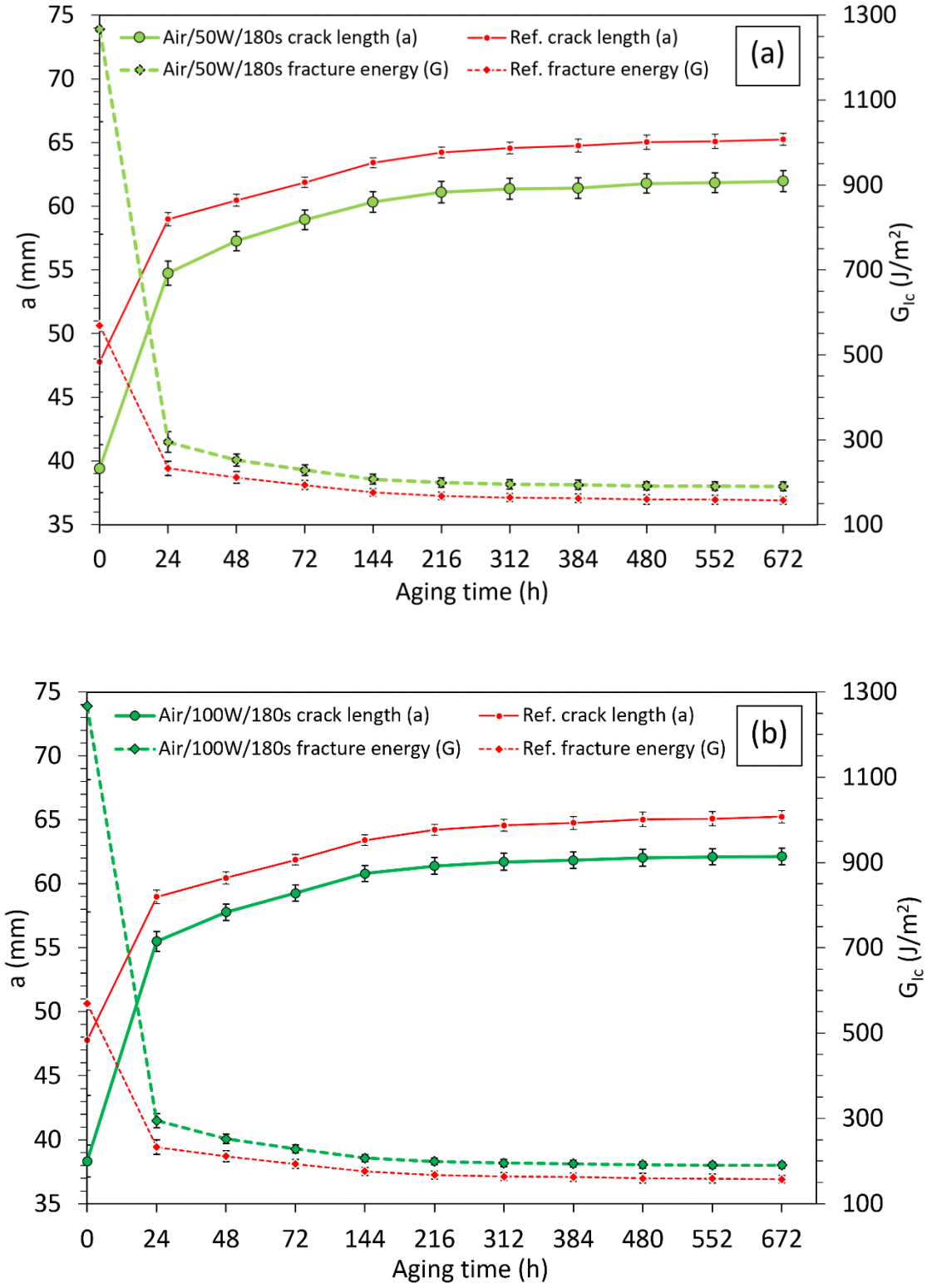

Fig. 5.14. Crack-propagation length, a, and related strain energy release rate, G_{Ic}, measured on the WT-samples plasma-treated with the following gas/power/time set-ups: (a) air/50W/180s, (b) air/100W/180s, (c) O_2/50W/60s and (d) O_2/150W/180s. Red lines are related to the abraded sample employed as a reference. For reasons of simplification, aging time on the abscissa is reported as not-to-scale. (Continues)

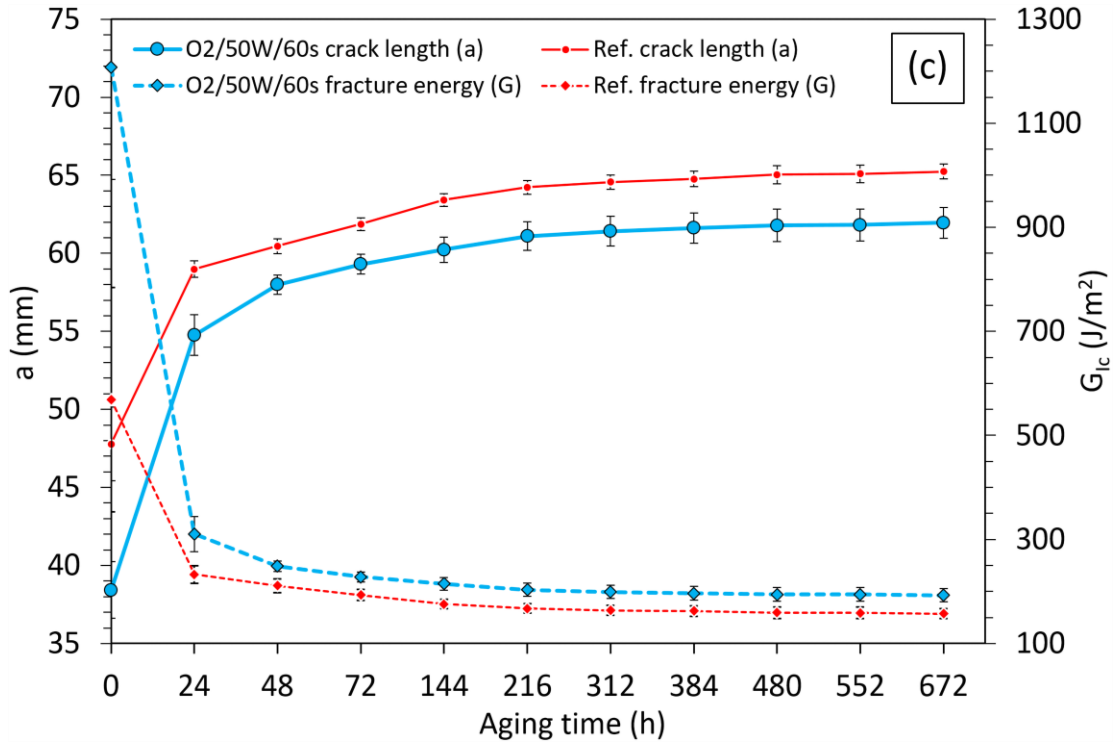

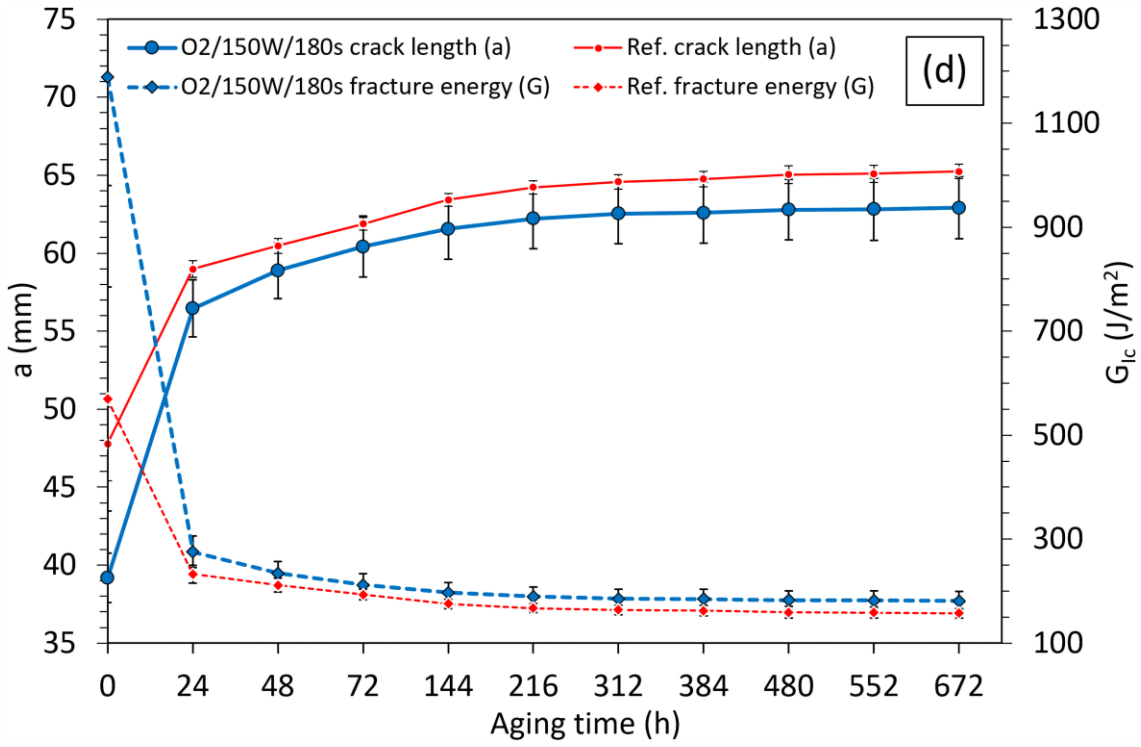

The estimated strain energy release is consistent with what could be expected for a toughened epoxy adhesive such as that employed. However, while the contrast between abrasion and plasma treatments is clearly observable, it is not easy to define whether the differences in

$G_{Ic,0}$ encountered among the samples differently plasma-treated are so significant. Indeed, the values of a_0 detected at this first stage varied by just over one millimeter, precisely from 38.3 to 39.4 mm. In this regard, note that use of the wedge test as well as the energy model expressed by **Eq. (5.1)** required some evaluations about aspects such as, first and foremost, accuracy of the crack-length measurement and law of variation of G_{Ic} with a. The former is related to the intrinsic difficulty in recognizing the precise position of the crack tip at each measurement. An average crack length was indeed provided as a result by measuring the crack extension at both sides available for every specimen, but crack front across the width of the specimen and its propagation could only be supposed during the test. A second aspect to be taken into account, as said, is related to how fracture energy, G_{Ic}, varies with the crack length, a, in **Eq. (5.1)**; indeed, it should be noted that the value of G_{Ic} results in an inverse relationship with the fourth power of a, and this implies that small variations in crack-length measurement produce wider variations in energy values.

The WT-specimens were then exposed to D4 aging in a climatic chamber. For each set, the conditioned samples showed a higher crack growth during the first 24 h. Crack of the abraded samples propagated by a further 11.2 mm on average, whereas LPP-treated samples exhibited increases of a which varied from 15.3 mm (with air/50W/180s) to 17.3 mm (with O_2/150W/180s). Fracture energy decreased accordingly, because of the fourth power influence. However, after 48 h, crack growth was much smaller, tending to reduce to zero over the aging period owing to a considerable reduction of the stress at the crack tip. Such behavior can be explained by equating the adherends of a WT-joint to a cantilever of length a (namely equal to the crack length) and considering the related equation, as suggested by Adams et al. [74]. The deflection d at the tip under a force P (in this case represented by the peel force exerted by the wedge on the adherends, i.e. T_2) is defined as:

$$d = \frac{Pa^3}{3EI} \tag{5.1}$$

where E is Young's modulus and I the second moment of area. Hence, maximum stress in a cantilever can be derived:

$$\sigma_{\max} = \frac{1.5Edh}{a^2} \tag{5.2}$$

Consequently, separation force $P = T_2$ decreases as a^3 so that the bending moment (namely, the rotation of the beams at the tip) decreases as a^2, resulting in the stress reduction at the crack tip observed as crack proceeds. Furthermore, it is interesting to note that the four plasma sets exhibited very similar asymptotic trends during the aging period, providing for lines which are explicative of a common behavior towards cleavage stresses.

After 672 h had passed, crack final increment was between 22.5 mm and 23.8 mm for the LPP-treated specimens, whereas 17.5 mm for the abraded ones; however, taking into account also a_0-value, the four plasma treatments allowed us to reach a total extension of the cracks

that was 3.7÷5.3% (i.e. 3.0 mm averaged on the four LPP cases) less than the control. In other terms, despite having shown considerable differences during the first phase at wedge insertion, plasma-treated samples presented a more prominent crack propagation during aging. However, a possible explanation of this behavior may be found in **Eq. (5.2)**: indeed, the a_0 of the abraded WT-specimen being longer than that obtained with the plasma-treated ones, the latter are subjected to higher stresses ($\sigma_{\max}$) at the crack tip; and this determines the higher crack-propagation rate observed.

After testing, the specimens were split open by hand. Typical WT-fracture surfaces representative of abrasion and LPP treatments (the case O_2/50W/60s is reported as an example) are displayed in **Fig. 5.15**, where the aforementioned two stages – namely wedge insertion, ①, and crack propagation, ② – are well distinguishable. In particular, control abraded specimens presented completely adhesive failure at region ①, whereas all the LPP-treated specimens, regardless of the process-parameter set, failed cohesively, confirming the effectiveness of such physical treatment observed in the previous analyses.

At region ②, for both types of treatments, degradation of the adhesive is observed developing mainly throughout the adhesive layer when plasma treatment was performed, and mainly at the adherend-adhesive interface with abrasion; however, it is believed that such a considerable degradation is presumably emphasized by the fact that it partially occurred when the crack had already grown and the adherends separated. Indeed, it appears considerably lower at that part of region ② corresponding to lower crack-propagation rate, i.e. where the adhesive and/or substrate underwent a brief, direct exposure to the environment. However, slight signs of crazing of the adhesive were observed, meaning that moisture diffusion (along the crack-front across the width of the specimen) would have made internal bonds weaker. It should be noted that, due to the aging cycle chosen, the consequences of this phenomenon may not only be chemical, but also mechanical. Indeed, molecules of water penetrate at the crack tip when $T_{cycle} > 0$°C, and freeze, increasing their volume, when $T_{cycle} < 0$°C; and this might provide for additional (and cyclic) cleavage stress at the tip. Hence, observation of region ② would justify the consideration previously drawn about the fact that crack-growth monitoring over the aging period can be considered as a test to evaluate hygro-thermal stability of the entire adhesive system as well as its overall capacity to resist to critical stress conditions. Conversely, a qualitative but meaningful result about effectiveness of all the LPP-treatments compared to the control was given when specimens were manually split open (region ③): whereas abraded samples easily failed adhesively, complete delamination of both CFRP-adherends occurred for all the plasma-treated samples. This should be intended as a further confirmation of the good adhesion conditions provided by the plasma treatments on the CFRP substrates.

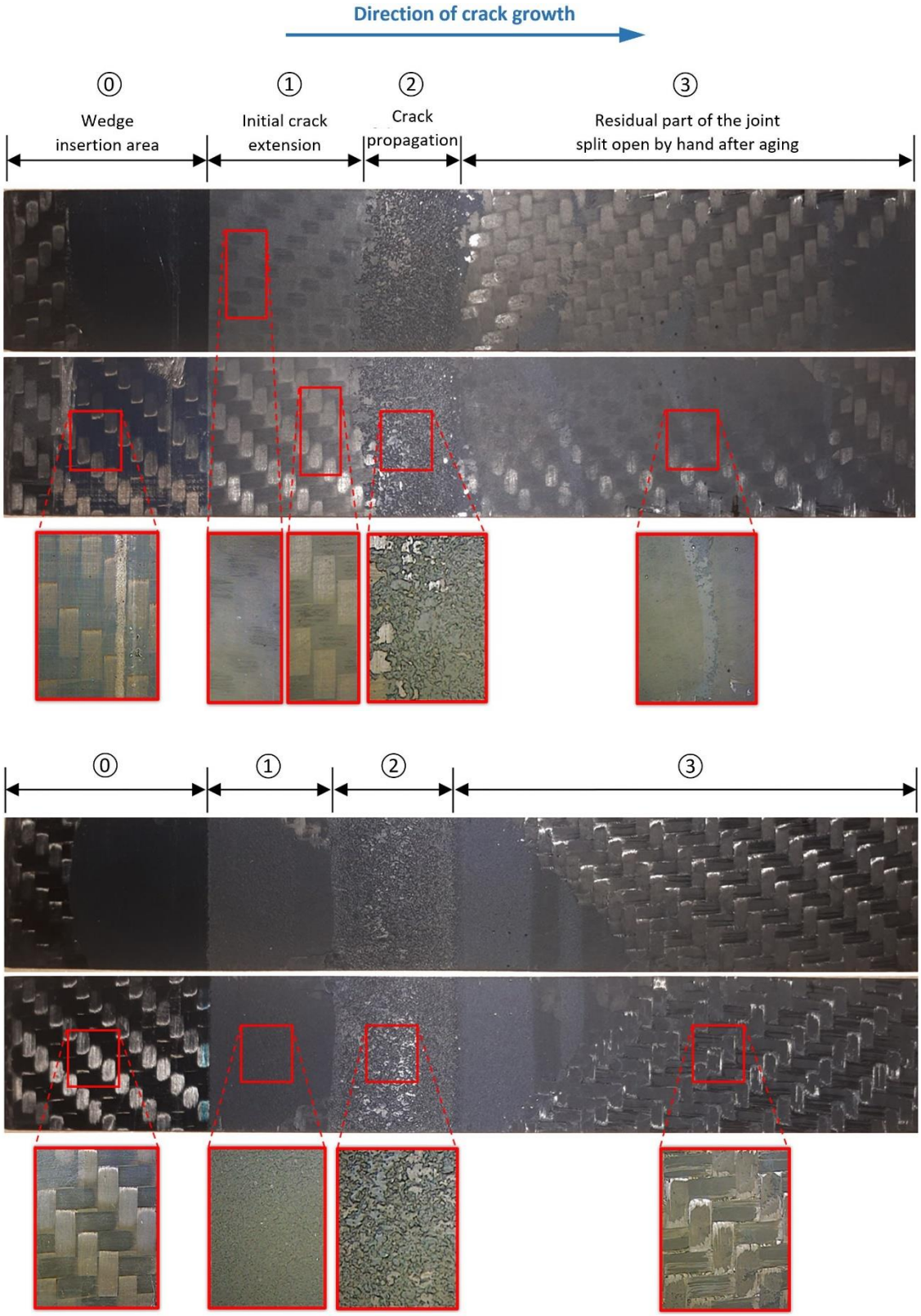

Fig. 5.15. Typical failure surfaces of (above) abraded and (below) LPP-treated conditioned WT-specimens. The details of the different regions of the specimens were acquired using a microscope with a 6.3X magnification.

5.3 *Part C*: Adhesive bonding of 3D-printed composites

One of the common issues of additive manufacturing of composite components is related to the small size of the printers, which limits the dimension of the components built. This requires different design criteria, typically based on a 'building-block' approach, leading to a manufacturing process of which assembly via adhesive bonding is an integral part.
Specifically, the mechanical and failure behavior of the CCF composite material built via AM was investigated when used as substrates for single-overlap adhesive joints, focusing on verifying how the additively-manufactured substrates respond to adhesive bonding when the interface interactions are increased by preparing the surface.
The experimental findings confirmed that, owing to the in-depth chemical functionalization of the surface, LPP treatment of 3D-printed CFRT materials resulted in enhanced shear strength of the joints. However, in this case, such a treatment led to adhesive-adherend interactions which were stronger than those existing between the subsequent layers laid down to build the base material. It follows that, in these conditions, the base material achieves its ultimate resistance, becoming the weak part of the adhesive system.

5.3.1 Preliminary characterization of base material

As described in previous Section 4.2.3, the substrates were produced by stacking subsequent layers having CCFs with unidirectional 0°-orientation with respect to the axial dimension of the specimens, to maximize the performance of the joint. Such a configuration was selected on the basis of a parallel, comprehensive experimental campaign focused on the evaluation of the effect of different CCF arrangements on the tensile and flexural properties of the 3D-printed composite materials, the results of which are summarized in **Fig. 5.16** (more details are also provided in Annex A).
Firstly, to define the maximum strength achievable by the additively-manufactured base material as a benchmark, tensile testing was performed following the specifications provided in **Table 5.7**. In particular, five tensile specimens were built following the construction criteria described in Section 4.2.3.1, and then tested to failure. As a result, the stress-strain curves displayed in **Fig. 5.17a** were obtained: the 0°-CCF laydown pattern led to high resistance and stiffness of the base material, which achieved average tensile strength of about 566 MPa. Failure occurred due to the sharp fiber breakage in the specimen core. Also, after complete rupture, a slight detachment of the roof/floor Onyx shell from the CCF core below was observed.
Furthermore, the flexural properties of the material were determined via the three-point loading test method described in Section 4.2.3.2. The main specifications of the test are provided in **Table 5.8**, in which the average maximum flexural strength is also reported.
In accordance with the tensile findings, the 0°-oriented specimens (**Fig. 5.17b**) resulted in an increased stiffness, with an average maximum flexural stress σ_f of 340.7 MPa.

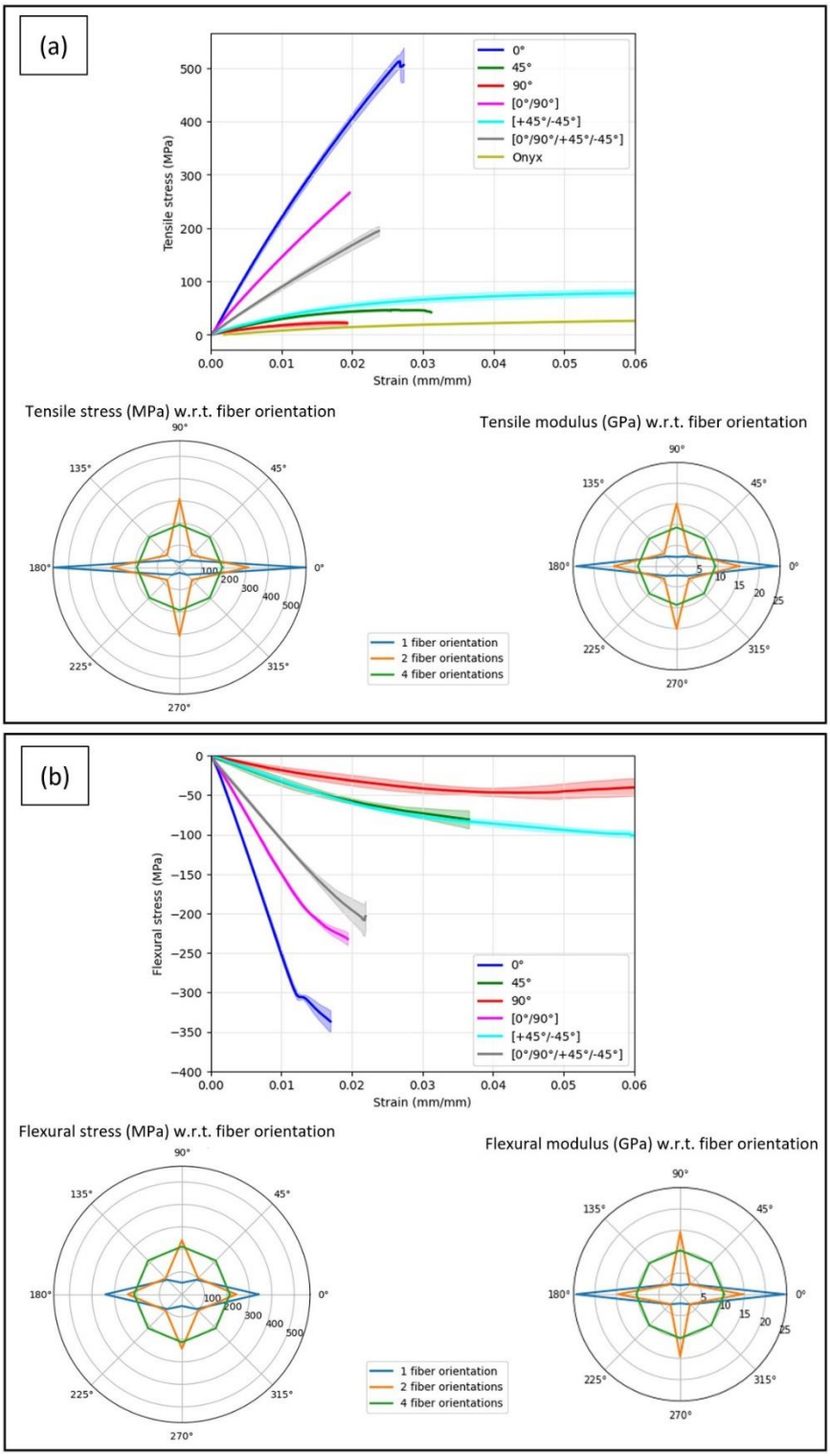

Fig. 5.16. Summary of the results obtained from (a) tensile and (b) flexural testing carried out to characterize the base material. Specifically, a comparison between the average stress-strain curves of different fiber orientations is provided: the shaded areas represent the standard deviations of the results for each test condition. Besides, the polar plots graphically report, for each test, the related values of stress (left) and elastic modulus (right) relative to unidirectional, bidirectional or multidirectional arrangements of the CCFs.

Table 5.7
Testing specifications and tensile properties of the base material according to ASTM D3039.

Method	Sample dimensions (mm)	Onyx layers	CCF layers	Tensile strength σ (MPa)	Strain ε (mm/mm)	Elastic modulus E (GPa)
Tensile	157 × 16 × 3	8	16	566.1 ± 13.6	0.03 ± 0.00	24.2 ± 0.2

Table 5.8
Testing specifications and flexural strength of the base material according to ASTM D7264.

Method	Sample dimensions (mm)	Onyx layers	CCF layers	Flexural strength $\lvert\sigma_f\rvert$ (MPa)	Flexural modulus E_f (GPa)
Flexure	153.6×14×4	8	24	340.7 ± 10.1	24.4 ± 0.4

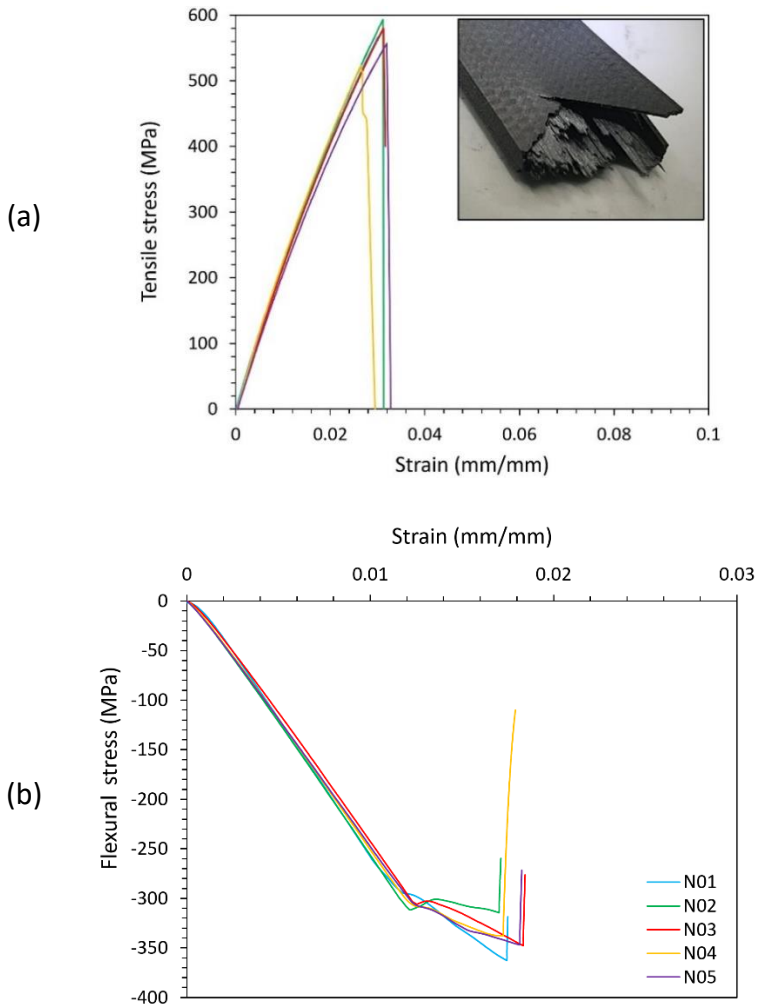

Fig. 5.17. Stress-strain curves acquired from (a) tensile testing and (b) three-point flexure testing on the base material.

5.3.2 Adhesive bonding

5.3.2.1 Post-treatment surface state

Morphological assessment via laser profilometry

A first analysis, focused on the detection of any morphological modifications brought about

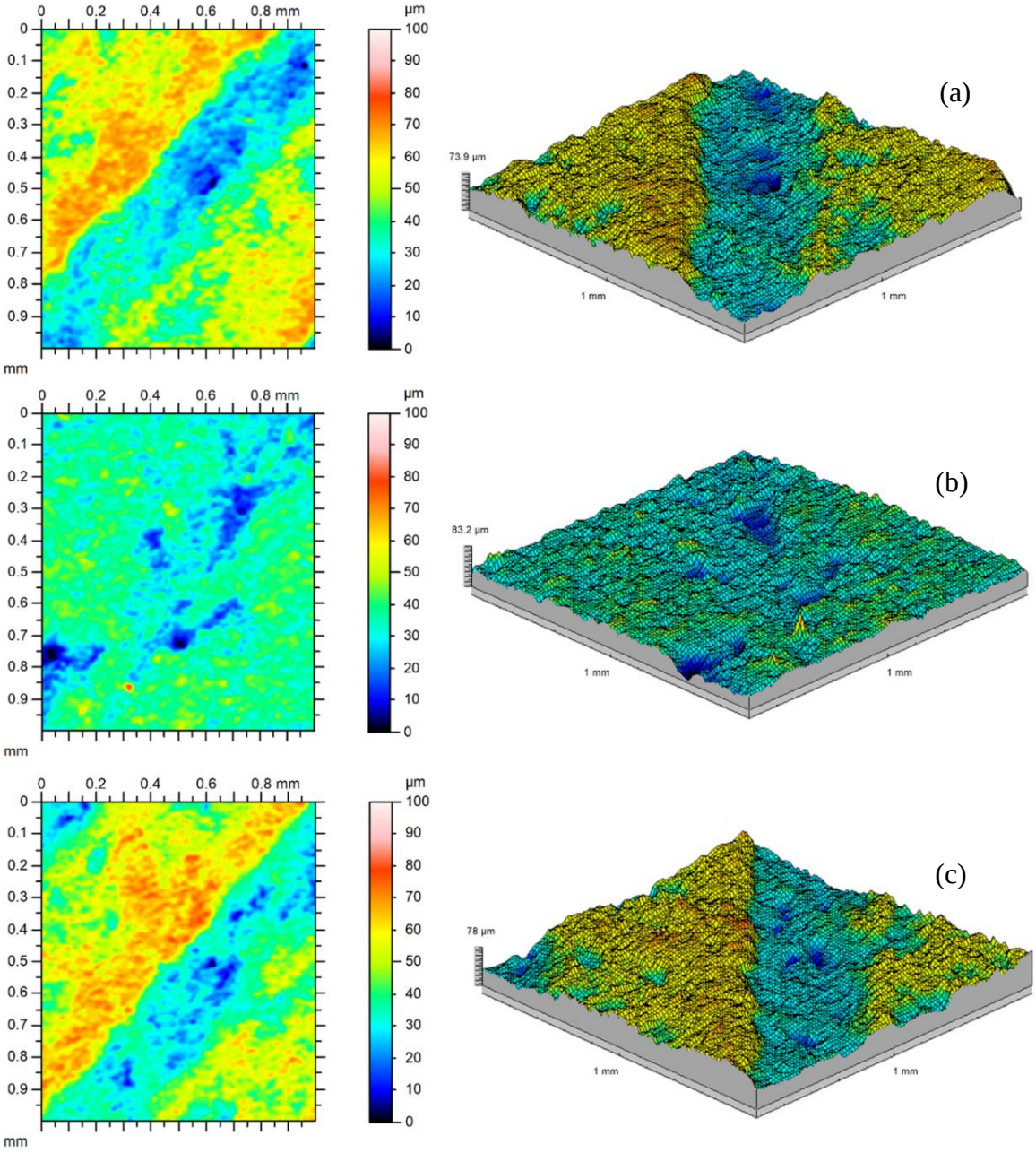

Fig. 5.18. Top-view images and related 3D topography maps of AM-CFRT substrates treated by means of the following methods: (a) solvent degreasing, (b) mechanical abrasion, or (c) LPP.

on the surfaces, was carried out. Indeed, firstly referring to the mechanical theory of adhesion, in many cases the success of adhesive bonding may be related to the solid interlocking between substrates and resin, which can be increased by acting directly on the surface roughness by means of mechanical treatments such as abrasion or sandblasting [82]. In this regard, refer to **Fig. 5.18**, which shows top-view and related 3D morphological maps acquired via laser profilometry on the three differently treated surfaces.
The roughness parameter S_q (i.e., root mean square height) was extracted from the areal acquisitions, in accordance with ISO 25178.
In the as-received condition (i.e., degreased-only), the surfaces presented a mean S_q value of 13.9 µm, as well as a typical 45°-pattern due to the material arrangement used to print the outer Onyx layer (**Fig. 5.18a**). In contrast, an in-depth morphological modification was obtained with mechanical abrasion (**Fig. 5.18b**): compared to the former, this surface was made smoother (S_q stood at 7.0 µm on average), and the aforementioned infill pattern was no longer identifiable. No significant variations from the as-received surface were instead observed after plasma treatment (**Fig. 5.18c**), the latter having left the surface unchanged both in terms of topological structure and roughness parameter values (again considering S_q, this stood at 13.8 µm on average).

Wettability and chemical state evaluation via XPS analysis

It is well known that topological evaluation cannot ignore wettability of the surface, since the non-wetting condition may prevent adhesive bonds from forming at all. Hence, a simple test was carried out by depositing droplets of deionized water on each surface to evaluate their wetting properties qualitatively. As shown in **Fig. 5.19**, a sharp transition from spherical to flattened droplet shape was observed after LPP treatment.

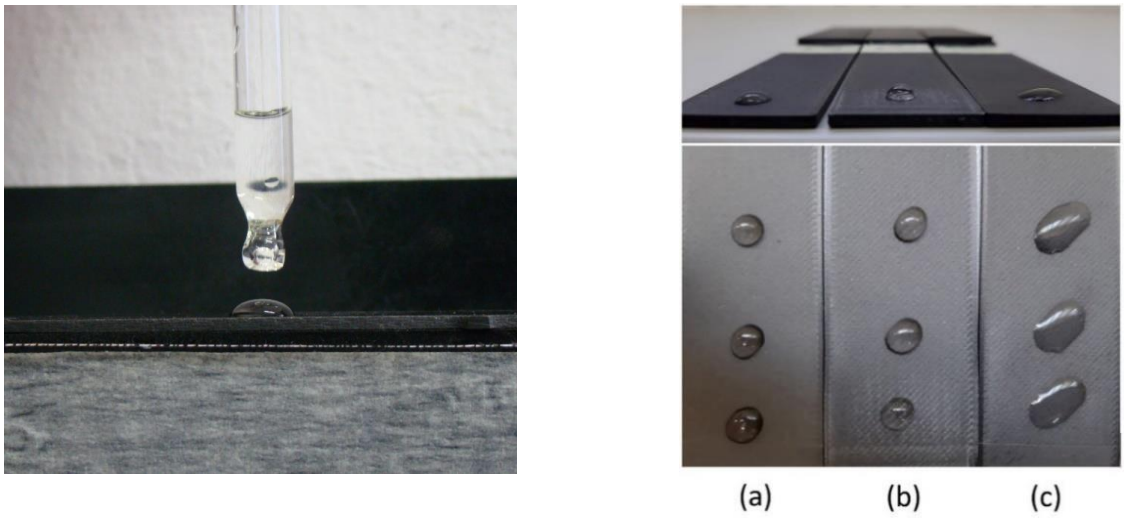

Fig. 5.19. Droplet deposition and surface wettability of (a) degreased, (b) abraded or (c) LPP-treated AM-CFRT substrates.

This has to be related to an oxidizing effect of plasma, which stimulates an increase of polar species on the polymer surface, developing its hydrophilicity.
XPS analyses of the printed CFRT were carried out before and after plasma treatment in order to investigate what chemical modifications occurred on the Nylon-6 surface and how these contributed to its wetting properties. Wide scan acquisitions allowed us to appraise the chemical composition of the substrates, within a 10-nm depth, comparing the three preparations (**Fig. 5.20**). As shown in **Table 5.9**, plasma treatment determined an increase in oxygen content together with a decrease of that of carbon, i.e., an oxidative effect that was reflected in a significant increase of the oxygen/carbon ratio (+133%) with respect to the degreased-only CFRT surface, which can be taken as a reference. No significant changes at the N 1s peak were observed instead, and thus the increase in the N/C ratio is only due to a decrease of C 1s.

Table 5.9
Atomic percentages of oxygen, carbon, and nitrogen, and related O/C and N/C ratios, obtained through XPS analysis in survey mode.

Surface treatment	Atomic percentage (%)				
	O 1s	C 1s	N 1s	O/C ratio	N/C ratio
Degreasing	26.0	67.9	6.1	38.3	9.0
Abrasion	23.5	70.1	6.4	33.5	9.1
LPP	44.1	49.8	6.1	88.6	12.2

Thus, starting from the low-resolution analysis, two energy regions were selected in order to focus on the specific effect of treatment in terms of surface oxidation and activation. These regions are located around the C 1s (282 ÷ 292 eV) and the O 1s (528 ÷ 540 eV) peaks. The results of these analyses are reported in **Fig. 5.21**; they demonstrate that the LPP treatment had a significant effect on the shape of both the carbon and oxygen peaks. On the other hand, spectra collected on degreased-only and mechanically abraded surfaces do not differ significantly one to the other and are in good agreement with that expected from a Nylon-6 surface.
Deconvolution of the C 1s peak (**Table 5.10**) allowed the identification of various carbon components related to: single bond between carbon and carbon or carbon and hydrogen (C-C, C-H) positioned at 285.0 eV, carbon singly bound to a C=O bond at 285.7 eV, or to nitrogen (C-N) at 286.6 eV.
A typical peak of the Nylon-6 corresponding to carbon forming single bond with nitrogen and double bond with oxygen (N-C=O) was recognized at 288.0 eV, while a further carboxyl group (COOH) was found at 289.0 eV. Thus, as shown by deconvolving C 1s, before vacuum plasma treatment C-C/C-H bonds were predominant, whereas treated substrates presented a simultaneous decrease of concentration of these species and rise of peaks corresponding to bonds between carbon and oxygen. Furthermore, the plasma-treated surface also appeared to be more reactive towards the atmosphere.

Table 5.10
Area percentage of each chemical species quantified from deconvolution of the C 1s peak.

Surface treatment	Area percentage (%)				
	C-C/C-H (285.0 eV)	C-C=O (285.7 eV)	C-N/C-OH (286.6 eV)	N-C=O/COO- (288.0 eV)	-COOH (289.0 eV)
Degreasing	71.2	13.9	6.2	6.5	2.2
Abrasion	69.1	14.6	7.1	7.4	1.8
LPP	62.7	12.2	7.3	12.0	5.8

Indeed, after plasma exposure, an increase in the carboxyl percentage was observed, but also an enlargement of the peak was obtained at 288.0 eV, meaning that new signals corresponding to COO^- species were present in addition to those attributed to the N-C=O bond. This observation suggested that plasma treatment changed the chemical state of the CFRT surface, forming new functional groups as a result of the break of the original single bonds C-C or C-H and local oxidation of them. Indeed, comparing pre- and post-treatment conditions, the decreasing trend of these bonds is believed to be the direct effect of the increase of various oxidative reactions that occurred during plasma treatment, which involved the generation of bonds between oxygen and carbon atoms. A reduction of C-C/C-H bonds (-12% compared to the degreased-only reference) was followed by a clear increment of oxidized species, mainly carboxyl. Indeed, free radicals can be created on the treated surfaces, which can then couple with active species from the plasma environment; these reactions are believed to be essential for the changes in the surface functionalities.
In parallel, the high-resolution survey on the O 1s spectrum and subsequent deconvolution of this peak also highlighted the presence of two different chemical species, confirming the high activation and oxidation of the plasma-treated Onyx surface (**Table 5.11**).

Table 5.11
Area percentage of each chemical species quantified from deconvolution of the O 1s peak.

Surface treatment	Area percentage (%)		
	C=O/C-OH (531.5 eV)	C-O-C (532.5 eV)	H_2O (533.4 eV)
Degreasing	59.7	27.6	12.7
Abrasion	62.8	26.5	10.7
LPP	58.0	35.3	6.7

The first, at about 531.5 eV, was interpreted as oxygen making a double bond with carbon (C=O) or carbon forming a single bond with hydroxyl (-OH); and the second, positioned at 532.5 eV, corresponding to a C-O-C group [84]. Thus, similarly to that found analyzing C 1s, such newly formed functional groups along with the introduction of additional groups ensure an enhancement of the surface polarity and, consequently, could develop its hydrophilic behavior.

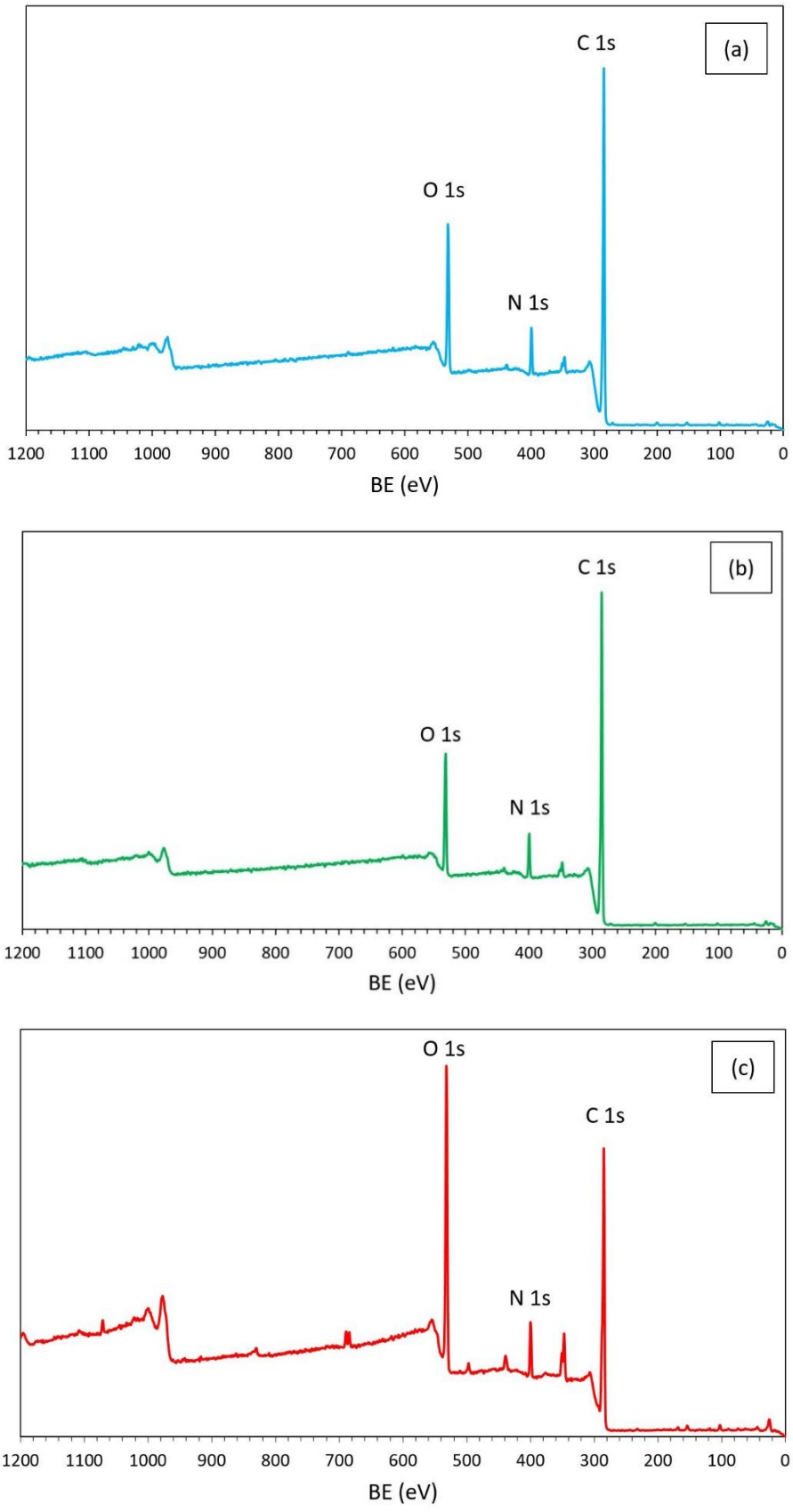

Fig. 5.20. Wide-scan XPS spectra of (a) degreased, (b) abraded or (c) LPP-treated substrates.

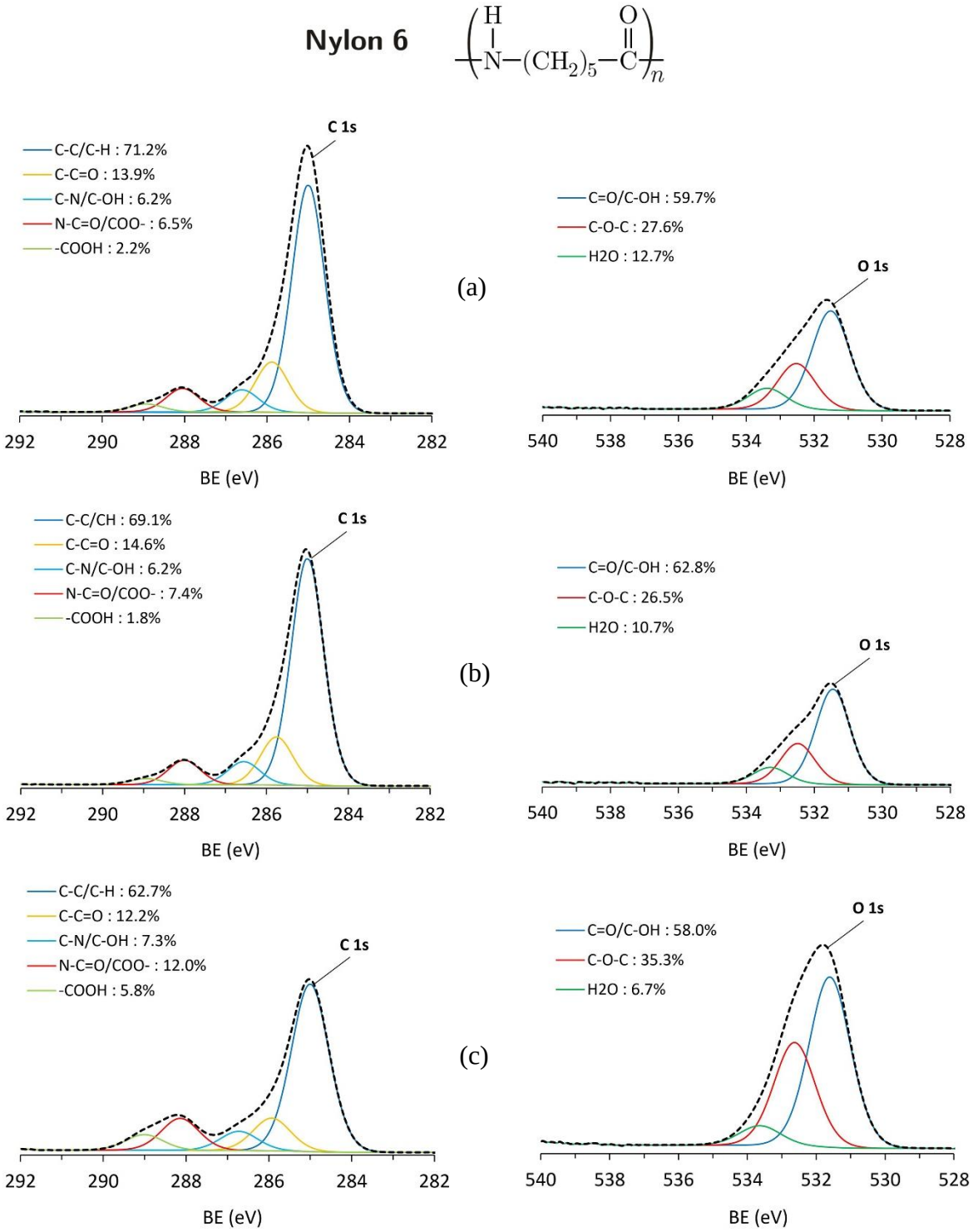

Fig. 5.21. High-resolution XPS spectra representing the C 1s (on the left) and O 1s (on the right) peaks acquired on the AM-CFRT surfaces after the following preparations: (a) solvent degreasing, (b) mechanical abrasion, (c) LPP.

5.3.2.2 Mechanical performance and failure behavior of the adhesive joints

Knowledge of the limits achievable by the system is particularly important considering that, for many applications, assembly via adhesive bonding is an integral part of the manufacturing process. Of course, the distinctive advantages of composites also have to be guaranteed by their joining. For this reason, performance of the base material and severity of the application should drive process engineers in the choice of adhesives and pre-bonding treatments able to satisfy quality requirements in line with those of the overall structure.
As the previous mechanical characterization showed, the 3D-printed composite base material has the potential for manufacturing components having strength and stiffness comparable to those of more traditional CFRP materials. This result, in principle, would make plasma one of the most suitable methods to prepare the composite surfaces and obtain quality joints. In line with the previous investigations on the CFRP reported here, indeed, the results shown in paragraph 5.3.2.1 confirmed that, also for the Onyx surface, low-pressure plasma treatment is effective in creating conditions of wettability and chemistry that are adequate to adhesive bonding. Despite this, owing to the intrinsic non-homogeneity of the base material, the application of plasma treatment on the 3D-printed composite substrates had an effect that was different with respect to that observed on conventional CFRP, as discussed in the following.
The surface treatments previously examined were tested, and their different effectiveness was exploited to detect and highlight those criticalities that might limit the application of adhesive bonding to 3D-printed CCF composite materials. In this regard, **Fig. 5.22** shows the load-displacement curves recorded testing the composite SLJs, whereas in **Table 5.12** the test results are listed, together with indications of the related failure mode observed.

Table 5.12
Significant results of shear strength measurements for the different treatment conditions.

Surface treatment				Maximum load (N)	TSS (MPa)	Failure mode
Degreasing				1394.6 ± 87.4	4.5 ± 0.3	AF
Abrasion				1812.2 ± 82.2	5.8 ± 0.3	AF
LPP	Gas	t (s)	P (W)			
	Air	180	50	5873.4 ± 134.4	18.8 ± 0.4	SF
			100	5274.6 ± 357.1	16.9 ± 1.1	SF
			150	4633.4 ± 305.8	14.8 ± 1.0	SF

Generally speaking, mechanical tests confirmed a remarkable increase in shear strength of the adhesive-bonded joints due to plasma treatment compared to traditional pre-bonding methods, such as simple degreasing (**Fig. 5.21a**) or mechanical abrasion (**Fig. 5.21b**). Tensile Shear Strength (TSS) of the degreased-only joints stood at 4.5 ± 0.3 MPa, whereas

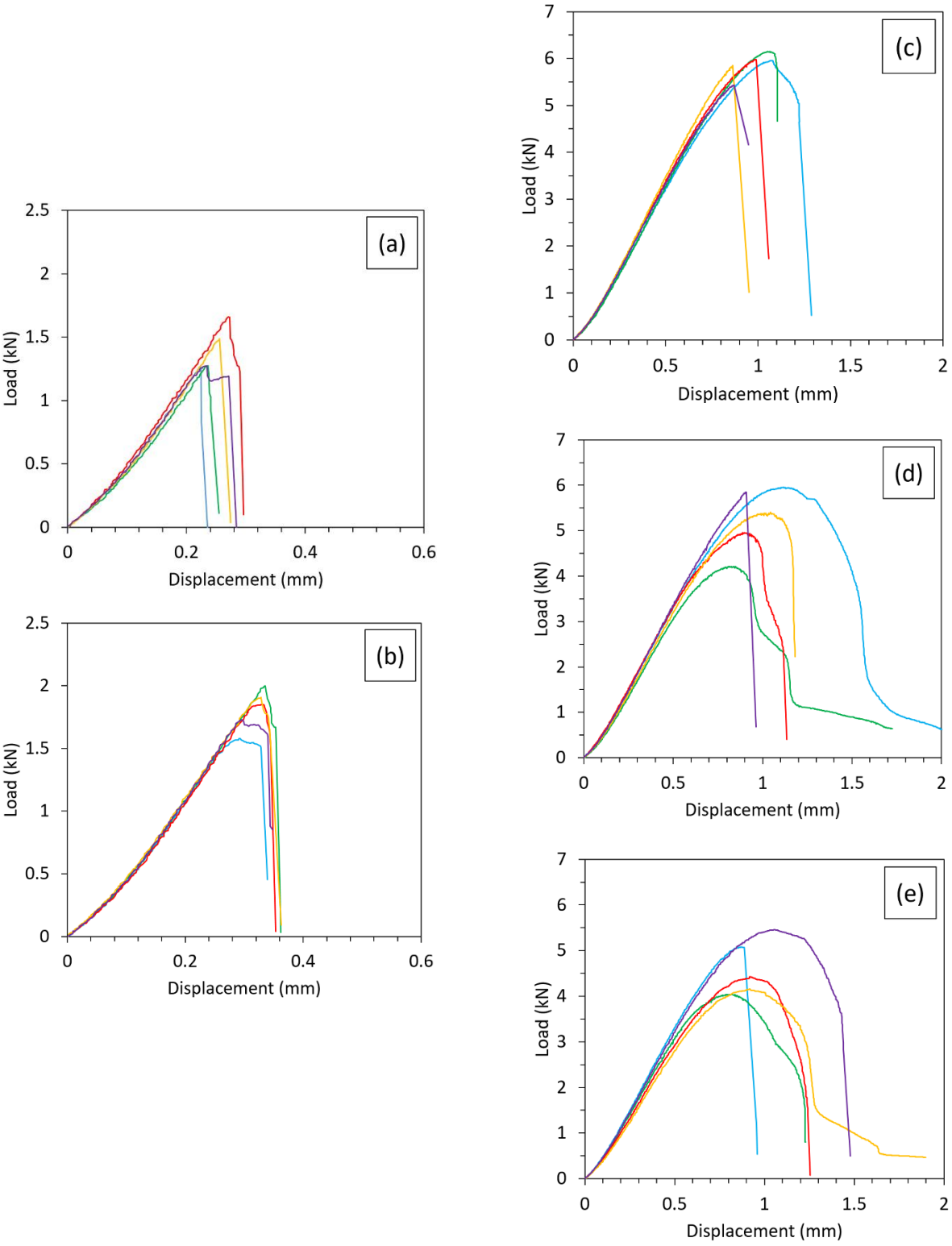

Fig. 5.22. Load-displacement curves obtained from TSS testing of joints adhesively bonded after the following preparations: (a) solvent degreasing, (b) mechanical abrasion, or LPP at (c) 50 W, (d) 100 W, (e) 150 W. To draw each graph, five SLJs per set of surface conditions were tested, and the curve referred to each repetition is displayed.

after mechanical abrasion of the faying surfaces, its value was about 29% more (5.8 ± 0.3 MPa).

To explain the enhanced joint resistance observed after abrasion with respect to the former, a consideration has to be made about the viscosity of the adhesive used. Indeed, speed and depth of the adhesive infiltration within the surface irregularities depend on the rheology of the adhesive itself, just as it is in this case, where the viscosity of DP490 epoxy adhesive decreased its penetration ability. Consequently, a reduction in roughness led to an improvement in the shear performance, since the actual contact area increased.

However, in both cases, failure was 100% de-adhesive in type (AF) since it always occurred at the interface between resin and substrate, thus proving weak adhesion interactions between the two. Indeed, after joint failure, one of the two contact areas appeared smooth as the adhesive layer (~0.25 mm in thickness) remained firmly attached to the other surface, as also detectable from the fracture profiles shown in **Fig. 5.23a** and **b**.

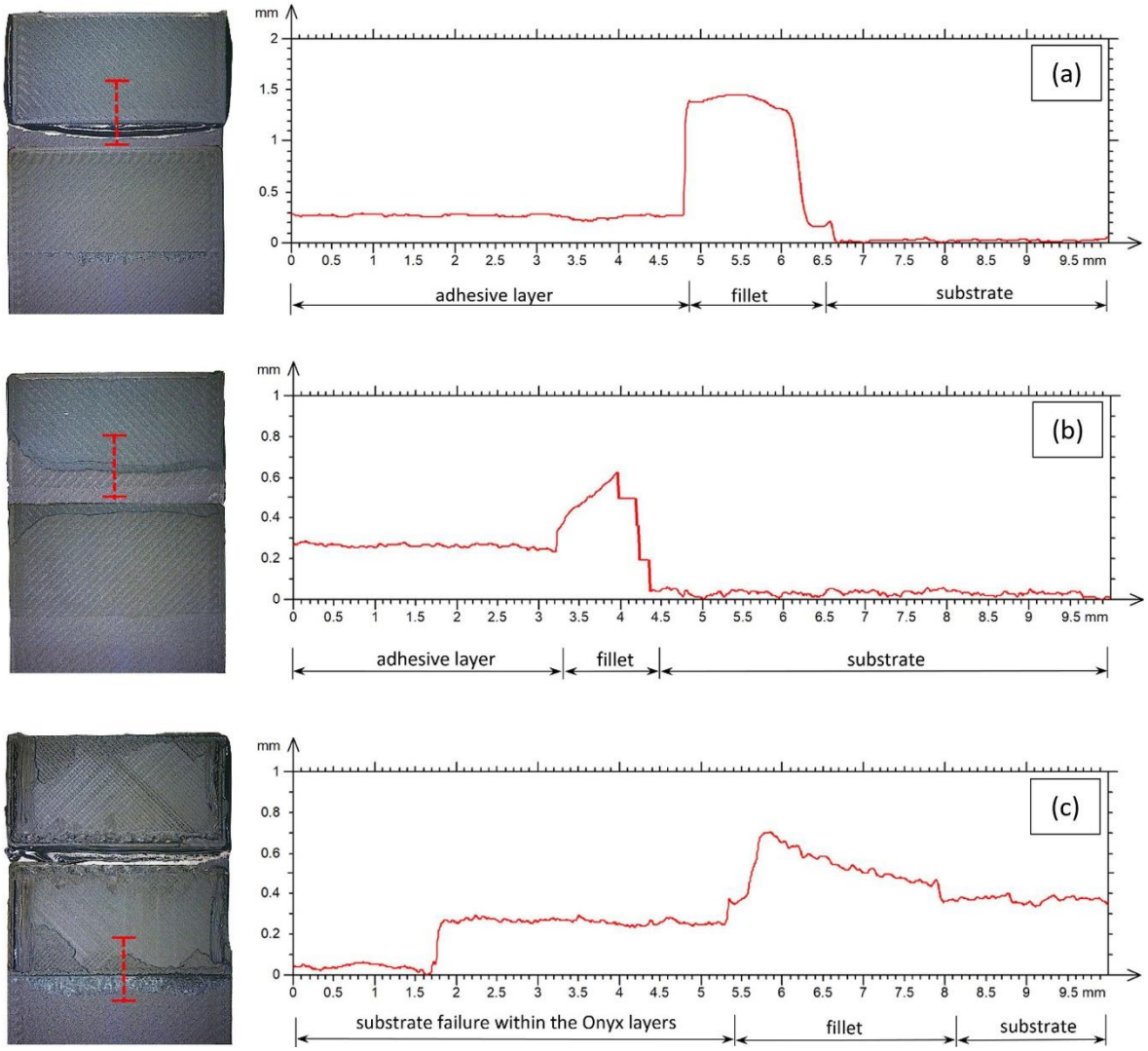

Fig. 5.23. Fracture areas and related failure profiles of (a) degreased-only, (b) mechanically abraded or (c) LPP-treated joints, acquired along the corresponding red dotted lines.

Contrariwise, the LPP treatment determined a significant improvement in the mechanical behavior of the joints, with an increase in shear strength up to 224% more than that of the abraded joints. Based on the preliminary surface analyses, the enhancement in mechanical resistance obtained using plasma has to be differently interpreted than the case before, not being attributable to changes in the contact area extent. Indeed, surface finishing of the LPP treated joints being the same as the degreased-only ones, similar considerations about the rheological properties of the adhesive should still be valid. Hence, the causes for this improvement have to be sought in the chemical state modification brought about by LPP. In particular, the increased number of polar groups supplied more reactive sites for interfacial bonding between the Onyx layer at the surface of the CFRT material and the epoxy adhesive applied, thus leading to better mechanical performance.
As previously pointed out, the enhancements in joint resistance are closely related to the power-time-gas combinations adopted during the process. LPP treatment was therefore performed using three power levels (50, 100 and 150 W) in an attempt to make any variations in mechanical or failure behavior evident. Indeed, from the previous analyses focused on the LPP treated CFRP substrates, it was highlighted that any variations in the treatment power were statistically more effective on the joint performance than the exposure time. It is reminded that, in that case, LPP treatment had led to cohesive failures, resulting in TSS-values ranging from 26.7 to 31.2 MPa on average.
Nevertheless, in the present case, the three differently-powered plasmas uniformly led to substrate failures (SF), although the deviation among the results appeared quite large. Thus, despite it not being possible to draw any conclusions about the influence of specific process parameters on the adhesion properties of the material, shear testing of the SLJ still highlighted two aspects of main interest, summarized as follows:

- with this adhesive system, mechanical abrasion alone cannot be considered as a valid pre-bonding solution to obtain quality joints, since the increase in shear strength relative to simple degreasing of the surfaces would not be enough in most of the applications in which composite materials are used. It follows that more effective treatments are needed to reach proper quality for the adhesive-bonded assemblies, making their performance adequate to that of the rest of the structure built in CCF-reinforced plastic. Regardless of the power set-up, LPP resulted fully effective as a pre-bonding treatment of the Onyx surface, leading to interfacial conditions that made the adhesive interactions between substrate and resin strong and stable;

- the stronger the adhesion forces at the adhesive/Onyx interface were, the more vulnerable the base material proved to be, the latter becoming the weakest part of the overall adhesive system. Indeed, as observable from the load-displacement curves related to LPP-treated joints (**Fig. 5.22c-e**), before reaching the ultimate load, a progressive reduction of the curve slope took place. This non-linear region has to be associated with plastic deformation and fracture propagation within the matrix of the composite. Despite the substrates having been built with the same conditions and having failed similarly, a lack

of repeatability was observed among the results, making each rupture unpredictable.

Focusing on the latter point, the identification of the joint failure mechanism was deemed fundamental to supply further information/data that might guide the additive criteria for composite printing. Indeed, as discussed earlier, the multilayer substrate did not prove its limits until a high-performing treatment was employed. In this case, failure profile measurements demonstrated that the cracks always propagated within the substrate following specific planes, which corresponded to certain built layers. In particular, two positions appeared to be weak points for the substrate: the Onyx-to-Onyx interface, where detachments between subsequent layers composing the outer shell of the specimen occurred (**Fig. 5.23c**); and the interface between the Onyx shell and the CCF layer just below (**Fig. 5.24**).

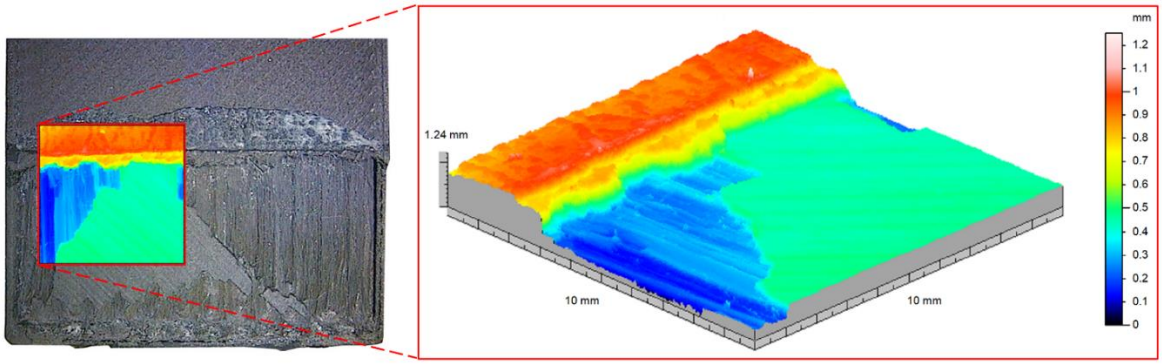

Fig. 5.24. Fracture area of an LPP-treated joint. Crack propagated both within the Onyx outer shell and at the Onyx–CCF interface.

Owing to the failure position, such behavior is believed strictly related to a particular failure mode observed from the tensile testing performed on the base material. With the 0°-CCF arrangement, as previously discussed, failure occurred due to the sharp fiber breakage in the specimen core. However, regardless of the fiber pattern in the sample core, after complete rupture, a slight detachment was observed of the roof/floor Onyx shell from the CCF layer below, as observable in **Fig. 5.25**, in which a detail of a failed 0°-CCF tensile specimen is shown. This is presumably due to effects related to the interlaminar bonding performance of the base material, and surely it also affects the joint performance when this is stressed to shear. Indeed, as Caminero et al. [47] stated, maximum achievable strength in 3D-printed CCF composites is limited by both the matrix/matrix and fiber/matrix interactions in portions that may be rich in porosities and voids. The latter are intrinsically due to the printing procedure, in which no pressure is applied after the layer is laid down. Thus, the absence of a further consolidation step leads to interlayer defects, typically resulting in material discontinuities – the number and extent of which are not easily predictable – that might be sites of stress concentration and crack initiation.

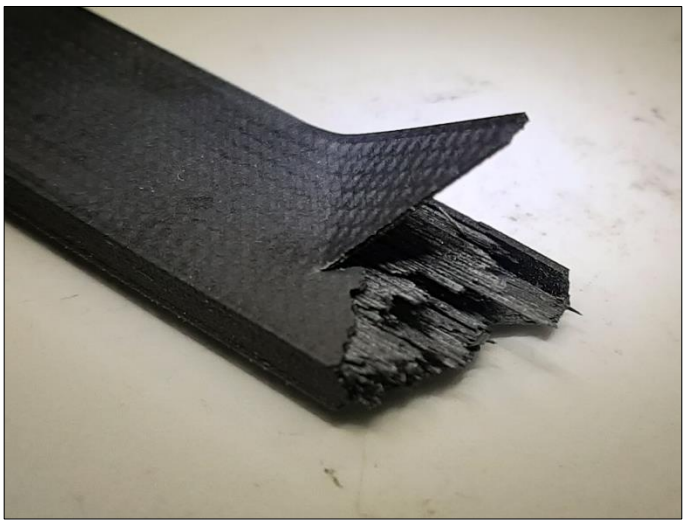

Fig. 5.25. Detail of the detachment of the Onyx shell from the CCF-layer after tensile testing of the base material.

The under-load behavior and failure mode of the plasma-treated joints were further emphasized by the mechanics of TSS test, to which the higher ductility of the Onyx (in direct contact with the adhesive) relative to the stiffer CCF-core also contributed. Indeed, during shear tests, the load is applied aligned to the centerline of the SLJ, but – depending on the substrate stiffness - it might also produce a slight bending moment that progressively makes the joint section rotate. In principle, the rigid adherend core, designed of multiple CCF layers, contrasts bending, minimizing its value. Nevertheless, the system is not homogeneous, and thus neither is its response. Indeed, based on the nature of the outer shell, during testing, greater deformations occur on the Onyx side. As previously discussed, the outer Onyx layer shows increased bonding capacity towards the adhesive after LPP treatments. However, such a condition makes the Onyx shell become an intermediate, ductile layer between the epoxy adhesive and the substrate core, thus having completely different mechanical properties from the latter. As schematized in **Fig. 5.26**, during shear testing, such a multilayer configuration of the joint makes the Onyx slip on the CCF core below, progressively causing interlaminar failure within the bulk and/or peeling from the composite support.

This behavior has a severe impact on the joint integrity and thwarts any effort made to optimize the system in making it robust in terms of adhesive selection and surface treatment. Indeed, both weaknesses of interface bonds between contiguous layers and material discontinuities are, at this stage, practical issues not yet solved for 3D-printed composite materials. The risk is to strongly limit the use of adhesive bonding for those applications in which traditional polymer composites are commonly joined through resins. This might reduce the interest that additive manufacturing of composites is gaining in many structural applications.

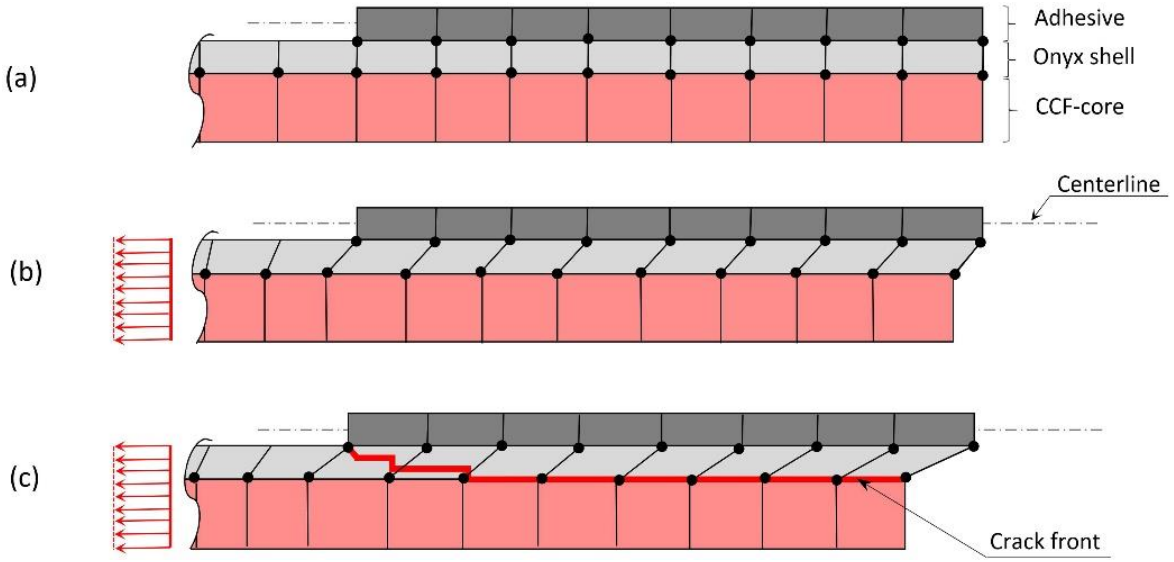

Fig. 5.26. Schematization of the mechanism of crack propagation at the Onyx-CCF interface during TSS testing of joints in high-performing conditions of treatment: (a) unloaded configuration, (b) under-load deformation and (c) subsequent slip of the Onyx layer on the CCF support, with crack propagation.

6. Conclusions

In *Part A*, a comprehensive experimental campaign was carried out in order to point out and discuss the effects of various pre-bonding techniques such as abrasion, peel-ply and LPP treatments, especially focusing on the engineering of the latter considering four different process gases (air, oxygen, argon, and nitrogen), at different powers and exposure times. At first, mechanical testing was performed on joints manufactured using CFRP made with hand lay-up method, arranging 5 layers of 5H-T800-258gsm carbon plies, pre-impregnated with epoxy resin. The surfaces were treated using the aforementioned techniques. From the mechanical characterization – which involved 36 different plasma-treatment conditions – it was possible to identify, for each gas, the optimal plasma combination of power and exposure time, which ensured reaching the highest shear strength of the joints. Considering also all further analyses of contact angle, morphology and chemical state of the CFRP surfaces for a subset of the most significant combinations of plasma treatment, the following conclusions can be drawn:

- Compared to the reference abraded joints, those prepared using plasma with air, oxygen, argon or nitrogen showed enhanced shear strength up to 44.7%, 41.7%, 38.1% and 35.5%, respectively. Failure was almost-completely cohesive in type in every set of joints so-treated, thus confirming the success of such a surface treatment.
  Nevertheless, some differences were detected among the cases examined. Specifically, air- and oxygen- plasmas resulted in more robust processes with respect to those generated using argon or nitrogen. It is worth noting that, in the former, effectiveness of the treatment seemed not to be greatly affected by power-time settings. As an example, concerning oxygen, although the highest shear strength corresponded to the highest values of both power and time, significant results were also achieved with short-time, low-powered processes. For these reasons, oxygen and air might be considered as preferable choices in terms of both efficiency and economy of the process;

- LPP treatment brought about an effective morphological modification of the CFRP surface, leading to creation of crater-shaped valleys that increased the mechanical interlocking between adhesive and adherend. Roughness increased accordingly, following a trend that seems to be in accordance with shear strength;

- Plasma treatments also result in a remarkable increase of the polar component of the SFE, thus causing enhancement of the capability of the substrate to be wet by the adhesive. In other terms, LPP allows the resin to penetrate more easely into any surface irregularities, and generate stable chemical bonds with the adherend. In particular, activation and rise in hydrophilicity of the CFRP surface could be related to the oxidizer effect of LPP itself, which appears with a strong increase of the oxygen/carbon ratio and a deep stimulation

of polar species produced by the bond between oxygen and carbon (*e.g.*, C-O, C=O, O-C-O, O-C=O).

Once the surface effects of LPP treatment had been identified, it was believed interesting to assess how such a preparation might affect joint durability. Therefore, the second stage of the work (*Part B*) was focused on evaluation of the behavior of adhesively-bonded joints subjected to severe hygro-thermal aging. A different configuration of the CFRP base material was used. Based on *Part A* results, LPP treatment was employed adopting air or pure oxygen as process gases, and working parameters such as power and exposure time were tested again in order to determine those treatment conditions to undergo an accelerated aging cycle. Thus, a preliminary testing campaign was performed under standard laboratory conditions to evaluate shear strength of SLJ, comparing effectiveness of LPP treatments to traditional mechanical abrasion of the adherends. At this early stage, experimental findings confirmed how this physical method provides competitive performance over abrasion, resulting in an enhancement of the shear resistance which stood at 4.0 to 21.4% using air and 5.4 to 25.0% with O_2.
The four sets of LPP-treatment conditions which provided the extremal values of increment were then subjected to an accelerated cyclic aging. The same conditioning was also adopted for abraded joints, which were employed as control references.
It was observed that:

- The post-curing effect provided by prolonged stay at 70°C results in a higher grade of polymerization of the adhesive. The LPP-treated joints failed cohesively, independently of the process parameters employed;

- Compared to mechanical abrasion, all plasma treatments investigated here turned out to be effective for both short- and long-term performance of adhesive joints, and the rate of decrease in mechanical resistance over time is believed to have been caused by a slight degradation of the resin due to plasticization. It follows that even process-parameter conditions considered less effective in the short-term could be adopted to preserve long-lasting shear resistance.

A wedge cleavage test (WT) allowed verification that all four LPP-treatments considered show comparable performances both at initial crack opening and during crack propagation over aging. In particular:

- The overall behavior of the plasma-treated specimens at the wedge insertion implies higher values of energy release rate, G_{Ic}, thanks to lower values of the initial crack length, a_0, compared to the abraded specimens. Observation of the fracture area confirmed the role of LPP treatments in generating strong adhesive bonds between adhesive and adherend: such conditions proved to be effective even when peel/cleavage stresses are exerted;

- Measurements carried out at the crack propagation stage (aging) demonstrated an overall hygro-thermal steadiness of the adhesive system employed. Crack-growth trend was in all cases asymptotic and crack length, a, increment tended to reduce to zero owing to the progressive reduction of the stress at the crack tip.
  Among all the differently treated joints, the final crack extension was nearly equivalent, meaning that the propagation rate during aging is independent of surface treatment and only depends on the properties of the adhesive, which are the same for the abraded and LPP-treated samples.

The knowledge gained about the effectiveness of plasma treatment on conventional composites was exploited in *Part C* of this work, in which the mechanical and failure behavior of an adhesive system made of CCF-composite substrates additively manufactured via FFF and epoxy adhesive was investigated. A comprehensive experimental campaign was carried out to demonstrate how such a novel system responds to adhesive bonding after different surface treatments, using conventional pre-bonding preparations (degreasing or abrasion) along with a more effective low-pressure plasma treatment. This allowed determination of the joint performance and identification of the limits of the 3D-printed composite, when its conditions are stressed in adhesive bonding by varying surface preparation.
From the experimental findings, the following main aspects were thus highlighted:

- Compared to traditional pre-bonding methods, LPP is fully effective also on AM composites having Nylon-6 matrix. Since no topological changes were brought about, with this adhesive system, the predominating adhesion mechanisms are those which represent a premise for strong interactions between surface and adhesive, involving chemical bonds. These characteristics translated into increased shear strength of the adhesive joints;

- The intrinsic non-homogeneity of the additively-built base material was also the limit for the adhesive system. Indeed, failure analysis pointed out that crack planes corresponded to specific printed layers, precisely positioned at the interface between the CCF core and the Onyx shell, or just within the Onyx shell. The presence of the latter is unavoidable due to the construction criteria followed by the slicing software, which does not allow outer uncovered CCF-layers. To overcome this limitation, a correction should be implemented directly on the 3D-printer software, allowing users to have more freedom in excluding, during creation of the Onyx shell, those portions of the built component selected for adhesive bonding. In parallel, more efforts should be made to improve the 3D-printing process with hardware solutions aimed at maximizing the interlaminar bonding performance, reducing the extent of material discontinuity in the bulk.

Annex: Substrate selection for Part C based on the evaluation of the tensile and flexural behavior of FFF composites manufactured by varying the CCF orientation

A.I – *Experimental set-up and mechanical evaluation*

Different configurations of test specimens were built to exhaustively characterize the 3D-printed composite parts and, specifically, evaluate the influence of the fiber orientation on their tensile and flexural resistance. Each set of samples was built on subsequent planes along the z-direction, each parallel to the printing bed ('flat' build mode): the CCF layers were laid down horizontally and continuously, with a fill type defined as 'Isotropic' within the Eiger® software. Following the design rationale graphically summarized in **Fig. I**, the fiber was at first arranged, layer by layer, according to unidirectional orientations: 0°, 90° or 45° angle with respect to the longitudinal direction of the specimen.

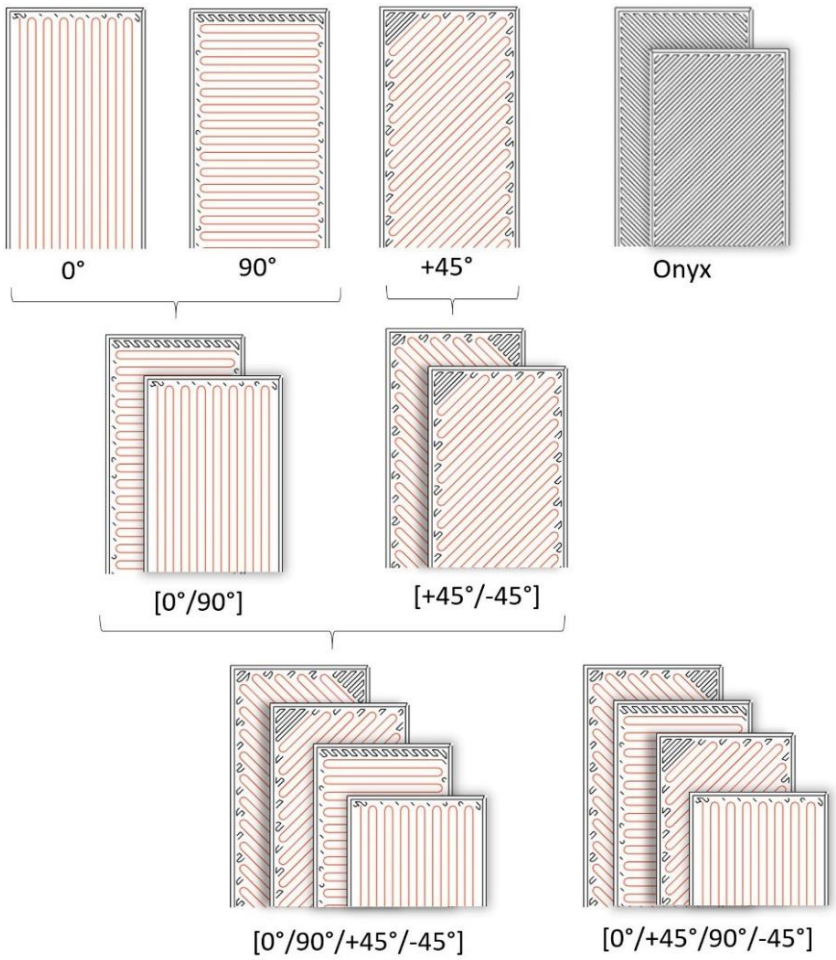

Fig. I. Scheme of the design rationale of the experimental campaign: taking the Onyx-only material as the reference wherever possible, the number of orientations of the CCF was progressively increased, combining unidirectional CCF patterns to obtain multidirectional samples.

Various combinations of the previous orientations were then considered in order to increase progressively the isotropy of the test specimens. This was done to better characterize the specific contribution of each fiber orientation to the mechanical response of the multilayer material. Specifically, two sets of specimens having $[0°/90°]_n$ and $[+45°/-45°]_n$ sequences (repeated n-times to generate the desired thickness) were printed, and a mixed-isotropic fiber pattern $[0°/90°/+45°/-45°]_n$, was also produced. Besides, a further set of samples made according to a CCF pattern $[0°/+45°/90°/-45°]_n$ was generated to evaluate whether the change of the lay-down base sequence affects the mechanical performance of the mixed-isotropic material. As then also made to manufacture the substrates, each specimen was built with four Onyx layers on the bottom and four Onyx layers on the top.
Furthermore, each layer built was made as a combination of two infill arrangements of the material: the infill made of CCF laid following one of the aforesaid directions; and a concentric infill, consisting of two Onyx rings placed along the specimen perimeter.
To assess the performance of the AM composite base material, tensile and three-point flexural test specimens were built according to the geometries suggested by the related standards, following the testing scheme summarized in **Table I**. Each configuration and testing condition was repeated five times (N=5), to enhance the accuracy of the results.
An Instron 8802 universal testing machine equipped with a 50 kN load cell was used to perform all the mechanical assessments.

Table I.
Summary of the mechanical testing and related test samples.

Testing method	Reference standard	Sample dimensions (mm)	Fiber	Orientation	Fiber Volume	Onyx layers	CCF layers
Tensile	ASTM D3039	157×16×3	Onyx	$[+45°/-45°]_{12}$	0%	24	0
			CCF	0°	52.1%	8	16
				+45°	51.2%	8	16
				90°	49.9%	8	16
				$[0°/90°]_8$	53.0%	8	16
				$[+45°/-45°]_8$	49.2%	8	16
				$[0°/90°/+45°/-45°]_4$	50.7%	8	16
				$[0°/+45°/90°/-45°]_4$	50.7%	8	16
Flexure	ASTM D7264	153.6×14×4	CCF	0°	55.9%	8	24
				+45°	54.7%	8	24
				90°	55.4%	8	24
				$[0°/90°]_{12}$	57.2%	8	24
				$[+45°/-45°]_{12}$	54.4%	8	24
				$[0°/90°/+45°/-45°]_6$	56.4%	8	24
				$[0°/+45°/90°/-45°]_6$	56.4%	8	24

A.II – *Mechanical results*

A.II.1 - Effect of the fiber arrangement on the tensile properties

Table II shows the results of the tests on the tensile performance of the specimens, having different fiber orientation with respect to the principal loading direction. These specimens were built in accordance with the geometries shown in Section 4.2.3.1.
A set of Onyx-only specimens[6], (whose stress-strain curves are shown in **Fig. II**) was also included in the analysis to provide reference values for the mechanical properties of the base material.

Table II.
Tensile testing experimental results.

Fiber	Orientation	Maximum tensile strength, σ (MPa)	Maximum strain, ε (mm/mm)	Elastic modulus, E (GPa)
Onyx	$[+45°/-45°]_{12}$	42.3 ± 1.4	0.39 ± 0.04	1.01 ± 0.02
CCF	0°	566.1 ± 13.6	0.03 ± 0.00	24.23 ± 0.20
	+45°	46.2 ± 1.1	0.03 ± 0.00	3.33 ± 0.06
	90°	23.7 ± 2.8	0.05 ± 0.01	2.23 ± 0.25
	$[0°/90°]_8$	308.9 ± 13.4	0.02 ± 0.00	15.12 ± 0.23
	$[+45°/-45°]_8$	78.8 ± 3.9	0.14 ± 0.02	4.22 ± 0.28
	$[0°/90°/+45°/-45°]_4$	192.5 ± 4.6	0.02 ± 0.00	9.35 ± 0.36
	$[0°/+45°/90°/-45°]_4$	220.9 ± 1.4	0.02 ± 0.00	11.08 ± 0.15

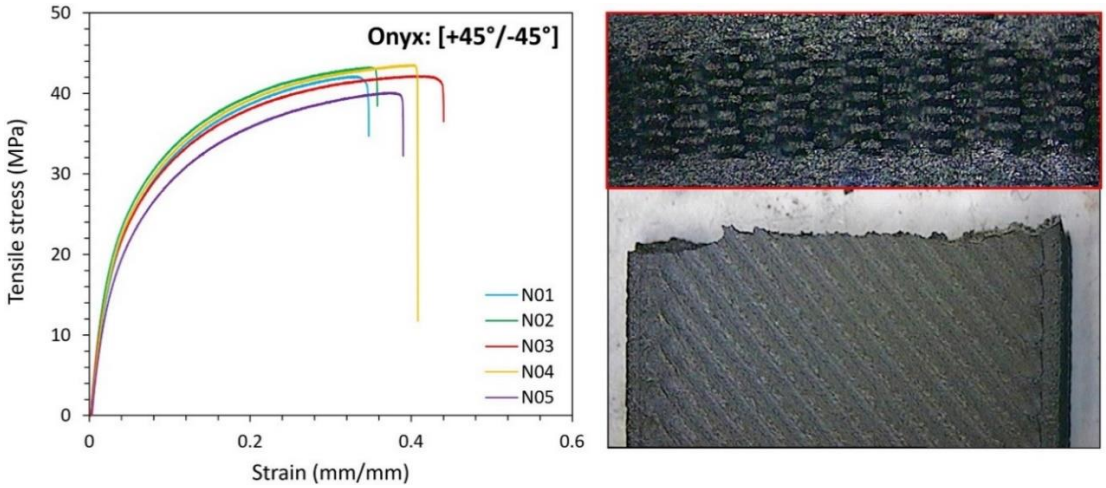

Fig. II. Stress-strain curves obtained from tensile testing of reference Onyx-only specimens and related failure.

[6] To make the results comparable, such control samples were manufactured by laying two concentric rings to generate the outer perimeter shell, filling the core of each specimen with Onyx.

- Unidirectional configurations of the tensile specimens

Among all the unidirectional configurations examined (**Fig. III**), the 0°-orientation of the CCF proved to be most efficient in providing resistance and stiffness to the composite material, since the fibers were aligned with the direction of the applied load.

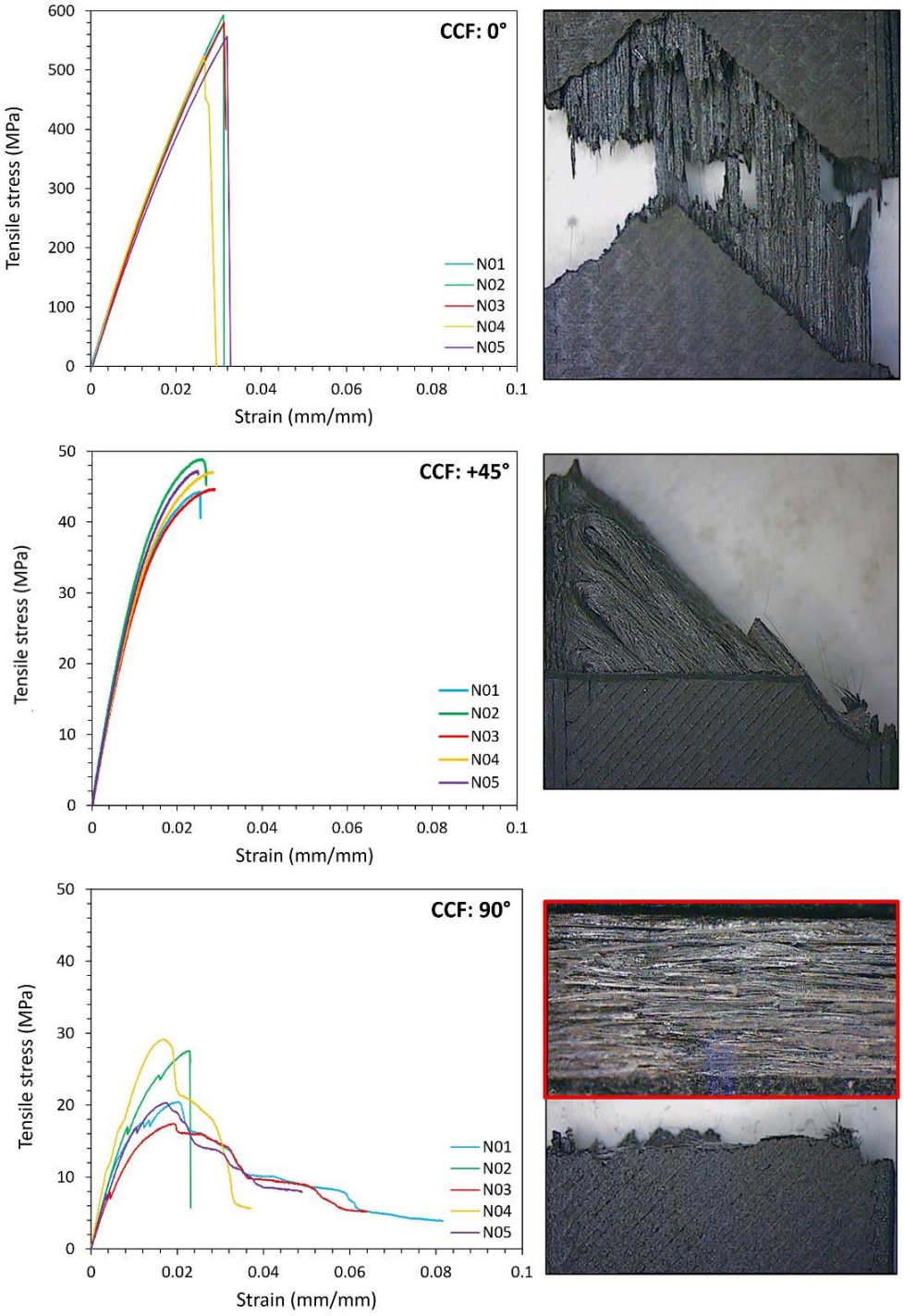

Fig. III. Stress-strain curves and failure modes obtained from tensile testing of AM composite materials printed with unidirectional CCF orientations.

With the longitudinal arrangement, most of the overall strength was due to the carbon fibers alone rather than to the Nylon matrix, which did not seem to play a significant role in the specimen performance. This aspect is all the more evident by observing both the related stress-strain curves and typical failure modes, which make it clear that properties such as high strength and stiffness, along with little deformation capability, led to sudden, brittle rupture of the specimens as soon as breakage of the reinforcement fibers occurred.
The effectiveness of the 0°-configuration is particularly evident if compared to the other specimens with unidirectional fiber arrangements. Indeed, the variation of both strength, σ, and elastic modulus, E, was not linear with the angle between the load and fibers direction. Notably, when increasing the fiber angle to +45°, a rapid loss in mechanical resistance was observed, resulting in an average σ-value that was only 8.4% more than that of the Onyx-only samples. Also E reduced significantly, standing at 3.33 GPa on average, i.e, only three times higher than that of the reference and eight times lower than the 0°-CCF. Such a condition was further emphasized by the 90°-orientation of the CCF. The latter led to strength values that were just over half of those recorded by testing the reference Onyx specimens (42.3 MPa).
Comparing the +45°- and 90°-CCF cases, it is possible to note that they shared a similar failure behavior, characterized by matrix debonding as a consequence of the progressive distancing of fibers initially adjacent. The slight difference in performance between the two, of course, has to be related to the direction of the fibers embedded in the sample core relative to the load applied. In particular, with a 90°-orientation of the CCF (i.e., perpendicular to the load direction), the mechanical behavior of the specimen proved to be worse than that of a polymer reinforced with chopped fibers, since the CCF is not oriented in such a way as to explicate its role in the ultimate resistance of the composite material. Indeed, as also observable from the related failure mode, the fracture ran transversally to the principal specimen/load direction. As mentioned above, also the +45°-CCF specimens showed similar fractures but cracks developed diagonally, according to the fiber lay-down configuration. Thus, in both cases, the detachment of the two parts occurred as soon as the failure of the polymer matrix had taken place.
The reason for such a remarkable difference between the latter cases and the reference is twofold. Concerning mechanical strength, it should be taken into account that the short fibers embedded in the Nylon matrix are directly involved in the mechanical performance of the Onyx-only specimen, these being oriented along the filament direction during extrusion. From a deformation point of view, it is worth noting that the presence of the CCF unavoidably increases the constraint grade within the material; it follows that the +45°- and, notably, 90°-orientations of the reinforcement alone are not only ineffectual but even detrimental since the fibers do not allow the matrix to deform. This greatly reduces the overall ductility of the so-loaded material and makes ultimate resistance of the specimen only dependent on the effectiveness of the matrix-to-fiber interfacial conditions on cross-sectional/diagonal planes.

- Multidirectional configurations of the tensile specimens

Each tensile sample was designed with both a concentric and mixed isotropic infill, where the latter was made by superimposing 16 CCF layers, with the following base sequences: [0°/90°], [+45°/-45°], [0°/90°/+45°/-45°] or [0°/+45°/90°/-45°].
The stress-strain curves and failure modes of both the sets of samples built using bidirectional sequences of the fibers are shown in **Fig. IV**.

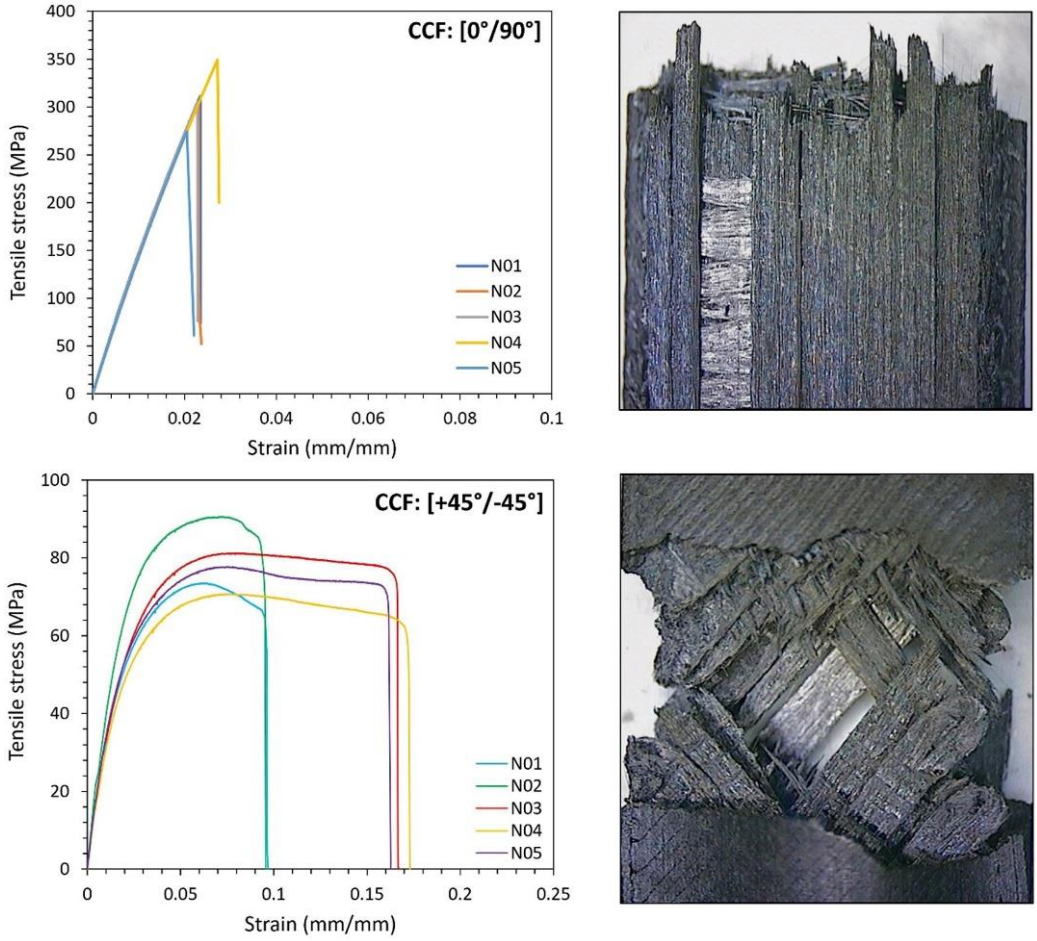

Fig. IV. Stress-strain curves and failure modes obtained from tensile testing of AM composite materials printed with bidirectional CCF orientations.

Given the symmetry of the layer number and orthogonality of the fibers, the specimens made according to the sequence [0°/90°] exhibited characteristics almost averaging those of the constituting base patterns. In particular, tensile strength stood at 308.9 MPa, namely 45.4% lower than that of the 0°-CCF samples; similarly, the elastic modulus was 62.4%. In contrast, the maximum strain achieved by the multilayer samples stood at values (2% on average) that were almost comparable to those reached with the unidirectional 0°-CCF samples, suggesting that most of the deformation is related to that of the continuous fibers on the corresponding layers. Such behavior finds confirmation in the failure mode, which was

mixed in type, involving fiber breakage at the 0°-CCF layers along with transversal matrix-to-fiber debonding at the 90°-CCF layers.
The [+45°/-45°] configuration was selected to evaluate the response of the previous configuration when subjected to a load applied diagonally with respect to the direction of the fibers. Compared to the +45°-CCF pattern alone, adoption of a symmetric configuration enhanced toughness, improving both tensile strength (+41.4%) and maximum strain (+78.6%). Also, the failure behavior appeared to be different from the previous, since fractures mainly occurred on interlayer planes rather than at the diagonal section. This might explain the increased deformability shown by the material, presumably related to shear phenomena between subsequent layers, which made the fibers stretch with respect to the original orthogonality, causing them partly to break.
It is well known that owing to the different possible loading modes and directions, most composite structures cannot be built following pre-defined orientation of the reinforcement fibers. Moreover, rigid design considerations have to be faced even when a prevalent direction of the fibers is to be defined, since it might lead to undesired loss of flexibility of the structure. This limitation pushes designers and manufacturers to build traditional CFRP parts by stacking the carbon plies to obtain a more isotropic behavior for the components. Transposing such considerations to additive manufacturing, a multidirectional set of specimens, characterized by a combination of the CCF orientations previously analyzed – [0°/90°/+45°/-45°] –, was made. In **Fig. V**, the stress-strain curves acquired during tensile testing are displayed, and a typical rupture zone of a multidirectional, quasi-isotropic test specimen is shown. As expected, such a multilayer configuration seemed to mediate the tensile behavior of the unidirectional-CCF samples, summarizing the observations made on their two-by-two coupling. Indeed, the tensile strength of the mixed-oriented CCF set stood at 192.5 MPa on average, namely 37% lower than the bidirectional [0°/90°]-CCF specimens, but almost three times higher than that obtained arranging the fibers according to a [+45°/-45°] pattern. Failure analysis demonstrated that each layer had contributed differently to the overall resistance of the additively-built structure of the specimen: in accordance with the previous observations, transversal detachment of adjacent fibers occurred on layers having 90°-CCF laydown, whereas net fiber breakage was detected on the ±45°- and, notably, 0°-oriented layers. However, despite the presence of multiple-orientation patterns, one may reasonably deem that, even in this case, the layers having the fibers aligned with the load direction affected the overall resistance of the laminate most significantly. Indeed, longitudinal fibers enhanced the specimen stiffness and resistance, allowing it to bear load levels that were remarkably higher than those responsible for the failure of the 90°-CCF or ±45°-CCF specimens. Therefore, one believes that the ultimate resistance of the laminate was reached as soon as the 0°-oriented fibers alone (on the relative layers) failed, entailing the sudden, brittle rupture observed. Similarly to that concluded regarding the [0°/90°] case, this would explain why the strain values related to this mixed pattern appeared almost the same as those acquired testing the 0°-CCF configuration: the longitudinal fibers, preventing the other layers from deforming, limited the overall sample strain capability. It is also worth noting that such behavior was not affected by the base sequence adopted to print the mixed

isotropic specimens; indeed, as reported in **Table II**, tensile testing of specimens having a [0°/+45°/90°/-45°] pattern provided for σ, ε and E values that were almost the same as those obtained from samples having base sequence [0°/90°/+45°/-45°].

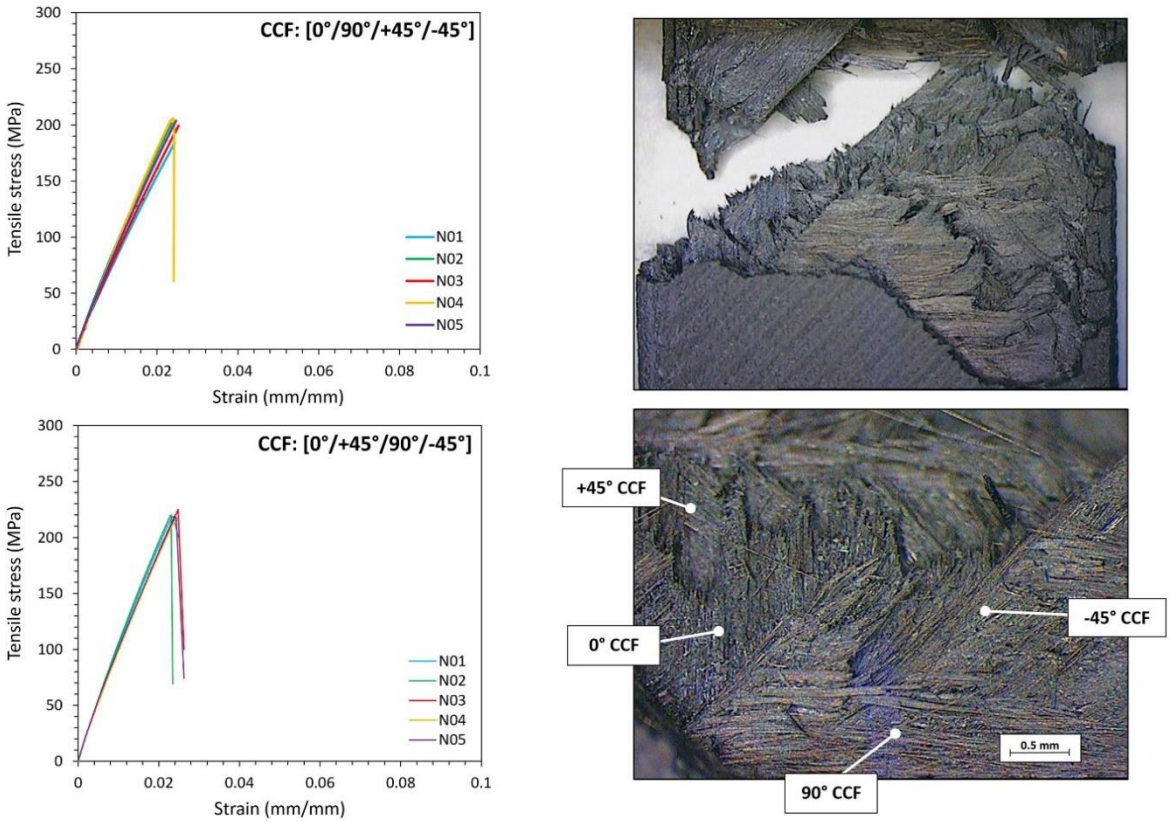

Fig. V. Stress-strain curves and failure mode obtained from tensile testing of AM composite material printed with quasi-isotropic infill patterns.

A.II.2 - Effect of the fiber arrangement on the flexural properties

The same various CCF orientations were adopted to build flexural samples having the dimensions described in Section 4.2.3.2, and a three-point flexure method was used to test them. Bending tests also highlighted how much the fiber orientation affects the mechanical response of the printed composite material, in terms of both flexural stress and strain capability. As a result, the stress-strain curves displayed in **Figs. VI** and **VII** were acquired, and the related maximum values of flexural strength and flexural elastic modulus E_f were extracted and summarized in **Table III**.

Table III.
Experimental results for the flexural testing.

Fiber	Orientation	Maximum flexural strength, $\lvert\sigma_f\rvert$ (MPa)	Flexural modulus, E_f (GPa)
CCF	0°	340.7 ± 10.1	24.39 ± 0.38
	+45°	92.0 ± 4.0	3.32 ± 0.47
	90°	51.8 ± 3.7	2.13 ± 0.17
	$[0°/90°]_{12}$	241.2 ± 4.0	14.62 ± 0.35
	$[+45°/-45°]_{12}$	101.8 ± 2.2	3.25 ± 0.33
	$[0°/90°/+45°/-45°]_6$	223.7 ± 6.4	10.29 ± 0.13
	$[0°/+45°/90°/-45°]_6$	212.9 ± 1.2	10.30 ± 0.30

- Unidirectional configurations of the flexural specimens

The flexural stress-strain curves of the sets of samples printed using unidirectional arrangements of the fibers are displayed in **Fig. VI**. In accordance with the tensile findings, the 0°-oriented specimens resulted in a high stiffness, with average maximum flexural stress σ_f of 340.7 MPa. It was especially interesting to observe that, in this case, failure occurred as soon as maximum compression load was reached, owing to the sudden breakage of the carbon fibers.

Contrariwise, with the +45°-orientation, maximum σ_f registered stood at 92.0 MPa, whereas flexure elastic modulus, E_f, was equal to 3.32 GPa. It should be noted that the diagonal CCF disposition typical of this configuration introduced an unbalanced condition in the specimen, making it twist around its longitudinal axis during bending. Such behavior led to sudden sliding of the beams from their position, causing the test interruption, despite the sample still being intact. Nevertheless, although it was not possible to experimentally evaluate the deformability of such configuration from that point on, based on the similarity of their flexural modulus, one can reasonably believe that the +45°-CCF samples would have presented flexural behavior resembling that of the 90°-CCF samples. Concerning the latter case, the so-made material led to an average maximum value of σ_f equal to 51.8 MPa and E_f equal to 2.13 GPa. With the transversal configuration of the CCFs, the specimens showed completely ductile behavior, which in fact did not allow the test to complete before the loading nose had reached the end limit of the testing machine[7].

Since the samples of the two types above were still undamaged after flexure, they were further bent to 180° using a press to make them fail. In both cases, fracture occurred along the cross section (transversal and diagonal, respectively), in accordance with that already

[7] This also led us to consider it meaningless to adopt an Onyx-only configuration as a reference and, thus, not to test any specimen of this kind for flexure.

observed on the corresponding tensile specimens.

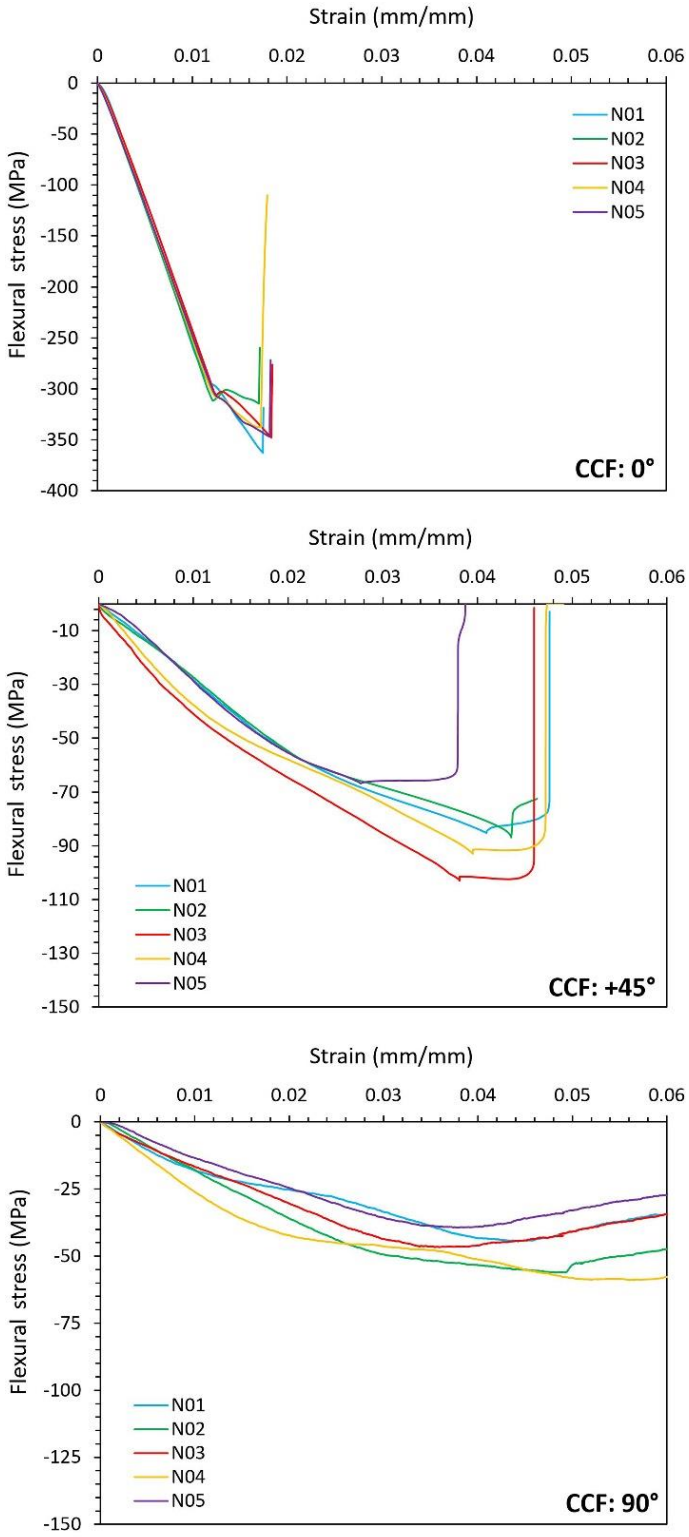

Fig. VI. Stress-strain curves and failure modes obtained from flexure testing of AM composite materials printed with unidirectional CCF orientations.

- Multidirectional configurations of the flexural specimens

From the flexural characterization of the multidirectional configurations considered, similar conclusions to those drawn after tensile testing were possible. In this regard, the reader is invited to refer to **Fig. VII**, which displays the flexural stress-strain curves acquired from bending tests performed in the four cases mentioned above.

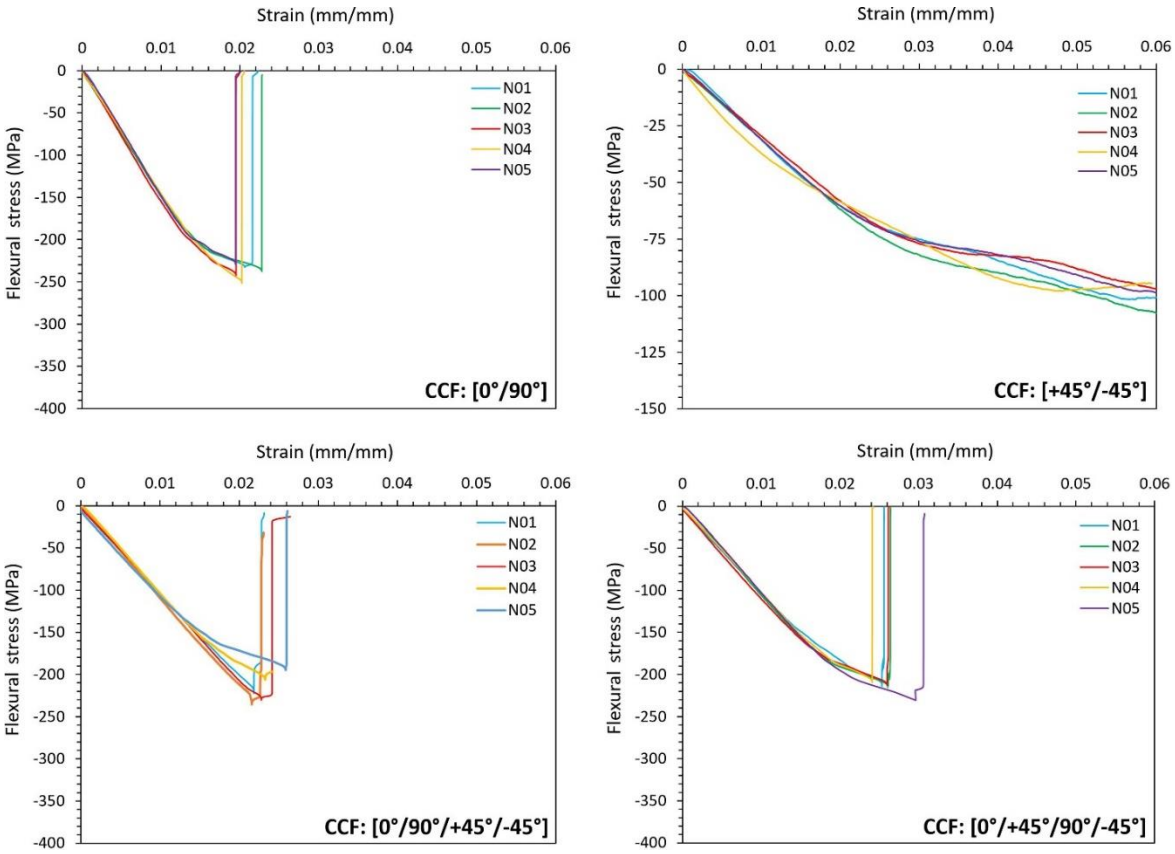

Fig. VII. Stress-strain curves obtained from three-point flexure testing of AM composite materials printed with multidirectional arrangements of the CCF.

The [0°/90°] sequence provided for stiff, high resistant composite beams, the flexural strength and modulus of which stood at 241.2 MPa and 14.62 GPa on average, respectively. Also under such load condition, failure occurred as a consequence of a mixed type fracture, from the observation of which it may be concluded that fibers arranged longitudinally affected the flexural resistance of the beam more.

In contrast, with the [+45°/-45°] orientation, maximum σ_f was -57.8% of that of the previous case. However, a remarkably higher ductility was observed (E_f stood at 3.25 GPa), and once again the test did not conclude with the specimen rupture. As previously done, the unbroken specimens were further bent to 180° using a press, but no failure occurred. Although qualitative, this result led us to reasonably conclude that a mixed-diagonal disposition of the fibers performs better than a single-diagonal one, providing for a more balanced structure of

the beam core, contrasting its torque during bending.
The aforesaid observations converged when the quasi-isotropic [0°/90°/+45°/-45°] sequence was tested for bending (**Fig. VIII**). As expected, the flexure-test results confirmed that strength and stiffness of the material are significantly dependent on the CCF-laydown used to build each layer. An average flexural strength σ_f equal to 223.7 MPa was obtained, showing slightly higher deformation than that achieved before failure by the [0°/90°] configuration. This is presumably due to the further [+45°/-45°]-layer contribution. Also in this case, the modification of the base sequence with the [0°/+45°/90°/-45°] pattern did not determine significant variations in the flexural behavior of the specimens, providing for values of both σ_f and E_f that were almost comparable to those of the base layer sequence previously analyzed.
Hence, regardless of the layer sequence employed, the experimental findings lead one to conclude that the advantages of a mixed-CCF configuration are more emphasized in flexure rather than in traction. Indeed, in the latter, it was observed that the layers having longitudinal fibers were those bearing almost all of the load applied. Contrariwise, the flexural behavior of the beam was considerably improved by superposing layers with multiple, alternate orientations of the continuous fibers, which seemed to collaborate better with each other, providing the best balance between resistance and deformability of the beam.

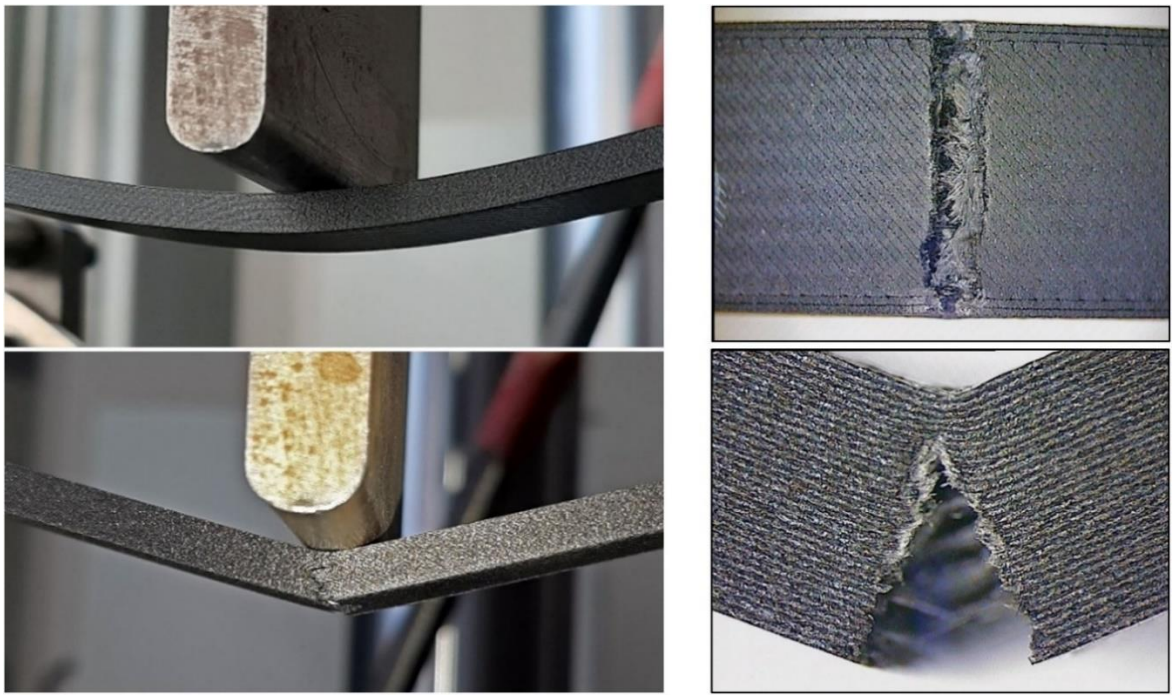

Fig. VIII. Flexure deflection and subsequent crack formation and propagation in a quasi-isotropic [0°/90°/+45°/-45°] CCF specimen.

References

[1] Friedrich K, Almajid AA. Manufacturing Aspects of Advanced Polymer Composites for Automotive Applications 2013:107–28. doi:10.1007/s10443-012-9258-7.

[2] Al-zubaidy H, Zhao X, Al-mihaidi R. Mechanical Behaviour of Normal Modulus Carbon Fibre Reinforced Polymer (CFRP) and Epoxy under Impact Tensile Loads. Procedia Eng 2011;10:2453–8. doi:10.1016/j.proeng.2011.04.404.

[3] Morioka K, Tomita Y, Takigawa K. High-temperature fracture properties of CFRP composite for aerospace applications 2001;321:675–8.

[4] Kumar SB, Sridhar I, Sivashanker S, Osiyemi SO, Bag A. Tensile failure of adhesively bonded CFRP composite scarf joints 2006;132:113–20. doi:10.1016/j.mseb.2006.02.046.

[5] Klapprott D, Li H, Wong R, Geisendorfer G. KEY FACTORS OF THE PEEL PLY SURFACE PREPARATION PROCESS n.d.

[6] Holtmannspötter J, Czarnecki J V, Wetzel M, Dolderer D, Eisenschink C. The Use of Peel Ply as a Method to Create Reproduceable But Contaminated Surfaces for Structural Adhesive Bonding of Carbon Fiber Reinforced Plastics. J Adhes 2013;89:96–110. doi:10.1080/00218464.2012.731828.

[7] Wingfield JRJ. Treatment of composite surfaces for adhesive bonding. Int J Adhes Adhes 1993;13:151–6. doi:10.1016/0143-7496(93)90036-9.

[8] Kanerva M, Saarela O. The peel ply surface treatment for adhesive bonding of composites: A review. Int J Adhes Adhes 2013;43:60–9. doi:10.1016/j.ijadhadh.2013.01.014.

[9] Schweizer M, Meinhard D, Ruck S, Riegel H, Knoblauch V. Adhesive bonding of CFRP: a comparison of different surface pre-treatment strategies and their effect on the bonding shear strength. J Adhes Sci Technol 2017;31:2581–91. doi:10.1080/01694243.2017.1310695.

[10] Davis M, Bond D. Principles and practices of adhesive bonded structural joints and repairs. Int J Adhes Adhes 1999;19:91–105. doi:10.1016/S0143-7496(98)00026-8.

[11] Wegman RF, Van Twisk J. Surface Preparation Techniques for Adhesive Bonding. Elsevier; 2013.

[12] Ebnesajjad S, Landrock AH. Material Surface Preparation Techniques. Adhes. Technol. Handb., 2014, p. 37–46. doi:10.1016/B978-0-8155-1533-3.50006-2.

[13] Palmieri FL, Belcher MA, Wohl CJ, Blohowiak KY, Connell JW. Laser ablation surface preparation for adhesive bonding of carbon fiber reinforced epoxy composites. Int J Adhes Adhes 2016;68:95–101. doi:10.1016/j.ijadhadh.2016.02.007.

[14] Oliveira V, Sharma SP, de Moura MFSF, Moreira RDF, Vilar R. Surface treatment of CFRP composites using femtosecond laser radiation. Opt Lasers Eng 2017;94:37–43. doi:10.1016/j.optlaseng.2017.02.011.

[15] Reitz V, Meinhard D, Ruck S, Riegel H, Knoblauch V. A comparison of IR- and UV-laser pretreatment to increase the bonding strength of adhesively joined aluminum / CFRP components. Compos Part A 2017;96:18–27. doi:10.1016/j.compositesa.2017.02.014.

[16] Tang L, Kardos JL. A review of methods for improving the interfacial adhesion between carbon fiber and polymer matrix. Polym Compos 1997;18:100–13. doi:10.1002/pc.10265.

[17] Montes-Morán MA, Martínez-Alonso A, Tascón JMD, Young RJ. Effects of plasma

oxidation on the surface and interfacial properties of ultra-high modulus carbon fibres. Compos Part A Appl Sci Manuf 2001;32:361–71. doi:10.1016/S1359-835X(00)00109-3.
[18] Tang S, Lu N, Wang JK, Ryu S, Choi H. Novel Effects of Surface Modification on Activated Carbon Fibers Using a Low Pressure Plasma Treatment 2007:1820–9.
[19] Shanahan MER, Vlonnier CB. Effects of plasma treatment on the adhesion of an epoxy composite 1996;16:129–35.
[20] Li R, Ye L, Mai Y. Application of plasma technologies in fibre-reinforced polymer composites: a review of recent developments. Compos Part A Appl Sci Manuf 1997;28:73–86. doi:10.1016/S1359-835X(96)00097-8.
[21] Tendero C, Tixier C, Tristant P, Desmaison J, Leprince P. Atmospheric pressure plasmas : A review 2006;61:2–30. doi:10.1016/j.sab.2005.10.003.
[22] D'Agostino R, Favia P, Oehr C, Wertheimer MR. Low-temperature plasma processing of materials: Past, present, and future. Plasma Process Polym 2005;2:7–15. doi:10.1002/ppap.200400074.
[23] Iqbal HMS, Bhowmik S, Benedictus R. International Journal of Adhesion & Adhesives Surface modification of high performance polymers by atmospheric pressure plasma and failure mechanism of adhesive bonded joints. Int J Adhes Adhes 2010;30:418–24. doi:10.1016/j.ijadhadh.2010.02.007.
[24] Molitor P, Barron V, Young T. Surface treatment of titanium for adhesive bonding to polymer composites: a review. Int J Adhes Adhes 2001;21:129–36. doi:10.1016/S0143-7496(00)00044-0.
[25] He P, Chen K, Yu B, Yue CY, Yang J. Surface microstructures and epoxy bonded shear strength of Ti6Al4V alloy anodized at various temperatures. Compos Sci Technol 2013;82:15–22. doi:10.1016/j.compscitech.2013.04.007.
[26] Marín-Sánchez M, Conde A, García-Rubio M, Lavia A, García I. Durability of titanium adhesive bonds with surface pretreatments based on alkaline anodisation. Int J Adhes Adhes 2016;70:225–33. doi:10.1016/j.ijadhadh.2016.07.001.
[27] Sargent JP. Durability studies for aerospace applications using peel and wedge tests. Int J Adhes Adhes 2005;25:247–56. doi:10.1016/j.ijadhadh.2004.07.005.
[28] Budhe S, Banea MD, de Barros S, da Silva LFM. An updated review of adhesively bonded joints in composite materials. Int J Adhes Adhes 2017;72:30–42. doi:10.1016/j.ijadhadh.2016.10.010.
[29] Reis PNB, Soares JRL, Pereira AM, Ferreira JAM. Effect of adherends and environment on static and transverse impact response of adhesive lap joints. Theor Appl Fract Mech 2015;80:79–86. doi:10.1016/j.tafmec.2015.07.004.
[30] Zafar A, Bertocco F, Schjødt-Thomsen J, Rauhe JC. Investigation of the long term effects of moisture on carbon fibre and epoxy matrix composites. Compos Sci Technol 2012;72:656–66. doi:10.1016/j.compscitech.2012.01.010.
[31] El Moumen A, Tarfaoui M, Lafdi K. Additive manufacturing of polymer composites: Processing and modeling approaches. Compos Part B Eng 2019;171:166–82. doi:10.1016/j.compositesb.2019.04.029.
[32] Quan Z, Wu A, Keefe M, Qin X, Yu J, Suhr J, et al. Additive manufacturing of multi-directional preforms for composites: Opportunities and challenges. Mater Today 2015;18:503–12. doi:10.1016/j.mattod.2015.05.001.
[33] Parandoush P, Lin D. A review on additive manufacturing of polymer-fiber composites. Compos Struct 2017;182:36–53. doi:10.1016/j.compstruct.2017.08.088.
[34] van de Werken N, Tekinalp H, Khanbolouki P, Ozcan S, Williams A, Tehrani M.

Additively manufactured carbon fiber-reinforced composites: State of the art and perspective. Addit Manuf 2020;31:100962. doi:10.1016/j.addma.2019.100962.
[35] Araya-Calvo M, López-Gómez I, Chamberlain-Simon N, León-Salazar JL, Guillén-Girón T, Corrales-Cordero JS, et al. Evaluation of compressive and flexural properties of continuous fiber fabrication additive manufacturing technology. Addit Manuf 2018;22:157–64. doi:10.1016/j.addma.2018.05.007.
[36] Singh R, Singh S, Singh IP, Fabbrocino F, Fraternali F. Investigation for surface finish improvement of FDM parts by vapor smoothing process. Compos Part B Eng 2017;111:228–34. doi:10.1016/j.compositesb.2016.11.062.
[37] Ahn D, Kweon JH, Kwon S, Song J, Lee S. Representation of surface roughness in fused deposition modeling. J Mater Process Technol 2009;209:5593–600. doi:10.1016/j.jmatprotec.2009.05.016.
[38] Harris M, Potgieter J, Archer R, Arif KM. Effect of material and process specific factors on the strength of printed parts in fused filament fabrication: A review of recent developments. Materials (Basel) 2019;12. doi:10.3390/ma12101664.
[39] Koch C, Van Hulle L, Rudolph N. Investigation of mechanical anisotropy of the fused filament fabrication process via customized tool path generation. Addit Manuf 2017;16:138–45. doi:10.1016/j.addma.2017.06.003.
[40] Brenken B, Barocio E, Favaloro A, Kunc V, Pipes RB. Fused filament fabrication of fiber-reinforced polymers: A review. Addit Manuf 2018;21:1–16. doi:10.1016/j.addma.2018.01.002.
[41] Kabir SMF, Mathur K, Seyam AFM. A critical review on 3D printed continuous fiber-reinforced composites: History, mechanism, materials and properties. Compos Struct 2020;232:111476. doi:10.1016/j.compstruct.2019.111476.
[42] Tekinalp HL, Kunc V, Velez-Garcia GM, Duty CE, Love LJ, Naskar AK, et al. Highly oriented carbon fiber-polymer composites via additive manufacturing. Compos Sci Technol 2014;105:144–50. doi:10.1016/j.compscitech.2014.10.009.
[43] Justo J, Távara L, García-Guzmán L, París F. Characterization of 3D printed long fibre reinforced composites. Compos Struct 2018;185:537–48. doi:10.1016/j.compstruct.2017.11.052.
[44] Blok LG, Longana ML, Yu H, Woods BKS. An investigation into 3D printing of fibre reinforced thermoplastic composites. Addit Manuf 2018;22:176–86. doi:10.1016/j.addma.2018.04.039.
[45] Chacón JM, Caminero MA, Núñez PJ, García-Plaza E, García-Moreno I, Reverte JM. Additive manufacturing of continuous fibre reinforced thermoplastic composites using fused deposition modelling: Effect of process parameters on mechanical properties. Compos Sci Technol 2019;181:107688. doi:10.1016/j.compscitech.2019.107688.
[46] Caminero MA, Chacón JM, García-Moreno I, Rodríguez GP. Impact damage resistance of 3D printed continuous fibre reinforced thermoplastic composites using fused deposition modelling. Compos Part B Eng 2018;148:93–103. doi:10.1016/j.compositesb.2018.04.054.
[47] Caminero MA, Chacón JM, García-Moreno I, Reverte JM. Interlaminar bonding performance of 3D printed continuous fibre reinforced thermoplastic composites using fused deposition modelling. Polym Test 2018;68:415–23. doi:10.1016/j.polymertesting.2018.04.038.
[48] Dickson AN, Barry JN, McDonnell KA, Dowling DP. Fabrication of continuous carbon, glass and Kevlar fibre reinforced polymer composites using additive

manufacturing. Addit Manuf 2017;16:146–52. doi:10.1016/j.addma.2017.06.004.
[49] Mohammadizadeh M, Imeri A, Fidan I, Elkelany M. 3D printed fiber reinforced polymer composites - Structural analysis. Compos Part B Eng 2019;175:107112. doi:10.1016/j.compositesb.2019.107112.
[50] Goh GD, Dikshit V, Nagalingam AP, Goh GL, Agarwala S, Sing SL, et al. Characterization of mechanical properties and fracture mode of additively manufactured carbon fiber and glass fiber reinforced thermoplastics. Mater Des 2018;137:79–89. doi:10.1016/j.matdes.2017.10.021.
[51] Mei H, Ali Z, Yan Y, Ali I, Cheng L. Influence of mixed isotropic fiber angles and hot press on the mechanical properties of 3D printed composites. Addit Manuf 2019;27:150–8. doi:10.1016/j.addma.2019.03.008.
[52] Yu T, Zhang Z, Song S, Bai Y, Wu D. Tensile and flexural behaviors of additively manufactured continuous carbon fiber-reinforced polymer composites. Compos Struct 2019;225:111147. doi:10.1016/j.compstruct.2019.111147.
[53] Al Abadi H, Thai HT, Paton-Cole V, Patel VI. Elastic properties of 3D printed fibre-reinforced structures. Compos Struct 2018;193:8–18. doi:10.1016/j.compstruct.2018.03.051.
[54] Pyl L, Kalteremidou KA, Van Hemelrijck D. Exploration of specimen geometry and tab configuration for tensile testing exploiting the potential of 3D printing freeform shape continuous carbon fibre-reinforced nylon matrix composites. Polym Test 2018;71:318–28. doi:10.1016/j.polymertesting.2018.09.022.
[55] Ye L. Application of plasma technologies in polymer composites : a review of recent developments 2006:73–86.
[56] Vesel A, Mozetic M. New developments in surface functionalization of polymers using controlled plasma treatments 2017.
[57] Law VJ, Mohan J, Neill FTO, Ivankovic A, Dowling DP. Air based atmospheric pressure plasma jet removal of FreKote 710-NC prior to composite-to-composite adhesive bonding. Int J Adhes Adhes 2014;54:72–81.
[58] Istituto Italiano della Saldatura. Processi di saldatura ad energia concentrata. Dispens. per la Qualif. di Int. Weld. Eng., n.d.
[59] Mandolfino C, Lertora E, Gambaro C, Pizzorni M. Durability of polyamide bonded joints: influence of surface pre-treatment. Int J Adhes Adhes 2018;86:123–30. doi:10.1016/j.ijadhadh.2018.08.002.
[60] Pizzorni M, Lertora E, Gambaro C, Mandolfino C, Salerno M, Prato M. Low-pressure plasma treatment of CFRP substrates for epoxy-adhesive bonding: an investigation of the effect of various process gases. Int J Adv Manuf Technol 2019;102. doi:10.1007/s00170-019-03350-9.
[61] Mandolfino C, Lertora E, Gambaro C, Pizzorni M. Functionalization of neutral polypropylene by using low pressure plasma treatment: Effects on surface characteristics and adhesion properties. Polymers (Basel) 2019;11. doi:10.3390/polym11020202.
[62] Pizzorni M, Lertora E, Mandolfino C. Low pressure plasma treatment of CFRP substrates for adhesive bonding : an investigation of joint durability under severe temperature-moisture conditioning. Int J Adhes Adhes 2020;99:102592. doi:10.1016/j.ijadhadh.2020.102592.
[63] Pizzorni M, Gambaro C, Lertora E, Mandolfino C. Effect of process gases in vacuum plasma treatment on adhesion properties of titanium alloy substrates. Int J Adhes Adhes 2018;86:113–22. doi:10.1016/j.ijadhadh.2018.07.007.

[64] Hamze H, Jimenez M, Deresmes D, Beaurain A, Nuns N, Traisnel M. Applied Surface Science Influence of processing gases on the properties of cold atmospheric plasma SiO x C y coatings. Appl Surf Sci 2014;315:531–7. doi:10.1016/j.apsusc.2013.12.108.
[65] Burakowski L, Petraconi G, Luís E. Evaluation of Carbon Fiber Surface Treated by Chemical and Cold Plasma Processes 3 . Results and Discussion 2005;8:281–6.
[66] Boentoro TW, Szyszka B. Protective coatings for optical surfaces. In: Piegari A, Flory F, editors. Opt. Thin Film. Coatings, Woodhead Publishing; 2013, p. 540–63. doi:https://doi.org/10.1533/9780857097316.4.540.
[67] EN ISO 1465:2009-07. Adhesives - Determination of tensile lap-shear strength of bonded assemblies n.d. doi:10.7208/chicago/9780226547404.001.0001.
[68] Sakai H, Fujii T. The dependence of the apparent contact angles on gravity. J Colloid Interface Sci 1999;210:152–6. doi:10.1006/jcis.1998.5940.
[69] Extrand CW, In Moon S. When sessile drops are no longer small: Transitions from spherical to fully flattened. Langmuir 2010;26:11815–22. doi:10.1021/la1005133.
[70] Wu S. Polar and Nonpolar Interactions in Adhesion. J Adhes 1973;5:39–55. doi:10.1080/00218467308078437.
[71] Wu S. Calculation of interfacial tension in polymer systems. J Polym Sci Part C Polym Symp 1971;34:19–30. doi:10.1002/polc.5070340105.
[72] EN ISO 9142:2003. Adhesives - Guide to selection of standard laboratory ageing conditions for testing bonded joints. n.d.
[73] ASTM International. D3762: Adhesive-Bonded Surface Durability of Aluminum (Wedge Test). ASTM Int 2006. doi:10.1520/D3762-03R10.2.
[74] Adams RD, Cowap JW, Farquharson G, Margary GM, Vaughn D. The relative merits of the Boeing wedge test and the double cantilever beam test for assessing the durability of adhesively bonded joints, with particular reference to the use of fracture mechanics. Int J Adhes Adhes 2009;29:609–20. doi:10.1016/j.ijadhadh.2009.02.010.
[75] ASTM International. ASTM D3039 - Standard test method for tensile properties of polymer matrix composite materials. Annu B ASTM Stand 2014. doi:10.1520/D3039.
[76] ASTM International. ASTM D 7264 - Standard test method for flexural properties of polymer matrix composite materials. Annu B ASTM Stand 2007. doi:10.1520/D7264.
[77] Vesel A, Mozetic M. New developments in surface functionalization of polymers using controlled plasma treatments. J Phys D Appl Phys 2017;50. doi:10.1088/1361-6463/aa748a.
[78] Moulder JF, Stickle WF, Sobol PE, Bomben KD. Handbook of X-ray Photoelectron Spectroscopy. 1992. doi:10.1002/sia.740030412.
[79] Lee H, Ohsawa I, Takahashi J. Effect of plasma surface treatment of recycled carbon fiber on carbon fiber-reinforced plastics (CFRP) interfacial properties. Appl Surf Sci 2015;328:241–6. doi:10.1016/j.apsusc.2014.12.012.
[80] Li S, Sun T, Liu C, Yang W, Tang Q. A study of laser surface treatment in bonded repair of composite aircraft structures. R Soc Open Sci 2018;5. doi:10.1098/rsos.171272.
[81] Advances in Contact Angle , Wettability and Adhesion. n.d.
[82] Baldan A. Adhesion phenomena in bonded joints. Int J Adhes Adhes 2012;38:95–116. doi:10.1016/j.ijadhadh.2012.04.007.
[83] Maeva E, Severina I, Bondarenko S, Chapman G, O'neill B, Severin F, et al. Acoustical methods for the investigation of adhesively bonded structures: A review. Can J Phys 2004;82:981–1025.

[84] Ektessabi AM, Hakamata S. XPS study of ion beam modified polyimide films. Thin Solid Films 2000;377:621–5. doi:10.1016/S0040-6090(00)01444-9.